INTRASEASONAL VARIABILITY: PROCESSES, PREDICTABILITY AND PROSPECTS FOR PREDICTION

A Thesis
Presented to
The Academic Faculty

by

Carlos D. Hoyos

In Partial Fulfillment
of the Requirements for the Degree
Doctor of Philosophy in the
School of Earth and Atmospheric Sciences

School of Earth and Atmospheric Sciences
Georgia Institute of Technology
May 2006

INTRASEASONAL VARIABILITY: PROCESSES, PREDICTABILITY AND PROSPECTS FOR PREDICTION

Approved by:

Dr. Peter J. Webster, Advisor
School of Earth and Atmospheric Sciences
Georgia Institute of Technology

Dr. Robert Black
School of Earth and Atmospheric Sciences
Georgia Institute of Technology

Dr. Judith A. Curry
School of Earth and Atmospheric Sciences
Georgia Institute of Technology

Dr. Predrag Cvitanović
School of Physics
Georgia Institute of Technology

Dr. Robert Dickinson
School of Earth and Atmospheric Sciences
Georgia Institute of Technology

Date Approved: April 10 2006

To Paula,

For her constant love, support, encouragement and much more during the past five years together. I can summarize by saying that my life with you by my side has been the best!!

ACKNOWLEDGEMENTS

I would like to sincerely express my gratitude to my advisor Peter J. Webster for his enthusiastic advising, for continuously providing excellent ideas and being strongly supportive of my work encouraging research independence. I also want to thank Judith A. Curry for her support and vision.

I want to thank the all the members in our research group for providing a nice working environment and also for all the enlightening academic discussions. I also want to thank Frederic Vitart, Mariano Hortal, Tim Palmer and Martin Miller at the ECMWF for all the support and help with the numerical experiments.

I am indebted with all professors during my graduate studies for teaching me all the fundamental physics behind the atmospheric and oceanic sciences. I will not forget their hard work and enthusiasm.

I want to thank my mother, Marina Ortiz, and my second family, Paula's family, for always being there when I needed them the most.

Lastly and most importantly, I wish to thank Paula, my wife, for all the academic and personal support. I cannot miss the opportunity to say that her questions were always the most difficult ones!!

TABLE OF CONTENTS

LIST OF TABLES

LIST OF FIGURES

SUMMARY

The intraseasonal variability is a very strong and coherent mode of oscillation observed in the Earth's climate. Rainfall variability in the intraseasonal timescale is particularly strong in the Tropics and it directly interacts with the South Asian monsoon during the boreal summer and with the Australian monsoon during the winter. Significant variability in the intraseasonal time scales is also found over Tropical Africa, as well as the Americas. A detailed analysis of the horizontal and vertical structure of the intraseasonal oscillation during both summer and winter is presented in this work considering the coupled ocean-atmosphere system. In addition, the role of the intraseasonal variability of the Southeast Asian monsoon is studied in detail.

From the applications point of view, the intraseasonal time scale is arguably the most important period of variability since higher predictability in this band will allow farmers in monsoon regions to adapt to the resulting dry and wet spells. However, extended forecasting of intraseasonal activity has proven to be a difficult task for the state of the art circulation models. In order to improve the forecasts of the Intraseasonal Oscillation (ISO) activity over the Southeast Asian monsoon region, a physically based empirical scheme was designed. The scheme uses wavelet banding to separate the selected predictand (e.g., regional precipitation in a sector of India, Brahmaputra river discharge.) and the set of predictors (e.g. OLR, 200mb and 925mb zonal wind over the equatorial Indian Ocean) into physically significant bands where linear regression followed by recombination of the bands is used to generate the forecast. Results of the empirical scheme suggest that isolating the evolution of the intraseasonal signal from higher frequency variability and noise improve the skill of the extended prediction. The hypothesis is that a similar phenomenon occurs in

numerical models: The strong intraseasonal signal observed in nature is eroded by high frequency errors due to the model parameterizations, especially in convection.

To evaluate the hypothesis, the ECMWF coupled ocean-atmosphere model was run in ensemble mode for 30 day periods initialized daily for 20 days before to 20 days after major intraseasonal oscillations, allowing the examination of the skill of the model relative to the phase of the oscillation. The forecasts represent well the observations for about 7 days after which the magnitude of the errors is greater than the signal itself. The results shows confirm the previous hypothesis, and show that errors in the convective regions due to the convective parameterization erode the intraseasonal signal in the model. An integration scheme for the coupled ocean-atmosphere general circulation model is developed in order to mimic the philosophy of the banded wavelet empirical scheme and used for 30-day forecasts. The propagation features associated to ISO activity appear greatly improved. More experiments are underway to confirm the earlier success of the Slow Manifold Model. The Slow Manifold integration scheme has been designed to be easily used as part of an operational system, providing global forecasts in the intraseasonal time scale.

CHAPTER I

INTRODUCTION

Climate variability has a strong impact on virtually all terrestrial ecosystems, affecting significantly different aspects of our society, particularly the agricultural and water resources sectors. Interactions between the different components of the climate system, which includes the atmosphere, the ocean, the land and its biomass, and the cryosphere are very complex and occur on many different times scales, resulting in diurnal, intraseasonal, seasonal, interannual, decadal, centennial, and millennial variability.

The present work mainly focuses on tropical intraseasonal variability, providing insights on the main characteristics of its life cycle and the implications for extended (20-30 days) weather forecasting. We refer to intraseasonal variability to those changes in the coupled ocean-atmosphere-land system that occur with a time scale between 25 and 80 days. These changes appear as quasi-periodic oscillations in many climate related variables, including winds in almost the entire atmospheric column, sea level pressure (SLP), sea surface temperature (SST), and, perhaps the most important from the society point of view, rainfall. Figure 1 shows an example of the impact of intraseasonal variability on rainfall over central India during wet phase of the Asian monsoon, generating periods of enhanced rainfall followed by intense dry spells with a periodicity of about 40 days. The summer of 2002, one of the driest in the 130-year record, is a remarkable case. Drought conditions persisted over India from mid-June to mid-July associated with a large-scale suppression of convection that originated over the equatorial Indian Ocean, generating losses around 6 billon USD.

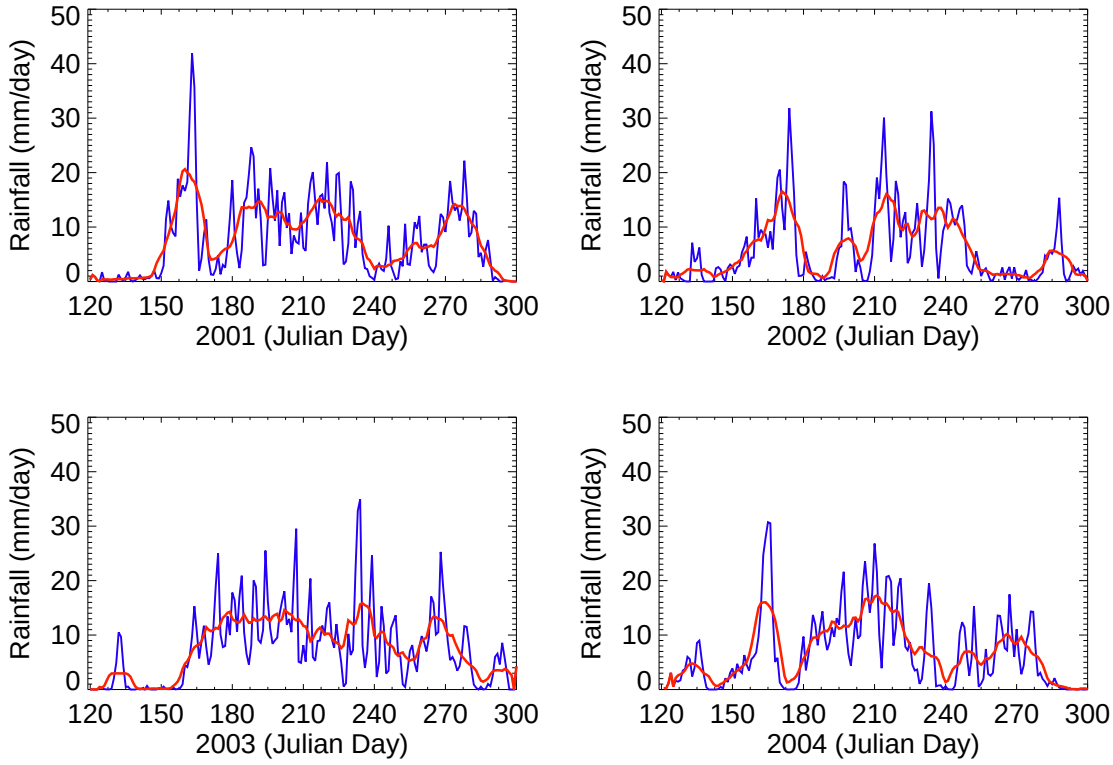

Figure 1: Daily GPI Rainfall (blue line) over Central India for the years 2001 to 2004. The red line represents the 10-day moving average. See Appendix A for a description of the GPI data set.

Intraseasonal variability is arguably the most important time scale for most agriculture related activities and decision-making, as well as many aspects associated with water resources management. This statement, that underlines the need of better intraseasonal forecasts, will be further discussed in Chapter 5.

In the following sections of this chapter, a short summary of our current knowledge of the intraseasonal variability is presented. Chapter 2 presents a global picture of the general features of the intraseasonal oscillation (ISO), including its horizontal and vertical structure, and emphasizing the differences in character between boreal summer and boreal winter, hereafter referred to as summer and winter. Chapters 3 concentrates on the regional features and effects of the ISO, with special attention to its influence in the South Asian Monsoon region, West and East Africa,

Australia, and the Americas. Statistical techniques developed to forecast intraseasonal variability associated to the South Asian Monsoon are presented in Chapter 4. Chapter 5 presents the results of a serial numerical experiment using the coupled ocean-atmosphere model of European Centre of Medium Range Weather Forecast (ECMWF) designed to study the skill of the state-of-the-art models in forecasting the observed ISO and the identification of potential error sources. While empirical tools are important in providing regional skillful forecasts, it is very important to be able to provide global self-consistent extended forecasts. In Chapter 6, a new numerical modeling technique to improve forecasts of intraseasonal variability forecasts is introduced. Conclusions of the work are presented in Chapter 7. A short compilation of all data sources used throughout the document is presented in Appendix A.

1.1 Intraseasonal Oscillations

1.1.1 General Features

Tropical rainfall exhibits strong variability on time scales of 25-80 days, referred to generically as intraseasonal oscillations. The ISOs are a naturally occurring component of our coupled ocean-atmosphere system and they significantly affect the atmospheric circulation throughout the global tropics and subtropics.

Tropical intraseasonal variability has been studied extensively since the 70's. Madden and Julian (1971, 1972) presented the first evidence of tropical ISO using spectral analysis of daily data of Canton Island (3S, 172W) station records. For this reason, ISOs are also known as Madden-Julian Oscillations (MJO), especially those intraseasonal events occurring during the boreal winter. Madden and Julian (1971, 1972) found evidence for a vertically-coherent tropospheric oscillation in the zonal wind, pressure and temperature fields at different levels over a broad range of periods that peaks between 41 and 53 days. Their analysis suggested that the oscillations were the result of an eastward movement of large-scale circulation cells starting over the

Indian Ocean. The eastward propagation of the atmospheric features was inferred by analyzing data from Balboa, Panama (9°N, 80°W).

MJOs tend to appear as coherent planetary scale waves of wavenumber 1 and 2 with a local intraseasonal period between 25-80 days. As the MJO moves eastward, positive anomalies in the convection increase as it propagates over the western pacific warm pool. When the MJO reaches the relatively cold water of the central Pacific, it dies leaving a residual Kelvin wave in the upper troposphere. Its typical propagation speed is about 5 m/s at the western Pacific (moist phase) and about 10 m/s to the east (dry phase). Besides rainfall signatures there are distinct patterns of lower-level and upper-level atmospheric circulation anomalies. These circulation features extend around the globe and are not confined to the eastern hemisphere. Thus, they provide important information regarding the regions of ascending and descending motion associated with particular phases of the oscillation (tropical waveguide teleconnection) over those parts of the tropics where rainfall is generally low or absent.

The magnitude of the MJO has an annual cycle, being more intense in the boreal winter (e.g., Hendon and Salby 1996). Also, the average period decreasing from 50 to 35 days from winter to summer of the Northern Hemisphere (Wang 1988). However despite being weaker in amplitude, the summer manifestation of the MJO, also known as monsoon ISO (MISO), probably influences directly a greater proportion of the world's population than its boreal winter counterpart. This is because during the winter the MJO activity remains trapped near the equator, while during summer, poleward propagating Rossby waves emanate from the near-equatorial MJO, some of them interacting with the Indian monsoon and influences the weather of the populous South Asia.

Rui and Wang (1990) proposed a four-staged life cycle for the intraseasonal convection anomalies: initiation, unstable intensification, maturity, and dissipation. The oscillations originate or become evident over equatorial Africa. Firm evidence of rapid

intensification is suggestive of an instability process, followed by a mature phase that is characterized by a weakening in the maritime continent and redevelopment over the western Pacific.

The MJO vertical structure (Rui and Wang, 1990) shows well defined relationships among Outgoing Longwave Radiation (OLR), zonal wind and vertical motion anomalies. Three pronounced features are evident. First, at the mature phase the upper-level divergence in the midtropics rising motion overlap the convection, while the lower-level convergence center is located at the leading edge of the convection region. Second, the amplitude of the zonal wind fluctuations at 200 mb is about twice that of 850 mb. And third, although 200 mb easterly anomalies and 850 mb westerly anomalies are coupled with equatorial convection in the eastern hemisphere, the phase speed of the wind anomalies exceeds that of convection. Therefore, the spatial phase relationship among OLR, 200 mb and 850 mb zonal wind anomalies change in the evolution process.

In general, only one fully developed MJO event exists in the tropics at a given time. Occasionally, two weak convective centers of the MJO with weak circulations may coexist, one being just initiated in the Indian Ocean and the other decaying in the central Pacific (Wheeler and Hendon 2004).

An interesting aspect of the large-scale cloud complexes associated with the oscillation was described by Nakazawa (1988). He studied the structure of the eastward-moving cloud masses with 3-hour geostationary OLR. He found that these cloud systems were composed of several eastward-moving super cloud clusters (SCCs). Each SCC was, in turn, composed of smaller cloud clusters (CCs) that moved westward. Each SCC has a horizontal scale on the order of 103 km and consists of a few CC whose scales are 102 km. The lifetime of the CC is only 1-2 days. New CC tends to form east of a fully developed CC. Hence, the apparent eastward propagation of the large-scale convective center of the MJO is due to consecutive development of new

convective systems, each on average slightly to the east of the previous one. Recent publications by Lau and Waliser (2005) and Zhang (2005) present in-depth reviews on general tropical intraseasonal variability.

1.1.2 Physical Mechanisms for the MJO

From the previous description, a full theory for the low-frequency oscillations on the tropics should explain:

1. The predominance of low-frequency oscillations in the broad period range from 30-60 days.

2. A zonal circulation with a preferred planetary scale (wavenumber 1 and 2).

3. Strong convection confined to the Indian Ocean and western Pacific sector but with upper tropospheric wind anomalies that propagate around the globe.

4. Convection and meridional winds anomalies that are trapped at the equator.

5. Seasonal variations of propagation and intensity, especially a clear northward propagation of the disturbance over India and East Asia during the northern summer monsoon season.

6. A horizontal structure, comprising a Kelvin-Rossby wave couplet (Rui and Wang 1990, Hendon and Salby 1994)

7. Vertical structure with baroclinic motion with an upward and westward tilt of vertical motion (Sperber 2003)

In the last 25 years, different mechanisms have been proposed to explain some of these MJO features, especially its slow eastward movement and its planetary scale. The theories can be grouped in the following categories:

- Cloud-Radiation interactions (e.g. Chang 1977, Hu and Randall 1994)

- Wave-CISK (Conditional Instability of the Second Kind) interaction (e.g. Lau and Peng 1987)
- Evaporation-Wind feedback (e.g. Emanuel 1987, Neelin et al. 1987, Wang 1988)
- Boundary layer feedback (Wang 1988, Blade and Hartmann 1993)

Because of the marked eastward propagation, different studies have tried to explain the ISO as a Kelvin wave. Although MJO resembles the theoretical atmospheric Kelvin wave, for a given phase speed that is as slow as that observed in the MJO, Kelvin wave theory would predict a fairly short vertical wavelength which does not appear to agree with the observations. Figure 2 shows the zonal wavenumber-frequency power spectra of the a) symmetric and b) antisymmetric components of OLR calculated from data for the period 1980-2005 as described in Wheeler and Kiladis (1999). Referring to the equatorially trapped wave theory originally presented by Matsuno (1966), the symmetric spectrum shows concentration of power corresponding to Kelvin, Rossby and Poincar'e waves while the antisymmetric spectrum shows variance associated to Yanai or mixed Rossby gravity waves. In addition, there is considerable variance between wavenumbers 1 and 4 and periods 30 to 90 days associated to the MJO that cannot be accounted for by Kelvin waves.

However, the equatorial wave theory used to derive Kelvin waves is basically inviscid because it did not include a frictional effect in the free atmosphere. Following ideas by Holton and Colton (1972), showing that the impact of vertical mixing on velocity and momentum by cumulus convection could act as a strong damping term, Chang (1977) included this mechanism referred to as cumulus friction and found in a simple model a slower zonal phase speed and faster vertical attenuation. He referred to this as viscous mode. Assuming that the main thermal sources of cumulus fraction in the Tropics are confined to the troposphere, the theory predicts that stratospheric

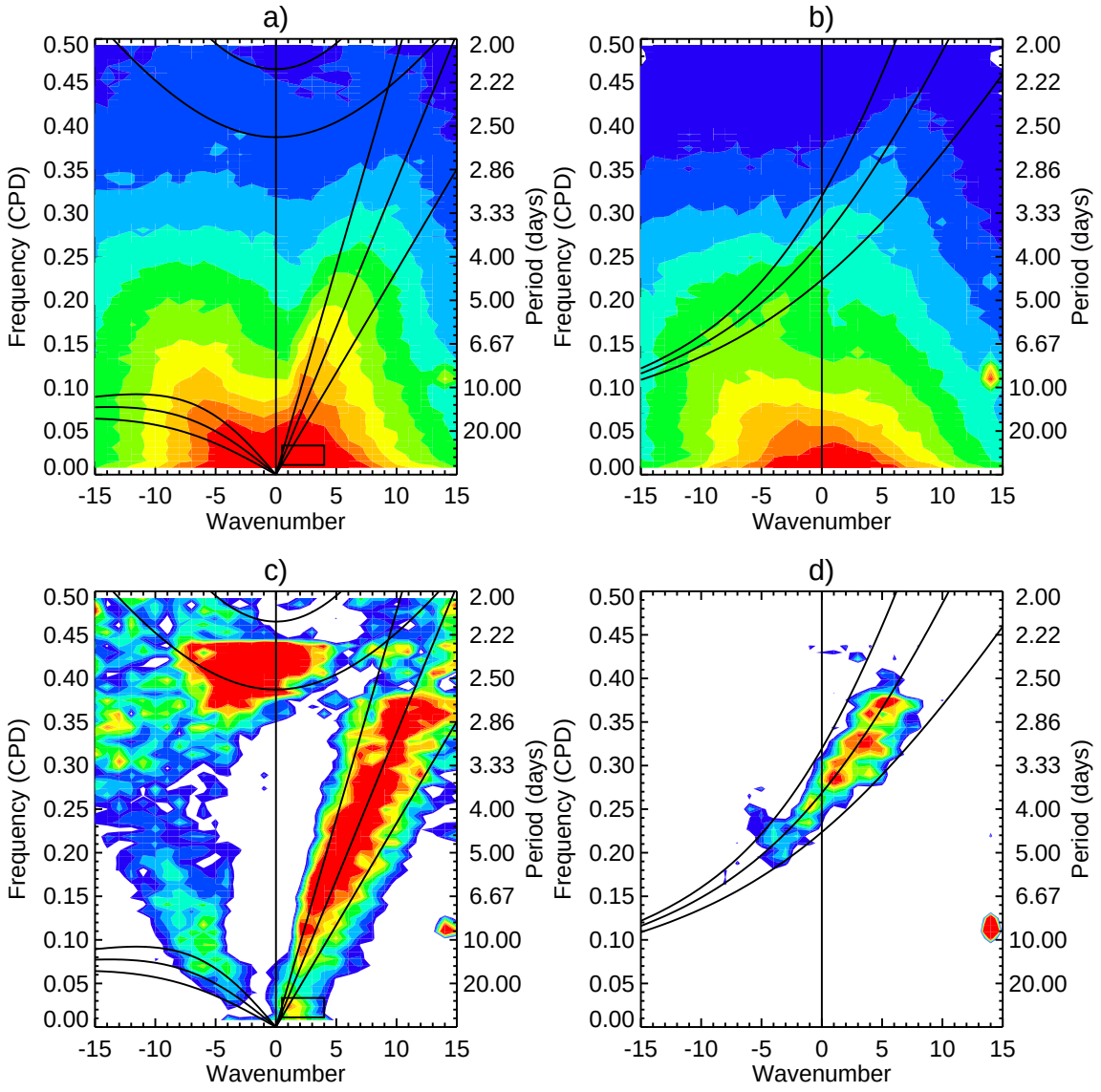

Figure 2: Zonal wavenumber-frequency power spectra of the a) symmetric and b) antisymmetric components of OLR calculated for the period 1980-2005 as described in Wheeler and Kiladis (1999). For both components, the power has been integrated between 15°S and 15°N and the base-10 logarithm has been taken for plotting purposes. Both symmetric and antisymmetric components have been scaled by the background spectra obtained by using many times a 1-2-1 filter both in frequency and wavenumber. c) and d) show the scaled spectra for the symmetric and antisymmetric components respectively. Superimposed are the dispersion curves of selected equatorially trapped waves for equivalent depths of 12, 25 and 50 meters. Positive (negative) wavenumber correspond to eastward (westward) propagating waves

waves behave like the regular inviscid Kelvin mode while the tropospheric waves behave like the viscous mode. However, results are very sensitive to the magnitude of the drag coefficient used. In real atmosphere the damping due to cumulus convection and other processes is probably more complicated than the simple linear drag term used in Chang (1977) analysis. However the agreement with observations when viscous processes are introduce suggest that the theory is relevant to the MJO.

Hu and Randall (1994) suggested that the MJO can be naturally explained as a response to localized low frequency oscillatory heating. They theorized that such an oscillating convective heat source was a result on nonlinear interactions between radiation, cumulus convection and surface moisture flux. No wave-convection feedback is required and low-frequency oscillations in precipitation result as an interaction between radiation and convection. However the theory does not explain why this type of oscillation almost exclusively starts over the Indian Ocean.

CISK, or Convective Instability of the Second Kind, provides a positive feedback mechanism, in which the release of latent heat in the cumulus formation provides energy, enabling a larger-scale convective system to grow. Lau and Peng (1987) using a non-linear CISK parameterization, considered two scenarios as the possible causes of MJO. The first scenario suggests that MJO is induced by a local oscillating heat source possibly involving feedback mechanisms among radiation, convection and dynamics (Webster 1983, Goswami and Shukla 1984). The second scenario assumes that MJO is the result of an internally forced heat source where an initial disturbance near the equator disperses away from the source region, eastward by Kelvin waves and westward by Rossby waves. The presence of an internal heating mechanism such as CISK may favor the generation of Kelvin waves. Overall, results of the oscillating heat source suggest that, in the absence of a basic flow, the entire tropical atmosphere oscillates coherently with a large-scale oscillatory heat source. Free waves propagating away from the source region are not present to any significant extent. In

contrast, Lau and Peng (1987) found that eastward propagation of the low frequency oscillation arises as a result of the interaction between convection and dynamics by the so-called mobile wave-CISK mechanism. Via this mechanism, the heat source feeds on the intrinsic east-west asymmetry of equatorial waves. As a result, Kelvin waves are selectively amplified, which in turns causes the heat source to propagate eastward. However the phase speed is still much faster than observed and is very dependent on the assumed shape of the vertical heating profile. In summary, wavelike heating functions (classic wave-CISK) fails to establish a highly organized eastward propagating super cluster.

Chang and Lim (1988) used a linearized model to investigate further the dynamics of Kelvin wave-CISK. In their experimental setup, heating was concentrated in a small longitudinal extension. From the dispersion relationship, two different modes are generated: a regular Kelvin wave and a Kelvin wave-CISK mode. Comparing the free modes (Kelvin wave) with CISK modes with the same speed, the CISK mode has a much deeper vertical structure. On the other hand, a free mode with a similar vertical structure as the slow CISK mode would propagate with a slower speed. Propagating Kelvin wave-CISK modes cannot exist in a single vertical mode CISK model. However, for the appropriate amplitude ratio and phase shift between different CISK modes (fast and slow), they can lock together into a propagating CISK mode. Interaction between vertical modes is needed to obtain the observed propagation speed. Chang and Lim (1988) conclude that in the Kelvin-wave CISK modes a portion of the heating energy is used or removed by the wave growth instead of being fully balanced by the acceleration due to propagation, explaining what was observed in Lau and Peng (1987). Kelvin wave-CISK modes have almost the correct propagation velocity and overall structure but it does not explain the Rossby wave-like structure present in the observations (e.g. Madden 1986).

Emanuel (1987) and Neelin et al. (1987) proposed independently an Evaporation-Wind feedback mechanism. Emanuel (1987) assumed that neither land-sea contrasts nor zonal asymmetry is needed to explain the basic mechanism of the oscillation. Emanuel (1987) states that unlike CISK, which regards convection as a way of releasing stored potential energy, convection is a way of rapidly distributing tropospheric heat acquired from the sea surface. The Evaporation-Wind feedback mechanism is described as follows: If the mean surface wind is from the east, perturbation easterlies will result in anomalously large flux of latent heat from sea surface. On the other hand, westerlies will be associated with reduced or negative anomalies of surface heat flux. If convection rapidly redistributes these anomalies through the troposphere this would lead vertical velocity anomalies with heating leading convection, causing the perturbation to propagate to the east. Model results with a very special treatment of convection favoring the rapid redistribution of heat throughout the troposphere and hence the evaporation-wind feedback, reproduce some aspects of the 30-60 day oscillation. Although there is some energy associated to wavenumber 1, the results of linear modeling used suggest that shorter waves should dominate the spectrum, contrary to observations.

Neelin et al. (1987) also considered evaporation-zonal wind perturbations feedback to explain MJO eastward movement with the following mechanisms: A region of anomalous latent heating on the equator will force anomalous easterly winds to the east of the region and westerlies to the west at low levels. Perturbations are superimposed to the mean easterlies as in the tropics. The strength of the surface zonal winds will increase to the east of the heating and decrease to the west; hence evaporation will also increase to the east and decrease to the west. The resulting evaporation enhancement leads to latent heating to the east of the wave. Under certain conditions the heating anomaly will increase to the east and weaken to the west, favoring or creating eastward propagating modes. Neelin's et al. (1987) modeling

experiment results, emphasizing the evaporation-wind feedback mechanism, produce an eastward-propagating, equatorially trapped mode with low phase speed. However, sources of low-frequency variability are more complex than this feedback since the suppression of the evaporation-wind feedback does not entirely remove the preponderance of eastward over westward moving low-frequency waves at the equator.

In general, linear instabilities resulting from the Kelvin wave-CISK and evaporation-wind feedback all favors the growth of small scales waves. Wang (1988) studied the MJO by properly introducing the boundary layer frictionally induced moisture convergence so that the perturbation heating is controlled either by wave convergence or by the zonal wind anomaly. In his experiment he assumes small amplitude motion in a rest state equatorial beta-plane in a two level model. Only two major heating processes are included: condensational latent heating and longwave radiation. He used a boundary layer, which is needed to determine vertical velocity at the top of the boundary layer. Results from the model reproduced very well the baroclinic structure of the MJO: oscillation in zonal wind at 150 and 850 mb are nearly out of phase as a manifestation of a direct heating-driven circulation. Results suggest that boundary layer friction play an important role in selecting the preferred zonal scale. However, the resulting phase speed is still higher than observations

Blade and Hartmann (1993) proposed the Discharge-Recharge mechanism as an explanation for the tropical low-frequency oscillations. This mechanism appears when the moist Kelvin wave propagation is inhibited by cold SST. In this case the ISO appears to be controlled by local instabilities, so that periodic generation of convective modes is ensured by cyclic oscillations of static stability. Here there are two timescales that add up to the 40-day time scale: the growth and duration times of the convection and the recharge times of the static energy in the unstable region.

In summary, to the date there is no a widely accepted theory to explain tropical intraseasonal variability. In fact, existing theories are independent and sometimes

contradicting. For example In Chang (1977), the origin of the oscillating heat source is not explained. Neelin et al. (1987) and Emanuel (1987) theory is disputable because eastward propagation depends on easterlies in a region where westerlies are predominant. Classical Wave-CISK treatment results in a phase speed twice as observed. In Lau and Peng (1987) wave-CISK formulation, which results in slower modes, the results are very dependent on the heating profile, which is specified. Also, wave-CISK cumulus parameterizations make these theories vulnerable to criticism. Wave-CISK theories suffer from what is called scale selection catastrophe, i.e., lack of selection of long waves and thus a too fast predicted phase speed. In general, what may seen to be success of some theories strongly relies on key assumptions in their parameterization.

Recently, Wang et al. (2005) and Stephens et al (2004) argued that the ISO is an instability of the coupled ocean-atmosphere system. Stephens et al. (2004) referred to the ISO as a "self-regulating oscillator" and defined a "destabilization" phase that rendered the system susceptible for a subsequent "convective" phase. The convective phase was followed by a "restoring" phase where the system stabilizes before entering into another period of destabilization. The period of time needed to destabilize the lower troposphere through the warming of the SST (by enhanced downward solar radiation during the suppressed phase) and the cooling of the upper troposphere (enhanced long-wave cooling) determined the time scale of the ISO. Wang et al. (2005) added a spatial aspect to the self-regulating oscillator of Stephens et al (2004). They noticed that the ascending region of the convective phase of the ISO in the eastern Indian Ocean produced a region of strong subsidence in the western basin, prompting a reduction of cloudiness and a destabilization period similar to the Stephens et al. concept. Wang et al. (2005) referred to sequence as "self-induction". The two theories are complementary and both point to the transition period between the suppressed and convective stages of the oscillation as critical elements of the ISO. It is important to note that both the self-regulating oscillation and the self-induction theories

refer to the coupled ocean-atmosphere system. Agudelo et al. (2005) hypothesized that physical processes associated with convection occurring during the transition between the suppressed and active phases are critical to the development of the onset and evolution of the ISO. Agudelo et al. (2005) showed that during the transition between suppressed and active phases, organized low-level moistening appears as the most important feature foreshadowing the deep convection. Convective Available Potential Energy (CAPE) also builds up during the transition phase. A combination of anomalously warm SST and ocean mixed layer, plus a strengthening low-level winds, together with large-scale subsidence promotes low-level moisture accumulation.

CHAPTER II

HORIZONTAL AND VERTICAL STRUCTURE OF THE INTRASEASONAL VARIABILITY

The intraseasonal component of the OLR over the tropics is commonly used as a proxy of the intraseasonal variability since negative OLR anomalies are associated with positive anomalies of convection and precipitation. Figure 3 shows the amplitude of the intraseasonal oscillation for the entire year as well as for boreal summer and winter independently. The Indian-West Pacific Ocean basin presents the strongest intraseasonal variability on the globe. As it will be discussed later, some of this variability is associated to eastward propagating convective signals while a fraction of the intraseasonal activity corresponds to standing oscillations. During the boreal summer, the region of maximum ISO amplitude is located predominantly to the north of the equator with regional maxima to the west of Sumatra and the western Ghats in India, the Bay of Bengal, and the South-China Sea. In the western hemisphere, important ISO variance is observed to the west of Central America. During winter, the ISO activity is mainly to the south of the equator, with maxima over the Indian Ocean, north of Australia, the South-West Pacific (South Pacific Convergence Zone), and Brazil. It is important to note that regions of high ISO activity coincide with regions of high SST (generally higher than 28 °C) and surface convergence, as shown in Figure 4. High SST guarantees the necessary source of moisture and atmospheric instability.

In order to study in detail the horizontal and vertical structure of the boreal winter and summer intraseasonal activity, both standing and propagating, a composite

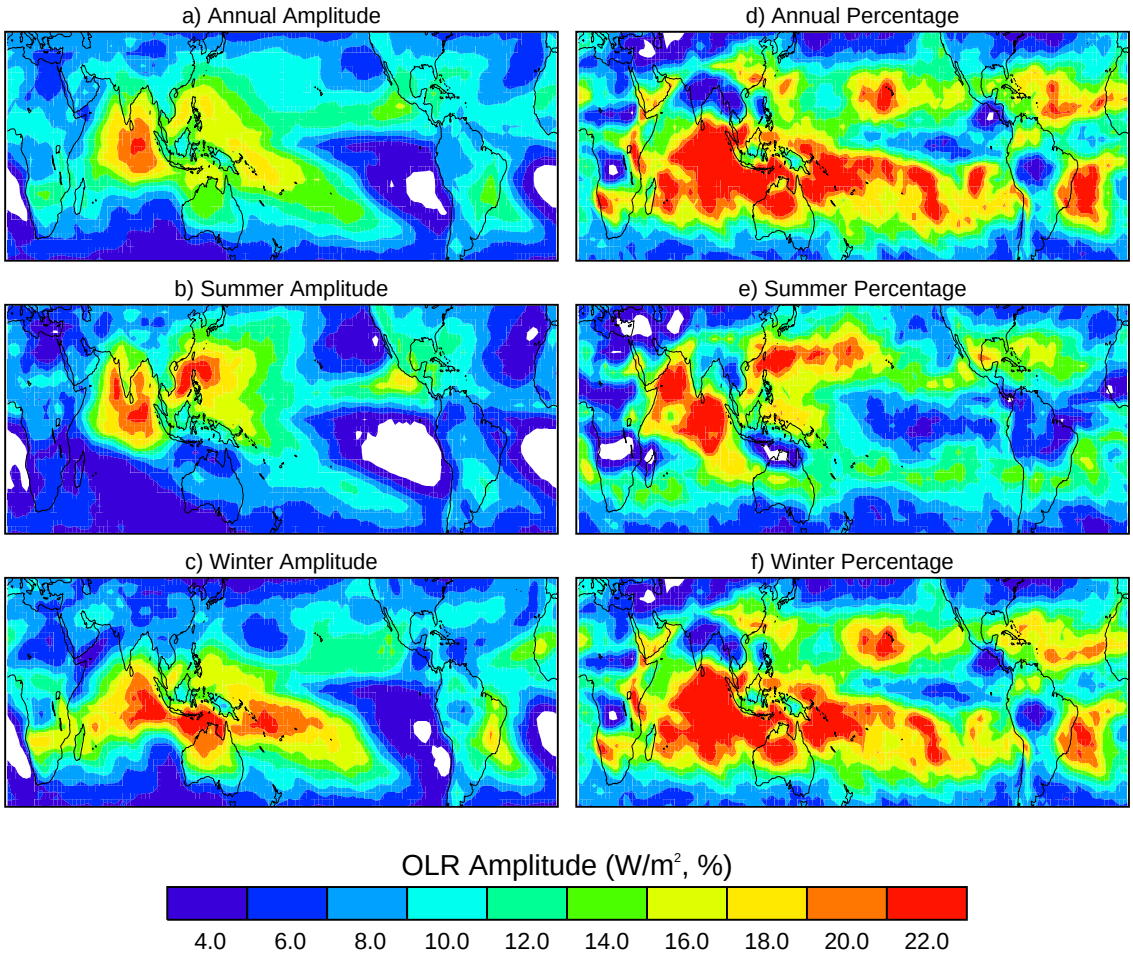

Figure 3: a) to c) Long-term (1980-2005) mean amplitude of the Outgoing Longwave Radiation (OLR) intraseasonal mode (25-80 day). d) to f) Percentage of the OLR variability in the intraseasonal band relative to the full variance. The results are presented for the entire year as well as for the boreal summer and winter. Wavelet analysis was used in order to represent the ORL variability in each grid point in terms of coefficients of a mother wavelet (Morlet in this case) for each time-step and each scale of analysis (e.g. Torrence and Compo 1998). See Appendix A for a description of the OLR data set.

analysis is performed. Using this technique, the most salient features of the evolution of the average ISO activity are elucidated. To construct winter and summer composites it is necessary to identify ISO events based on a relevant index of ISO activity. The goal of the present analysis is to separate events that are eastward propagating to those that appear to be standing oscillations. In order to select MJO events,

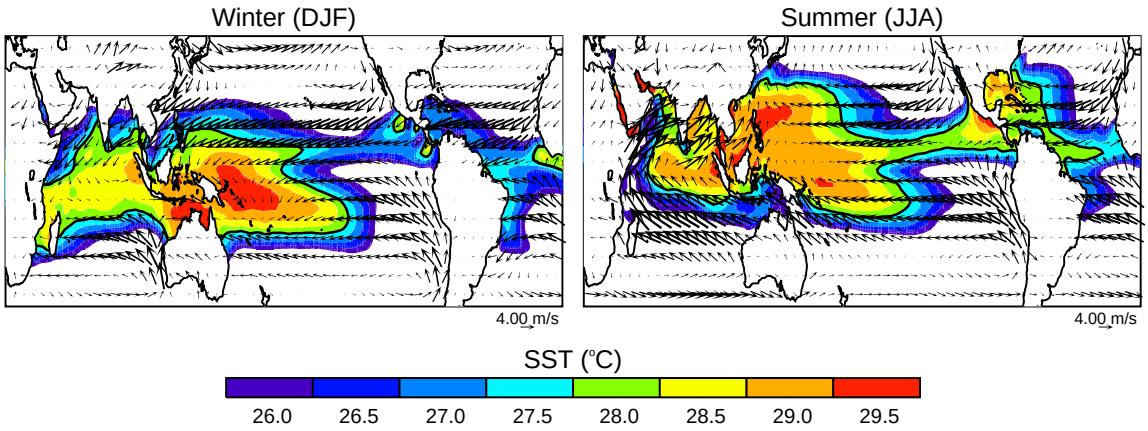

Figure 4: Long-term average of Sea Surface Temperature (SST) and 10-m winds for the boreal winter and summer. Optimally Interpolated SST and NCEP/NCAR Reanalysis are used in this figure. See Appendix A for description of both datasets.

i.e., eastward propagating ISO events, five different indices were used simultaneously. Since observations show that MJO starts over the Indian Ocean and then propagates towards the western Pacific, intraseasonally (25-80 day) filtered OLR over the Indian Ocean (10°S-10°S, 70-90°E) is used as one of the MJO indices. Dates corresponding to OLR minima in the intraseasonal band with magnitude greater than one standard deviation are selected as potential MJO events.

However, not all the selected dates based on the intraseasonal OLR index correspond to eastward propagating events. Four indices, based on Empirical Orthogonal Functions analysis (EOF), are used as the first step to decide whether or not the selected dates could potentially correspond to MJO events. In general, the EOF-based indices are constructed based on the two leading modes of near-equatorial atmospheric fields. The two principal component (PC) time series vary mostly on the intraseasonal time scale. For example, one of the indices, the All-season Real-time Multivariate MJO Index (Wheeler and Hendon 2004), is constructed from the projection of the daily observed data onto multiple-variable EOFs from OLR, 200mb and 850mb zonal wind with the annual cycle and components of interannual variability removed. Additional indices are based on EOF analysis of OLR (independently),

EOF of band pass filtered 30-90 day 850mb zonal winds (Maloney and Kiehl 2002), and extended EOF analysis of velocity potential (http://www.cpc.noaa.gov). If an initially selected date corresponds to a maximum greater than one standard deviation, within the following ten days, in at least two of the four EOF based indices, the event is considered to be an MJO. Figure 5 exemplifies the selection procedure. Initially 46 events were selected as MJO events during winter and 37 during summer in the period from 1980 to 2004. Additionally, the evolution of every selected event was studied (by following its life-cycle) to eliminate further events not showing coherent eastward propagation anomalies of OLR. 38 events were finally selected as winter MJO events and 31 as summer events.

The position of each of the MJO events was tracked daily using OLR intraseasonal variability. A convective region was defined as the area with negative anomalies of OLR associated to the ISO greater than 10 W/m^2. The geometric center of the convective area was found for each of the first 20 days of the oscillation and for all events during both winter and summer in order to estimate the average track of the MJO. In this case, Day 0 corresponds to the start of the convective event over the central Indian Ocean. Figure 6 shows the average track of the MJO for winter and summer using all events previously selected. The Figure provides an idea of the average intensity of convection and its location as well as the variability of the latter. In both cases, the track of the center of convection is positioned in the respective summer hemisphere. Similarly, in both cases the peak of convection is reached around day 10, when the center of the instability is to the west of Sumatra, during winter the convection is stronger in this location. On the other hand, the track of the winter MJO is less variable than the track during summer as revealed by the standard deviation of the convection geometric center. During winter, the track tends to be parallel to the equator while during summer the center of convection propagates northeastwardly across South and Southeast Asia.

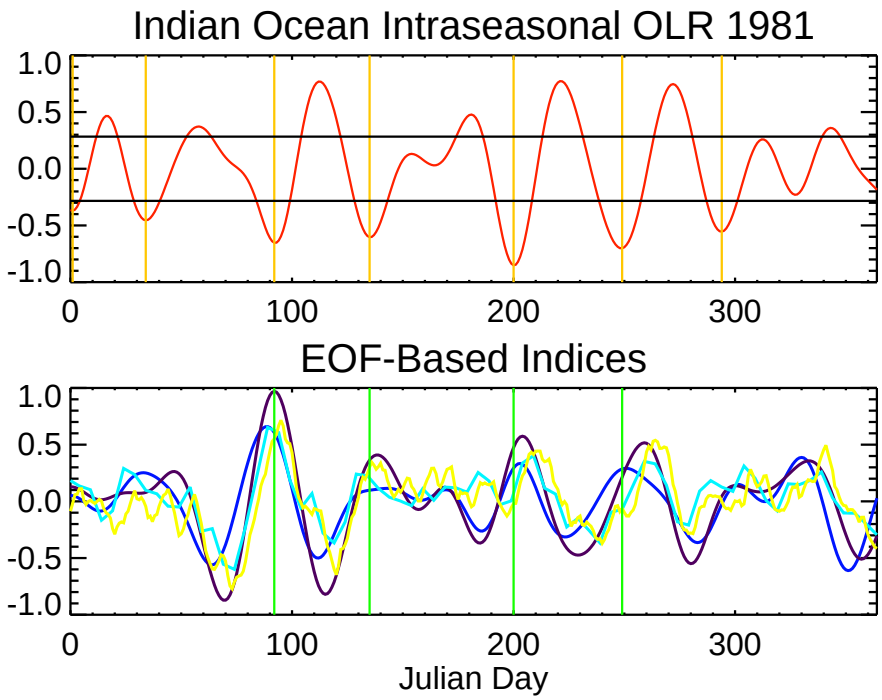

Figure 5: Selection of MJO events: The top diagram shows the intraseasonally filtered (25-80 day) OLR over the Equatorial Indian Ocean (10°S-10°S, 70-90°E) for 1981. Dates corresponding to OLR minima with magnitude greater than one standard deviation are initially selected as potential MJO events. The bottom diagram shows four EOF-based indices: based on the two leading PCs of OLR (blue), 850mb zonal winds (purple), extended EOF of 200mb velocity potential (light blue), and multiple-variable EOF (yellow). If an initially selected date correspond to maxima greater one standard deviation, within the following ten days, in at least two of the four EOF based indices, the event is regarded as an MJO.

The composite horizontal and vertical structure of MJO is presented in the following sections. Variables such as OLR, sea level pressure (SLP), 200mb and 925mb winds, vertical velocity, velocity potential and stream function at different levels, as well as the meridional and zonal stream functions were analyzed. Horizontal velocity potential and stream functions are estimated using NCEP-NCAR Reanalysis winds by numerically solving Laplace equation. Mass stream functions are also estimated using the same data set, following the definitions in Peixoto and Oort (1992) and Hartmann (1994).

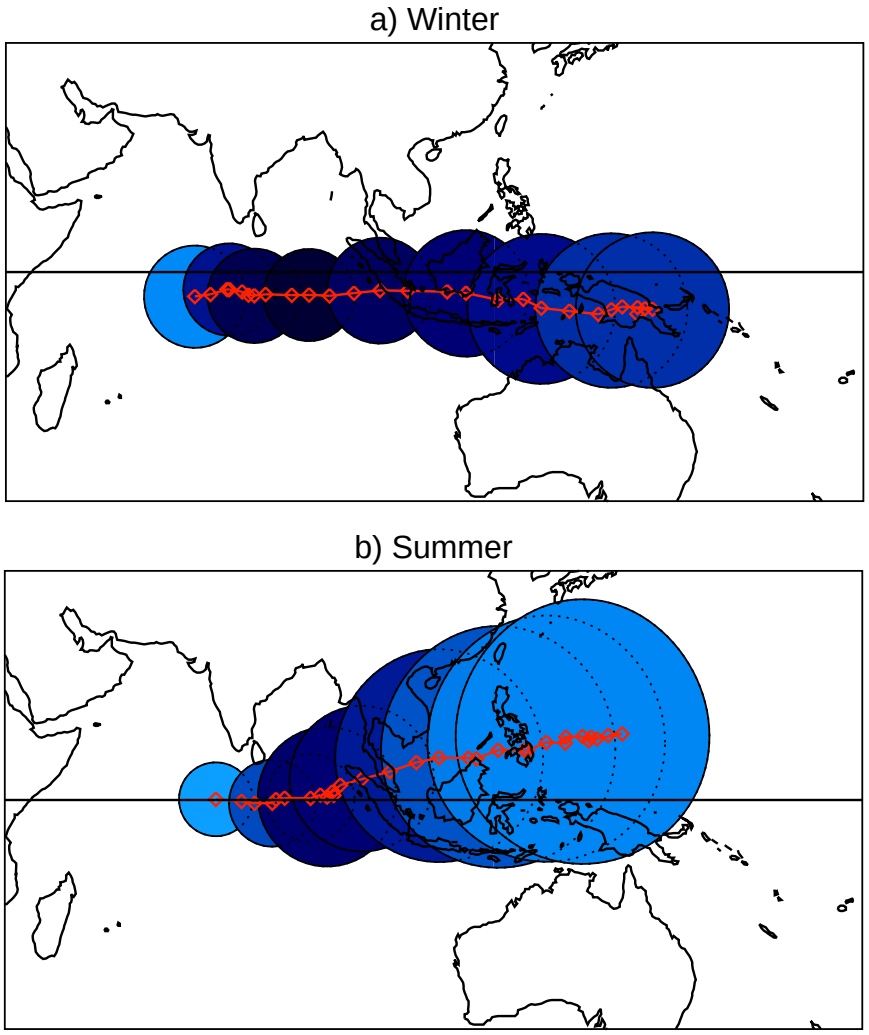

Figure 6: Average track of the MJO during a) winter and b) summer obtained from 38 (31) winter (summer) MJO events. The read line corresponds to the average position of the convective region geometrical center during 30 days after the start of the oscillation in the Indian Ocean. The size and color of the circle, shown every three days, correspond to half standard deviation of the location of the convection center and the average intensity of convection, respectively. Dark blue corresponds to more intense convection. The circle radius was found as the hypotenuse of the meridional and latitudinal standard deviations. The convective region is defined as the area with negative anomalies of OLR greater than 10 W/m^2.

2.1 Structure of Winter MJO

2.1.1 Horizontal Structure

Figure 7 shows the composite evolution of OLR for winter MJO based on 38 intraseasonal convective events over the Indian Ocean displaying the characteristic eastward

propagation. Day 0 corresponds to maximum convection over the central equatorial Indian Ocean. The eastward propagation is evident during both the active or convective phases (negative OLR anomalies) and the suppressed or quiescent phases (positive OLR anomalies). Prior to Day 0, the preceding suppressed phase developed over the Indian Ocean and propagated eastward, interacting with the Australian monsoon. The association of MJO with regional rainfall will be discussed in the following chapter. Once the suppressed phase has moved out of the Indian Ocean, a convective phase develops over the ocean around Day -10. While the ISO convective peak is reached over the ocean, it is interesting to note that same sign anomalies are also observed over Africa leading by about 5 days those in the central Indian Ocean. In addition to the eastward propagation, the convective anomaly also moves over the warm waters of the SPCZ. Most of the convective signal vanishes after the dateline associated with the cooler water. Although weak, a link is observed between ISO convection over the warm pool and to the west of the Central America coast, where there exists a secondary intraseasonal variability peak (Figure 3). It is also important to point out the anomalies of OLR arising over southwest Asia, over most of the Arabian Peninsula and Pakistan. These anomalies appear when the activity over the Indian Ocean is at a maximum and are out of phase. I.e. convection over the Indian Ocean is associated with subsidence over Southwest Asia and vice versa. The composite evolution of vertical velocity intraseasonal anomalies (not shown here) closely matches that of the OLR.

Velocity potential at 200mb shows the most discernible signal of an eastward propagating oscillation of wavenumber one associated with the MJO (Figure 8). In contrast to the convective signal, the anomalies in the 200mb winds do not disappear over the central and east Pacific and continue to propagate to the east and circumnavigate the globe. Negative velocity potential anomalies are associated with positive anomalies of convection and vice versa. 200mb stream function composite shows the

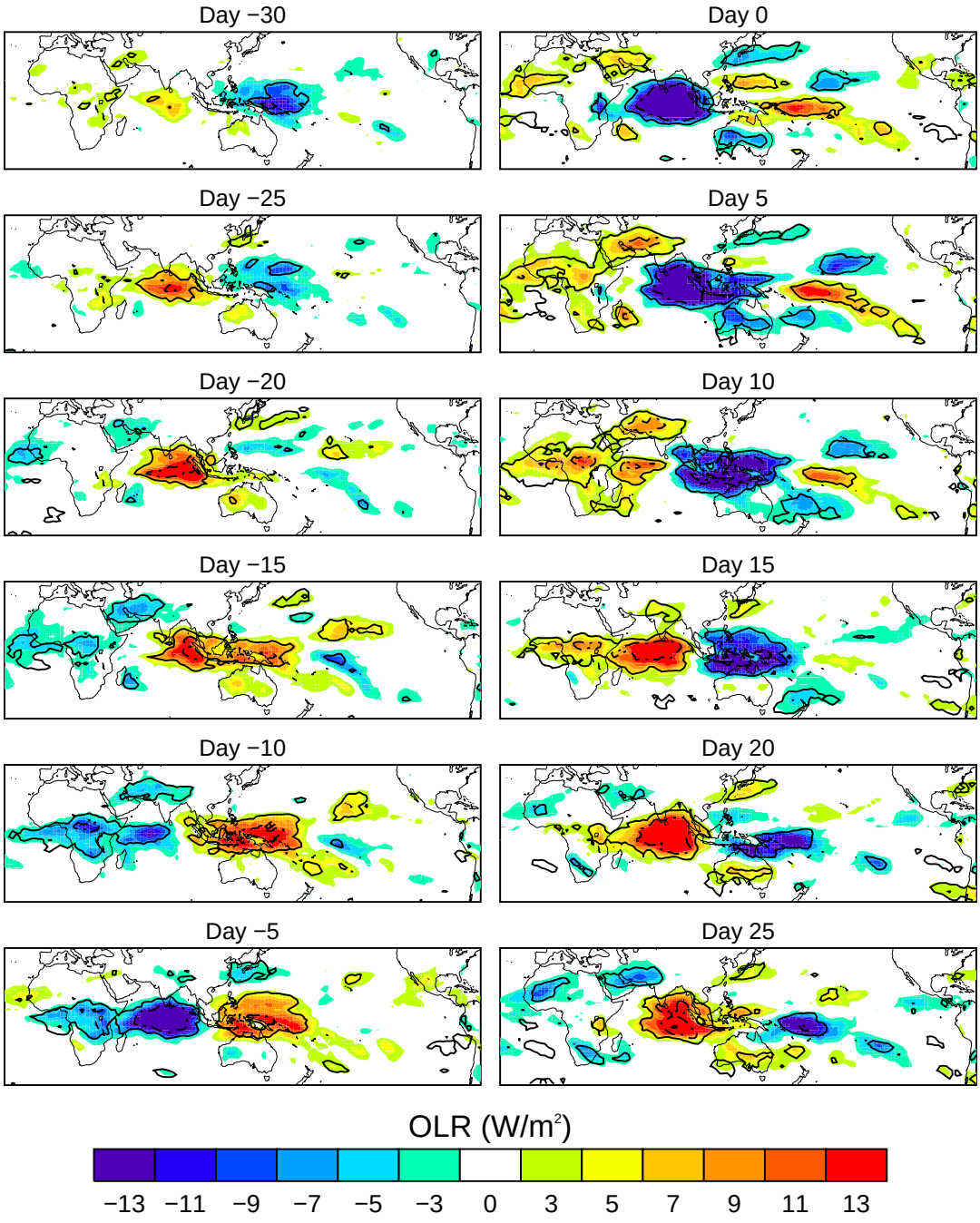

Figure 7: Composite evolution of OLR for winter MJO from Day -30 to Day 25 based on 38 events. Day 0 corresponds to maximum convection (minimum OLR) over the central Indian Ocean (10°S-10°S, 70-90°E).

corresponding circulation structure (Figure 9). While the propagation of the velocity potential anomalies resembles the features an eastward propagating Kelvin wave, the

most salient feature of the stream function shows a remarkable resemblance to the observed horizontal structure of the circulation, and anomalies of the 200mb geopotential height (not shown here) are associated with a equatorially-trapped Rossby wave. Geopotential height anomalies suggest that the observed anomalies are a combination of Rossby-Kelvin activity. Two strong slightly off-equatorial anticyclones, associated with positive geopotential height anomalies, develop to the west of the convective anomalies, accompanied of two weaker cyclones and their corresponding negative geopotential height anomalies to the east of the convection. The elongated shape of the outer cyclonic structure also suggests the Kelvin wave-like nature of the oscillation. Equatorial westerly winds related to the Kelvin wave appear responsible for the observed elongated cyclones. Due to the elongation, present during both active and suppressed phases, the cyclones/anticyclones located to the east of the convective anomaly reach the Americas potentially impacting indirectly the atmospheric conditions through teleconection-like pattern. Circulation and geopotential height anomalies appear stronger in the winter hemisphere.

Intraseasonal variability has a strong signature in SLP. Figure 10 shows the composite evolution of SLP and the 925mb stream function. Surface highs and lows associated to both ISO phases, suppressed and active respectively, also propagate eastward over the Indian Ocean towards the western Pacific. One salient feature is the apparent bifurcation of the SLP anomalies once it reaches the western Pacific and the convective anomaly vanishes when it reaches colder surface water. The southern branch of the SLP anomaly moves into the SPCZ enhancing convection; the northern branch potentially accounts for the maintenance of weak negative OLR anomalies observed around Days 5-15 over the central Pacific north of the equator. The SLP anomalies appear to last longer than those of OLR most likely because deep convection is not supported by cold waters. As it will be discussed next, the summer ISO

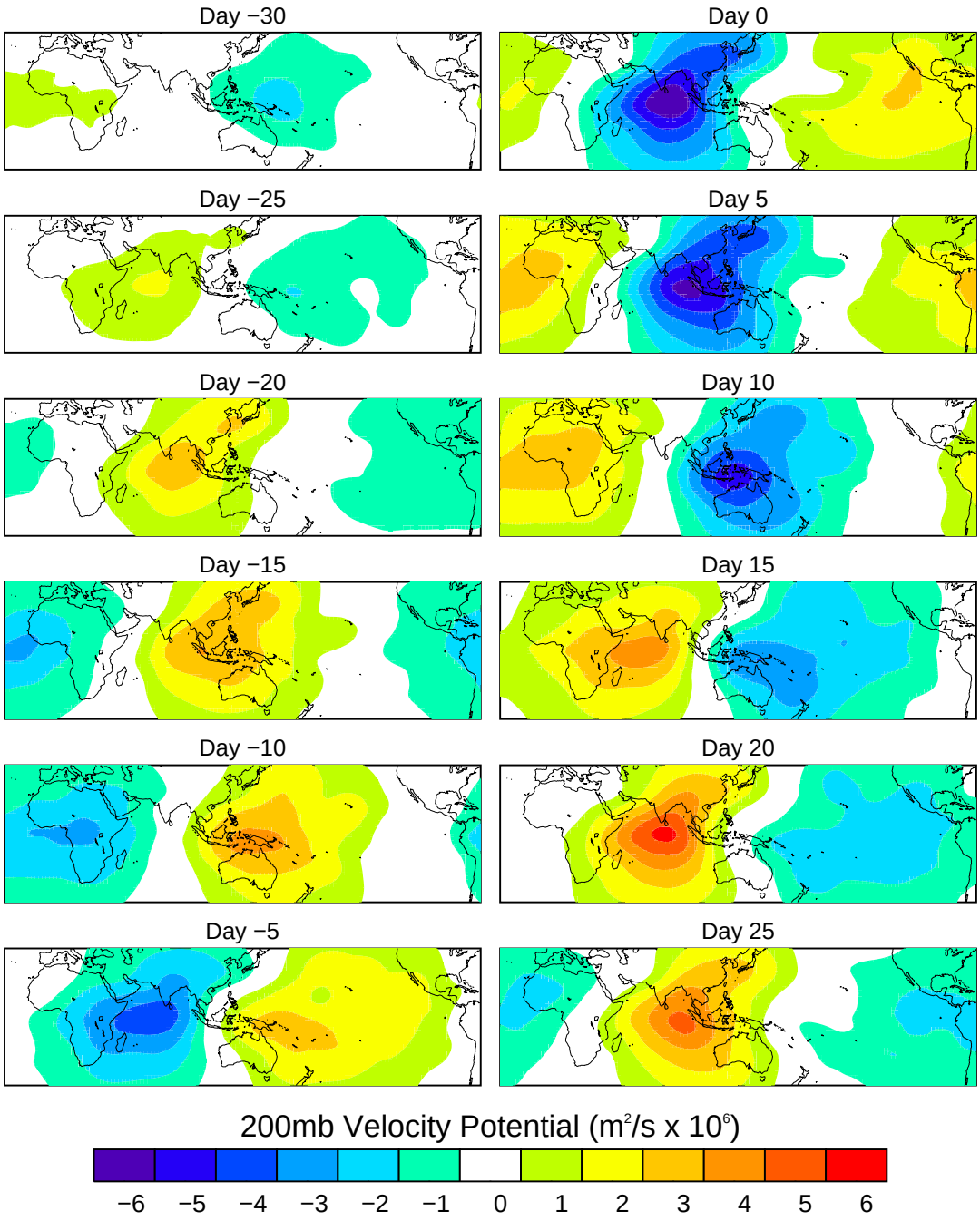

Figure 8: Similar to Figure 7 but for the winter 200mb velocity potential.

undergoes a similar and stronger bifurcation but over the Indian Ocean. Near surface streamlines closely follow isobars off-equatorially. Over the equator, streamlines converge into surface lows enhancing convection.

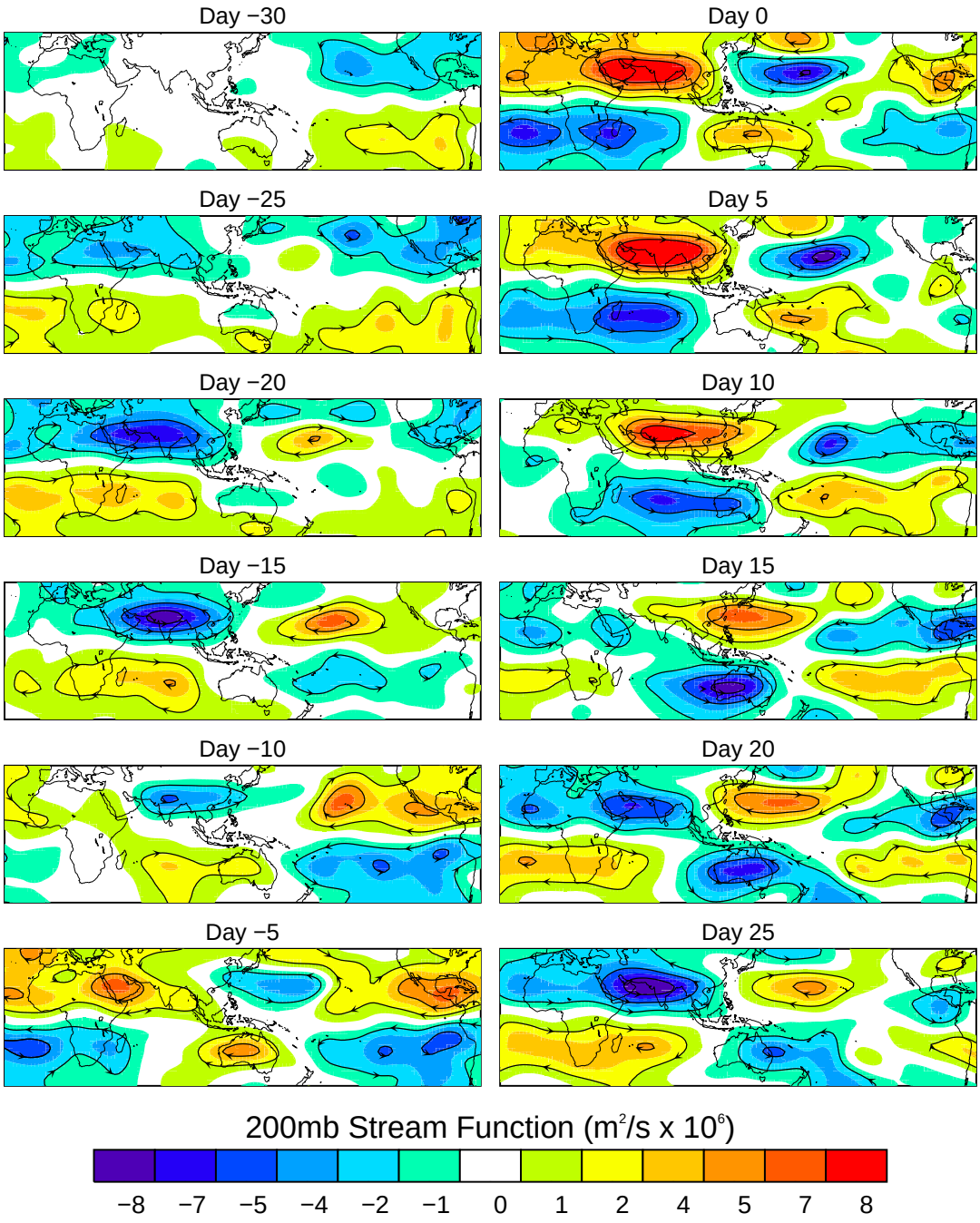

Figure 9: Similar to Figure 7 but for the winter 200mb stream function. Arrows show the direction of the circulation.

Not only the long-term structure of the SST is important for the development of ISO but its intraseasonal behavior also appears to play an important role for the propagation of the convection. The composite evolution of SST shows a coherent

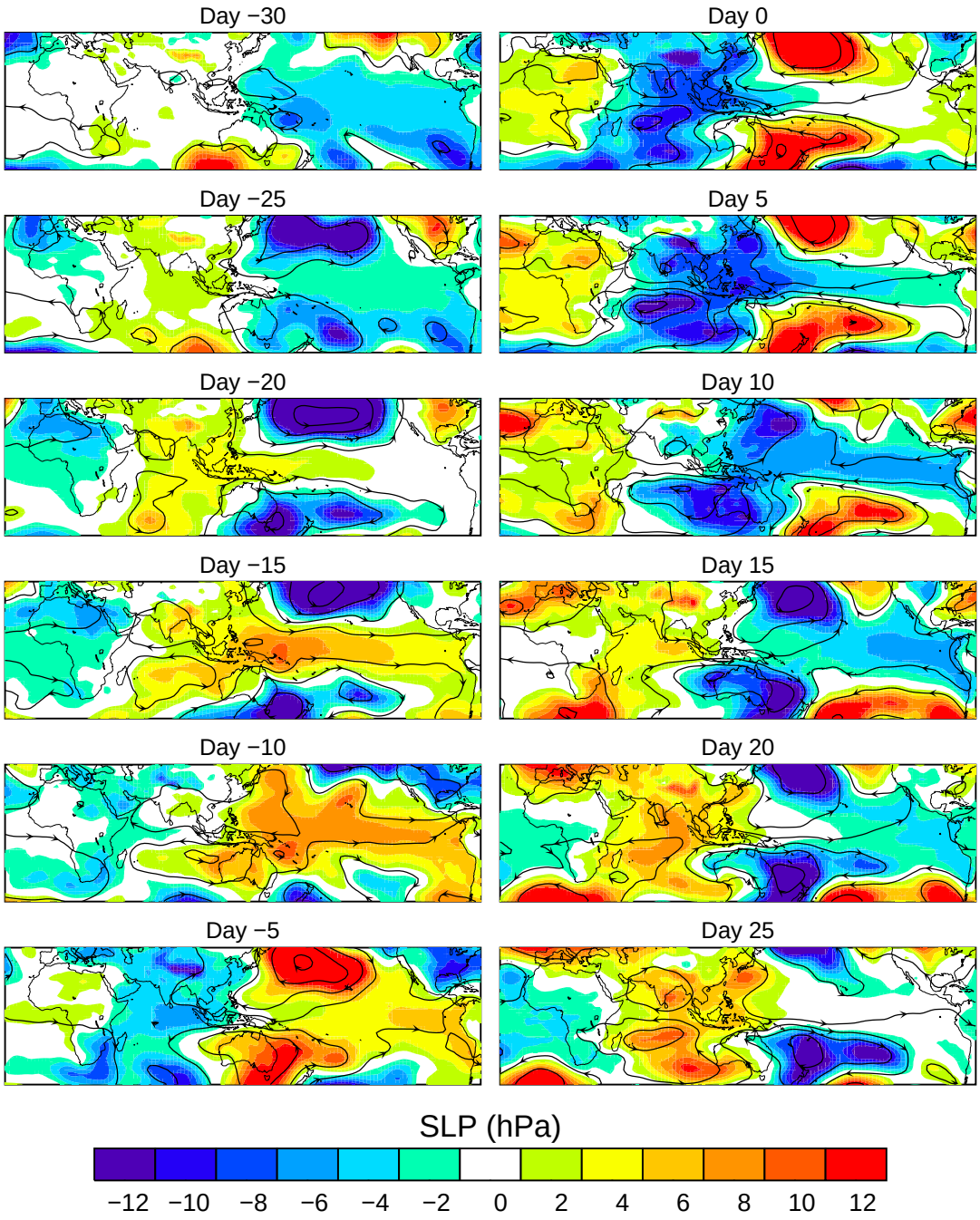

Figure 10: Similar to Figure 7 but for the winter SLP and 925mb stream function. Arrows show the direction of the circulation.

variability with the previously studied variables, and in particular with OLR (Figure 11). During the quiescent phase the lack of clouds facilitate the heating of the surface of the ocean. Weak low-level winds also intervene in the process by not promoting

evaporation and mixing, mechanisms that act to cool the surface. Then, elevated equatorial SST tends to drive surface convergence and convection, playing a key role in the triggering of the active phase. Once the cloud fraction increases with the convection, the amount of solar radiation reaching the surface is considerably reduced, inducing surface cooling and damping the atmospheric instability. Considering the magnitude of SST variability, one degree amplitude in the intraseasonal band is substantial. SST anomalies also propagate eastward, with positive anomalies leading convection.

2.1.2 Vertical Structure

The vertical structure of the winter MJO, like the horizontal structure, is very robust. In this section, the zonal and meridional features of the vertical structure of the MJO are described.

The vertical structure of the velocity potential and stream function present interesting features related to change in strength and sign of the anomalies throughout the troposphere. Figure 12 shows, the day for the maximum convection over the central Indian Ocean, the composite structure of velocity potential and stream function for several levels in the vertical. The most striking features, evident in both variables, is the change in sign and magnitude of the anomaly from top to bottom of the troposphere. In absolute value, the greatest anomalies appear at 200mb and the lowest at 400mb. Below 400mb the sign of the anomalies changes and re-intensify, reaching a secondary magnitude maximum around 600-700mb. The sign reversal of the velocity potential and change of direction of the circulation as observed in the streamlines indicate a change of divergence mainly at 200mb to convergence below 400mb. In other words, convergence is not restricted to the surface, occurring in most of the tropospheric column. If mass balance is considered, this explains why the largest ISO anomaly occurs at 200mb. While convergence extends through a thick

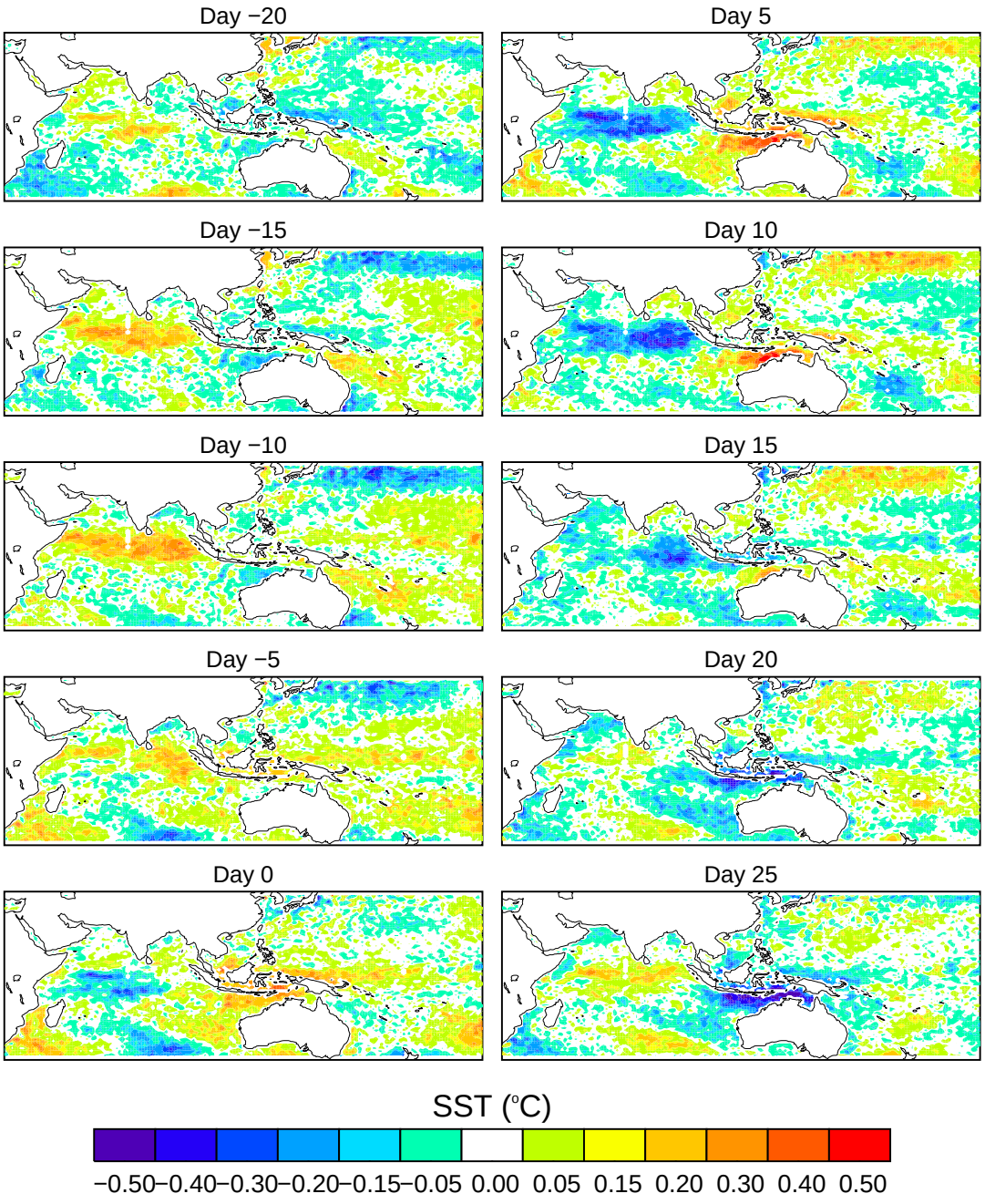

Figure 11: Similar to Figure 7 but for the winter SST.

atmospheric layer, divergence, taking place in a thin layer, has to be much larger in order to conserve the mass balance. This is also an important feature as it gives clues that help understanding why the ISO convective envelope is so intense and long-lasting. When convergence occurs at many atmospheric levels, the convection

tends to be more robust and resilient against higher frequency atmospheric fluctuations that could potentially erode the convective envelope. Additionally, there is a southwest-northeast tilt in the velocity potential anomalies, especially evident for anomalies over the Indian Ocean.

The zonal mass stream function shows the anomalous longitudinally oriented circulation cells associated with the ISO (Figure 13). Figure 13 clearly shows subsidence over regions of negative convective anomalies and vice versa. The zonal slice of vertical velocity anomalies along the equator shows consistent features with those seen in Figure 13. For the convectively suppressed (active) phase, the most extensive circulation cells longitudinally are those with descending (ascending) branches over the Indian Ocean and extending to the east. This cell has its corresponding ascending (descending) branches over the West Pacific. Its eastern complementary cell (over the Pacific) is also considerably large. This feature is particularly clear at Day 0 and Day 20. These cells also propagate to the east but they become narrower as they approach colder waters in the central Pacific. Additional narrower cells also appear as a coherent element of the ISO vertical structure and might constitute potential teleconnections. For example, active conditions over the Indian Ocean appear to correspond very coherently to subsidence over South America and vice versa. This feature in the vertical structure is likely the explanation of the localized intraseasonal variability maximum observed over equatorial South America during winter (Figure 3, winter percentage).

Figure 14 shows the evolution of the meridional mass stream function over the Indian Ocean (70°-90°E), hence depicting the anomalous latitudinal circulation cells. Two circulation cells with ascending branches over the equator (Hadley-like) appear with the convective anomalies. The converse situation is also true. A couple of details are noteworthy. Prior to both active and suppressed convection over the Indian Ocean, the cell in the summer hemisphere develops earlier than its winter

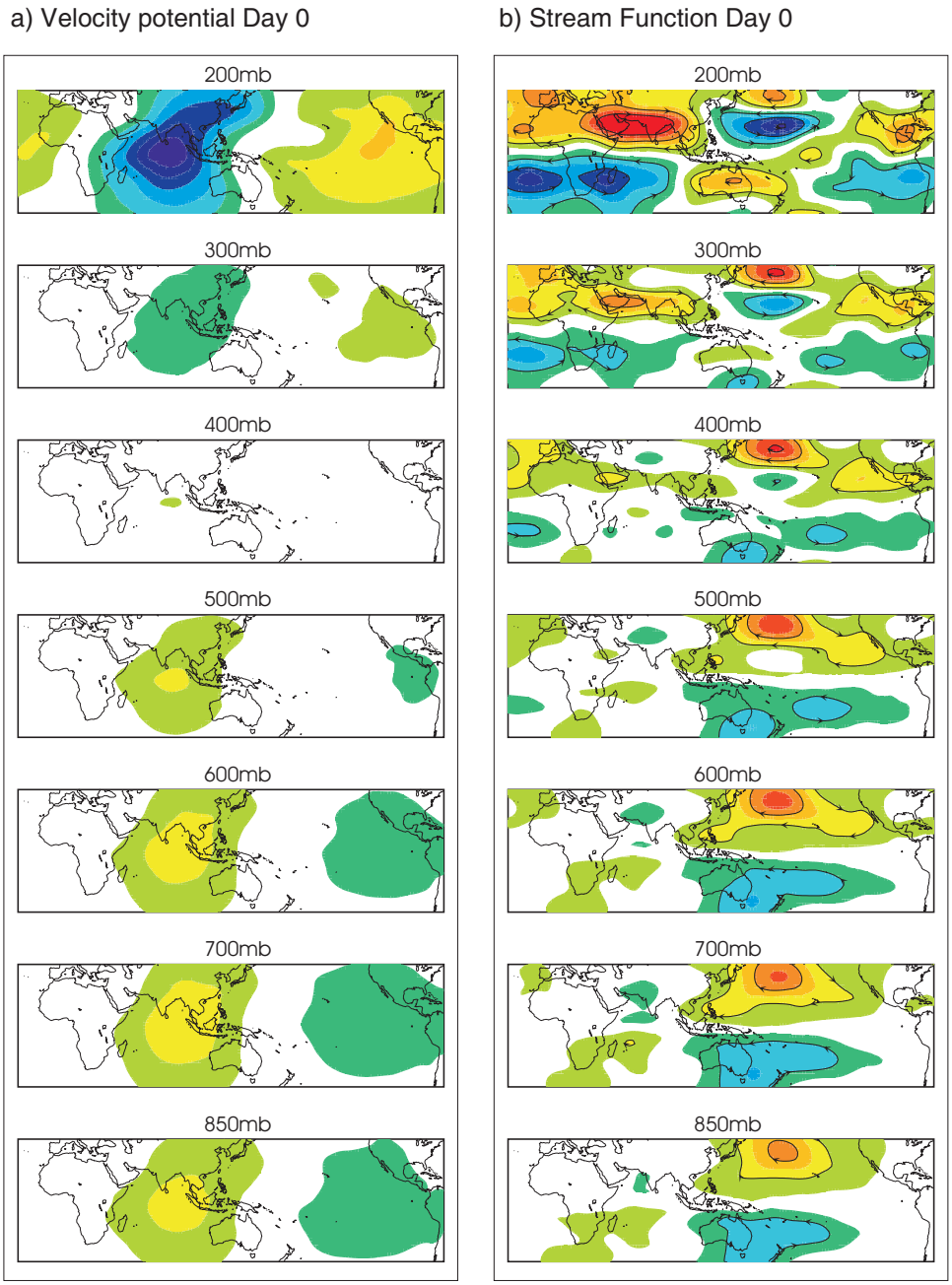

Figure 12: Anomalies at Day 0 (maximum convection over the Indian Ocean) for many levels within the troposphere for a) Velocity potential and b) stream function. Color tables are the same as those used in Figures 8 and 9 respectively.

counterpart. The summer-hemispheric cell also appears broader than but not as tall as its winter counterpart.

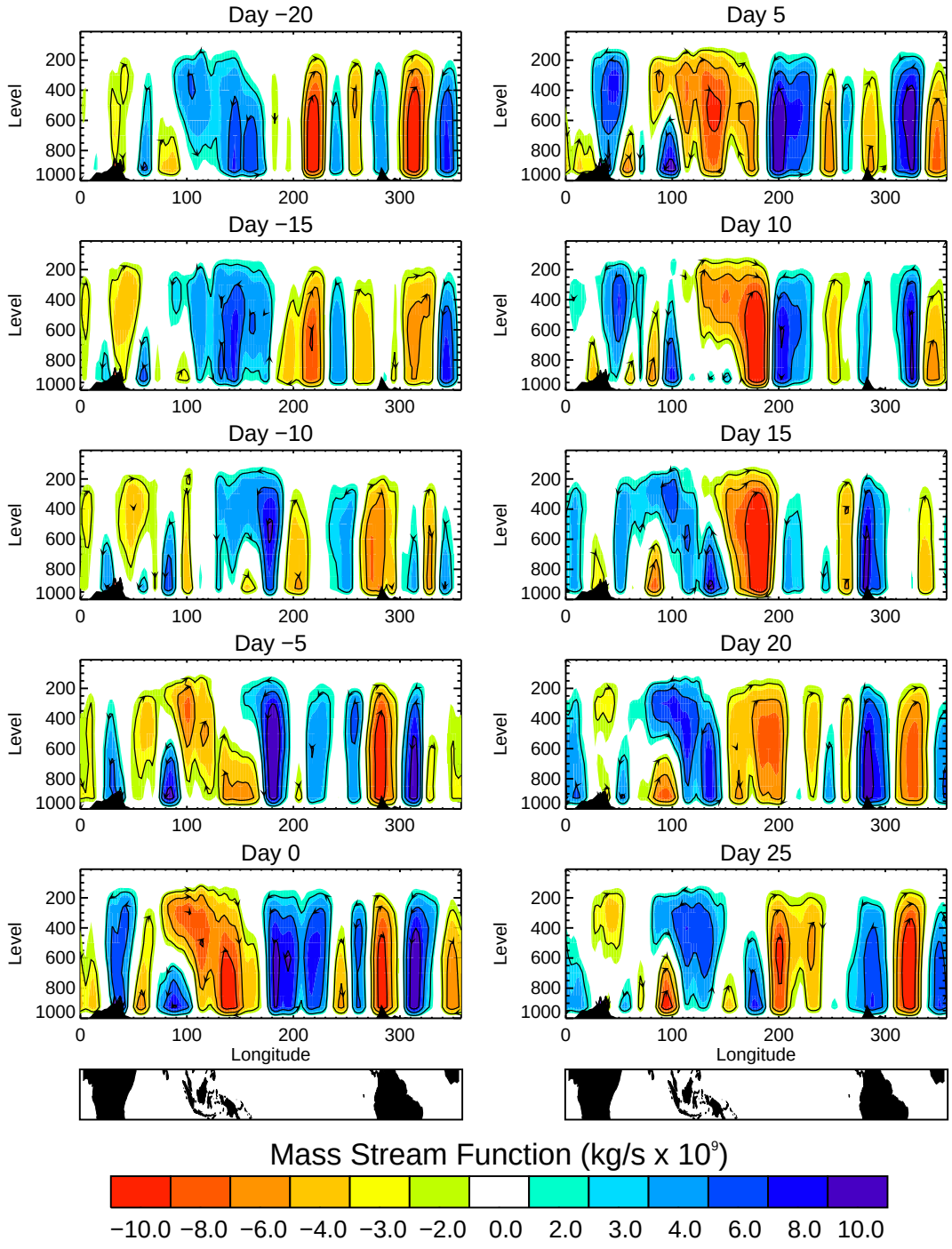

Figure 13: Composite evolution of the zonal mass stream function during winter computed between 10°S and 10°N.

2.2 Structure of Standing ISO During Winter

In addition to the eastward propagation intraseasonal variability, which truly appears as the most coherent mode in this band, non-propagating convective anomalies are

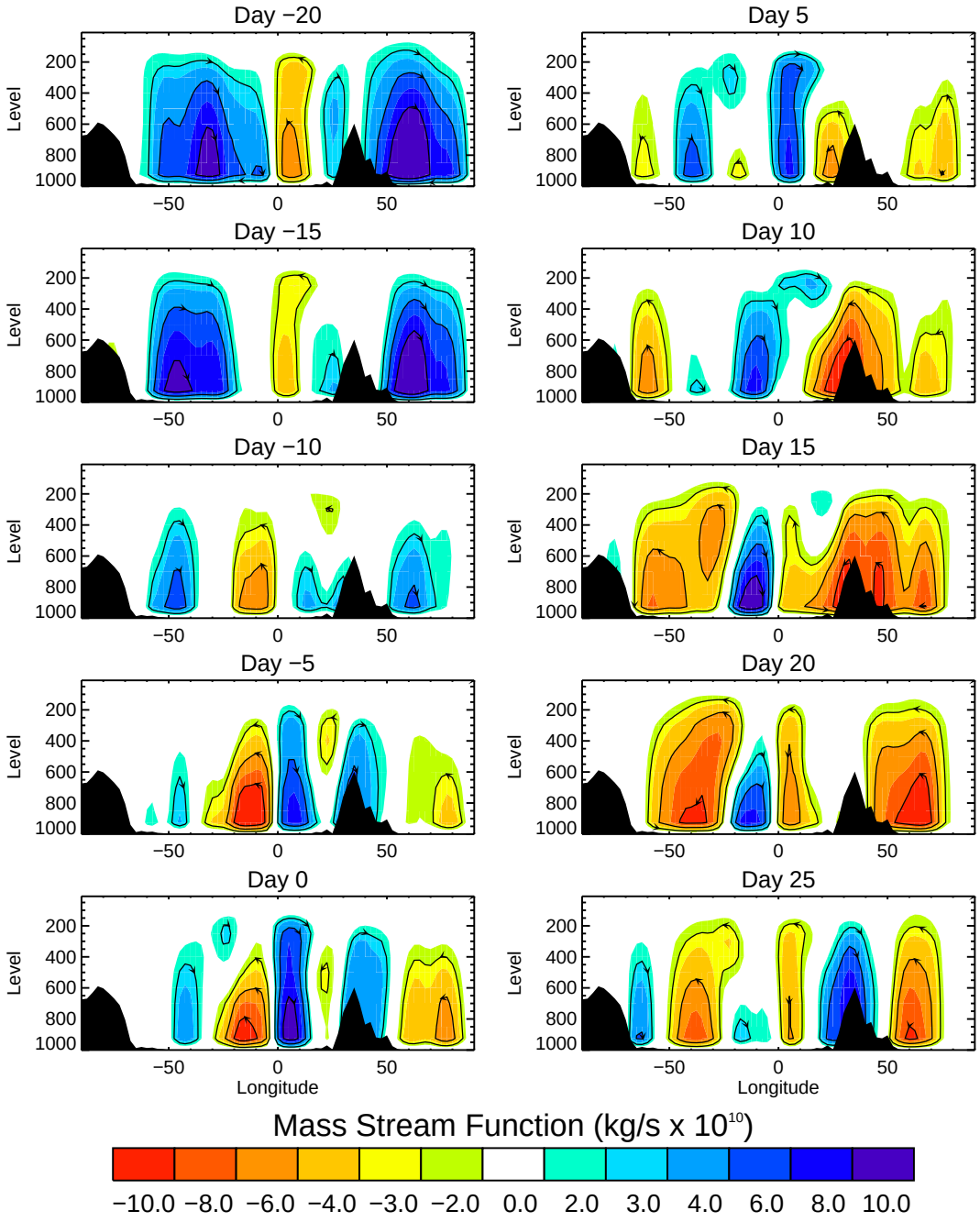

Figure 14: Composite evolution of the meridional mass stream function during winter computed between 70°E and 90°E.

also observed in the data. Events of this nature where identified for the two major intraseasonally active regions, central Indian Ocean (10°S-10°S, 70-90°E) and Western Pacific (10°S-10°S, 150-170°E). Dates for composite analysis where selected from

intraseasonally filtered OLR over both regions (independently). Events showing eastward propagation were discarded. 20 events for the Western Pacific and 17 for the Indian Ocean were finally selected.

Figure 7 and Figure 16 show the evolution of the OLR composites for the Western Pacific and Indian Ocean cases respectively. As expected, there is no evidence of any type of zonal propagation, which validates the selection of the events, yet there are important OLR anomalies evolving locally. In a similar manner as for the winter MJO cases, composites were computed for different variables. In general, the composite structure does not show any large-scale robust feature worthy of mention. Composites of most variables show localized evolution, and some times the structure is so weak that using the same color scale employed for the MJO cases results in blank maps. In particular, velocity potential anomalies show very weak divergence anomalies and hence even weaker convergence. Zonal mass stream function show local narrow cells responding for the convective anomalies without connecting both the Indian Ocean and the West Pacific.

2.3 Some Insights on the Initiation and Evolution of the Winter MJO

Knowing the details of the horizontal and vertical structure of the ISO is a very important step in order to understand its impacts on rainfall variability over different regions, development of empirical or statistical forecasting schemes for extended forecasting range (20-30 days), evaluating the skill of numerical models, understanding potential teleconnections, among others. However, the question that remains is what do we know about the oscillation itself by analyzing collectively all structural features? For example, how does this structural view helps us understand why the MJO propagates to the east and why it starts over the Indian Ocean. The following paragraph presents some ideas on these issues.

It was shown that regions with high intraseasonal variability coincide very well

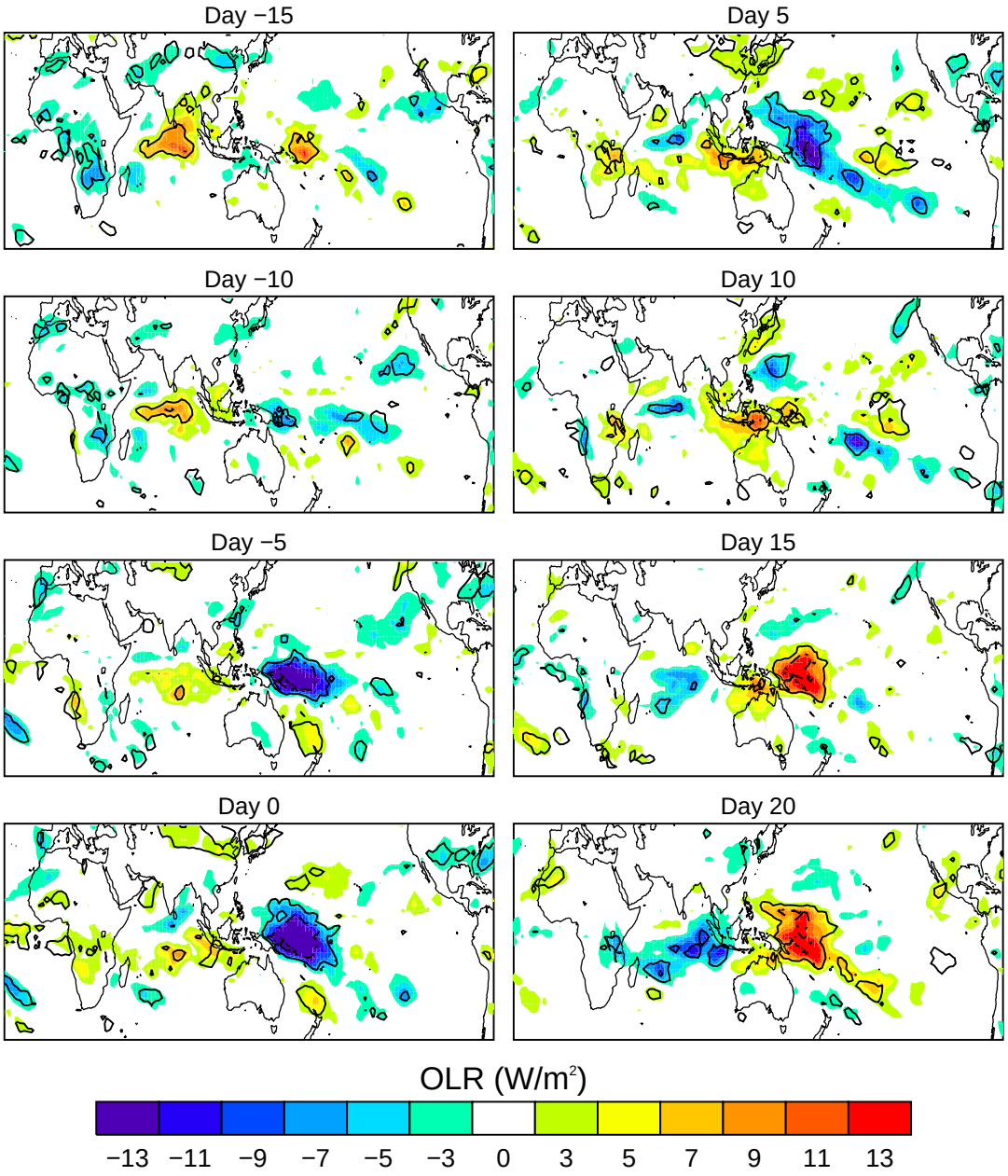

Figure 15: Composite evolution of OLR for winter non-MJO events developing as a standing instability over the Western Pacific based on 18 events. Day 0 corresponds to maximum convection (minimum OLR) over the west pacific (10°S-10°S, 150-170°E).

with regions with long-term mean SST above 28°C. When the SST is high, the source of the necessary energy to maintain the moist convection observed in association to the ISO is provided as well as the source of instability. While it is not a unique relationship, it is well known that SST and convection are correlated. SST anomalies

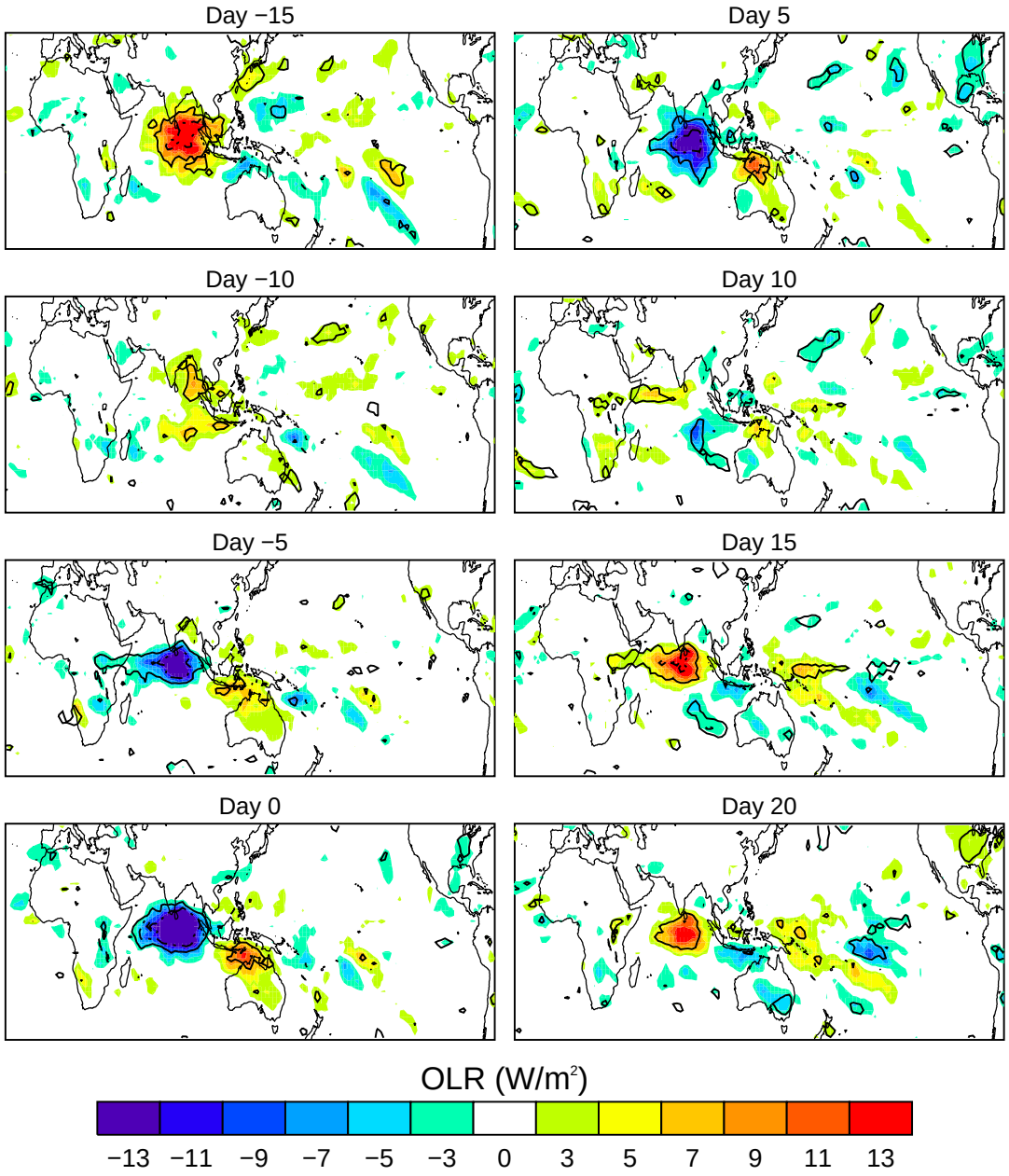

Figure 16: Similar to Figure 15 but for winter non-MJO events developing over central Indian Ocean (10°S-10°S, 70-90°E). 17 events where used in this case.

cause changes in atmospheric boundary layer temperature creating anomalous surface pressure gradients, winds and low level mass convergence which may lead to convection (Lindzen and Nigam, 1987). Waliser and Graham (1993) showed that over the West Pacific warm pool the maximum convective activity occurs, on average, for SST

of about 29.5°C. From the climatology point of view, the only region in the globe where sustained enhanced (stationary and/or propagating) convection for extended time periods (20-30 days) could take place is the Indian-West Pacific Ocean basin. This then, defines a unique aspect of this region.

If positive anomaly of SST develops over the Indian Ocean, a subsequent convective anomaly follows. The time needed to destabilize the lower troposphere through the warming of the SST (by enhanced downward solar radiation during the suppressed phase) and the cooling of the upper troposphere (enhanced long-wave cooling) over the Indian Ocean is the determinant of the local timescale of the ISO. This also implies that the depth of the oceanic mixed layer is very important for the ISO timescale. The zonal circulation established by the convection over the Indian Ocean is such that it generates a region of strong subsidence over the Western Pacific, favoring an increase of SST, and the following destabilization of the atmosphere. High SST over the West Pacific in combination with subsidence results in the low-level moistening of the atmosphere and the build-up of CAPE, preconditioning the atmosphere for deep convection. While these processes lead to convection over the western Pacific, the cloudiness associated with convection over the Indian Ocean reduces the solar radiation reaching the surface, cooling the surface of the ocean, switching off the convective anomalies. This results in the apparent eastward propagation of the large-scale convective center of the MJO due to consecutive development of new convective systems, each on average slightly to the east of the previous one as noted by Nakazawa (1988).

An increase in atmospheric convection leads to the release of latent heat in the middle troposphere. Studies by Webster (1972), Gill (1980), Lau et al. (1989) among others have shown that the dominant large-scale atmospheric response to the heated air column is a Kelvin-Rossby wave combination that propagates eastward, where the Kelvin and Rossby modes combine to produce a zonally asymmetric circulation. The

composite structure of the MJO also shows a Kelvin-Rossby structure. While in linear models the propagation speed and vertical structure of the Kelvin-Rossby mode depends on the amplitude and shape of the vertical profile of the heating (Chang 1977; Hartmann et al. 1984), the theory provided accounts, at least in part, for the observed MJO structure. Houze et al. (2000) suggests that it is crucial to consider the mesoscale organization of the convection, that is, the manner in which the deep convection is organized into horizontally extensive complexes with mesoscale circulations and stratiform precipitation regions in order to obtain more realistic vertical heating profiles and hence a more realistic vertical structure of the Kelvin-Rossby mode.

In addition to the propagating mode, non-propagating intraseasonal variability is also observed in the Indo-Pacific warm pool during winter. As mentioned before, the Indian Ocean and the Western Pacific are the only two places that could potentially sustain large-scale ISO activity. When the oscillation starts over the Indian Ocean, there are two possibilities. If the anomaly is large, generating extensive circulation cells, eastward propagation originates for the reasons explained before. If the anomalous cell is weak, the resulting oscillation does not propagate since the conditions that precondition the atmospheric column for deep convection over the western Pacific are not present. If the anomaly starts over the West Pacific, in general, the most likely result is a standing oscillation. The reasons are the colder water to the east inhibiting eastward propagation, and the Kelvin-Rossby wave structure in the atmosphere resulting from the vertical heating tends to propagate eastward.

These ideas, resulting from the diagnostic analysis presented here and recent works by Stephens et al. (2004), Wang et al. (2005) and Agudelo et al. (2006), need to be tested in a modeling framework.

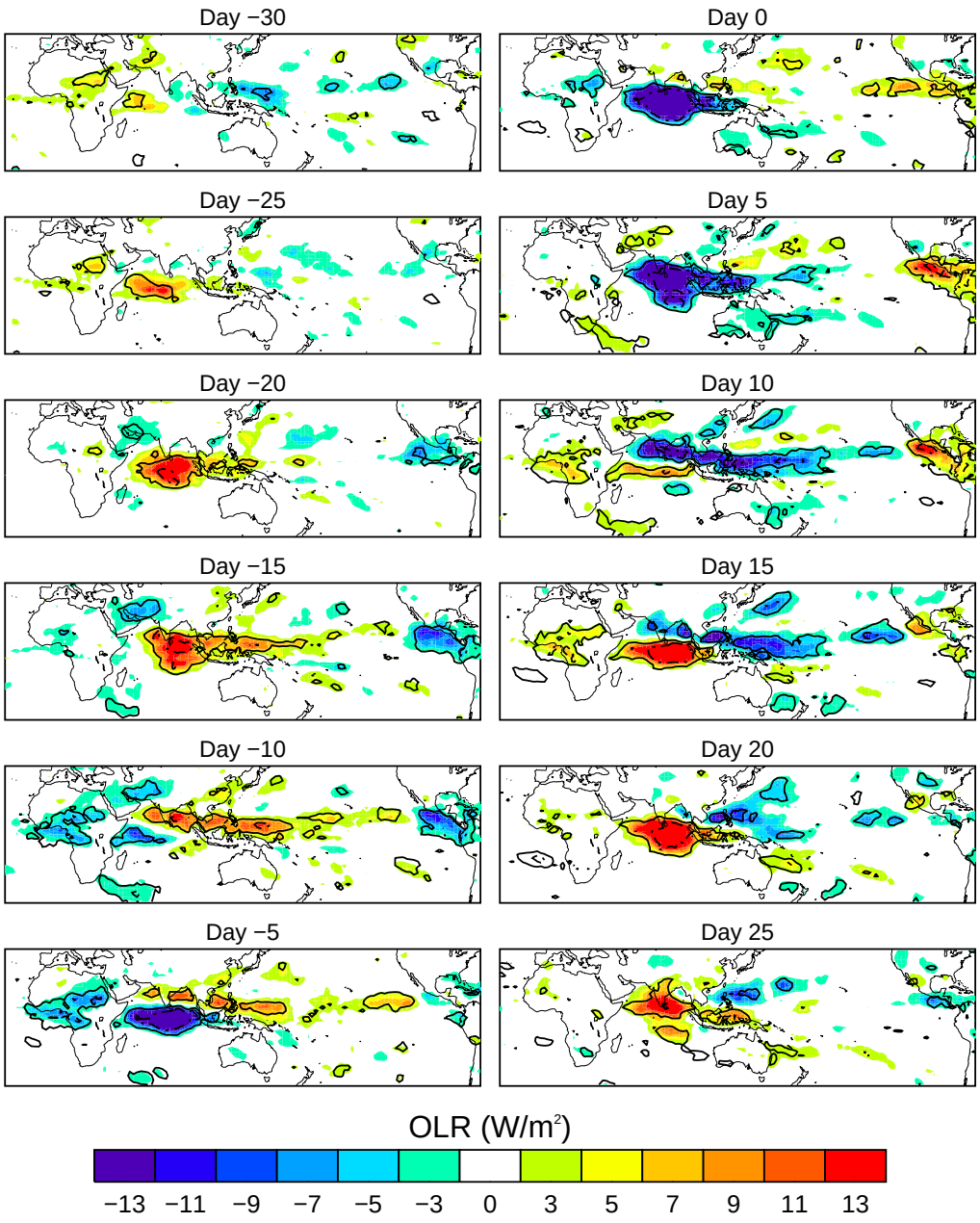

Figure 17: Similar to Figure 7 but for OLR during summer MJO based on 31 events.

2.4 Structure of Summer MJO

While some of the features of the winter MJO are shared by the summer MJO, there are still some fundamental differences between them. This section is dedicated to emphasize the most important differences.

2.4.1 Horizontal Structure

In addition to the eastward propagation of the OLR anomalies which in general is weaker than during winter and not as parallel to the equator, positive and negative convective anomalies propagate northward, affecting Southeast Asia during the summer monsoon, resulting in wet and dry spells (Figure 17). Because of the strong interaction between the monsoon and the summer realization of the MJO, the latter is also known as Monsoon ISO (MISO). Details of the propagation affecting precipitation will be explored in the following chapter. In addition, an important feature is the relationship to the anomalies observed over West Africa, also under monsoon conditions, and northern South America and Central America. Convection over West Africa is virtually in phase with the central Indian Ocean, with the former perhaps leading the latter by a few days. On the other hand, convection over the tropical Americas and the Indian Ocean appear almost perfectly out of phase. Convection in the SPCZ is not considerably modulated by the ISO during summer.

The structure of the 200mb velocity potential is perhaps the most similar feature shared by winter and summer MJO (Figure 18). There are two main differences however. One is the magnitude of the anomalies, with velocity potential anomalies associated to MJO weaker during summer than winter. The second and perhaps the most notorious difference is related to the horizontal tilt. While during winter the tilt was southwest-northeast, during summer the tilt is southeast-northwest. The 200mb stream function also presents fundamental differences (Figure 19). During summer, the structure is noisier than during winter, and presents weaker or non-existent anticyclones to the west of the convective anomaly, and broader and stronger cyclones to the east of the anomaly. In particular, the anticyclone in the northern hemisphere is considerably weaker and not parallel to the equator as it is during the winter. In fact, the configuration of the anticyclones appears to be tilted southwest-northeast (see Day 10). On the other hand, broader cyclones to the east could

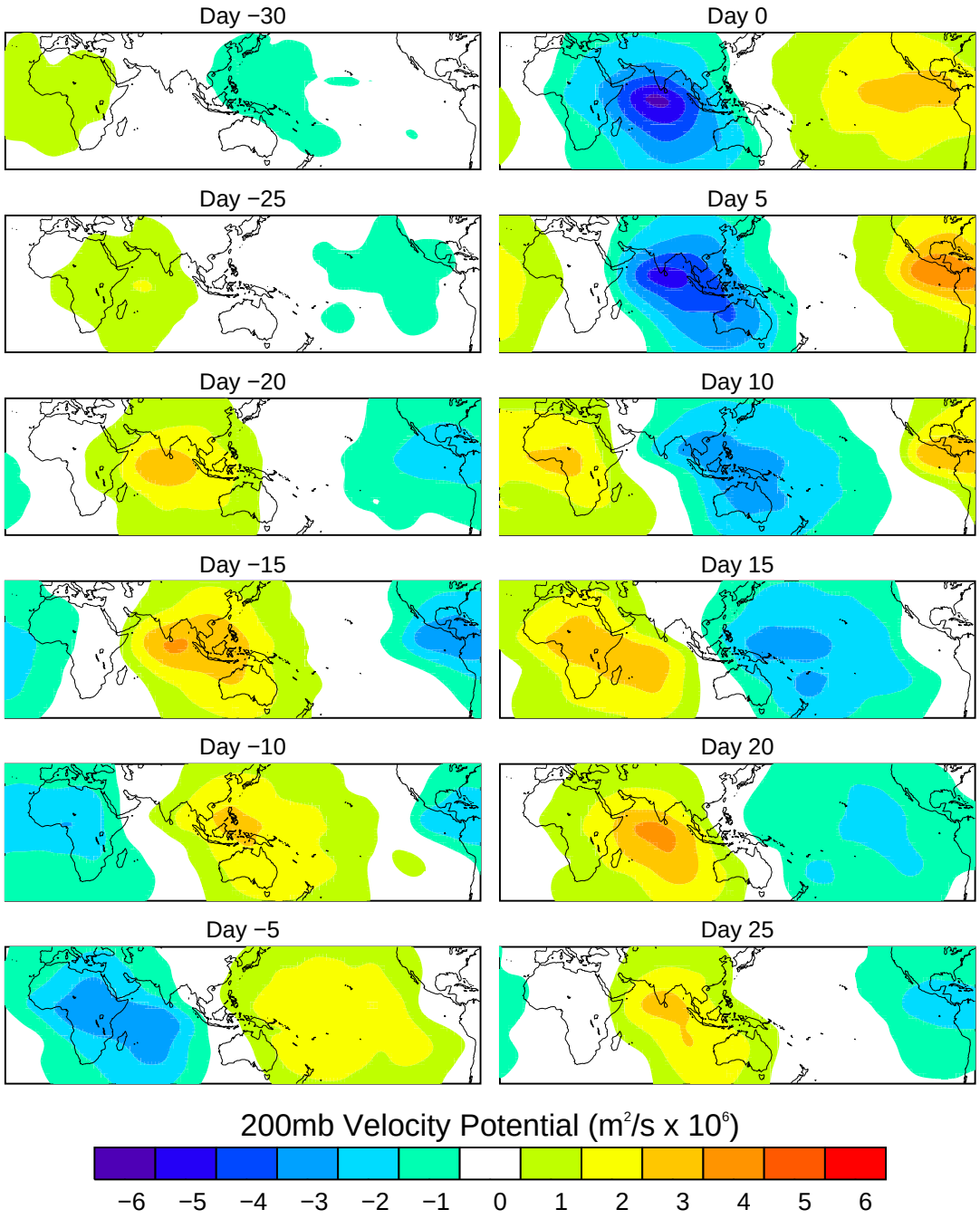

Figure 18: Similar to Figure 7 but for 200mb velocity potential during summer MJO.

potentially result in a stronger teleconnection between the summer MJO and the Americas. During summer, the eastward propagation of the circulation cells, while present, is not as clear as during winter.

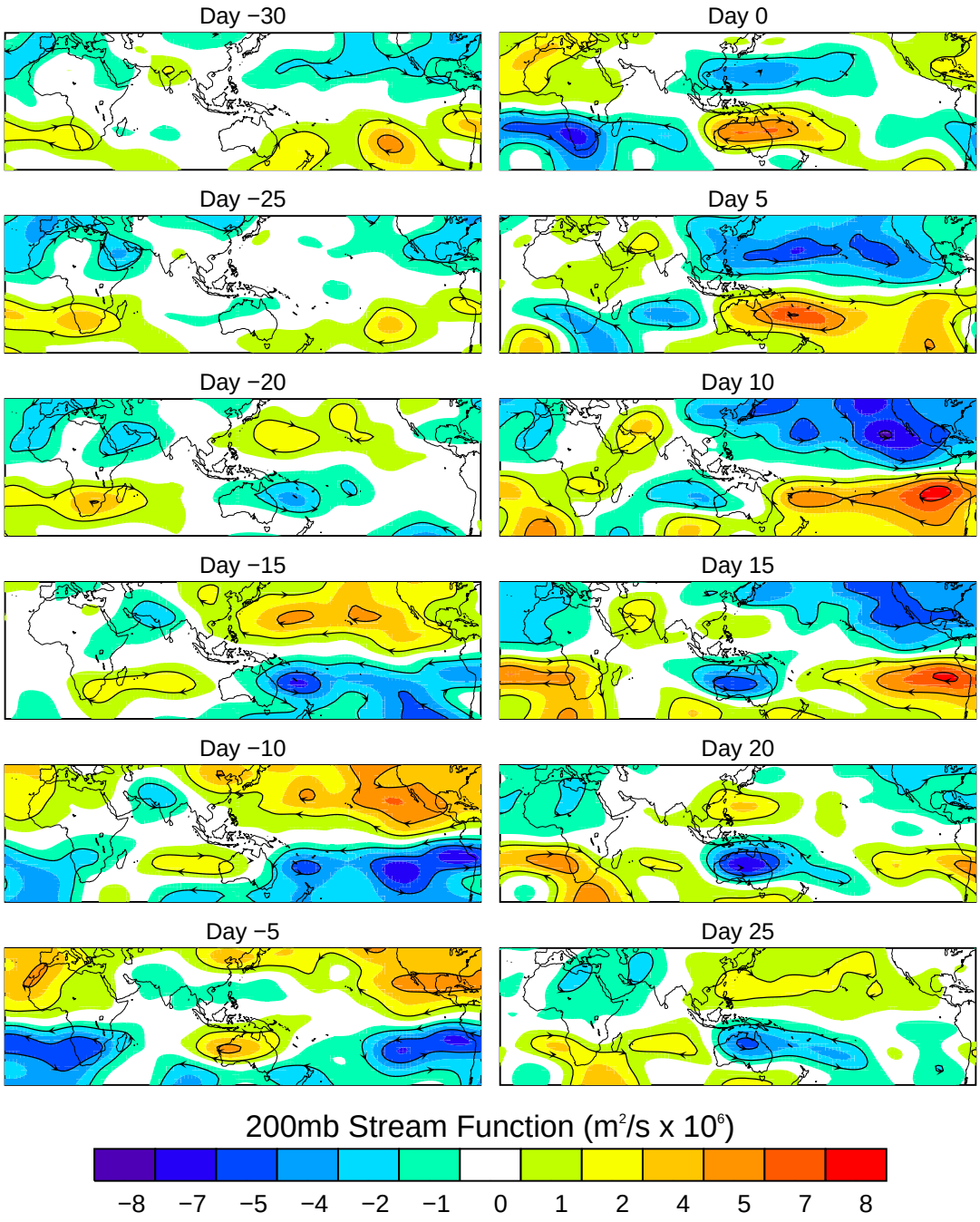

Figure 19: Similar to Figure 7 but for 200mb stream function during summer MJO. Arrows show the direction of the circulation.

Closer to the surface, the differences between summer and winter MJO are substantial. SLP anomalies during summer (Figure 20) reveal a bifurcation of both low and high surface pressure related to enhanced and reduced convection respectively.

While SLP anomalies during winter also showed a bifurcation, in this case over the Pacific, during summer the bifurcation is more prominent and it takes place over the Indian Ocean, directly and strongly affecting the South Asian monsoon and precipitation over Australia. Due to the earlier bifurcation of the SLP, around Day 15, during summer, negative anomalies of SLP are present over Asia, and during winter, the entire continent is under the influence of an anomalously high SLP. SST anomalies also show the coherent northward propagation during summer, with smaller ISO anomalies over the equator and larger ones over the Bay of Bengal compared to the winter case (Figure 21). Another major difference with the winter MJO is the considerable SST changes observed along the coast of China during summer. During winter, the anomalies near China are not as large as are those off the coast of northern Australia.

2.4.2 Vertical Structure

The vertical structure of the velocity potential and stream function present similar features as those already described for the winter case (Figure 22) with convergence in a thick tropospheric layer and divergence confined to a relatively thin layer. As mentioned before, the stream function anomalies to the west of the convection are very weak throughout the entire troposphere.

Since the northward propagation in the Indian Ocean sector is very strong during summer, an analysis of the zonal mass stream function between 10°S and 10°N is not very informative in this case. The composite structure of the meridional mass stream function however, nicely shows the northward propagation over the Indian Ocean of the circulation cells inducing subsidence and convection over the continent (Figure 23).

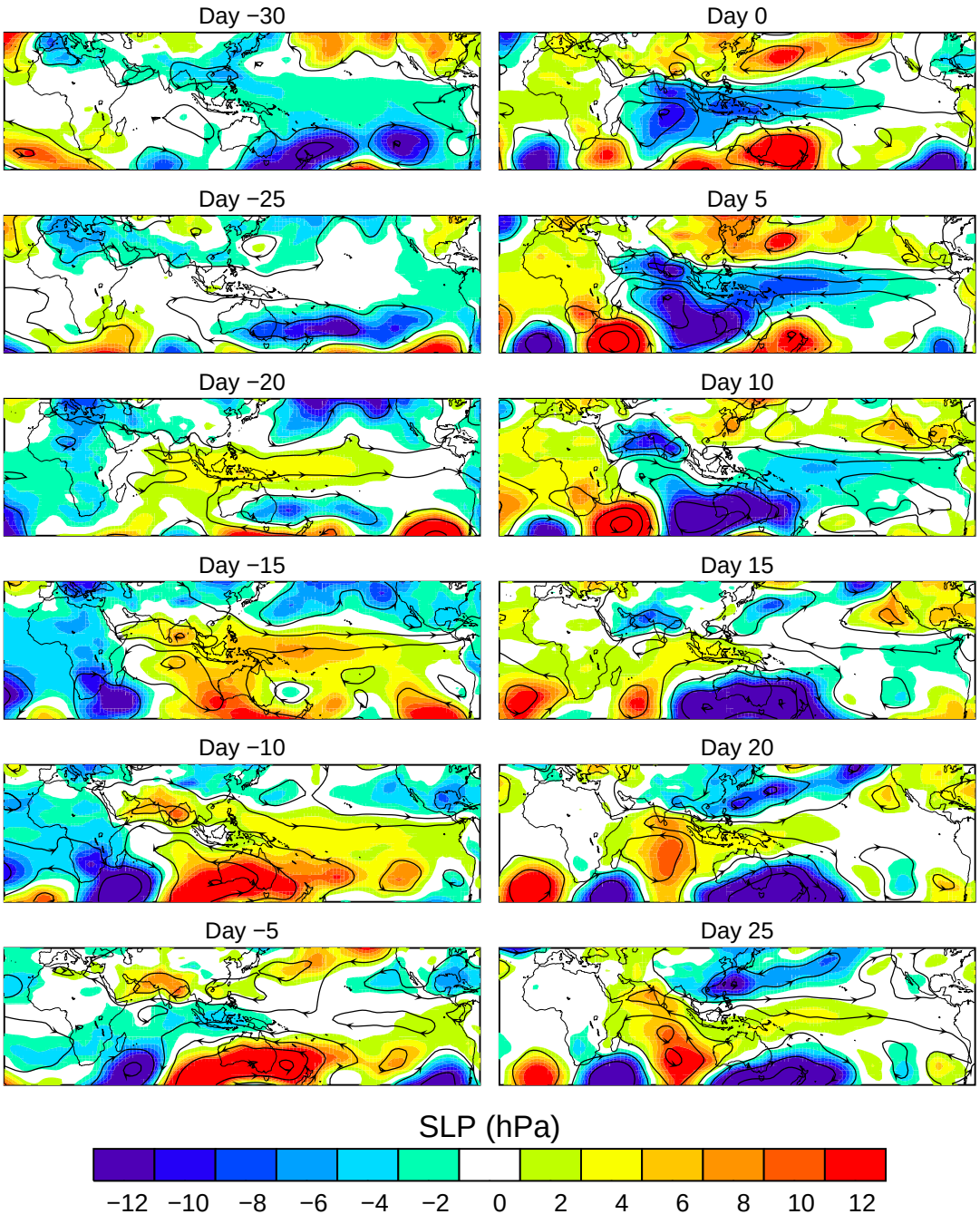

Figure 20: Similar to Figure 7 but for the SLP and 925mb stream function during summer MJO. Arrows show the direction of the circulation.

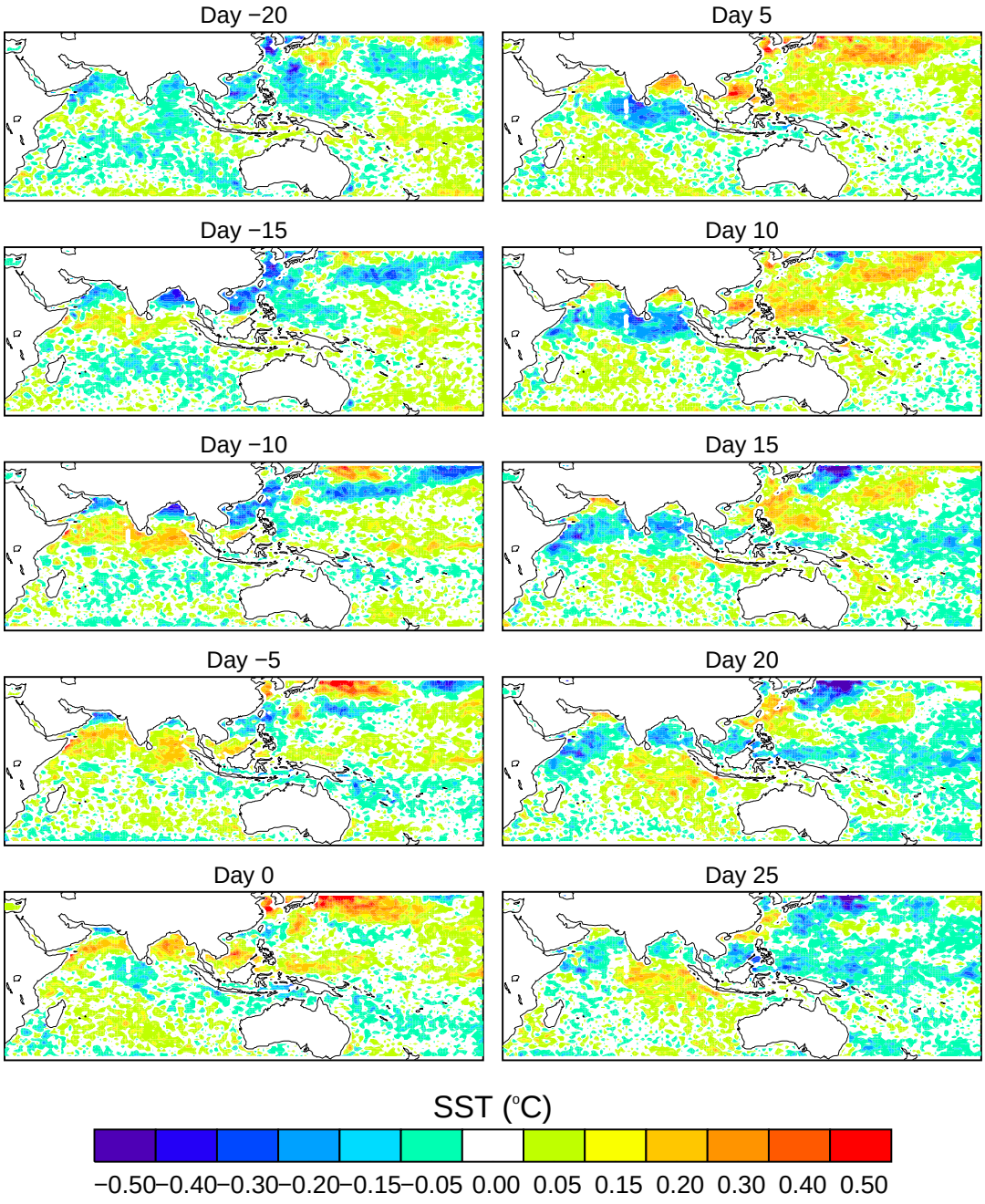

Figure 21: Similar to Figure 7 but for SST during summer MJO.

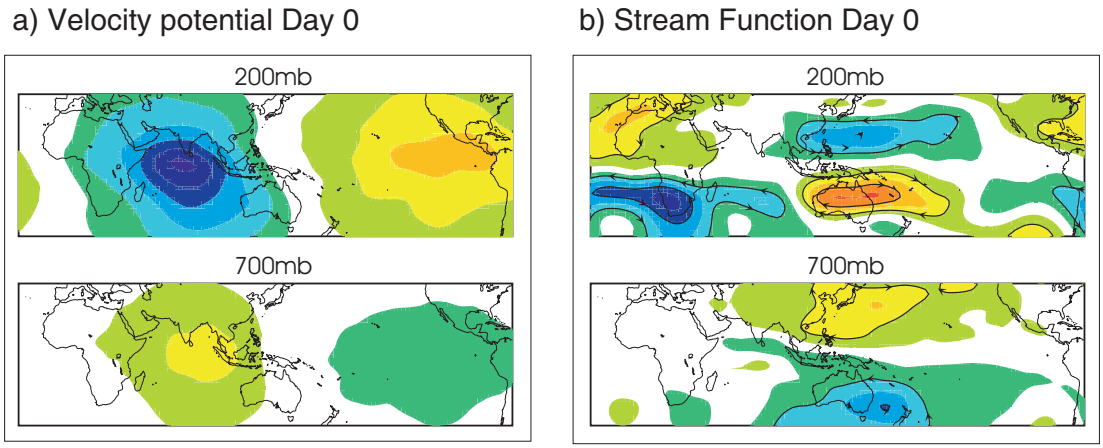

Figure 22: Similar to Figure 12 for summer MJO. 200mb and 700mb fields are shown.

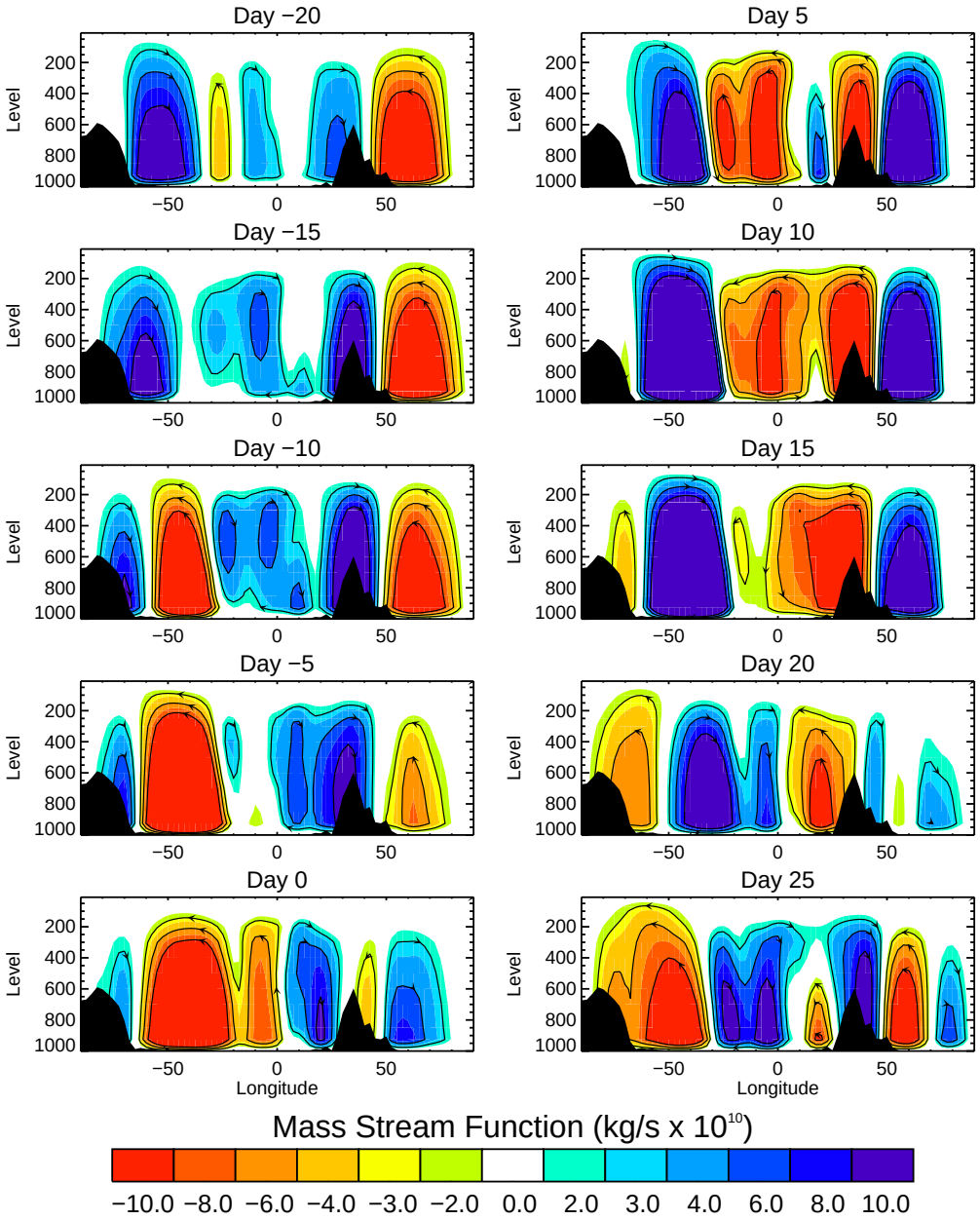

Figure 23: Similar to Figure 14 for summer MJO.

CHAPTER III

REGIONAL IMPACTS OF INTRASEASONAL VARIABILITY

The MJO and in general Intraseasonal Variability plays a very important role in global climate variability, with direct and indirect effects on regional rainfall variability, SST, potentially triggering El Nino events, among others. The onset and active-break activity of the Asian-Australian monsoon system is strongly influenced by the propagation and evolution of MJO events. The development of persistent North Pacific circulation anomalies during Northern Hemisphere winter has been linked to the evolution and eastward progression of convective anomalies associated with MJO events (e.g., Liebmann and Hartman 1984; Higgins and Mo 1997; Mo 2000). In fact, a link has been shown between rainfall variability along the western United States and the position of MJO convective anomalies (Mo and Higgins 1998). In addition, MJO convective activity has been linked to precipitation variability over Mexico and South America as well as to wintertime circulation anomalies over the Pacific-South American sector (Nogues-Paegle and Mo 1997; Paegle et al. 2000). Studies have also shown that particular phases of the MJO are more favorable than others in regards to the development of tropical storms/hurricanes in both the Atlantic and Paci?c sectors (Maloney and Hartmann 2000; Mo 2000; Higgins and Shi 2001). The propagation of MJO events over the western Pacific Ocean has been found to significantly modify the thermocline structure in the equatorial eastern Pacific Ocean via their connection to westerly wind bursts (e.g., Hendon et al. 1998). This latter interaction has even been suggested to play an important role in triggering variations in El Nino-Southern

Oscillation (ENSO; e.g., Lau and Chan 1988). Recently, Waliser et al. (2005), found the existence of a systematic modulation of upper ocean productivity by the ISO. During summer, there is an inverse relationship between chlorophyll amounts and rainfall over the Bay of Bengal.

Among all the impacts of ISO, perhaps the most frequent and important in terms of the amount of people directly affected is the modulation of summer Southeast Asian monsoon, generating wet and dry spells. It is for that reason that this chapter focuses on studying the role of intraseasonal variability in the nature of Southeast monsoon precipitation.

3.1 Role of Intraseasonal Variability in the Nature of South-East Monsoon Precipitation

A fundamental requirement for agricultural development and water resource management in the South and Southeast Asian region is a better predictive capability of internal and external variability of summer monsoon rainfall on time scales ranging from weeks to several years (e.g. Parthasarathy et al. 1988, Gadgil 1996, Webster et al. 1998, Lal et al. 1999). In addition, as the Asian summer monsoon is a major component of global climate dynamics, it has the potential of imparting variability on the climates of other regions (e.g. Webster and Yang 1992, Webster et al. 1998, Kirtman and Shukla 2000). Therefore, improvements in the predictability of the monsoon may lead to increased predictability elsewhere. The fundamental hypothesis of this study is that a greater understanding of the physical processes that determine the mean seasonal precipitation patterns in the monsoon will lead to better predictions and provide milestones for numerical climate modeling.

The fundamental mechanism that drives the monsoon circulation is generally agreed upon. Essentially, this is the cross-equatorial pressure gradient formed by the differential heating between the land masses of the summer hemisphere and the oceans of the winter hemisphere. However, the spatial and temporal variability of

monsoon precipitation is far more complicated than that which can be expected from a slowly varying cross-equatorial pressure gradient. In fact, the processes that produce the specific spatial distribution of even the long-term mean precipitation are not clearly understood. Different processes, phenomena and geographic features have been suggested as modulators of monsoon precipitation such as local and regional effects of orography (e.g. Grossman and Garcia, 1990, Grossman and Durran 1984, Xie et al. 2005), propagation characteristics of the MISO, which involve both the ocean and the atmosphere (e.g. Lawrence and Webster 2002; Jiang and Wang 2004, Wang et al. 2005), propagation of biweekly signals from the South China Sea (Annamalai and Slingo 2001), and land-atmosphere feedback (e.g. Webster 1983). All of these features of the monsoon in isolation or in combination appear as possible candidates. In essence, the cross-equatorial pressure gradient describes the annual cycle of the monsoon but little of its character.

This section is an attempt to determine the mechanisms responsible for the variability and structure of summer monsoon rainfall on different time scales and regions within Asia. Figure 24 provides a geographical reference for the regions discussed in the section. These regions include: East Indian Ocean (EIO; 5°S-5°N, 85°-95°E), Bay of Bengal (BoB; 13°-23°N, 87°-96°E), Central India (CI; 16°-23°N, 74°-82°E), Gangetic Plains (GP; 23°-30°N, 74°-89°E), Western Ghats (WG; 8°-19°N, 71°-76°E), and Cambodia (CMD; 8°-16°N, 101°-109°E).

Figure 25a shows the spatial distribution of the mean cumulative rainfall from June to September (JJAS) over the period 1979-2004 using the Global Precipitation Climatology Project (GPCP) data, as well as the mean annual cycle of rainfall over the six regions previously described (Fig. 25b). The standardized JJAS rainfall from 1979 to 2004 for each region is shown in Figure 2c. It is evident from Figure 25a that there is a complex spatial pattern of rainfall associated with the Asian monsoon system, with localized precipitation maxima to the west of the WG foothills in India

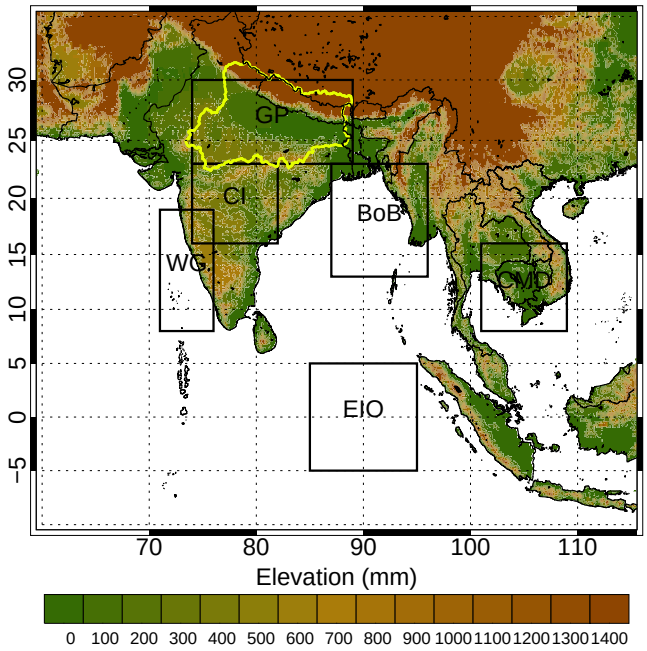

Figure 24: Geographical reference for the regions discussed in the text. EIO: East Indian Ocean (5°S-5°N, 85°-95°E), BoB: Bay of Bengal (13°-23°N, 87°-96°E), CI: Central India (16°-23°N, 74°-82°E), GP: Gangetic Plains (23°-30°N, 74°-89°E), WG: Western Ghats (8°-19°N, 71°-76°E), and CMD: Cambodia (8°-16°N, 101°-109°E).

with a total of 810 mm during JJAS, the East side of the BoB with 1380 mm, and over CMD with 1030 mm. While the overall driving mechanism of the monsoon is the slowly varying cross-equatorial pressure gradient force, the rainfall is strongly regional with maxima occurring over the ocean regions and not over the Asian continent nor the Indian subcontinent as initially noted by Grossman and Garcia (1990). In fact, the BoB possesses the largest global maximum of boreal summer rainfall on the planet. It is interesting to note that total summer precipitation drops almost linearly between the Bay of Bengal (>1200 mm), across central India (800 mm) and into Pakistan (200-300 mm).

The rainfall maximum over the EIO (860 mm) does not have a monsoon-like annual cycle and is relatively constant throughout the year (Fig. 25c). However, it has been shown to be intimately related to monsoonal intraseasonal variability (e.g. Webster et al. 1998, Lawrence and Webster 2002). In contrast to the near-equatorial precipitation, summer rainfall further north and east over the BoB and Southeast Asian countries commences in May. Over most of continental Indian, rainfall, however, starts later during June (Fig. 25b). In fact, a number of studies consider the EIO as the source region of monsoon intraseasonal variability which possesses the largest amplitude of all monsoon precipitation variations (e.g., Webster et al. 1998, Lawrence and Webster 2002, Waliser et al. 2003a,b) producing active and break periods of the South Asian monsoon on 25-80 day time scales.

In the BoB, precipitation occurs as a maximum parallel to the Burma Mountains (Fig. 25a) as noted by Grossman and Garcia (1990) and Xie et al. (2005). But what are the main processes that determine the rainfall maximum? Is the maximum produced by the mean onshore flow from the basic southwesterlies of the monsoon producing rainfall through orographic uplift? Does the freshness and warmth of the Bay itself play any role so that if there were no Burmese Mountains there would still be a regional precipitation maximum? Furthermore, for whatever the reason there

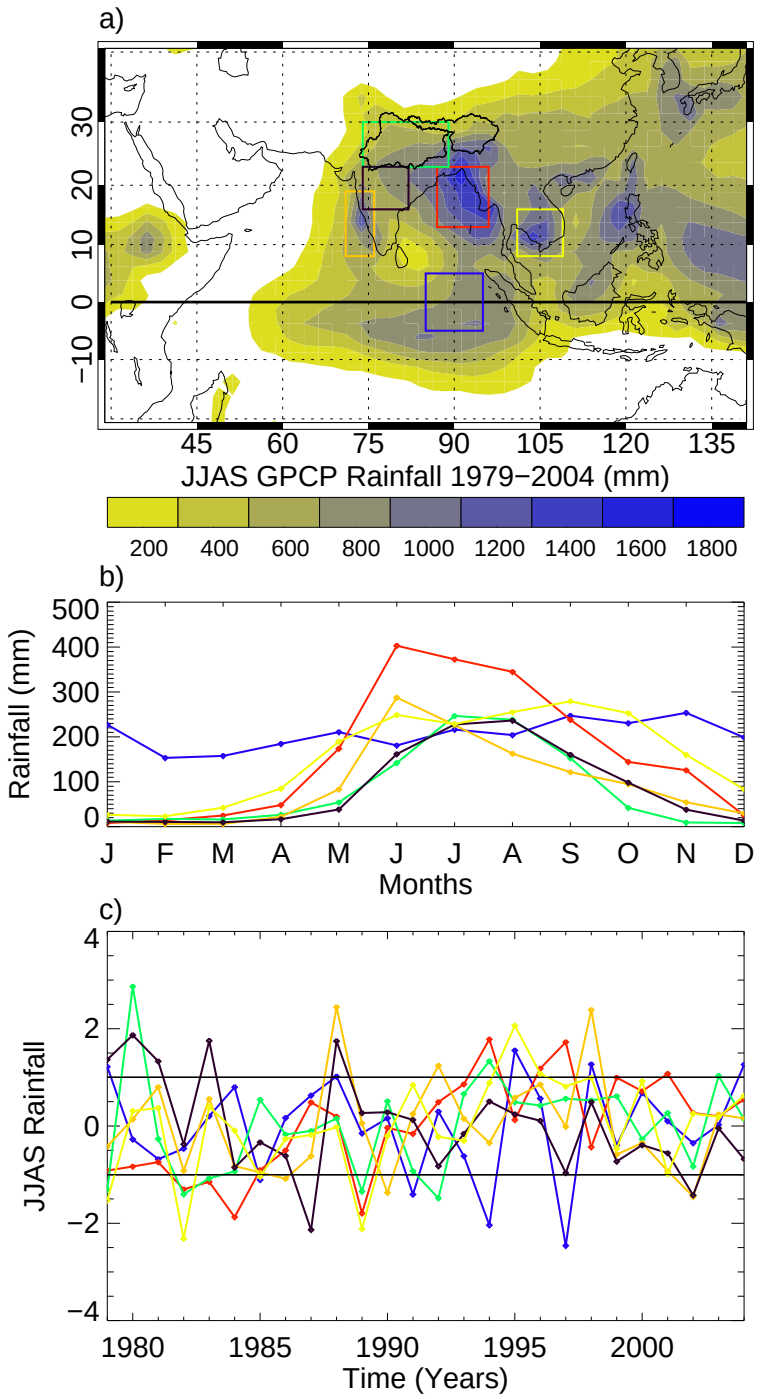

Figure 25: a) Mean South and Southeast Asian summer monsoon rainfall (June to September; JJAS) averaged from 1979 to 2004 using the monthly GPCP data, b) mean annual cycle of rainfall over six regions outlined in Figure 1, and c) the standardized JJAS rainfall from 1979 to 2004 for the same regions showing interannual variability of the rainfall.

is a maximum in the BoB, what time scales of motion that contribute to its existence? Zuidema (2003), Grossman and Garcia (1990), Xie et al. (2005) examined this question but the first study considered only two summers while the latter two used monthly data. Thus it is difficult to determine the role of intraseasonal variability or synoptic events, for example, in producing the maximum. BoB precipitation has proven to be very difficult to model which is evident form the results of the Atmospheric Model Intercomparison project as summarized by Gadgil and Sanjani (1998) and Sperber and Palmer (1996). In fact, simulation of mean monsoon precipitation in general has been allusive in models. It is important to determine whether or not these failures result due the poor representation of orography, for example, or the omission of specific phenomena such as tropical intraseasonal variability.

The complexity of the summer monsoon rainfall is not restricted to spatial patterns but also to its variation in time. The monsoon possesses a strong temporal variability ranging from the diurnal, through synoptic and intraseasonal, to interannual timescales. In fact, this complicated structure extends to the relationship between interannual variability of each of the monsoon regions we consider. These inter-regional correlations are summarized in Table 1 for the period 1979-2004. The complexity may be seen by comparing the interannual correlations between the BoB, CI and GP which we may expect to be highly correlated. The JJAS seasonal rainfall correlation between the BoB and the CI is 0.41 which is higher and of the opposite sign to that between the BoB and CI (-0.32). The reason for this dissimilarity in magnitude and sign between the correlations is unclear. Furthermore, why is the correlation larger between BoB and CMD larger than between the BoB and the GP? Why is the precipitation in EIO so poorly correlated with all of the monsoon regions? The All-India Rainfall Index (AIRI: Parthasaraty et al. 1987) correlates well with CI, moderately with GP and WG but very weakly with BoB. Are the relative weaknesses of the correlations or even their absence between regions indicating that other higher

Table 1: JJAS rainfall correlations among different regions for the period 1979-2004.

Region	EIO	BoB	CI	GP	WG	CMD	AIRI
EIO	1.00						
BoB	-0.27	1.00					
CI	0.10	-0.32	1.00				
GP	-0.18	0.41	0.20	1.00			
WG	0.29	0.05	0.49	0.08	1.00		
CMD	0.07	0.46	0.07	0.41	0.38	1.00	
AIRI*	-0.16	0.11	0.60	0.40	0.48	0.28	1.00

* Obtained from the Indian Institute of Tropical Meteorology (www.tropmet.res.in)

frequency variability links different parts of the monsoon? Also, noting the relative poorness of the correlations between different regions within India and the various regions with the AIRI, how representative is this index which is used extensively in prediction schemes and when attempting to find links between El Niño Southern Oscillation (ENSO) and monsoon precipitation? Lawrence and Webster (2001), for example, have suggested that the AIRI is unrepresentative of precipitation in the BoB.

3.1.1 Background on the ISO-Monsoon Connection

Yasunari (1979, 1980) was among the first to document the connection between marked northward propagation of clouds and convection generating major "active" and "break" periods of the Indian monsoon with the eastward-propagating cloud disturbances in the equatorial Indian Ocean. Sikka and Gadgil (1980) studied the latitudinal position of the maximum cloudiness zone (MCZ) associated to the Intertropical Convergence Zone, attributing the northward migration to variations in the surface heating produced by the existence of two different MCZ, one along 15°N and the other near the equator. Krishnamurti and Subrahmanyam (1982) showed that the meridional length scale of this propagating mode is approximately 3000 km, and its meridional phase speed is about 0.75° per day.

Different mechanisms have been proposed to explain the northward propagation associated with the MISO. Webster (1983) suggested that the land surface heat flux into the atmospheric boundary layer plays a role in destabilizing the atmosphere ahead of the convection, leading to a northward shift of the convective zone. Goswami and Shukla (1984) proposed that a convection-thermal relaxation feedback generates a standing oscillation between the equatorial and monsoon MCZs, in a similar way to Sikka and Gadgil (1980) arguments. Wang and Xie (1997) proposed a mechanism in which Rossby waves emanate from the eastward propagating disturbance forming a convection front that tilts northwestward from the equator as the wave moves eastward, resulting in an apparent northward propagation. Lawrence and Webster (2002) analysis supports this mechanism. Kemball-Cook and Wang (2001) suggested that the ocean-atmosphere interaction contributes to the northward propagation changes in surface latent heat fluxes associated with changes in wind speed may change the sea surface temperature (SST) to the north of the convection. Weaker winds increase SST, generating moisture convergence into the boundary layer, destabilizing the atmosphere, hence moving the convection northward. In a recent modeling study, Jiang and Wang (2004) proposed a mechanism in which the strong vertical shear leads to the generation of barotropic vorticity and divergence to the north of the convection promoting a northward shift of the moisture convergence in the boundary layer. Jiang and Wang (2004) also proposed a moisture-convection feedback mechanism in which moisture advection by the mean southerly in the boundary layer and advection of the mean specific humidity gradient by the perturbation wind lead to the northward shift of the convective heating generating the northward observed propagation. In general, observations suggest that most likely it is a combination of the proposed mechanisms that results in northward propagation of the ISO during summer.

3.1.2 Overview of summer monsoon precipitation

Even though the amplitudes of the rainfall maxima shown in Figure 25a change from year-to-year, they remain as persistent climatological features. However, as suggested by the correlations shown in Table 1, the respective changes in seasonal rainfall from year to year for the different regions do not appear to be interrelated, suggesting strong internal variability in the monsoon system, possibly associated with intraseasonal activity. Figure 26 shows the rainfall anomalies for each JJAS period between 1997-2004 relative to the long-term mean. Large amplitude and large scale interannual variability is evident. Most often anomalies of different sign lie across different parts of South and Southeast Asia. Over India, the spatial complexity of the patterns calls into question, once again, the usefulness of using the AIRI as a measure of Indian monsoon rainfall variability. Only in 2002 is all of India dominated by an anomaly of the same sign. The identification of high amplitude internal monsoon variability that pervades the years shown in Figure 26 would be very important as it may obscure signals of the interaction between the monsoon system and other major phenomena of the global climate such as ENSO system.

Spectral analysis of daily time series of rainfall reveal the importance of the intraseasonal variability present in monsoon rainfall. Figure 27 shows the average wavelet spectra for the rainfall over the six regions obtained using techniques described by Torrence and Compo (1998). The solid line shows the average spectra and the shaded region encloses plus and minus one standard deviation. In general, rainfall in all regions shows high variability within the season in time scales ranging from about 7 to 60 days. Over EIO, the amplitude of the intraseasonal activity appears even stronger than the annual cycle, with a marked spectral peak at 30 days, and a secondary peak around 15 days. This intraseasonal activity over the Indian Ocean is not exclusive of summer. In fact, variability in the intraseasonal band is usually stronger during winter (e.g. Salby and Hendon 1994). But, over the other regions

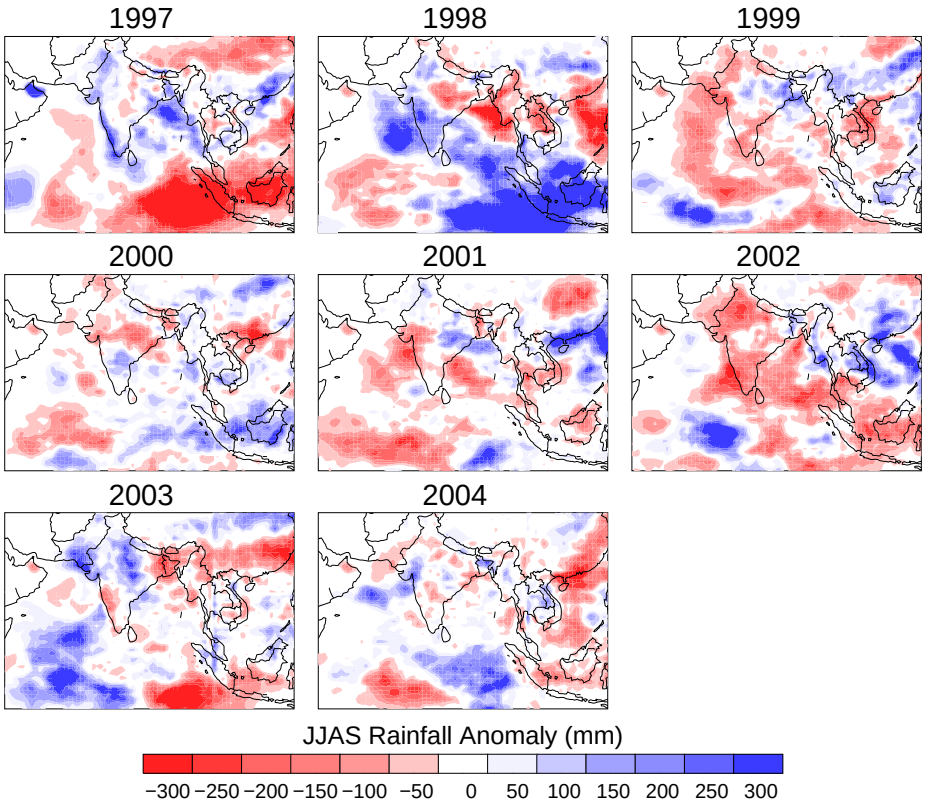

Figure 26: JJAS Rainfall anomaly for each year from 1997 to 2004 using the daily GPCP data.

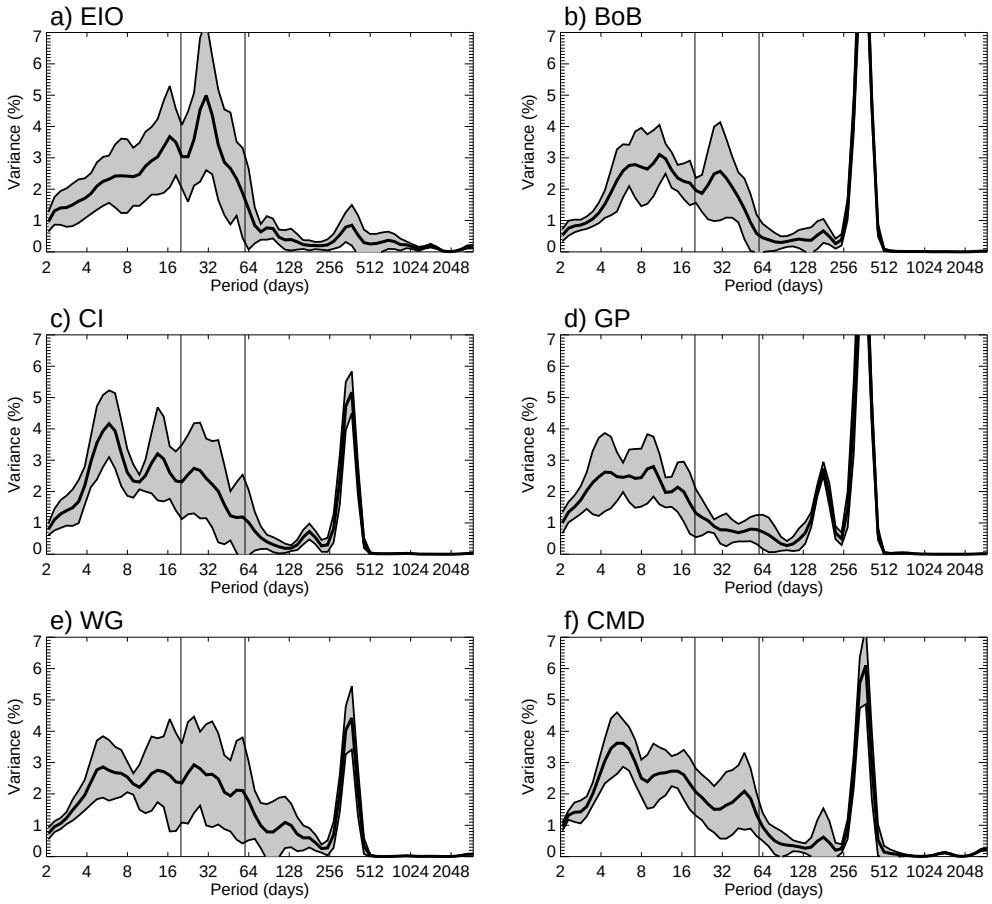

Figure 27: Summer average wavelet spectra for 1997-2004 daily GPCP rainfall for each region of Figure 24. The shaded area represents plus and minus one standard deviation of the summer spectra.

considered, high intraseasonal activity is confined to the summer, with magnitude and periods that fluctuate notably from year to year as is evident in the average wavelet spectra and the magnitude of the deviation around the average.

From the summer average wavelet spectra, it is possible to identify some important aspects related to variability of rainfall within a wet summer season. For the BoB, in addition to the spectral peak corresponding to the annual cycle, there are two distinctive peaks at 10 and 30. A strong annual cycle peak is common to all regions except for the EIO. Over CI, the rainfall record shows important spectral peaks at 6, 13, and 25 days, indicating important variability differences with the BoB region.

While the wavelet spectrum of rainfall over the GP also shows intraseasonal 25-80 day variance during some years, it is not large enough to appear as a peak in the average spectrum. There, however, there is a broad spectral peak between 4 and 9 days. The absence of a significant peak poses a conundrum. Since the JJAS rainfall correlation is higher between the BoB and the GP than between the BoB and CI, why are the spectral characteristics of the variability closer among the BoB and CI?

For the WG, the average spectrum shows a broad peak between 5 and 50 days, indicating a more complicated temporal structure of the rainfall, most probably due to interaction between the combined effect of the large-scale monsoon intraseasonal variability and orography. Over CMD, the most distinctive peak after the annual cycle is located near 6 days, probably associated with propagating easterly waves from the Pacific Ocean, with a secondary peak around 45 days.

3.1.3 Intraseasonal Variability during summer

If the monsoon intraseasonal oscillation is the dominant large-scale feature of the monsoon (see review Webster et al. 1998), which in general develops over the EIO and propagates first eastward along the equator to the eastern reaches of the ocean (Yasunari 1979, 1981, Sikka and Gadgil 1980, Lawrence and Webster 2002, Jiang and Wang 2004), what local features modulate the intraseasonal monsoon rainfall signal so the average spectra are different in each region such as those evident in Figure 27? Quite possibly the differences may depend on the specifics of the nature of the northward propagation, differences between oscillations, different nature of ocean-atmosphere and the land-atmosphere feedbacks. In some manner, these processes aggregate to cause interannual variability of the intraseasonal mode.

Figure 28 shows the mean amplitude of the JJAS intraseasonal 25-80 day rainfall variance for each year from 1997 to 2004 as well as for all the years (multi-year). The mean amplitude in a spectral band is defined as the standard deviation of the filtered

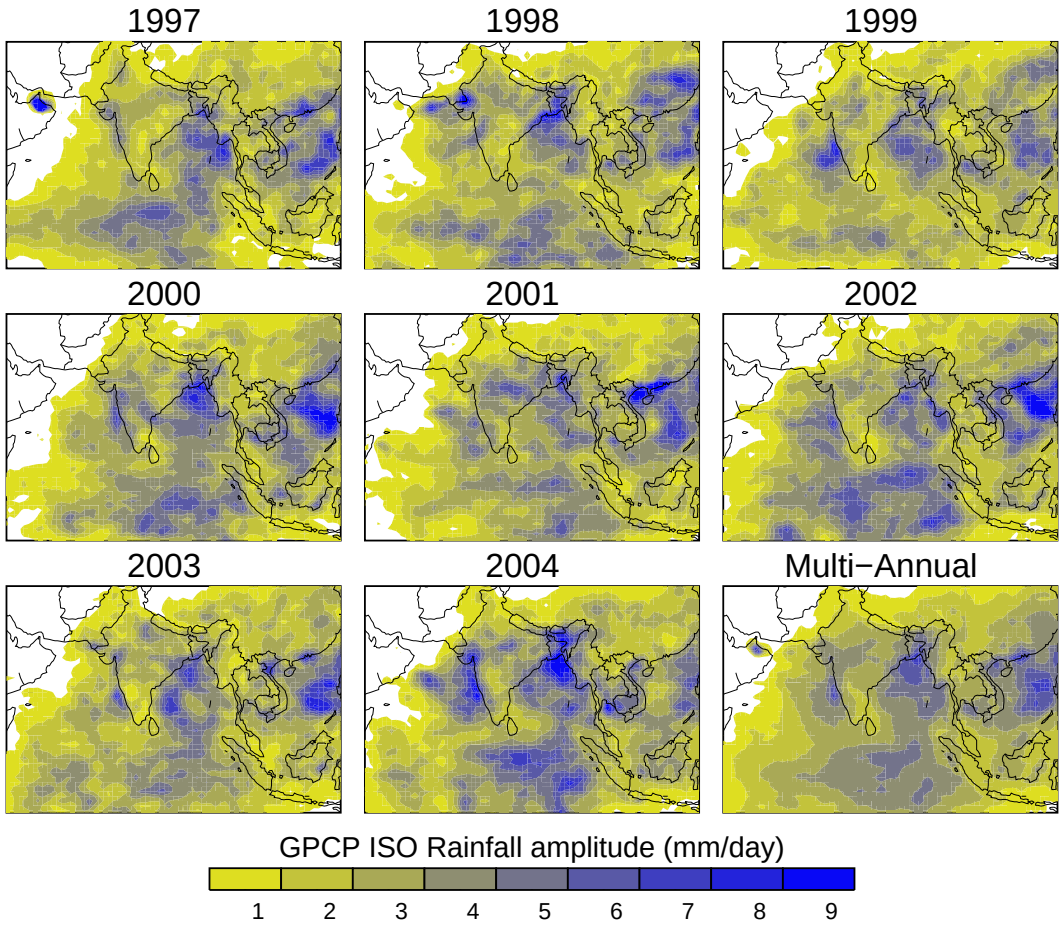

Figure 28: Mean amplitude of the summer MISO (25-80 day) associated GPCP daily rainfall for each year from 1997 to 2004 as well as the multi-annual average amplitude.

variable in the band or, alternatively, the square root of the variance contained in the selected time span and spectral band. Areas of maximum intraseasonal activity vary strongly in magnitude and location from year to year, with the most recurrent feature being the high intraseasonal variability over the EIO and the BoB.

Figure 29 shows the cumulative intraseasonal rainfall for JJAS, obtained by simply adding the band-passed rainfall time series for each day from June 01 to September 30 at every individual grid cell highlighting the locations where prolonged active and break phases of the monsoon occur. In essence, the distribution of positive and negative anomalies of rainfall associated with cumulative MISO activity can be regarded as the most important internal characteristic of interannual monsoon variability. Here

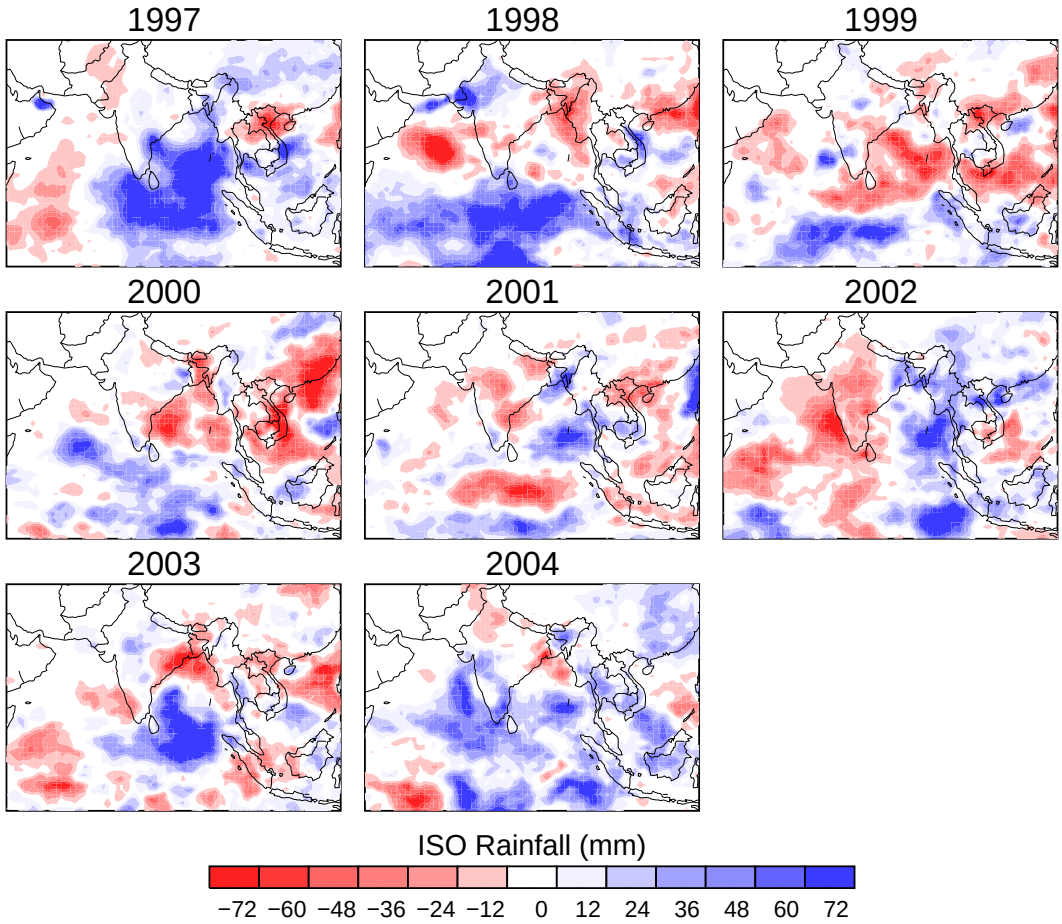

Figure 29: Cumulative intraseasonal (25-80 day) rainfall from the daily GPCP product during JJAS for each year from 1997 to 2004.

we define internal variability as variability that does not arise through remote teleconnections with other phenomena like ENSO, but rather from instabilities within the system.

In the manner described above, we hypothesize that summer intraseasonal activity may be considered as an instability of the monsoon system, which in general is not affected by the long-term background state of the ocean-atmosphere system outside the Indian Ocean basin and different teleconnections. As a consequence it appears that it is necessary to consider the distribution of the interannual internal variability in order to explain some of features of JJAS rainfall anomalies observed in Figure 26. Perhaps the most prominent variation from average is the 2002 drought over India,

which coincides with large amplitude negative anomalies of MISO rainfall over the Indian subcontinent (Figure 26).

Figure 30 shows the variability of the 25-80 band-passed daily rainfall plotted against 4-20 day rainfall variance, for all maxima in 4-20 day variance band and for all regions of the analysis. Spectral analysis showed high variability in the 25-80 and 4-20 day bands in the regions of analysis. There are two major points that suggest that the variability in the 4-20 day band is mainly contained in the 25-80 day band, especially in the EIO, BoB, and CI. One is that the 4-20 day variance time series (not shown) presents intraseasonal variability and the other is that, as observed in Figure 30, most of the major peaks in the 4-20 day variance correspond to a maximum or a very high value (above one standard deviation) in the 25-80 days band-passed rainfall. This indicates that rainfall variability in the 4-20 day band is preferentially present during active periods of the monsoon intraseasonal oscillation.

Similarly, most of the monsoon sub-synoptic variability appears to be contained within the intraseasonal envelope of convection. Figure 31a shows the average wavelet spectrum of the 3-hourly TRMM rainfall over the BoB illustrating, in addition to the variability in the 4-20 and 25-80 day bands, that there is a very strong diurnal cycle of precipitation. The amplitude of the diurnal cycle is modulated by the envelope of convection in the 4-20 and 25-80 day bands, with greater amplitude during the peak of the intraseasonal event (see Figure 31b).

3.1.4 Composite Analysis of summer intraseasonal variability

The relatively regular behavior of the summer MISO (e.g., Webster et al. 1998, Lawrence and Webster 2002, Waliser et al. 2003a,b) has been used to great effect in forecasting discharge of Ganges and Brahmaputra rivers and regional rainfall over India (e.g., Goswami and Xavier 2003, Webster and Hoyos 2004). In order to study in detail the structure of the MISO over the Indian Ocean and Southeast Asia, dates of

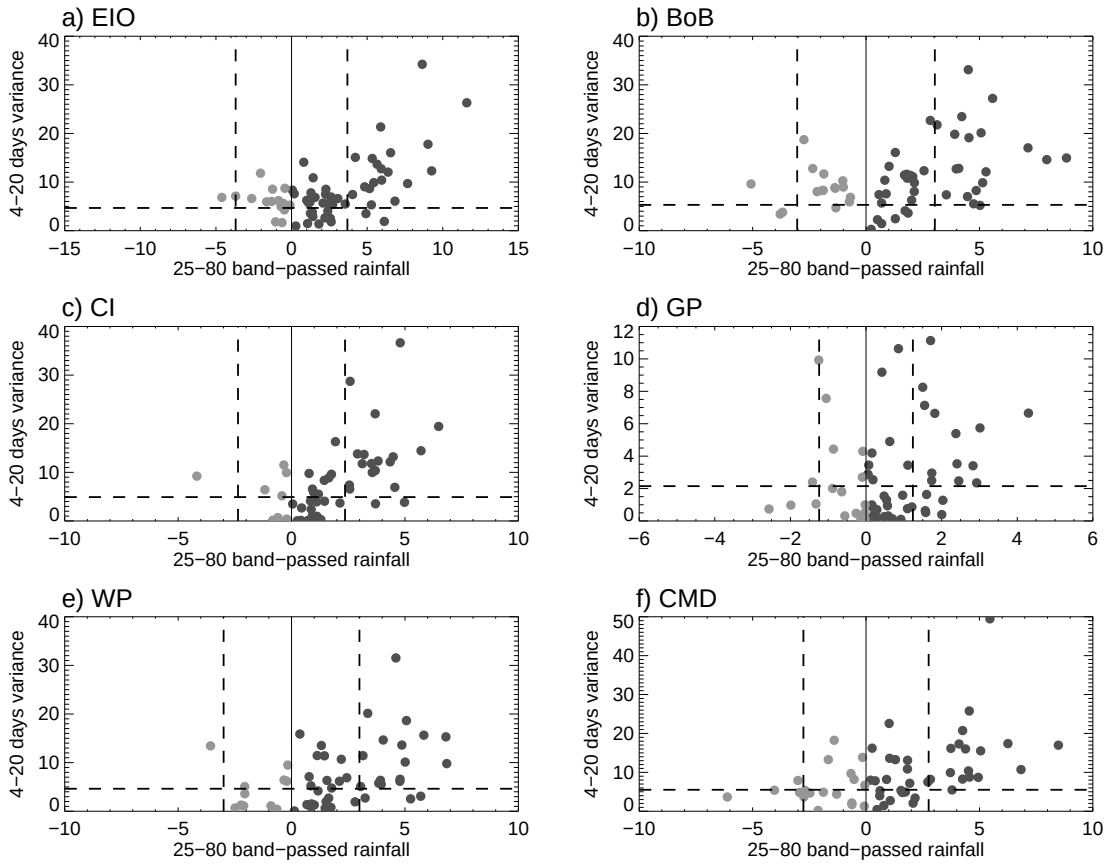

Figure 30: 25-80 band-passed daily GPCP rainfall anomalies plotted against 4-20 day rainfall variance anomalies for all maxima in 4-20 day variance for each region (Fig. 24). The horizontal dashed line represents one standard deviation of the 4-20 day rainfall variance and the vertical dashed lines plus and minus one standard deviation of 25-80 day rainfall. Dark (light) circles represent positive (negative) 25-80 day band rainfall anomalies.

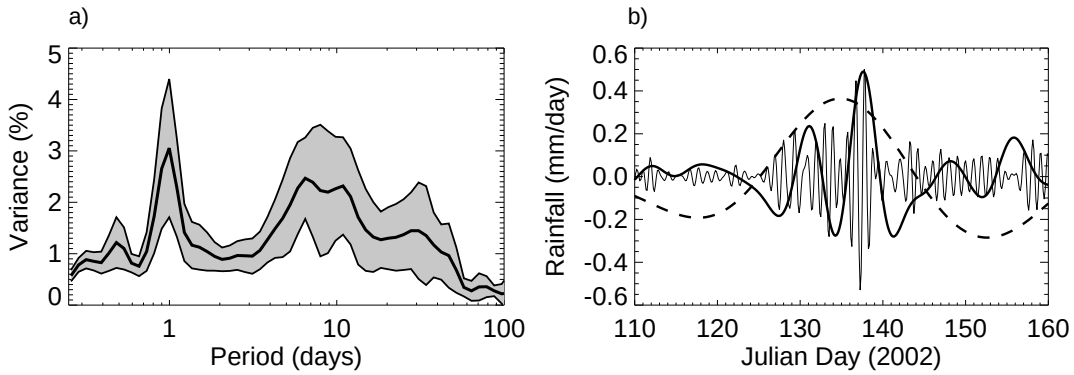

Figure 31: a) Average wavelet spectrum of the 3-hourly TRMM rainfall over the BoB from 1998-2004. The shaded region encloses the average spectrum plus and minus one standard deviation. b) 3-hourly TRMM rainfall variability in different time scales during one full intraseasonal event during summer 2002. The figure shows rainfall in the 25-80 day band (dashed line), 5-20 day (thick solid line), and the diurnal cycle (thin solid line).

maximum rainfall associated with intraseasonal activity (25-80 day band-passed data) with magnitudes greater than one standard deviation in the band were selected for the regions shown in Figure 24. The composite evolution of several fields was studied. It was found that SST, surface pressure, lower tropospheric winds and rainfall itself (or OLR) emerge as the most coherent fields to explain the fundamental features of the intraseasonal activity.

For the BoB, a total of 24 cases were selected in the period 1997-2004, and from those 16 cases are classified as what we refer as canonical MISO, four classified as having developed in situ, and four as developed through orographic interactions under break conditions over the Bay of Bengal. The classification of the events was done by studying the evolution of each individual event.

3.1.4.1 BoB Composites: Canonical MISO

Figure 32 show the composite behavior of 25-80 day band-passed daily rainfall, 925 hPa winds, sea level pressure and SST, respectively. The canonical structure corresponds to an intraseasonal event that starts as a convective anomaly in the equatorial

Indian Ocean, followed by an eastward propagation which splits, with southward and northward propagating branches, usually off the west coast of Sumatra, introducing positive anomalies of precipitation over the BoB. The event develops (around day -20) over warm surface waters and low pressure at the equator. Around the same time, the BoB is under break (dry and suppressed) conditions, associated with the previous MISO, and high surface pressure with a corresponding anticyclonic circulation driving the air to the southwest over the Bay away of the Burma Mountains. The high-pressure system also expands into the Arabian Sea and India. These cloud-free conditions favor SST increases over the BoB and are integral parts of the MISO cycle. The equatorial low level surface pressure and associated convection propagates to the east accompanied by surface cooling from freshening winds and increased surface evaporation. By the time the anomaly reaches the west coast of Sumatra (day -10), the waters at the north of the Bay warmed under the prior anticyclonic conditions, inducing the northward propagation of the surface low pressure from the equator introducing positive anomalies of rainfall. As the instability evolves, the surface low pressure center is located over India (day 0) driving moist air towards the eastern side of the Bay and the Burma mountains (see Fig. 29) where orographic lifting enhances precipitation resulting in the observed maximum parallel to the mountain range (Fig. 30). By day +5, reductions in insolation and freshening of winds cool the surface waters of the BoB, acting as a negative feedback on MISO convection. At about the same time, the following break phase starts developing in the equatorial Indian Ocean induced largely by subsidence of air resulting from the convection further north (Wang et al. 2005). The observed lags in convection in composite pattern are corroborated by estimation of wavelet coherency and phase lag between daily BoB and EIO rainfall (e.g. Torrence and Webster 1999). On average during the summers from 1997 to 2004, the mutual wavelet coherence in the intraseasonal 25-80 day band is 0.55 and their phase difference is about 120° (15 days in this time scale) leading

the rainfall over the EIO.

3.1.4.2 Variability within the BoB Canonical MISO

Earlier we noted (Figure 30 and 31) that the intraseasonal rainfall band contains higher frequency activity. We now consider this containment in greater detail. Composite analysis of 64 intense precipitation events in the 4-20 day band (not shown) confirms that the higher frequency events develop in-situ mainly over the northern part of the BoB with no significant propagation, and that about 75% of the events developed during MISO active conditions. Figure 33 displays the spatial distribution of the mean amplitude of the summer (JJAS) 4-20 day rainfall variability. The features are remarkably similar to the multi-annual structure of intraseasonal variance shown in Figure 28. This resemblance provides further evidence of the simultaneous coexistence of both modes of rainfall variability.

Figure 34 shows time-latitude sections of intraseasonal GPCP rainfall and 3-hourly TRMM rainfall for two strong MISO events occurring during May 1999 and May 2002. The features observed in these two examples are common for almost all events analyzed in the period 1998-2004. The diagram shows clearly the northward propagation of the envelope of convection from the equator enclosing individual southward propagating storms possessing marked diurnal cycle (as in Figure 31). Webster et al. (2002), using brightness temperature data for the JASMINE experiment (1999), and Zuidema (2003), analyzing brightness temperatures from INSAT (summer 1998) and Meteosat-5 (summer 1999), found similar propagating diurnal systems during the active phase. The convection generally begins around midnight with decay around noon further south (Zuidema 2003). According to Webster et al. (2002) these southward propagating convective bands significantly perturb the surface fluxes and occasionally propagate into the Southern Hemisphere redeveloping on the second night. The

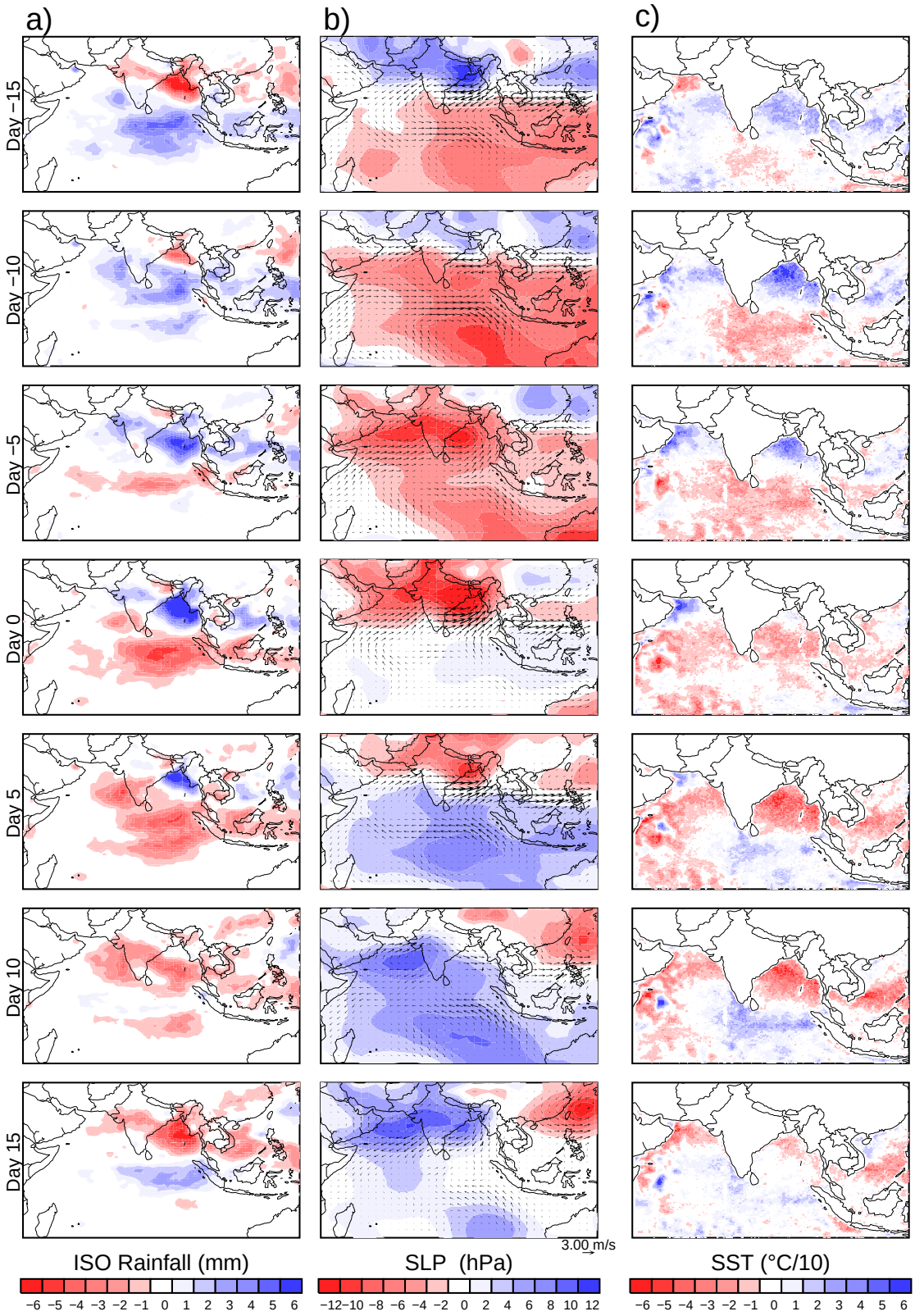

Figure 32: Composites of 25-80 day band-passed a) GPCP daily rainfall b) 925 hPa winds and sea level pressure (SLP) from the NCEP/NCAR reanalysis, and c) TMI SST for 16 canonical MISO events over BoB. Day 0 corresponds to the maximum MISO rainfall over the BoB.

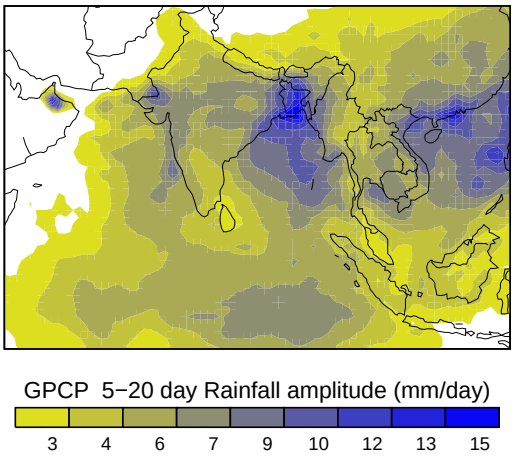

Figure 33: Mean amplitude of the summer (JJAS) 4-20 day spectral band GPCP daily rainfall.

longer period of data considered in this work allow us to conclude that such southward propagating storms are a robust features of the active phases of the MISO over the BoB.

3.1.4.3 In-situ and orographically driven convection over the BoB

In addition to the northward propagating MISO, there is a class of disturbances that forms in situ in the BoB. These are very similar to the canonical type of intraseasonal variability but without the observed propagation either along the equator or poleward from the equator to the northern BoB in contrast to the canonical form (Figs. 36-38). Rather, a dipole-like system is observed with positive anomalies of rainfall over the EIO and suppressed conditions over the BoB around Day -20, and the reversed conditions at Day 0 (Figure not shown). In this case, warm surface waters in the BoB induce convection, eroding the high sea level pressure established during the suppressed phase allowing the formation of the low-pressure system.

In the intraseasonal band, there is a sequence of low and high-pressure systems associated with active and break phases, respectively. Under special conditions of stability and atmospheric moisture over the BoB, and the correct location of the

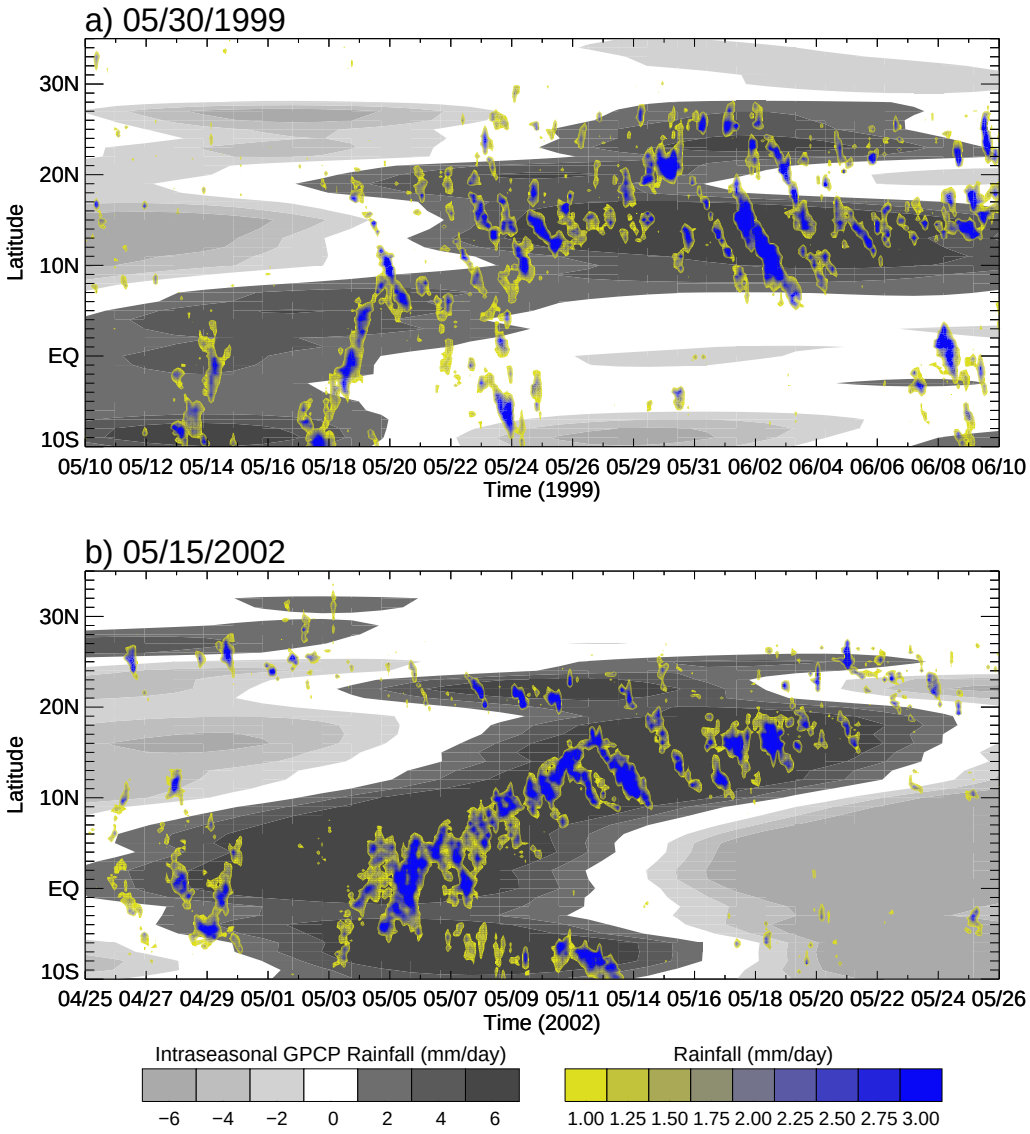

Figure 34: Time-Latitude diagram of intraseasonal (25-80 day) GPCP rainfall shown in grey scale and 3-hourly TRMM rainfall in yellow/blue color for two maximum events over the BoB.

high-pressure system, orographically uplift producing rainfall is possible. A high pressure system situated to the south of the BoB, generates anticyclonic circulation that drives the air towards the Burma mountain range, where the air is mechanically lifted setting up the conditions for rainfall over the Bay. Figure 35 shows the evolution of the 25-80 day band-passed rainfall, SLP and 925 hPa winds for a case where rainfall was orographically induced. Day 0 corresponds to June 17 2003. Given the fact that only four of these cases were identified in the period 1997-2004, it is better to show a particular case than the composite structure based on a few cases. Figure 35 shows clearly break conditions over the BoB around day -20, with negative anomalies of rainfall and positive anomalies of SLP. At Day -15, the high pressure center is located in the southern part of the BoB around 8-10 N, establishing an anticyclonic circulation produces flow towards the mountains near the border of Burma and Bangladesh forcing ascent resulting in rainfall. After Day 0 (not shown in the figure), the rainfall system propagate northwestward generating positive rainfall anomalies over the GP. Figure 35c shows the horizontal cross-section of raw near surface rainfall rate (TRMM 2A25-V6 product) and QuickSCAT winds over the BoB during Day -7 (June 10 2003), as well as the vertical distribution of rainfall along the central line of the retrieval, illustrating the direct influence of the topography in the generation of rainfall over the eastern margin of the BoB during large-scale suppressed conditions. While this type of rainfall over the BoB in the intraseasonal band is not as common as the canonical type, it still contributes to the seasonal maximum over the Bay.

3.1.4.4 Regional Impacts of the Canonical MISO

The canonical monsoon intraseasonal oscillation not only affects the rainfall over the BoB, but also over CI, GP, WG, and even CMD. Figure 36 shows composite time-latitude diagrams of 25-80 day band-passed rainfall, SLP and zonal winds, and SST from day -25 to day 15 for the selected active MISO events over BoB (16 events), CI

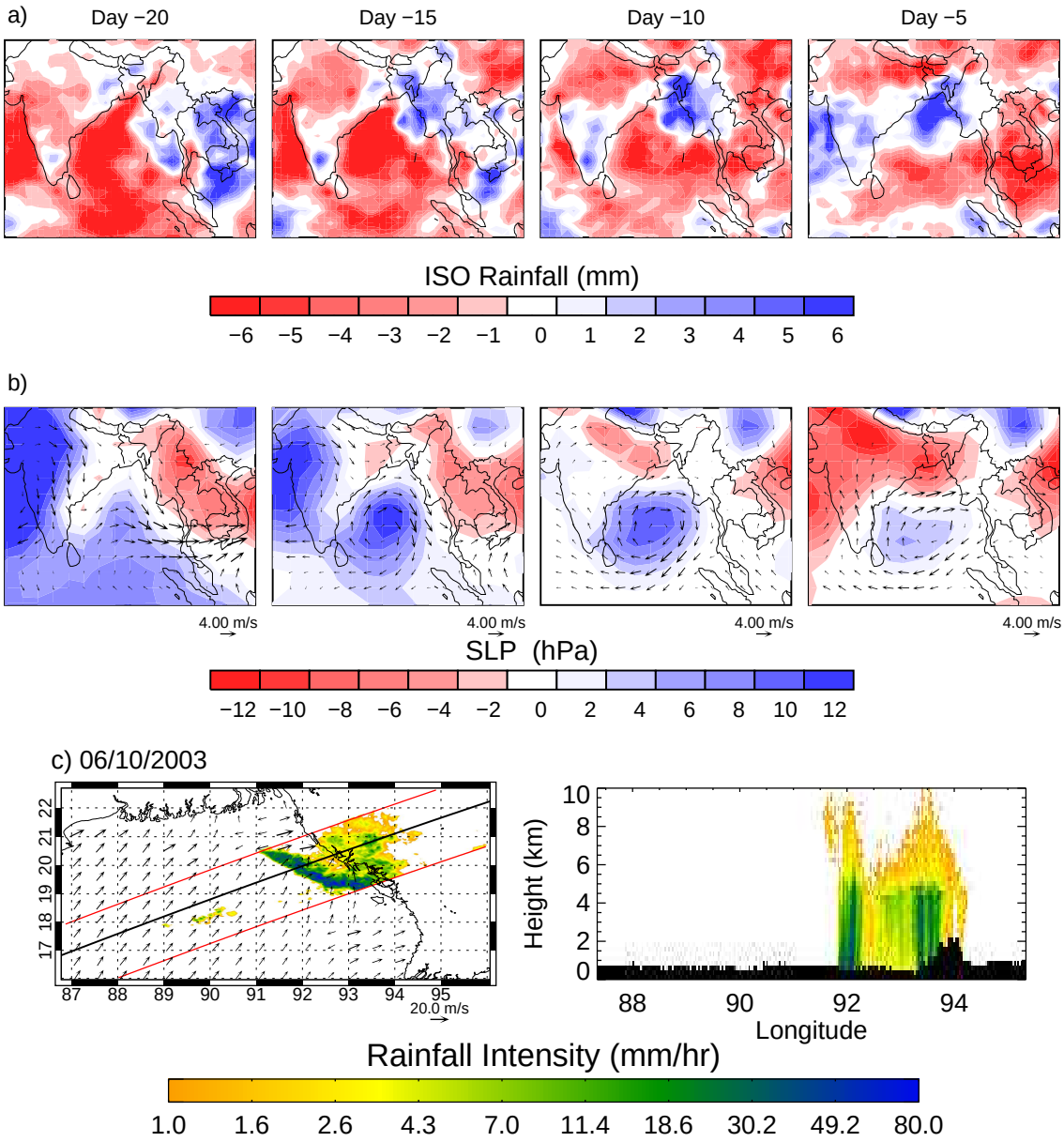

Figure 35: Evolution 25-80 day band-passed a) GPCP rainfall, and b) NCEP/NCAR SLP and 925 hPa winds showing orographically driven precipitation. Day 0 corresponds to 6/17/2003. c) Horizontal cross-section of near surface rainfall rate (TRMM 2A25-V6 product) over the BoB on 6/10/2003 and vertical distribution of rainfall along the black line. Measurements are only available inside the red lines. Black indicates no retrieval. QuikSCAT winds are superimposed in the left panel.

(15), GP (10), WG (18), and CMD (12). In order to study the main differences in the intraseasonal oscillation propagation that affect different regions, the time-latitude diagrams are constructed for different longitude spans, 65°-75°E, 75°-85°E, and 85°-95°E. While the canonical monsoon intraseasonal oscillation is a relatively repeatable large-scale phenomenon, the MISO evolution occurs in such way that in some cases the maximum convective activity is located over the BoB while in other cases over CI or other regions. Possibly, small differences in the background state are responsible for the differences in the MISO propagation. The general feature observed in the figures is the northward propagation of the convective envelope, including signals in the precipitation, sea level pressure, zonal winds and SST fields.

The composite structure based on the activity over the BoB, shows positive intraseasonal variability anomalies of SST leading the equatorial development and northward propagation of the enhanced convection. The low pressure anomaly propagates at the same time and at approximately the same speed as the rainfall anomalies, while the lower tropospheric zonal wind anomalies appear to propagate at a slower pace. This is an important observation for the potential prediction of active and break phases of the Southeast Asian Monsoon since slower propagation directly implies more memory in the dynamical system and hence higher predictability. For the BoB composites, the propagation of sea level pressure and wind anomalies are strong in all longitude bands in the Indian Ocean (65°-75°E, 75°-85°E, and 85°-95°E) and are representative of the large-scale dynamical features of the MISO. However, these anomalies are weak over Sumatra (95°-105°E, not shown), where the convective signal fades. On the other hand, the strongest convective signal is largely confined to the 85°-95°E. Northward propagation of convection is also observed in the other longitudinal bands but with much weaker amplitude. A similar structure is observed in the SST fields, where the signal over 85°-95°E is much stronger than over 65°-75°E. The composites for CI show a very similar structure of SLP and lower troposphere

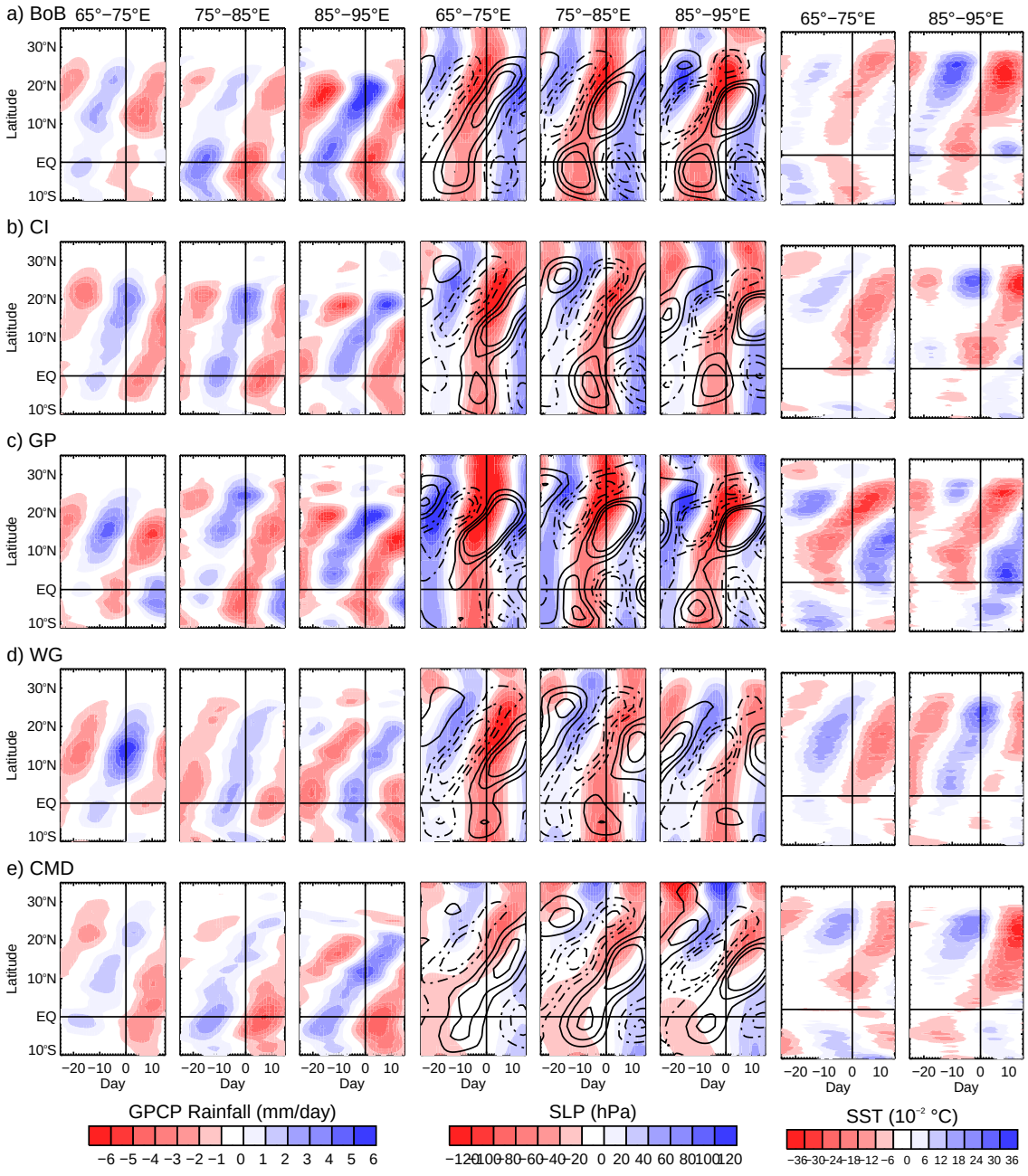

Figure 36: Composite Time-Latitude diagrams of 25-80 day band-passed GPCP rainfall, SLP and zonal winds, and SST from day -25 to day 15 for a) BoB (16 events), b) CI (15), c) GP (10), d) WG (18), and e) CMD (12), over 65°-75°E, 75°-85°E, and 85°-95°E. Solid contours represent westerly winds, dashed contours easterly winds and the magnitudes are 0.5, 1.0 and 1.5 ms^{-1}.

zonal winds to the BoB, and a more homogeneous convective activity and SST signals over the Indian Ocean. For the GP, the 75°-85°E time-latitude diagram shows that the convective anomaly penetrates further north than the average canonical MISO events. In this case, the SST diagrams show a much slower propagation of the MISO related anomalies.

For the WG composites, the sea level pressure, zonal wind, and precipitation anomalies are stronger on the west side of the Indian Ocean, suggesting an earlier northward propagation and precipitation compared to the canonical MISO over the BoB. The SST diagrams in this case show similar features in the west and east sides of the Indian Ocean. The composites for Cambodia show, in general, a much weaker propagating signal in all variables, in part because the convective signal tends to bifurcate before reaching Sumatra, and to weakening further east.

3.1.4.5 Stratiform versus Convective Rainfall

In general, precipitation has two main classifications: convective and stratiform (Houze 1993). Convective precipitation regions are generally identified with intermittently strong vertical velocities, high rain rates, small horizontal dimension, and intense and horizontally inhomogeneous radar echo. Stratiform precipitation areas are characterized by statistically small vertical velocities, low rain rates, widespread horizontal dimension, and horizontally homogeneous radar echo. The microphysical processes dominating the growth of particles to precipitation size in convective regions is collection, while the dominant precipitation growth mechanism in stratiform regions is vapor diffusion.

Knowing the convective-stratiform partitioning in the tropics is very important for a number of reasons. Perhaps the most important one, and linked to the present study, has to do with the accurate determination of the heating profile. As mention before, the spatial and vertical structure of the atmospheric response (Kelvin-Rossby

packet) strongly depends on the vertical structure of the heating profile. Convective and stratiform regions have fundamentally different latent heating profiles, with deep convective regions having heating throughout the vertical with maximum in the mid-troposphere, and stratiform regions with cooling in the lower troposphere and warming in the top of the troposphere. Schumacher and Houze (2003) develop a convective-stratiform separation algorithm using TRMM PR data in order to partition the tropical rainfall and acquire a better understanding about the heating profiles. The algorithm determines whether the radar echo is convective or stratiform based on the vertical profile of reflectivity and the horizontal variability of the echo. Since they originally grouped the data into monthly precipitation, the convective-stratiform partitioning associated with ISO is not captured in their analysis and has not been analyzed previously. This separation, however, is necessary in order to be able to force models with the correct heating anomalies associated with the ISO.

Recently, C. Schumacher (personal communication) has reprocessed the data for the period 1998-2003 in order to obtain pentad (5-day average) rainfall in the tropics. This temporal resolution is appropriate to study intraseasonal variability. The structure of the mean rainfall during summer (JJAS) from Schumacher's products is very similar to that in Figure 25 using the GPCP data set. Mean convective and stratiform rainfall show the BoB maximum parallel to Burma's mountain range. Table 2 shows the average summer total (cumulative+stratiform), convective and stratiform rainfall over the regions shown in Figure 24. Stratiform rainfall is about 30% of the total precipitation in all regions.

Figure 37 shows the average wavelet spectra of convective and stratiform rainfall for the regions in Figure 24. As shown before, the most important spectral band corresponds to the intraseasonal variability. A salient feature is that the spectral characteristics of convective and stratiform rainfall are remarkably similar in most regions, and principally for those over ocean. Not only the spectral features are

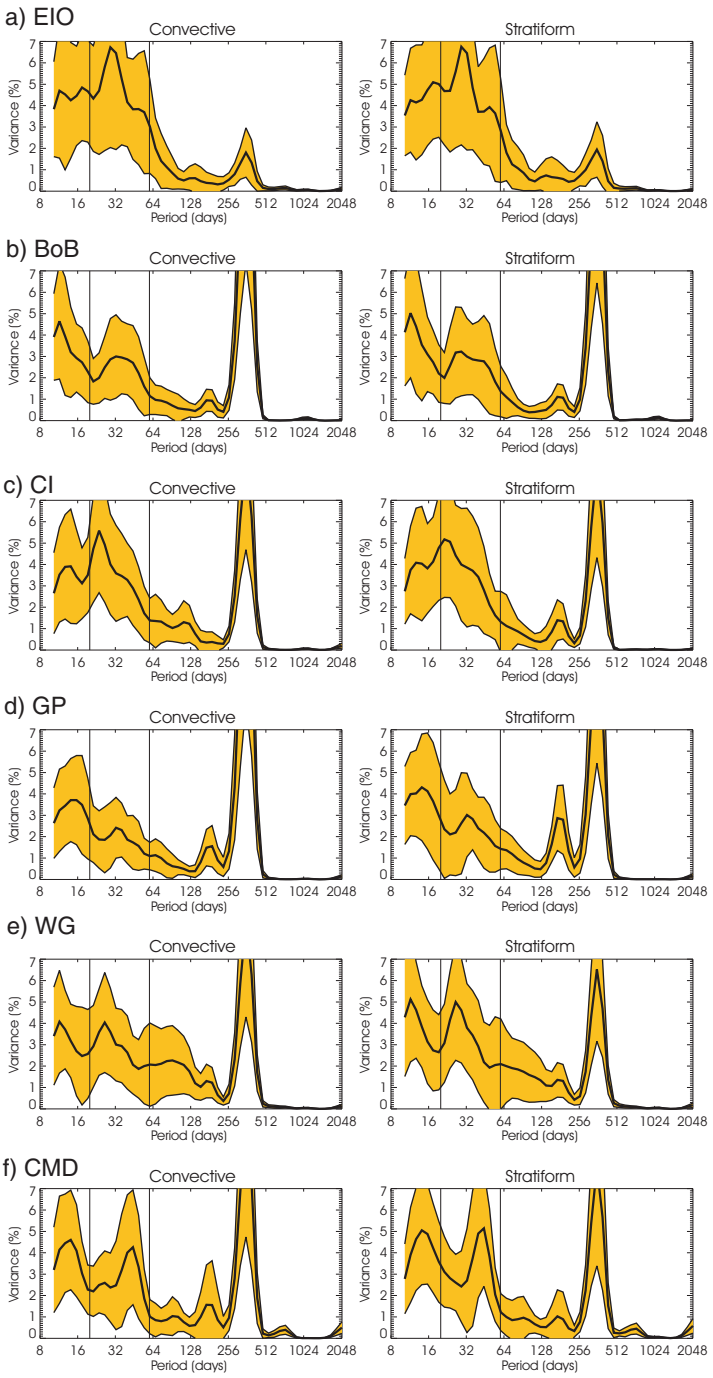

Figure 37: Summer average wavelet spectra for 1998-2003 pentad convective and stratiform rainfall for regions in Figure 24. The black line represents the average spectrum and the shaded area represents plus and minus one standard deviation of the summer spectra.

Table 2: Cumulative Rainfall (mm) during JJAS for the regions in Figure 24.

Region	Total	Convective	Stratiform
EIO	546.5	376.0	170.5
BoB	1196.3	852.5	343.8
CI	528.9	365.2	163.7
GP	551.5	410.5	141.0
WG	786.4	552.4	234.0
CMD	659.3	484.5	174.8

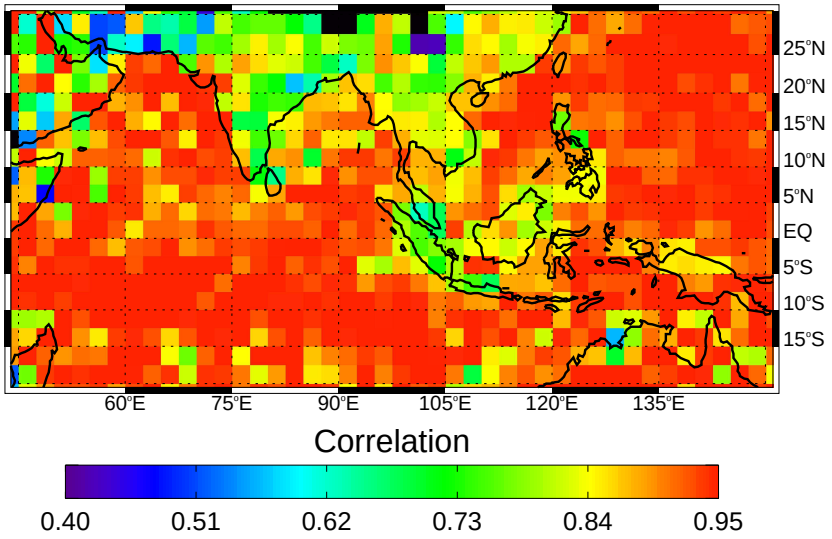

Figure 38: Correlation map between convective and stratiform rainfall. The correlation between both components is computed for periods during summers of 1998-2003 where convective rainfall rate is greater 5 mm/hr.

similar, but also the correlation between both convective and stratiform is very high. Figure 38 shows the correlation map between convective and stratiform rainfall for the summers of 1998-2003 (JJAS) where convective rate is over 5 mm/hr. While the correlation is in general high, it appears even higher over the ocean regions than over land regions.

The evolution of intraseasonal convective and stratiform rainfall relative to active events (17) over the BoB also shows similarity. Figure 39 shows a composite time-latitude diagram of intraseasonal total, convective and stratiform rainfall. Day 0 corresponds to active events over the BoB. The northward propagation from the

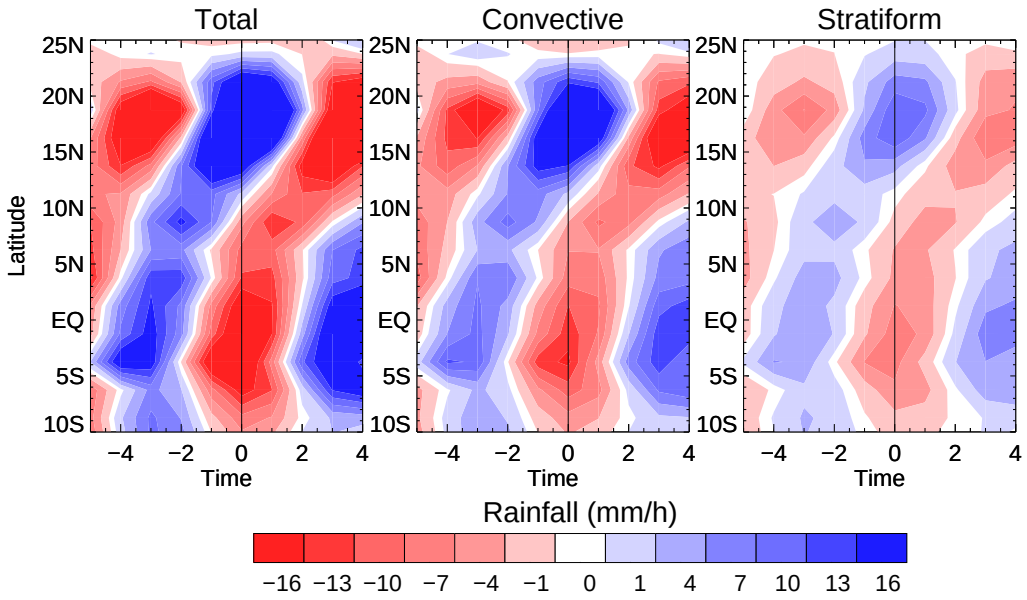

Figure 39: Composite time-latitude diagrams averaged between 75°-85°E of 25-80 day band-passed a) total, b) convective and c) stratiform rainfall. Data provided by C. Schumacher was used in this diagram.

equator to the BoB, of both active and suppressed conditions, is observed in the convective and stratiform rainfall. The only discernible difference is the magnitude of the intraseasonal anomalies.

All similarities observed between convective and stratiform rainfall support the findings of different field experiments showing that almost all convection occurs in association with stratiform rain (Houze 1997). Houze (1997) showed that the younger parts of the cumulonimbus clouds are 100% convective. Later, when convection decays, clouds become stratiform and co-exist with the embedded convective columns of rapid updraft. Stratiform rainfall generally occurs more frequently in the tropics, yet convective rainfall accounts for most (70%) of the cumulative rainfall, because its intensity is so much higher.

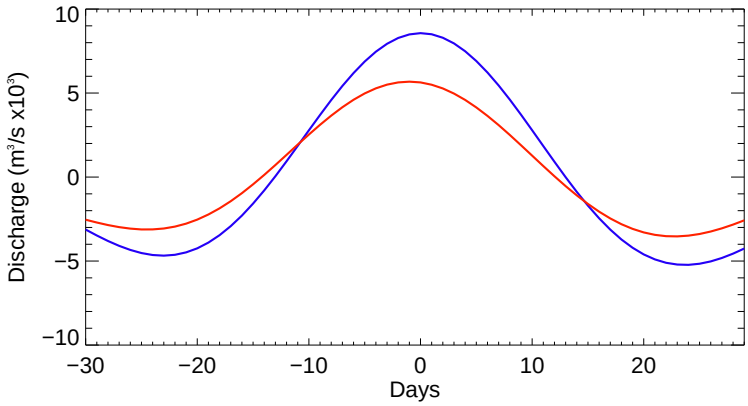

Figure 40: Ganges and Brahmaputra intraseasonal (30-100 day band) variability composite based on 27 Ganges active events (maximum discharge).

3.1.4.6 ISO related impacts on Ganges and Brahmaputra Discharge

Discharge of rivers Ganges and Brahmaputra, very important for both India and Bangladesh for agricultural, energetic and natural disasters related decisions, also shows variability in the intraseasonal band. In this case, the spectral peak is slightly shifted to lower frequencies compared to the rainfall spectrum, most likely do to the low-pass filter effect introduced by the basin. Composite analysis of daily intraseasonal discharge variability reveals an in-phase relationship between both Ganges and Brahmaputra (Figure 40). The composites were constructed based on 27 active events of Ganges discharge from 1996 to 2004 obtained from filtered daily time series in the 40-100 day spectral band. Ganges and Brahmaputra daily discharge record was kindly provided by the Bangladesh government.

In order to establish the link between Ganges and Bramaputra discharge and ISO related rainfall and knowing that both rivers covariate in phase in the intraseasonal band, composites of daily GPCP rainfall were constructed based on the same 27 Ganges active events. Figure 41 shows the evolution of the composites from Day -20 to Day 5. The diagrams show maximum rainfall anomalies over the basins about 15 to 20 prior the maximum discharge in both basins and also an interesting progression

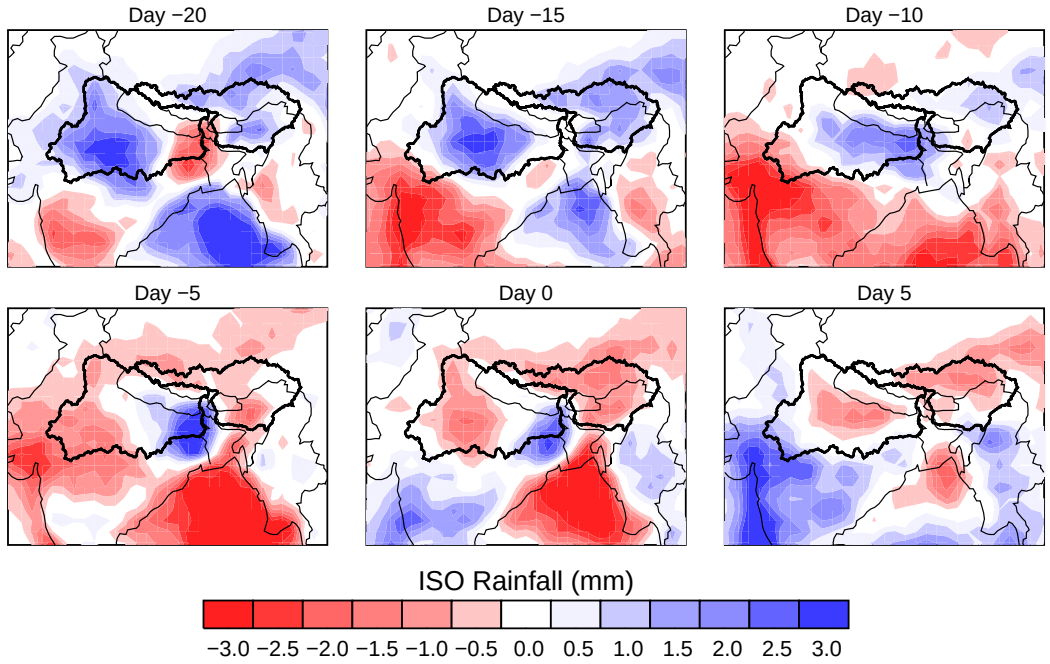

Figure 41: Composite evolution of GPCP rainfall relative to active events of Ganges discharge. The contour of both basins is shown to facilitate the analysis.

over the Ganges basin. The positive rainfall anomalies observed over the basin before the maximum discharge start in the farthest areas from the basin outlet around Day -20, and move closer to it as time progresses. A similar effect is observed for the Brahmaputra when the composites are constructed using active events based on its discharge (figure not shown). This progression provides the explanation for the low-pass filter introduced by the basin, which acts not only as an integrator but also as a moving average operator of the rainfall time series. The river discharge in both basins lags about 20 days the peak ISO rainfall over the BoB. This lag is advantageous for prediction and the memory introduced by the basin relative to the arrival of the large-scale ISO active event should be taking into account, when designing empirical forecasting scheme of Ganges and Brahmaputra discharge.

In order to verify the nature of the composites from the hydrological point of view, isochrone maps where estimated in a simplified manner for both Ganges and

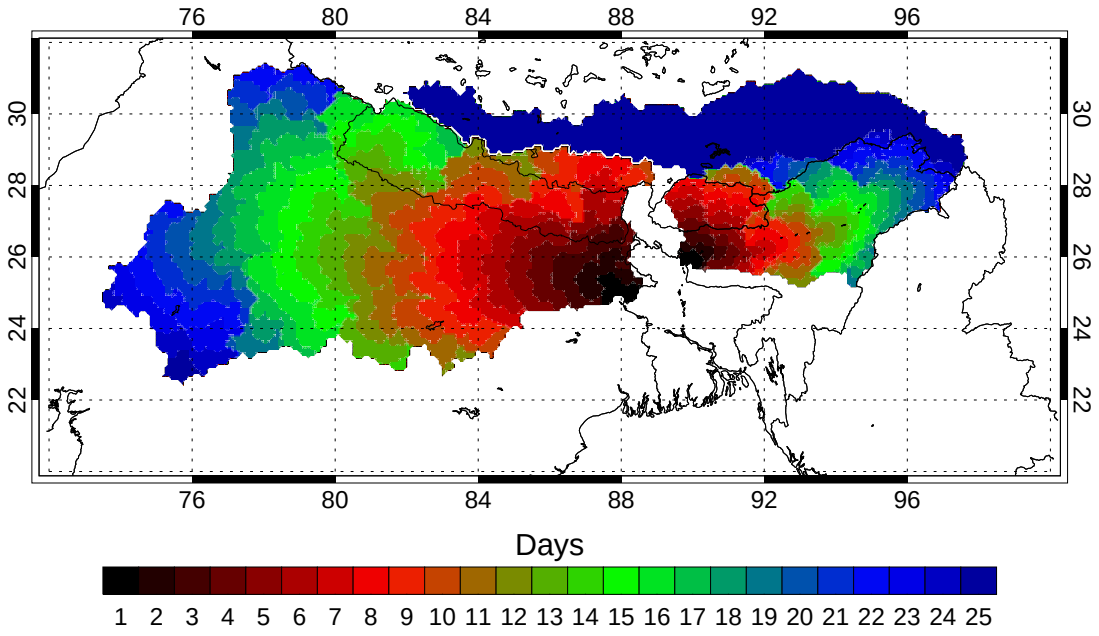

Figure 42: Isochrones map for rivers Ganges and Brahmaputra. For Brahmaputra, water falling over the farthest area (northwest) takes more than 25 days to reach the basin outlet.

Brahmaputra. Isochrones were estimated by first using a flow routing algorithm (Ramirez and Velez 2002) and a digital elevation model (DEM) of the region to find the path and the distance of every grid cell to the outflow of the basin. The regional DEM was extracted from a global DEM (GTOPO30) with horizontal resolution of 30 arc-seconds (approximately 1 km). It was assumed that the average velocity within the entire basin network, including hillslopes and channels, is 1 m/s. For detailed applications, hydraulic and terrain considerations are necessary to estimate the network velocity, probably different at every grid cell. However, for the goal of this study, and given the resolution of the rainfall (1 degree 120 km), 1 m/s is a reasonable assumption. Figure 42 shows the estimated isochrones map, in days, for Ganges and Brahmaputra basins. In this context, the isochrones map should be interpreted as an approximation of the average time that takes a parcel of liquid water located in some location within the basin to reach the outlet of the basin.

The estimated isochrones map provides hydrologic support to the features observed in the composites. There is a very high degree of spatial coherency of the distribution of positive rainfall anomalies and their temporal occurrence (composite day) with the isochrones map. For example, for the Ganges basin, the geographic location of the rainfall anomalies at Day -20 correspond almost one-to-one with isochrones of 17 to 23 days. This level of spatial coherency is observed for Days -15 to 0, supporting as well the hypothesis of the basin acting as a low-pass filter.

3.1.4.7 Other non-canonical MISOs

In addition to the positive anomalies of rainfall introduced by the canonical MISO, localized anomalies also need to be considered in the GP, CI and over the BoB. In general, when positive rainfall anomalies grow over these regions, suppressed conditions are established over the equatorial Indian Ocean in a dipole-like structure.

Over CMD, besides the canonical MISO, 25-80 day activity also grows to the north of east Indonesia and propagates westward modulating rainfall over CMD and surrounding countries. The westward propagation is shown in Figure 43 in longitude-time composites (7°-15°N) of 25-80 day band-passed rainfall, SLP, zonal winds, and SST. The westward propagating high-pressure system generates an anticyclonic circulation to the east of Vietnam. In the longitude-time diagrams this appears as an easterly anomaly since the zonal winds are averaged over the southern half of the high. The inverse situation is observed with the propagation of the surface low. In this case, positive, non-propagating anomalies of SST lead the development of the instability and the subsequent propagation.

3.1.4.8 4-20 day Variability

On the 4-20 day time scale, the variability over the northeast BoB and WG develops predominantly in an in situ fashion. Figure 44 shows composite structure from 51

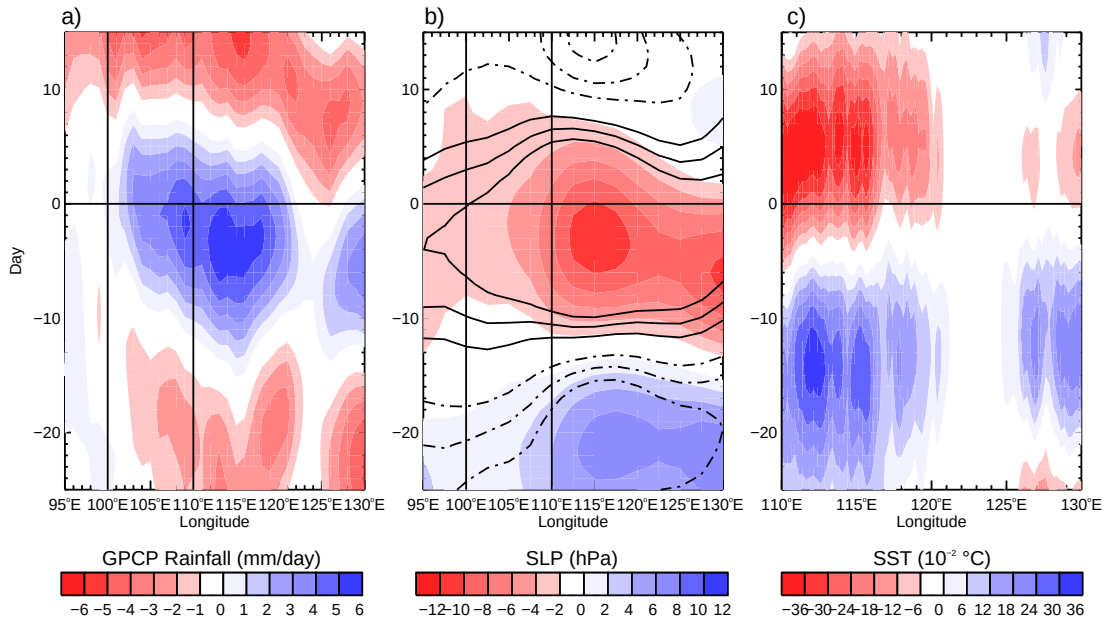

Figure 43: Composite longitude-time diagrams of 25-80 day band-passed a) rainfall, b) SLP and zonal winds, and c) SST over 7°-15°N, based on 7 CMD westward propagating events.

events over CI. The figure displays a coherent westward propagation of positive convective anomalies and corresponding low-pressure systems towards CI from the Gulf of Thailand and the South China Sea, affecting rainfall in the south and central BoB. In some of the strongest cases in the composite set, the anomalies reach the Arabian Sea. The SST composite evolution suggests relatively small positive SST anomalies over the BoB leading the propagation of the convective system. The magnitude of the SST variability in this band is smaller than the amplitude in the 25-80 day band, suggesting a weaker ocean-atmosphere coupling/interaction in the 4-20 day band. The SST is most probably being forced by changes in solar radiation reaching the surface. The 51 CI events were reclassified as occurring during active or break MISO periods to evaluate possible differences. In total, 31 events coincide with an active phase and 19 with a suppressed phase, confirming the fact that higher frequency variability occurs within the MISO envelope. The reclassified composite structure does not show any significant differences in the eastward propagation.

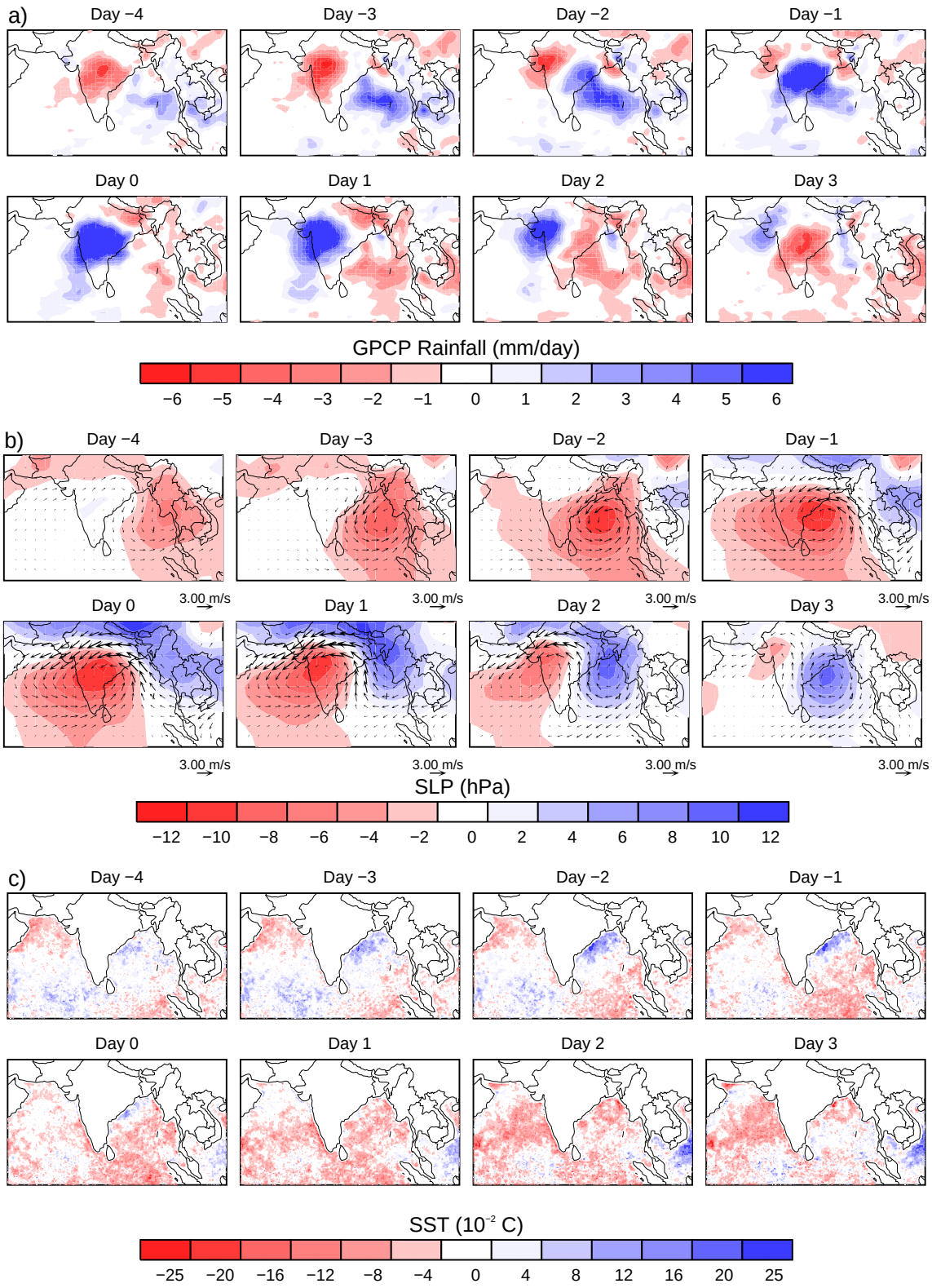

Figure 44: Composites of the 5-25 day band-passed GPCP daily rainfall, SLP and zonal winds, and SST for 51 westward propagating events over CI. Day 0 corresponds to the maximum rainfall in the band.

Figure 45 shows the composites structure for the 55 CMD cases, with a developing instability to the east of Philippines which subsequently propagates to the west generating copious rainfall over CMD and surrounding countries. These events also tend to reach the south of the BoB and, in some cases, the Indian subcontinent. When the instability is in its initial stages, the South China Sea possesses positive anomalies of SST which lead the westward propagation. In a similar manner to the CI case, the magnitude of the anomalies is relatively small. Overall, variability in the 4-20 day band over CMD shows a similar structure than previously explained for the 25-80 time scale.

3.2 West African - South Asian Monsoon Connections

Most of the rainfall over West African occurs during summer in association with the monsoonal circulation as shown in Figure 46. The summer rainfall band is relatively narrow, even over the continent, with maxima over Guinea and Nigeria (Figure 46a). The rainfall presents a marked annual cycle, although flatter/wider than for the South Asian counterpart. Spectral analysis shows that in addition to the annual cycle, there is a very important broad peak (about 35% of the variance) around 4 days and a secondary peak (about 10% of the variance) around 25 days (Figure 47). The 4-day peak corresponds to synoptic-scale easterly perturbations known as African Easterly Waves (AEWs). These waves are prominent during the months of June to early October, with approximately 60 events in any given year, and ranging from 2000km (Carlson, 1969) to 4000km (Burpee, 1972) with a period of 3-5 days. In addition to the 4-day variability, the smaller, but physically significant peak corresponds to intraseasonal activity. To the date, very few studies have investigated the West African monsoon intraseasonal variability. Recent studies by Sultan et al. (2003), Matthews (2004), and Collins et al. (2006) examine some of the basic features of this variability. Collins et al. (2006) pointed out a potential association of the West

African and the Indian Monsoon ISO. Here, further evidence of this connection is presented.

In a similar manner as described above, composite analysis of rainfall, SLP and 925mb winds was performed based on 21 active events of rainfall over West Africa. Results are very similar using both regions outlined in Figure 46. Figure 48 presents the composite evolution for the region western-most region (0-15N, 25W-10W). There are two main features in the diagram. One refers to the nature of the oscillation over Africa and the other to the connection to the Indian Ocean MISO. Over Africa, the anomalies associated to the oscillation appear over a narrow band along the Gulf of Guinea coast, similar to that of the summer mean rainfall (Figure 46), also extending into the ocean. This oscillation, that modulates the magnitude of the rainfall associated to the AEWs, appears to grow and vanish over the same location, with no apparent propagation. It is also important to note that there is no a strong local signal of SLP and 925mb winds over West Africa associated to the ISO.

Perhaps the most intriguing aspect of the oscillation is its high degree of coherency with the MISO. The composite structure shows an in-phase relationship between active phases over West Africa and Central Indian Ocean, and the corresponding out-of-phase association between West Africa and Bay of Bengal and India. In other words, the full structure of the MISO, including rainfall, SLP, and near surface wind patterns, is recovered when compositing based on West African dates. This is an important finding since the MISO has been traditionally analyzed within the Indian Ocean without considering any links outside the basin different to the West Pacific warm pool. The mechanisms of this connection need to be further investigated.

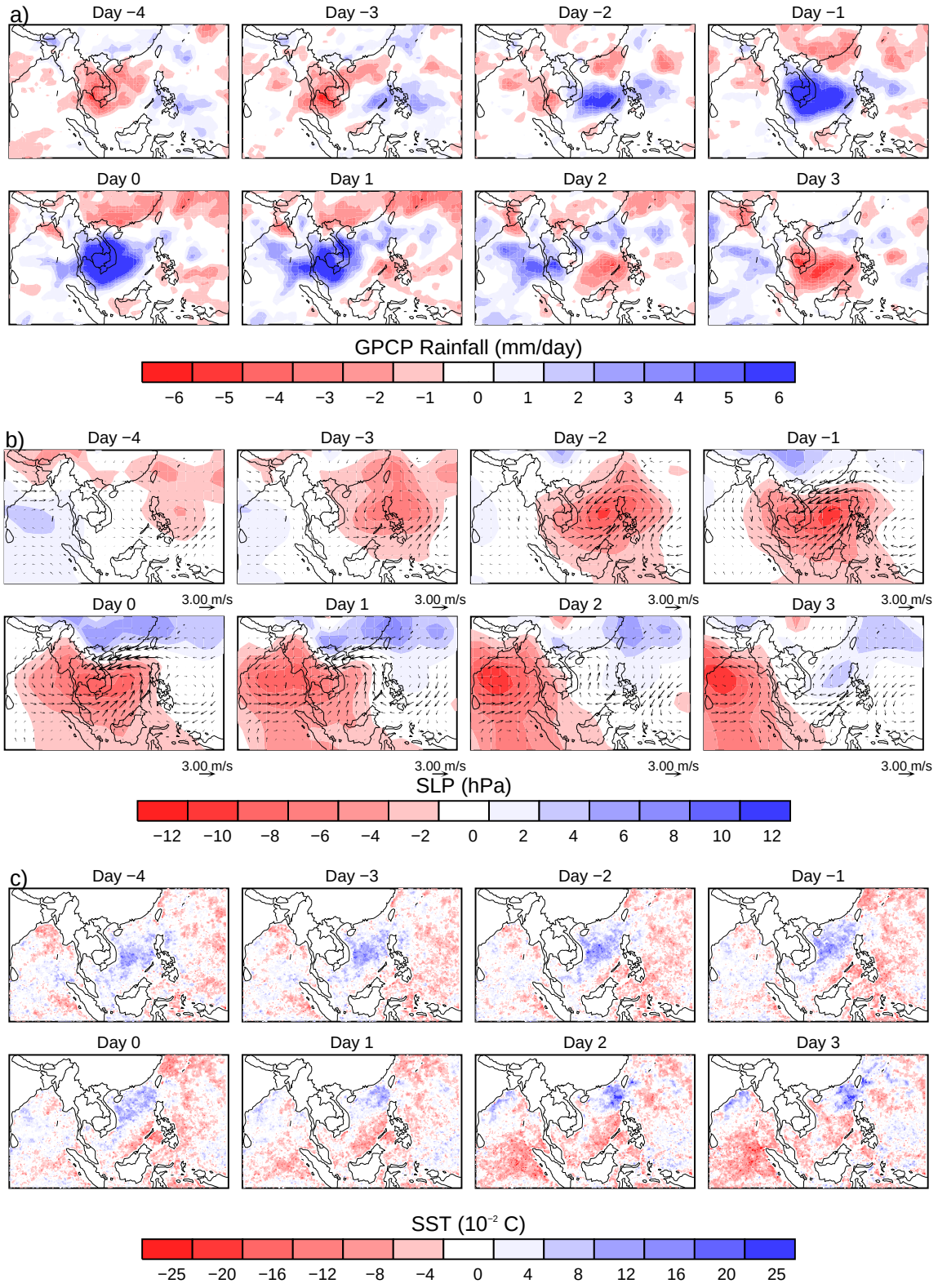

Figure 45: Same as Figure 44 for 55 events for CMD.

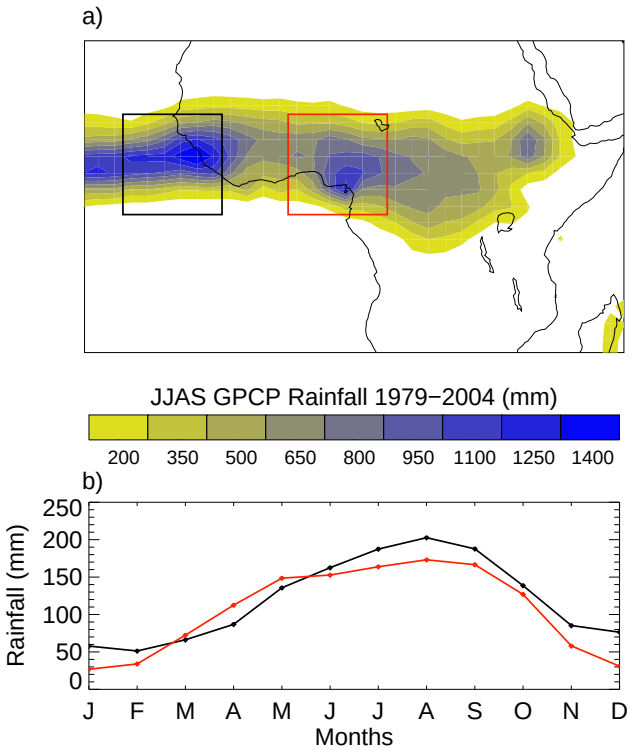

Figure 46: Mean West Africa summer rainfall (June to September; JJAS) averaged from 1979 to 2004 using the monthly GPCP data, b) mean annual cycle of rainfall over the two regions outlined in a).

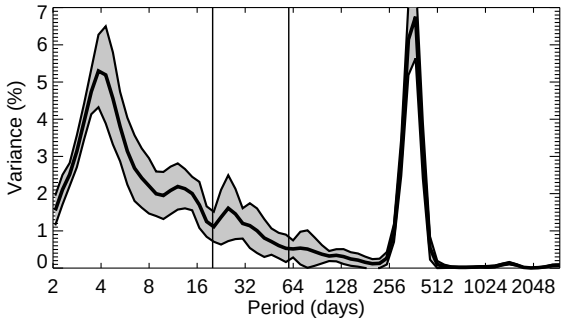

Figure 47: Summer average wavelet spectra for 1997-2004 daily GPCP rainfall for the western region in Figure 51 (0-15°N, 25°W-10°W). The shaded area represents plus and minus one standard deviation of the summer spectra.

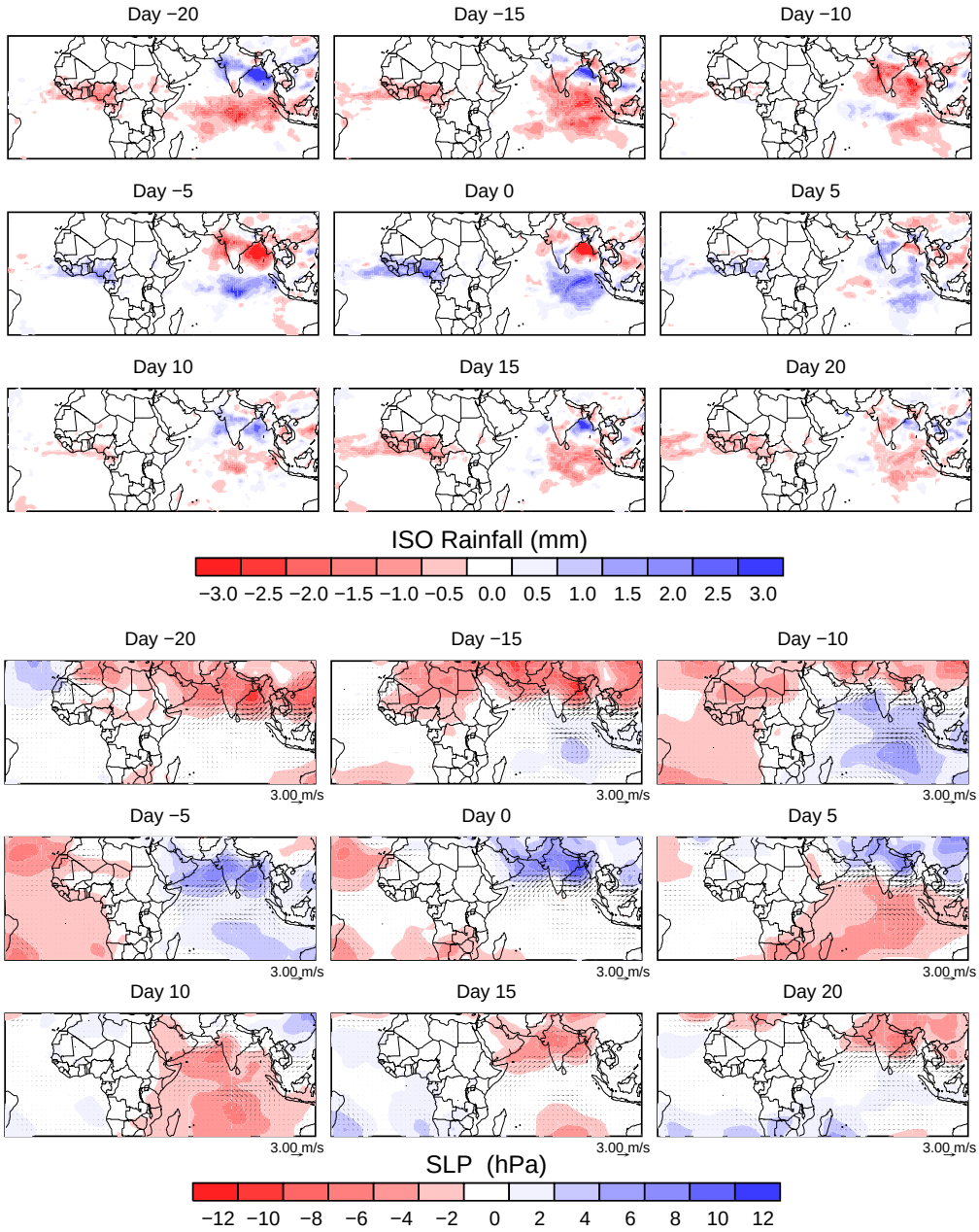

Figure 48: Composites of 25-80 day band-passed a) GPCP daily rainfall b) 925 hPa winds and sea level pressure (SLP) from the NCEP/NCAR reanalysis for 21 intraseasonal active events over West Africa (Figure 46).

CHAPTER IV

STATISTICAL FORECASTING OF INTRASEASONAL VARIABILITY: PREDICTION OF MONSOON RAINFALL AND RIVER DISCHARGE ON 15-30 DAY TIME SCALES

The economy of India, a country with a population of over 1 billion people, strongly depends on agriculture which accounts for the 34% of the Net Domestic Product. Rice and wheat are the main crops. Food grain production strongly depends on the amount of rainfall and radiation received during the summer; thus rainfall variations may cause severe droughts and crop loss.

During the summer of 2002, drought conditions persisted over India from mid-June to mid-July following a later than average arrival of seasonal monsoon rain By the end of summer, the average summer Indian rainfall totaled 711 mm or 19% below normal. With the exception of the area near the foothills of the Himalaya in the very north of India, where above average rainfall occurred, most of India was in deficit with the state of Rajasthan 64% below normal. Figure 49 provides a geographical reference for the locations discussed in the text. The summer of 2002 was the sixth driest in 130 years (Table 3).

The failure of the 2002 monsoon rains was not anticipated. The official Indian Meteorological Department seasonal outlook issued in mid-April called for an essentially normal monsoon with seasonal rains about 1% lower than normal. Other forecasts

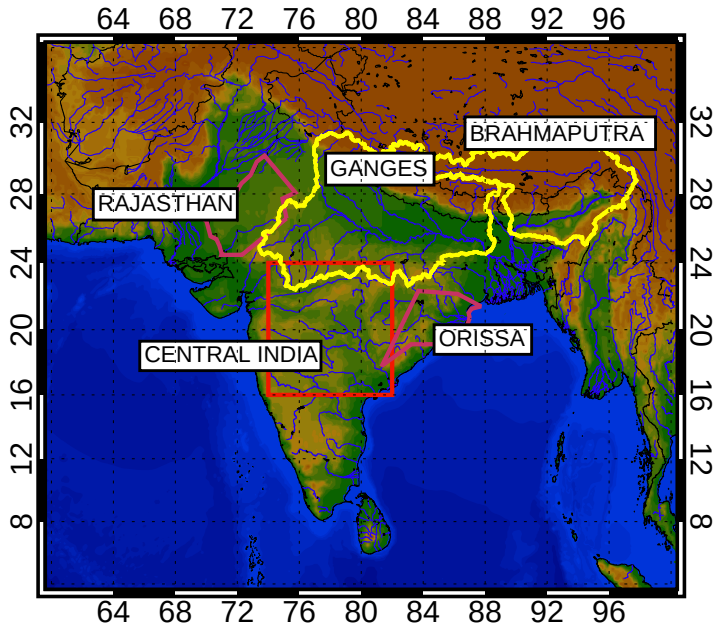

Figure 49: Geography of locations discussed in the text. The catchment areas of the Brahmaputra and Ganges are outlined in yellow, the Indian states of Orissa and Rajasthan and Rajasthan, and the country of Bangladesh are outlined in red.

Table 3: Years of mean seasonal rainfall deficiency >10% below average during the last 130 years. Rainfall is averaged over the entire Indian subcontinent. The summer of 2002 was the fifth lowest on record. Data from Institute of Tropical Meteorology, Pune, India, courtesy of Dr. Rupa Kumar Kolli (Mean summer rainfall: 835 mm. Standard deviation: 85 mm)

YEAR	%	YEAR	%	YEAR	%
1873	-11	1920	-15	1972	-24
1877	-30	1928	-10	1974	-12
1899	-26	1941	-13	1979	-15
1901	-15	1951	-17	1982	-13
1905	-16	1965	-11	1985	-11
1910	-13	1966	-23	1986	-13
1918	-24	1968	-12	1987	-17
				2002	-19

suggested similar outcomes. For example, predictions made by the International Research Institute for Climate (IRI) and European Centre for Medium Range Weather Forecasts (ECMWF) made in the spring for the 2002 June-August period suggested slightly below average precipitation in the south of India but normal elsewhere. The

effects of the mid-season drought were disastrous to India's agrarian economy, especially since the drought occurred early in the monsoon season when agriculture is at a most susceptible stage. The severe reduction in agricultural productivity resulted in hardship and suffering for millions of people and a significant economic loss to the country. Only stores of rice accumulated over a period of years by the Government of India prevented an even greater disaster.

Figure 50a and 50b show precipitation time series averaged over central India for the period 1986 through 2002 and details of the rainfall distribution for the four-year period 1999-2002, respectively. The climatological 103-year average summer rainfall has been superimposed. Estimates of rainfall come from the GOES Precipitation Index (GPI) product (Arkin and Meisner 1987, Joyce and Arkin 1997). Deficits in summer rainfall of similar magnitudes to that of 2002 are relatively rare. A comparison between the long-term mean annual cycle of rainfall and the rainfall in 1999-2002 years (Figure 50b) underlines three important characteristics of the South Asian monsoon. First, the mean seasonal cycle is smooth with rainfall starting sometime in late May, reaching a maximum in July and then slowly decreasing through September. During this period 80% of the India's annual rainfall occurs. Second, the rainfall distribution in any one-year is made up of a series of low frequency sequences of rainy periods ("active" periods) with intervening dry periods (monsoon "breaks") each lasting 10-30 days. The magnitude of the intraseasonal variability is far greater than the magnitude of the interannual variability (e.g., Webster et al. 1998, Waliser et al. 1999). Third, the smoothness of the mean annual cycle of precipitation suggests that there is no preferred time for the large amplitude active and break periods of the monsoon to occur.

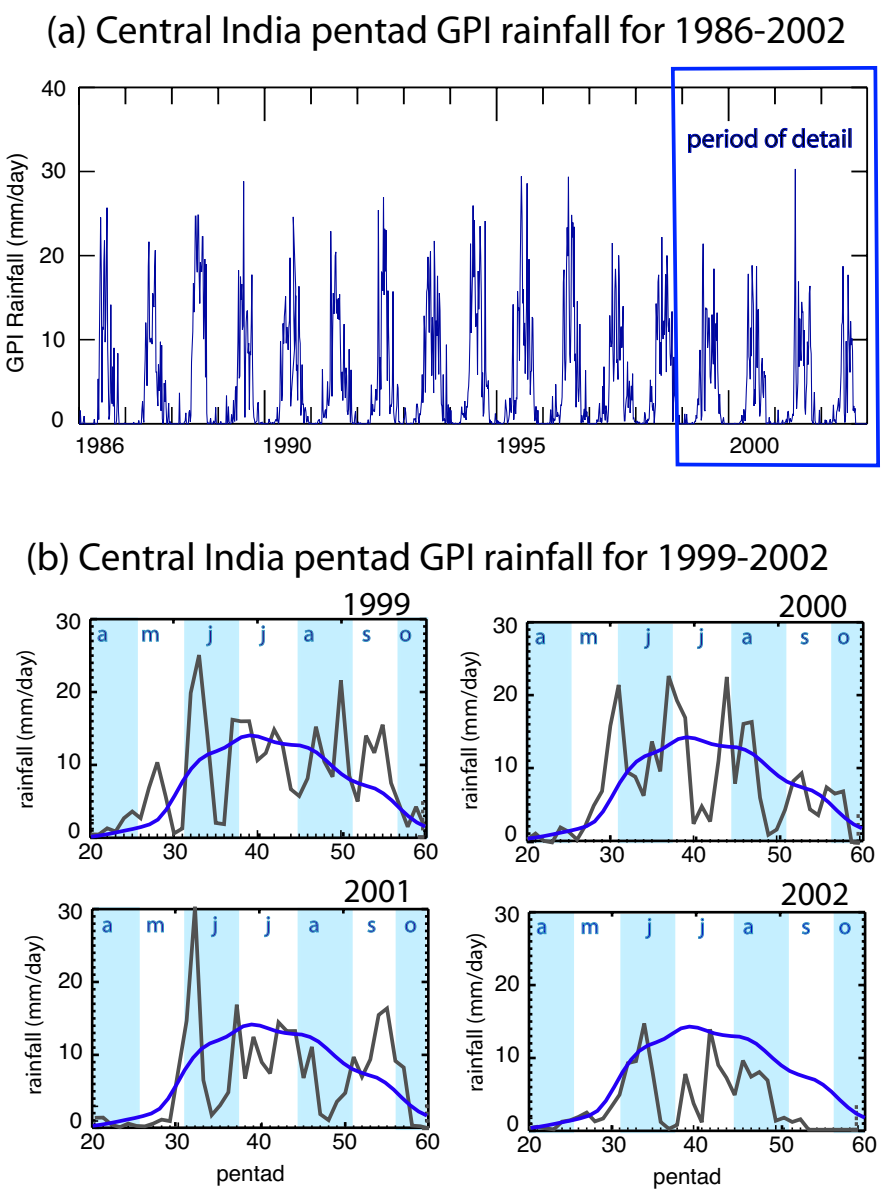

Figure 50: a) Satellite-derived GOES Precipitation Index (GPI) averaged over the Central India region (see Figure 51) for the period 1986-2002. A large annual cycle is modulated by a relatively small interannual variability. Within each summer season there are large variations of rainfall on time scales of 20-40 days. b) Details of precipitation for the period 1999-2002 (box Figure 52a) plotted as average rain rate per pentad. Each year exhibits peaks ("active" monsoon periods) and valleys ("breaks" in the monsoon) of rainfall rate. The smoothness of the long-term averaged annual cycle of precipitation (blue curve) suggests that there is no preferred timing for intraseasonal variability and that it occurs randomly throughout the summer. Light blue and white background bands indicate months ("a" April, "m" May, etc.). Data from Joyce and Arkin (1997).

4.1 Utility of seasonal forecasts of All-India rainfall

Prediction of the mean seasonal Indian monsoon rainfall has a long history. For the most part, prediction has employed empirical methods. The most common predictand has been the El Niño-Southern Oscillation phenomenon (ENSO), winter and springtime snowfall over Eurasia and the sea-surface temperature (SST) variability in the Indian Ocean and the northwest equatorial Pacific Ocean. Overall, about 30% of the variance can be explained by ENSO indices (e.g., Shukla and Paolino 1983, Shukla and Mooley 1987, Shukla 1987) with El Niño normally associated with below average summer Indian precipitation and La Niña with above average summer rains. Early promise of a strong relationship between Eurasian snowfall and Indian summer rainfall (e.g., Hahn and Shukla 1976, Dickson 1984) has waned under more exacting scrutiny (Bamzai and Shukla 1999). Empirical schemes involving other factors such as Indian Ocean SSTs are discussed in Hastenrath (1986, 1987), Harzallah and Sadourny (1997) and Clark et al (2000). The common feature of all of these schemes is that they tend to wax and wane on interdecadal time scales (Torrence and Webster 2000). The reason for the variability of predictability between ENSO and the monsoon is not understood. It may stem from subtle relationships between monsoon strength and Pacific SST, because some physical processes has been ignored which may occasionally interfere with monsoon-ENSO connections, or because of the interference of stochastic events.

Let us assume, for the sake of argument, that forecasts of the seasonally averaged rainfall over India are skillful and that the long-term statistics are robust. How useful would accurate "broad brush" forecasts of the monsoon be to a user community? Figure 51 shows 10-day running means of precipitation in a box in central India (upper left panel) for years with regional annual rainfall between -16 to -19% (upper right panel), between 2% (lower left panel) and between +16% to +19% (lower right panel) using data compiled by Kripalani et al. (1991) which is described in detail

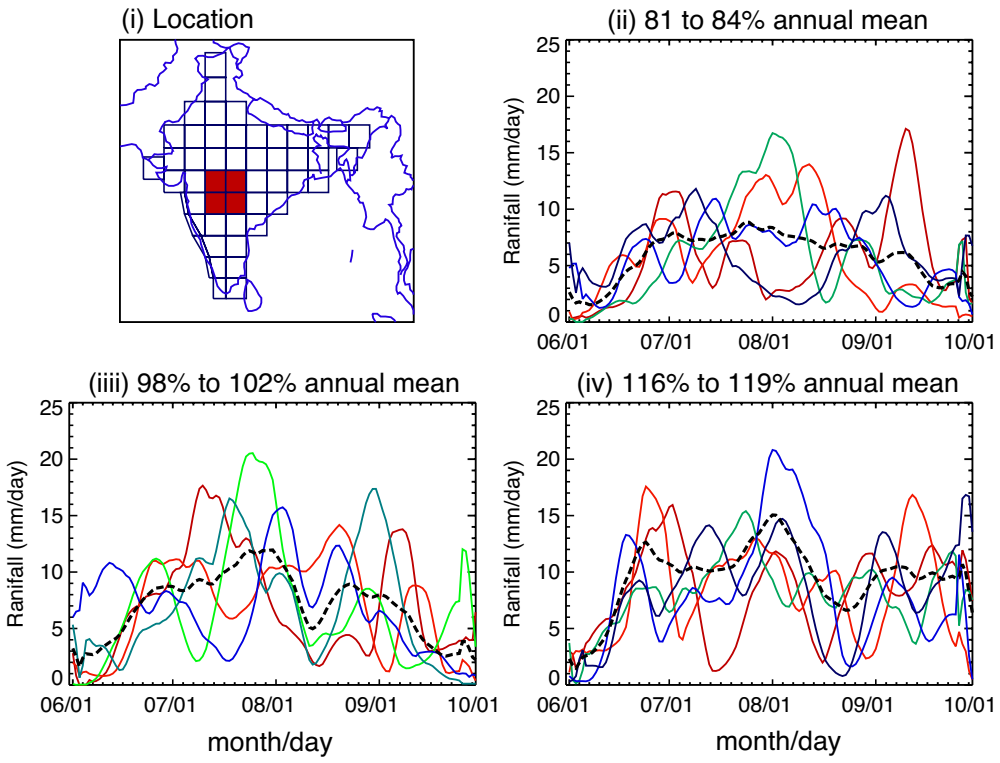

Figure 51: 10-day running means of GPI precipitation rate in central India (panel i) for years which the summer rainfall is between 81% and 84% of the summer mean (years 1905, 1907, 1912, 1925, 1929; panel ii), between 98% and 102% (years 1937, 1957, 1966, 1967, 1976, 1980; panel iii) and between 116% and 119% (1910, 1948, 1953, 1954; panel iv). Heavy dashed curves show the mean seasonal precipitation for each category. Data compiled by Singh et al. (1992) and provided courtesy of Dr. Rupa Kumar Kolli of the Institute of Tropical Meteorology, Pune, India.

by Singh et al. (1992). The dashed line shows the average annual cycle for each category. Irrespective of the abundance of the rainfall in a season, large amplitude active and break periods occur irregularly at different times of the season. Figure 52 shows three sets of seasonally averaged all-India rainfall distributions: wet (seasonal average >110% of average), normal (within 10% of average) and dry years (<90% of average). Whereas there is a tendency for the wet and dry categories to contain more districts that have the same sign as the overall anomaly, there are swaths of districts of opposite signed anomalies across India as well. The two "normal" years (panel ii) are even more variable.

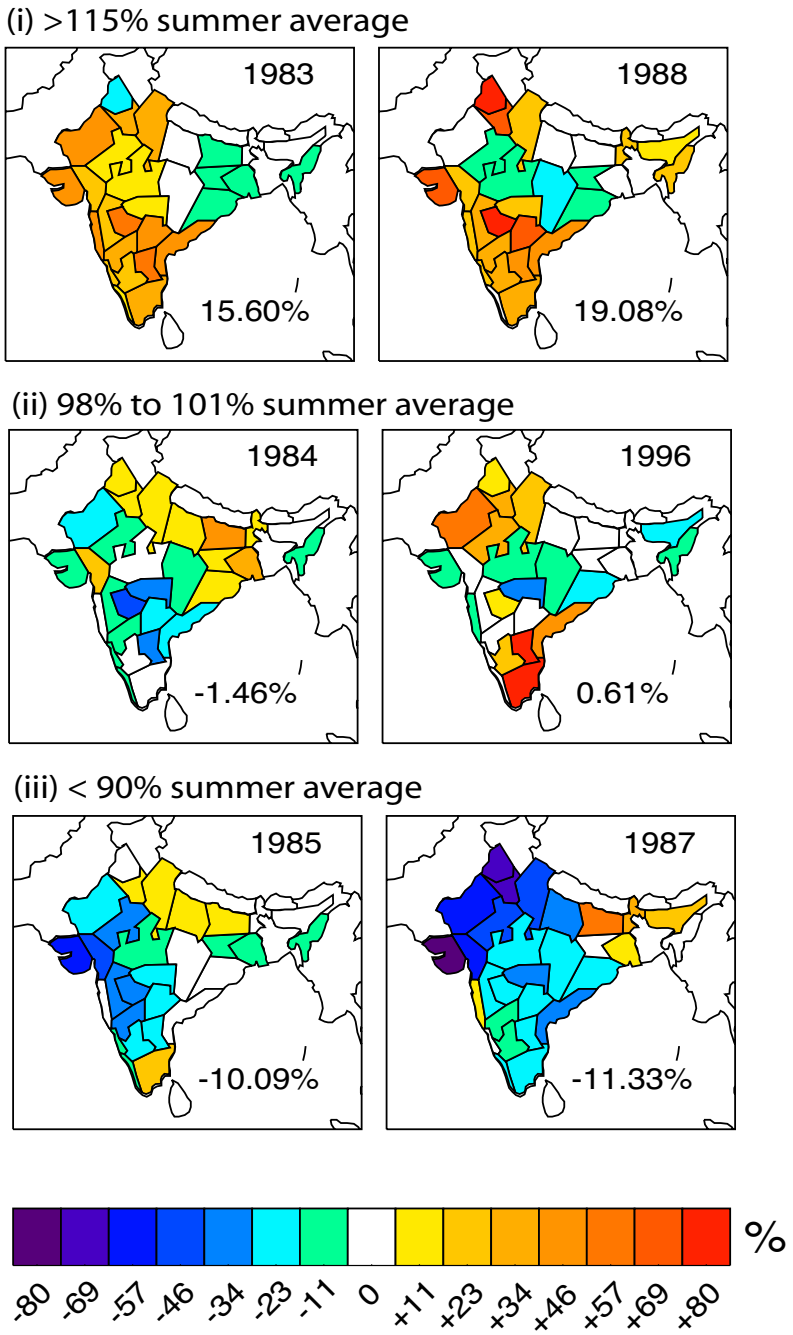

Figure 52: Spatial variability of rainfall (% of district summer average) for years where the All-India seasonally precipitation averaged was (i) >115%, (ii) approximately normal and, (iii) < 90%. Irrespective of category, there is great spatial variability throughout India. Data from Parthasarathy et al. (1995).

In summary, it would be difficult for even a skillful forecast of the all-India seasonal rainfall to provide regional communities with information that could be used effectively in agriculture or water resource management. This does not mean that accurate seasonal forecast would not be useful. A number of studies (e.g., Gadgil 1996, Webster et al. 1998) have shown that Indian crop yields are negatively correlated with the occurrence of El Niño. Selvaraju (2003) has quantified the effect on Indian agriculture noting that El Niño costs India about USD 800M while La Niña provides a gain of some USD 400M to the national economy. Thus, broad-brush assessments may be useful at the level of national commodity markets.

4.2 Utility of intraseasonal monsoon forecasts

It has become increasingly apparent that skillful and timely forecasts of monsoon intraseasonal variability may provide optimal information for regional agriculture and water resource management. For example, in CFAB (2002), which deals with the impact of climate forecasts on agriculture in Bangladesh, it is noted that: "... the minimum length of a forecast which will allow a farming community to respond and take meaningful remedial actions against either flood or drought is about 10 days. An optimal forecast period is in excess of 3 weeks". WMO (2001) also notes that one of the most important problems, especially in monsoon regions is the forecasting of intraseasonal variability. Gadgil et al (1999), referring to the impact of active and break periods on groundnut production in India notes: "the occurrence of some climate events such as wet/dry spells have a large impact on the productivity of the crop. Dry spells induce moisture stress(impacting)growth and development (and) dry/wet spells trigger the growth of pests/diseases/ weeds and hence have an impact on the yield." . An immediate application of a forecast of intraseasonal variability would be the "tailoring of operations" discussed by Gadgil et al. (2002), who note further that an easy option is the choice of a sowing date which does not involve

any additional costs but could involve losses if the farmer chooses to skip the first planting opportunity and the second does not arise. Gadgil et al. (2002) support their conclusions with data relating sowing date with final yield.

The references above speak to the general issue of the agricultural consequences of forecasts of monsoon variability. But are there specific examples of where skillful intraseasonal forecasts could have made a significant impact such as the mid-summer drought in 2002? Potential impact of such forecasts is discussed in a report prepared by the Asian Disaster Preparedness Center (ADPC) for the Indian Agricultural Department on the consequences of the 2002 Indian drought. It was noted that; "Assuming that a prediction of the July drought had been available by the third week of June 2002, and of the revival of the monsoon rains by second week of July 2002, the forecasts would have helped to preserve farm income and ensured food security and reduce relief expenditure by at least 60% of the present cost (i.e., around 6 billion USD). a 20-day forecast during monsoon 2002 in India could have mitigated the impacts of the droughts in several parts of India to a significant extent" (ADPC 2004).

During the last few years, research efforts to understand, simulate and predict intraseasonal variability has increased substantially. Whereas there has been significant progress, the results of modeling intraseasonal variability have so far been mixed. For example, Slingo et al. (1996) found that only a few of the models studied possessed intraseasonal variance comparable to observations. Later studies, on the other hand, that concentrated on the boreal summer intraseasonal variability (Sperber et al. 2000, 2001, Waliser et al. 2003a, Waliser et al. 2003b) found a variety of responses by different models some of which possessed greater than observed variability. Despite the inter-model differences in the simulation of the monsoon, the totality of results suggests potential for the eventual numerical prediction of the intraseasonal variability (e.g., Waliser et al 2003c). Earlier innovative modeling work by Krishnamurti et al.

(1990, 1992, 1995) will be discussed later. A more complete review of progress in the modeling, simulation and numerical prediction of intraseasonal variability, plus plans for model improvement and innovative experimentation can be found in Waliser et al. (2003d).

There has been moderate success in empirical prediction of intraseasonal variability. For example, von Storch and Xu (1990) used principal oscillation pattern (POP) techniques to identify and predict large-scale intraseasonal features in the tropics. Anomaly correlations between the observed and predicted upper tropospheric velocity potential fields were about 0.6 after 7 days that represented a considerable improvement on persistence. Waliser et. al (1999) developed a statistical model using filtered out-going long wave radiation data (OLR) in the band 20-70 days. Anomaly correlations of 0.9 at 5 days were found but decreased to about 0.5 at 20 days, similar to the results of Wheeler and Weickmann (2001) and Lo and Hendon (2000). Also, Mo (2001) using Singular Spectral Analysis (SSA) and Maximum Entropy Method (MEM) techniques, found regional anomaly correlations as high as 0.6 at 20 days.

It is fair to conclude that the skill of models in simulating and predicting intraseasonal variability will increase in time to the level where useful forecasts will be produced numerically. However, until that time is reached, it seems prudent to continue to develop empirical forecasts in the spirit of von Storch and Xu (1999), Waliser et al. (1999), Wheeler and Hendon (2001), Lo and Hendon (2000) and Mo (2001), as discussed above.

In this study, the goal is the prediction of intraseasonal oscillations in the South Asian monsoon region using a new type of statistical model: a physically-based statistical scheme that combines wavelet analysis and linear regression which we refer to as the wavelet banding (WB) method. The concept of wavelet banding comes from a scheme developed by Poveda et al. (2001) for hydrological forecasting in Colombia. Predictors are chosen from the analyses of monsoon intraseasonal oscillations

(MISOs) presented in Chapter 2 and 3.

4.3 Predictands, predictors and statistical schemes

A critical aspect of a physically based empirical scheme is the choice of a set of predictors. To identify these predictors we seek recurrent factors in the morphology of the MISO, based on the composite analysis.

4.3.1 Predictands and predictors

The predictand can be any factor for which there exists a long-term time series and is usually directly applicable to some problem. Whether or not the predictand possesses predictability depends, in the present context, to the degree to which it is determined by the MISO. Examples of predictands used in this study are: rainfall over the central India, rainfall in the Indian states of Orissa and Rajasthan, and the river discharge of the Brahmaputra and Ganges at the borders of India and Bangladesh. Since in situ precipitation measurements are difficult to obtain in a timely manner, we use satellite precipitation estimates such as GPI that have been produced in pentad form since 1986. The government of Bangladesh has made daily river discharge data for the Brahmaputra and the Ganges available from 1986-present.

There are two philosophies used for choosing predictors: "frequentist" (von Storch and Zwiers 1999) and Bayesian (Leonard and Hsu 1999). In the former technique, predictors are chosen principally from their statistical relationship with the predictand. For example, Walker's initial efforts to predict monsoon variability (e.g., Walker 1923) came from the examination of a wide range of climate parameters that has seemingly no apparent physical relationship. Ultimately, this a posteriori technique broke down for prolonged periods (e.g., Kumar et al. 1999, Torrence and Webster 2000). The second technique chooses predictors based on their physical relationship with the predictand. Simply, the predictors are chosen in an a priori fashion based on the physics of the phenomenon one is trying to predict. Here the predictors become the Bayesian

priors of the system.

Table 4 lists the predictors used in the study together with the geographic domain where they were calculated and the source of the data used in the computation. As the scheme is used in experimental operational mode in the Climate Forecasting Applications in Bangladesh project (CFAB) the data must be easily accessible and readily available. There are ten predictors in all each of which identifies a critical aspect of the MISO phenomena. Predictors 2 and 9 characterize the large-scale convection over central India and the equatorial Indian Ocean, respectively. The lower tropospheric basin-wide wind field is characterized by predictors 1 and 6 (Arabian Sea surface zonal and meridional wind components), 5 (strength of the 925 mb Somalia Jet), and 8 (equatorial central Indian Ocean zonal wind component). Predictor 4 describes the equatorial upper tropospheric wind structure. Predictor 10 is an index depicting the location where the equatorial upper tropospheric westerlies become easterlies at 200 mb. During the evolution of a MISO the upper tropospheric easterlies change their intensity and location. Predictor 10 depicts these changes. Predictor 7 provides information about the location and intensity of the monsoon trough. The central India soil moisture is included following its suggested importance in the timing of intraseasonal oscillations by Webster (1983).

Notice that SST is not used as a predictor despite its clear significance. Webster et al. (1998) and Lawrence and Webster (2002) found a 0.5 °C cooling with the advent of the disturbed phase of the MISO. These estimates come from the Reynold's SST product (Reynolds and Marsico 1993). However, in situ measurements reported in Sengupta et al. (2001) and Webster et al. (2002) suggest that the oscillation of the SST during the evolution of a MISO may be at least a factor of two larger. It is thought that the underestimation is caused by a cloud bias in the Reynold's SST product. Other products are appearing such as the TRMM TMI that do a far better

Table 4: Predictors used in the MISO statistical prediction scheme. Predictors are chosen so as to constitute a complete description of the evolution of the MISO.

No	Field	Region	Source
1	Arabian Sea 10 m zonal wind	10° N-15°N, 65°E-75°E	NCEP
2	Central India OLR	15°N-25°N, 70°E-85°E	NOAA
3	Central India Soil Moisture	15°N-25°N, 70°E-85°E	NCEP
4	Eq. Indian Ocean 200 mb zonal wind	5°S-5°N, 70°E-85°E	NCEP
5	Somalia Jet 925 mb meridional wind	2°S-8°N, 65°E-75°E	NCEP
6	Arabian Sea 10 m meridional wind	10°N-15°N, 65°E-75°E	NCEP
7	Central India surface pressure	15°N-25°N, 70°E-85°E	NCEP
8	Eq. Indian Ocean 10 m zonal wind	5°S-5°N, 70°E-85°E	NCEP
9	Eq. Indian Ocean OLR	5°S-5°N, 70°E-85°E	NOAA
10	Tropical 200 mb easterly jet index	20°N-30°N, 70°E-100°E	NCEP

job of estimating SST in the presence of clouds. However, as yet the data set is not sufficiently long to build a meaningful training period.

Figure 53 shows a composite of the central India GPI precipitation in the 20-70 day band. Similar composites are made for each of the predictors (Figure 54). The solid black line shows the mean composite behavior and the blue lines and shading show the one standard deviation about the mean. Day 0 is defined as the occurrence of maximum precipitation in the 20-70 day band. All quantities are shown for 7 pentads before and after day 0. Both the predictand and the predictor set show a tight structure before and after day 0 with robust behavior during the life cycle of the composite MISO.

Figure 54 shows the necessary behavior required of all predictors for substantial precipitation to occur over central India as depicted in Figure 53. The behavior depends not only on the magnitude of a predictor at a particular time but also on the tendency of the predictor. For example, 3 lags prior to the rainfall maximum the OLR over the equatorial Indian Ocean (predictor 9) must be negative (indicating substantial convection at the equator). But, in addition the convection has to be weakening so that the OLR has a positive tendency. At the same time, the surface pressure over central India (predictor 7) must be decreasing and so on. In this manner,

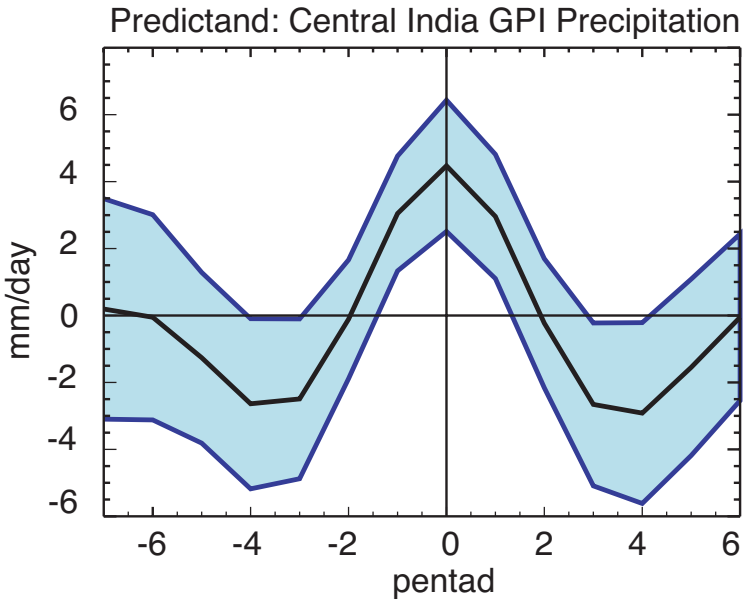

Figure 53: Composite of the central India precipitation relative to maximum GPI precipitation occurring in the central India region in the 20-70 day band. The shaded blue area displays the variance of the predictors within 1 standard deviation.

the predictors set up a list of conditionals for precipitation to occur over central India. If, for example, the OLR over the equatorial Indian Ocean were to continue to become more negative then this would not lead to a precipitation maximum over central India suggesting that northward propagation of convection is not occurring. In the above example we choose only two predictors (7 and 9). In reality we have 10 predictors each having its own conditional behavior for the precipitation event to occur. The problem then reduces to building a statistical prediction scheme that takes into account the conditional behavior of the entire set of predictors.

4.3.2 Statistical Scheme

Having chosen the predictand and the sets of predictors, we have a choice of a number of statistical tools that will produce a forecast. We choose a linear regression scheme to relate the predictand and the predictors. However, before the linear regression process is executed, we employ a "wavelet banding" technique to the predictand and

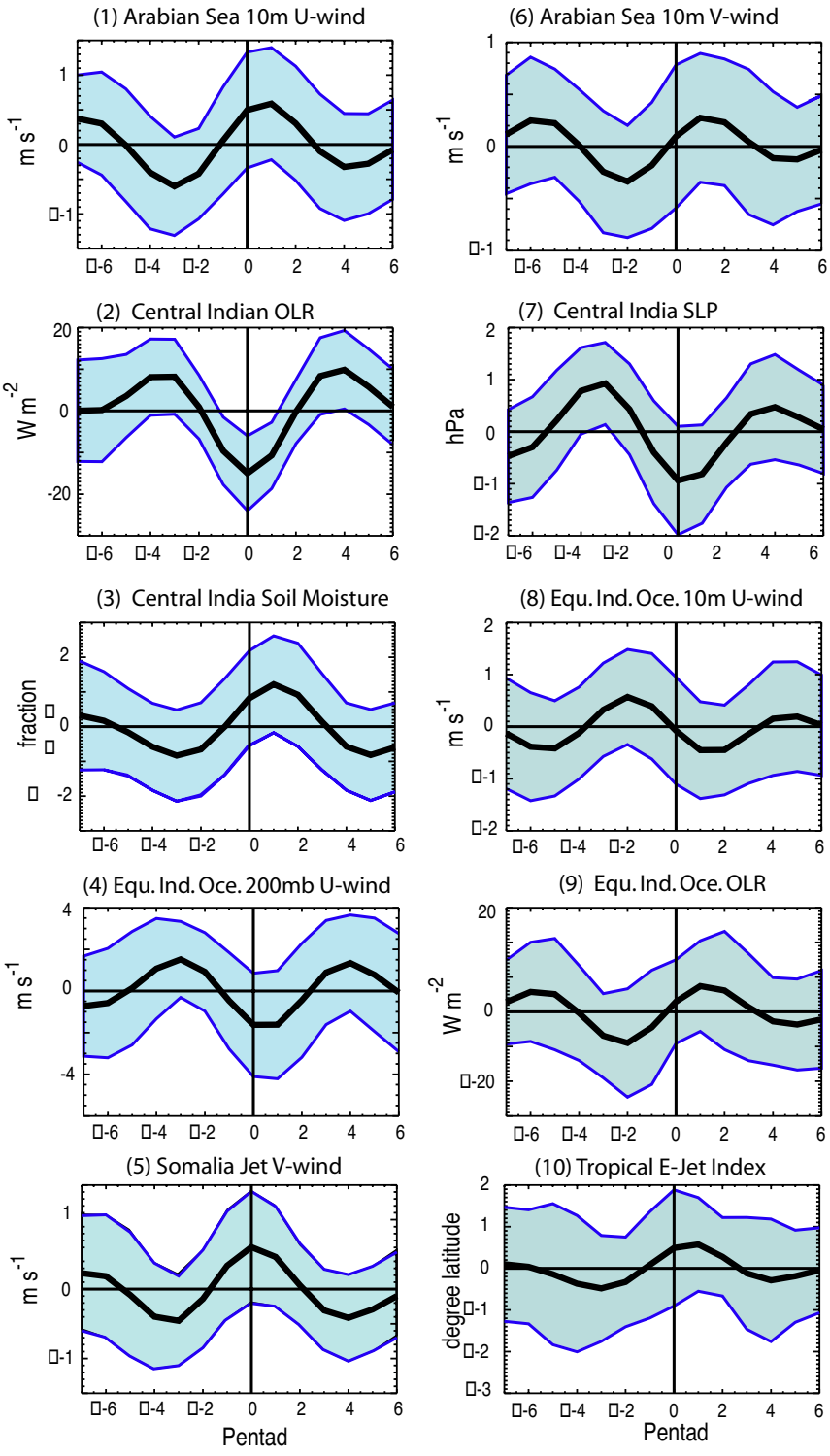

Figure 54: The ten predictors used in the analysis. The regions over which they were calculated are detailed in Table 4 together with a list of data sources. The heavy black line shows the time evolution of the mean predictor. Overall, the predictors show a robust and behavior consistent with the morphology of the MISO quite well.

to the predictors to sort the time series into specific spectral bands. This technique is described below. Together, the wavelet banding and the linear regression are referred to as the Wavelet Banding method or WB method.

In common with the other statistical schemes discussed later, the WB method is "blind" in that only past data is used in the forecasts described in subsequent paragraphs. That is, for a forecast starting at some time $t = t_1$ for a future time $t = t_2$, only predictand and predictor data collected prior to $t = t_1$ is used. Thus, each future point is independently forecast with a regression model constructed for each period to be predicted. For example, GPI precipitation data is available from 1986 to the present date. A 20-day forecast of central India precipitation from May 1, 2002, will use data from 1986 until May 1, 2002. For the next forecast initialized on May 5, 2002, data up to May 5, 2002 will be incorporated.

Wavelet banding: In general, geophysical time series are the result of nonlinear interactions between several physical processes occurring within a broad set of temporal and spatial scales. This means that time series are often made up of combinations of various frequency regimes with contributions present throughout the entire temporal domain or localized in time. The impact of these irregular transients makes forecasting of low frequency events difficult. Consider a predictor such as the central India GPI precipitation. The WB method uses times-series Morlet wavelet analysis (e.g., Torrence and Compo 1998) of the predictand up until the time of the forecast. Figure 55 shows the wavelet spectra of the pentad GPI precipitation product averaged over the central India region (see Figure 49) for the entire data period. From the average wavelet spectra (Figure 55c) the frequency bands of strongest and statistically significant variance are isolated. Four significant spectral regions are found: 5-20 days, 20-75 days, 75-230 days and >230 days. For each forecast, the wavelet is recomputed. Using the frequency bands defined in the wavelet analysis of the predictand, the predictors are analyzed identically. That is, for each of the four frequency

bands there is one predictand and 10 predictor time series. So, in total, there are four predictands and 40 predictors. These time series are spectrally separated using inverse wavelet filtering which works in the same sense as Fourier filtering (e.g. Torrence and Compo, 1998).

Lag Regression Scheme: A simplified version of the general scheme is shown in Figure 56 for one band and just three predictors. Four future values are to be predicted. As each value represents a pentad, this implies a 20-day forecast in steps of 5 days. Figure 56a shows all of the knowledge of the state of the system that is available at the time of the forecast. To forecast the first step (i.e., pentad 1 or day 5, marked as the heavy arrow) we lag the predictor variables one position with respect to the predictand variable (Figure 56b). The shaded box contains all of the information that will be used. Note that if the original dataset has n points, the fitting to forecast the first point will be performed using $(n-1)(p-1)$-tuples where p is the number of predictors. That is, if y were the predictand, the values used to perform the fitting would be $y(2)$ to $y(n)$, and if X were the predictor set, the values used would be from $X(1)$ to $X(n-1)$. If the regression equation is $R(X(t))$, the predicted value would be calculated as $y(n+1) = R(X(n))$. Figure 56c shows the same procedure for the prediction of the second value $y(n+2)$. In this case, the predictors are lagged two positions and the data used to fit the predictand is from $y(3)$ to $y(n)$ and $X(1)$ to $X(n-2)$. Figures 56d and e show the same procedures for the $y(n+3)$ and $y(n+4)$, respectively. In general, to forecast the m^{th} future value of y (i.e., $y(n+m)$, where $m << n$), the regression equations are constructed using $n - m(p+1)$-tuples from $y(1+m)$ to $y(n)$ and $X(1)$ to $X(n-m)$.

Having set up the system, we require a regression technique. We choose the simplest; a multiple linear regression scheme (LIN), so there will be four sets of regression equations, one for each band identified in the wavelet analysis. All the regression coefficients are determined independently in each band. To obtain the

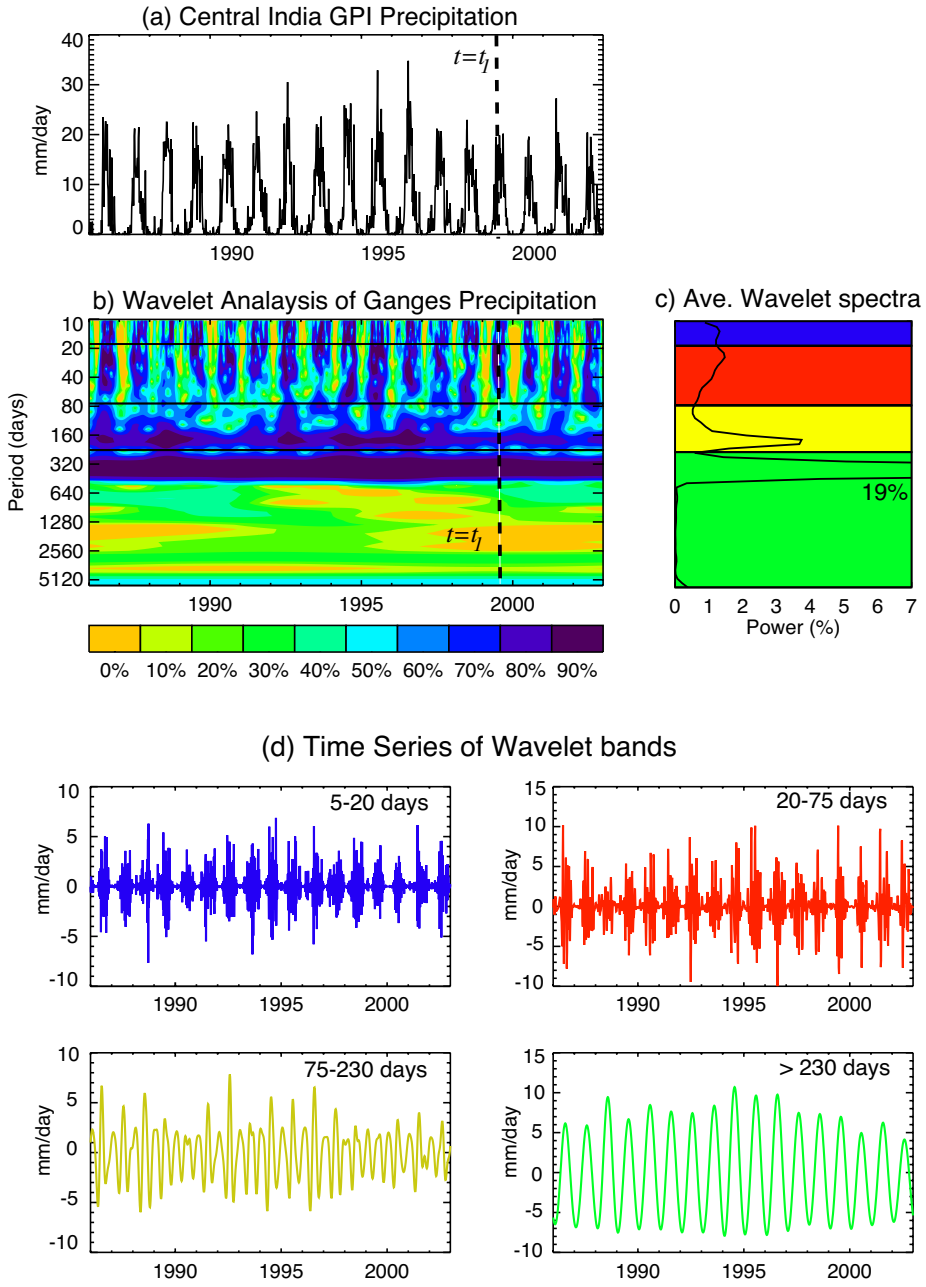

Figure 55: Description of the "wavelet banding" (WB) technique: (a) Time series of a predictor, in this case the GPI rainfall estimate over central India from 1986 through 2002; (b) Wavelet analysis of the predictand for the same period; (c) The average wavelet spectra over the period 1986-2002. The wavelet bands are chosen from regions within the average spectra that are statistically significant. These bands are: 5-20 days, 20-75 days, 80-230 days and >230 days; and, (d) Time series of the four wavelet bands. For a forecast initiated at $t = t_1$ (vertical line), wavelet analysis and the identification of the wavelet bands would be undertaken on data collected at $t < t_1$. Note that the resultant bands (panel d) possess amplitudes with varying coefficients. All of the predictors (Table 4) are banded identically. The wavelet banding and the careful choice of predictors are the fundamentals basics of the statistical scheme.

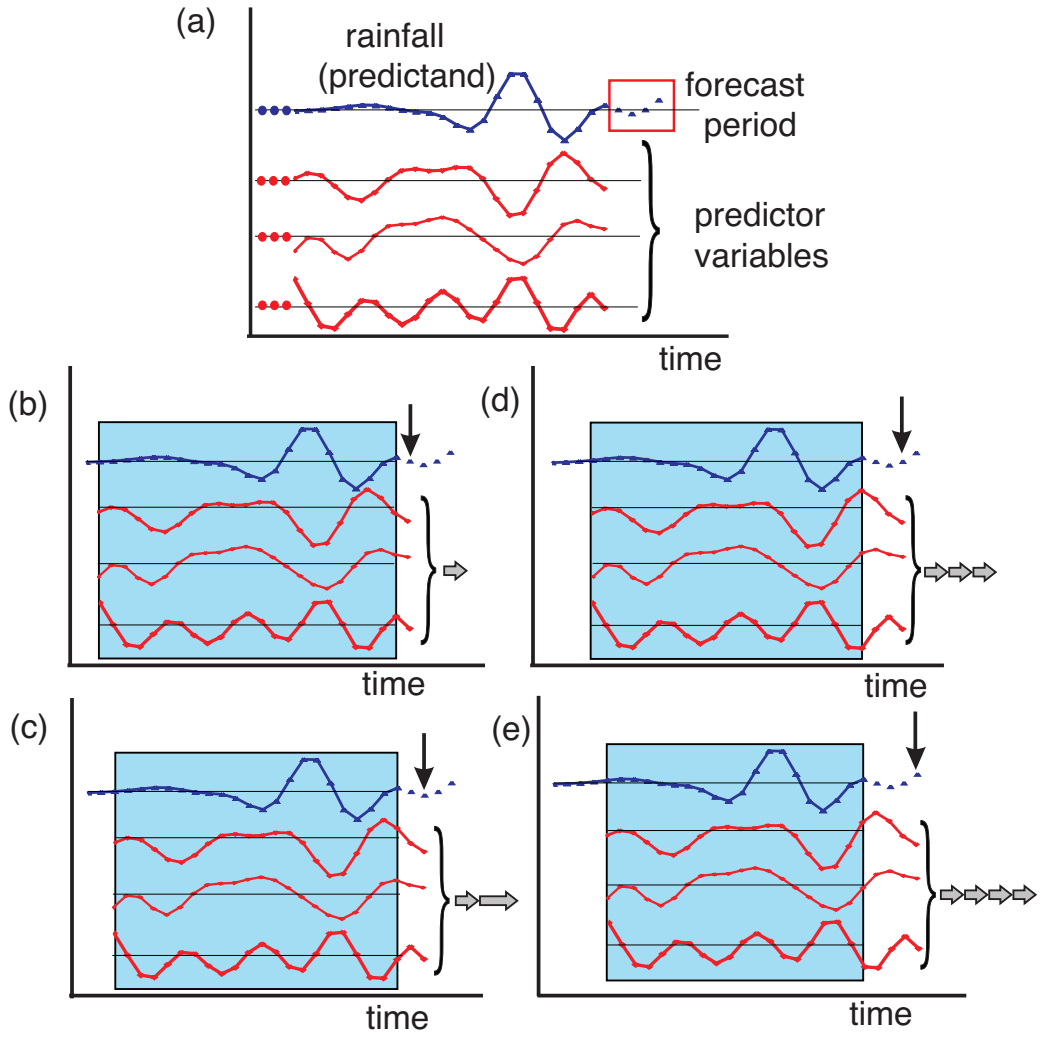

Figure 56: General forecast algorithm for four future values (20 days) of the predictand. (a) Blue curve represents one band of the predictand (e.g., the 20-80 days band of central India rainfall) up to time $t = t1$. Red curves show predictor set (here simplified to three) from the same wavelet band as the predictor. Three other predictand-predictor sets exist to represent the other wavelet bands (not shown). (b) The forecast of the first value (downward arrow) comes from lagging the predictors one step in time (horizontal arrow). Blue boxes contain all the information that will be used to construct the predictand equations. (c)-(e) Forecasts of successive values of the predictand. Here we use a linear regression scheme to advance each of the wavelet bands. At the end of the process, the bands are recombined to provide the total forecast values of predictand.

final forecasted value, the predictions in all bands are added together. The isolation of bands in a time series by wavelet analysis is the key factor in the WB statistical scheme (see appendix) because it allows the regression tool to identify, independently in each band, the existing relationship between the predictand and predictors. That is, the "noise" from other spectral bands is not allowed to affect the construction of the regression equation. The isolation of one band from the noise in another was the basis of the numerical scheme proposed by Krishnamurti et al. (1990). The implementation of the regression scheme results in the production of sets of multi-linear time series with time-dependent coefficients. In this manner, the coefficients of the regression equations vary over time as different predictors change in their relative importance. In fact, this property can be gleaned from correlograms of the predictands and the predictors (not shown) that indicate different variables assume ascendancy in various frequency ranges.

4.4 Predictions

4.4.1 Forecasts of central Indian precipitation

Figure 57 shows 20-day (4 pentads) forecasts for the central India region. Forecasts for the summers of 1999-2002 are displayed. The gray line represents the GPI observation record and the blue lines show the forecast values made 20 days prior using the WB technique with linear regression summed over the four spectral bands using information only available at the time of the forecast. Overall, the 20-day forecasts manage to discern the phase of the major variations of the pentad GPI rainfall quite well. Most peaks and valleys align fairly accurately with observations. Whereas the amplitude of the forecasts is generally underestimated, it is rare that extrema in forecasts and evaluation fields are missed. Based on hindcasts for the period 1992-2003, the anomaly correlations for 15, 20, 25, 30 days for the central India rainfall predictions are 0.88, 0.76, 0.73, 0.66, and 0.58 respectively.

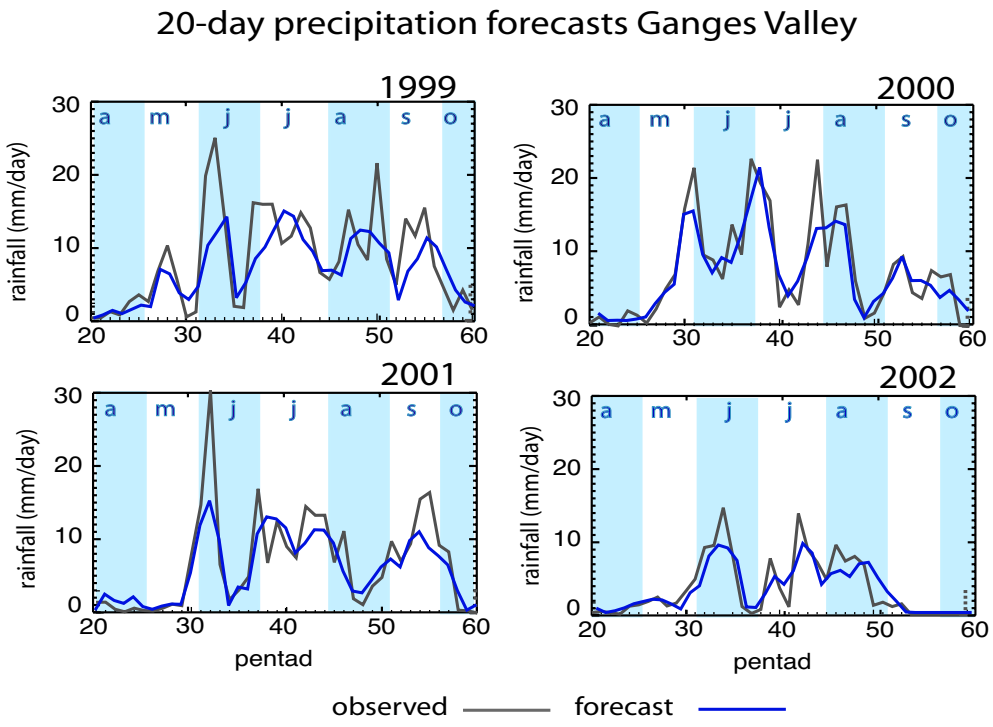

Figure 57: 20-day forecasts of precipitation averaged over the central India for the summers of 1999-2002. Blue lines indicate 20 day (4 pentads) forecasts while the dark gray lines indicate observational validations using area averages of the GPI precipitation. The WB forecast scheme manages to forecast the phase of the rainfall variability with significant skill although the amplitude of high frequency peaks is underestimated by the scheme. Blue and white background denotes months.

In addition to forecasting of intraseasonal variability of the monsoon, the scheme also appears to determine the commencement of the monsoon rains over the central India with some accuracy. These determinations include a number of "false onsets", as identified by Flatau et al. (2001). As this MISO specific statistical system picks up the commencement of rains, it seems that there is some support for the hypothesis that the onset of the monsoon is the first MISO of the summer season (Webster et al. 1998, Flatau et al. 2001).

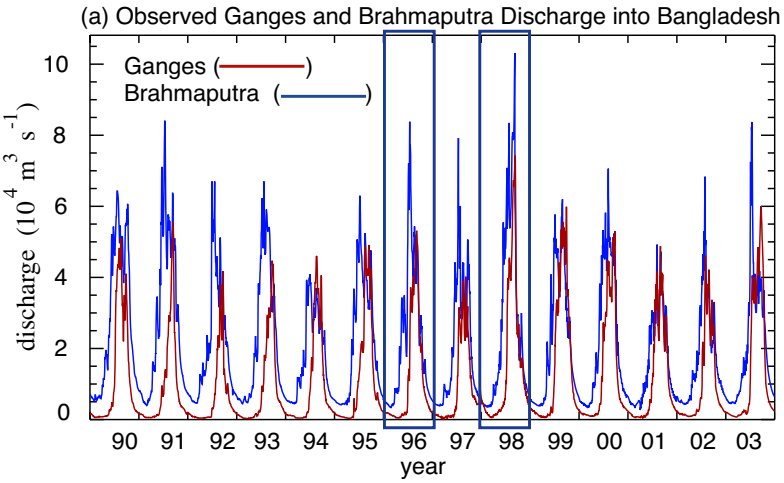

Figure 58: River discharge (104 $m^3 s^{-1}$) of the Ganges (red) and the Brahmaputra (blue) at their entry points into Bangladesh for the years 1990 through 2003. The time series show a great difference in the characteristics of the discharge of the two rivers but both show interannual and intraseasonal variability. Two years are highlighted: 1996 and 1998. During the latter year floodwaters covered over 60% of Bangladesh for a three-month period.

4.4.2 Forecasts of Brahmaputra and Ganges River Discharge

The Brahmaputra and Ganges River basins have drainage areas of 589 and 1,073 10^3 km^2 and average discharges of 630 and 490 km^3 year-1, respectively. The rivers rank as the 6th and 11th largest on the planet in terms of discharge into the ocean. The common feature of the two river systems is that they both pass through Bangladesh into the top of the Bay of Bengal. In so doing, they create annual flooding causing various degrees of disruption to life, agriculture and commerce in Bangladesh. Due to the unavailability of discharge data, only discharge measured at the borders of the country is used for flood forecasting in Bangladesh. Consequently, flood forecasts with only 2-days lead times are currently possible in Bangladesh. The period is determined by the average flow-through time between the borders and the Bay of Bengal. A time series of the discharge of the two rivers is shown in Figure 58.

A strong relationship exists between the discharge of the two rivers into Bangladesh and the rainfall in the catchment regions. It is a nonlinear relationship that takes into

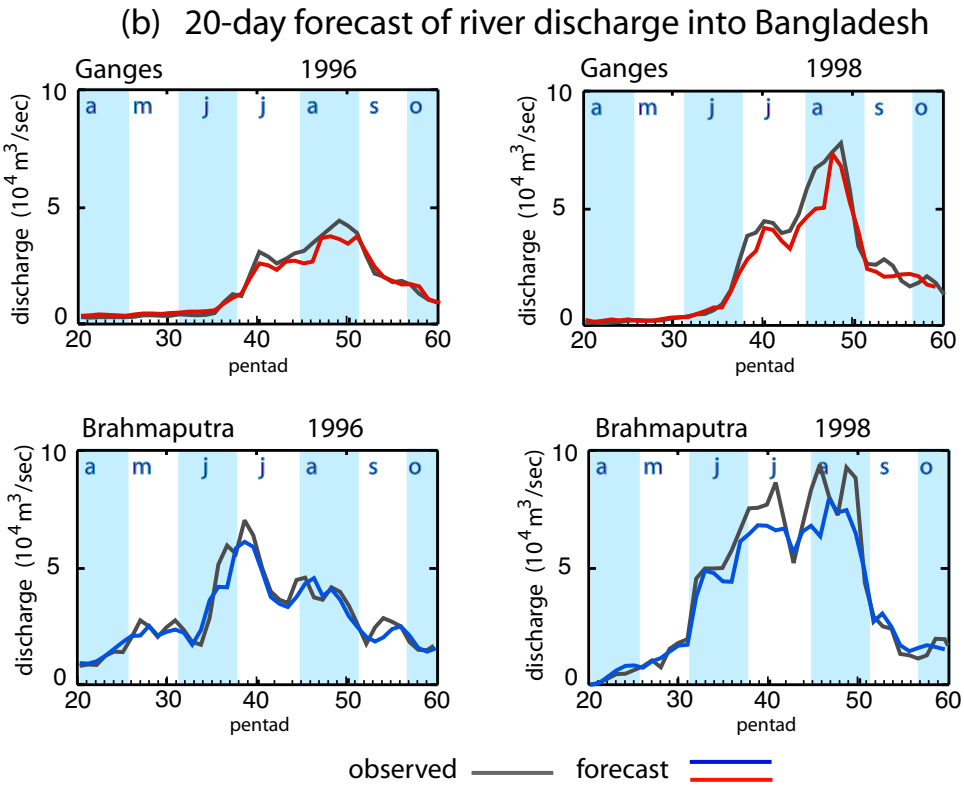

Figure 59: 20-day forecasts of discharge into Bangladesh by the Bayesian WB scheme for the years 1996 and 1998. Black lines show the 20-day forecasts while the blue and red lines show the observed discharge of the Brahmaputra and Ganges respectively.

account land-use practices, evapotranspiration, water retention and etc. To forecast river discharge, we use the two time series of Brahmaputra and Ganges river discharge (Figure 58) as predictands. Given the strong relationship between integrated rainfall and discharge, we use the same predictors shown in Table 4. Figure 59 shows the observed (gray curves) and the 20-day forecasts (red and blue curves) of the Brahmaputra and Ganges for the years 1998 and 1999. The statistical scheme, trained on discharge data from 1986 until the time of the initiation of a forecast, shows useful skill in forecasting discharge into Bangladesh from both rivers.

4.4.3 Scale dependence of precipitation forecasts

Large gradients in total seasonal precipitation occur from the eastern to the western parts of central and northern India 2000 mm in Orissa to 450 mm in Rajasthan. The areas of the two states are roughly 30 and 15% of the central India region, respectively. The question is whether or not the statistical scheme works with sufficient skill to be a useful on areas the size of these Indian states.

Figure 60 shows 20-day GPI precipitation forecasts for the states of Orissa and Rajasthan. The overall mean rainfall is reproduced quite well including much of the intraseasonal variability. However, it should be noted that the overall skill is less than that found for central India for any of the four years. 20-day forecasts using the WB method explained about 79% of the variance of central India precipitation and 74 and 75% of the variance for Rajasthan and Orissa, based on 10 years of hindcasts. Once again there is an underestimation of the amplitude of the peaks and also occasionally a peak may be missing such as during the summer of 2000 in Rajasthan during late July and early August.

4.4.4 Comparison of skill with other statistical techniques

We compare briefly measures of skill of the WB scheme with the skill from other models. In particular, we choose the linear regression model (LIN), used earlier as a component of WB, a multivariate adaptive regression splines model (MARS: Friedman 1991), and an artificial neural network model (ANN). The MARS procedure builds flexible regression models by fitting separate splines (or basis functions) to distinct intervals of the predictor variables. Both the variables to use and the end points of the intervals for each variable referred to as knots are found via a brute force, exhaustive search procedure. Variables, knots and interactions are optimized simultaneously by evaluating a "loss of fit" (LOF) criterion. In addition to searching variables one by one, MARS also searches for interactions between variables, allowing any degree

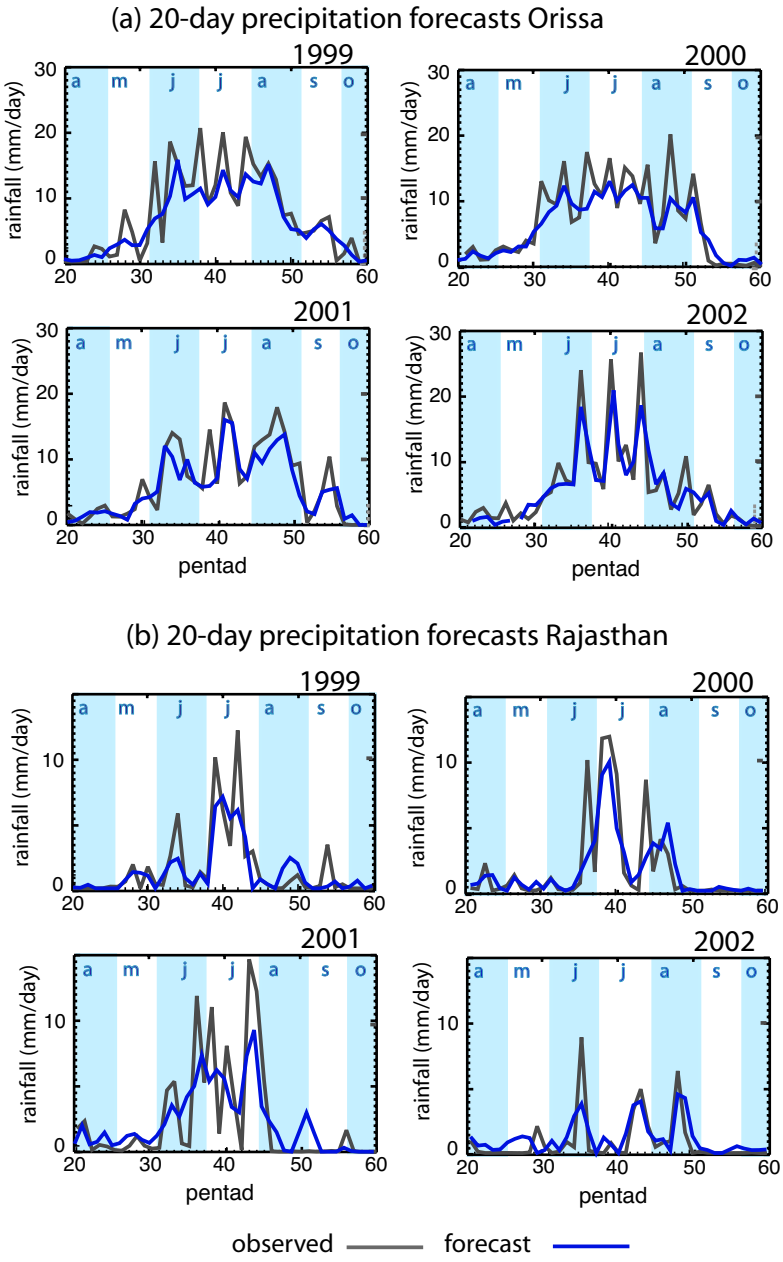

Figure 60: Same as Figure 57 except for 20-day forecasts of precipitation for the Indian states of Orissa and Rajasthan. Even though the area of each state is significantly smaller than the central India region, the WB scheme still manages to capture the major intraseasonal events some time in advance albeit with reduced skill.

of interaction to be considered. The "optimal" MARS model is selected in a two-phase process. In the first phase, a model is grown by adding basis functions (new main effects, knots, or interactions) until an overly large model is found. In the

second phase, basis functions are deleted in order of least contribution to the model until an optimal balance of bias and variance is found. For this work, the optimal MARS scheme found has a maximum of 6 basis functions, allowing second order interactions (no more than two predictors interacting per basis function). ANN is a data processing system that can learn the relationship between two data sets. This is done using an adaptive recursive algorithm which minimizes the error resulting from estimating one data set from the other. This process is also known as training, and a trained network can be used to estimate or forecast the predictand. ANN are known to be optimal discriminators because theoretically they are able to reach the Bayes limit in any classification problem. In fact the Bayes limit corresponds to the optimal classification performance. If ANN are able to reach it, that means ANN always do better or at least as well as any other conventional method. Unfortunately this is only true if the network architecture as well as the learning algorithm are perfectly chosen, generally a very difficult task. The architecture of the ANN used is a standard feed-forward, backpropagation updating network with 4 layers: input, two hidden with 5 and 2 nodes, and output.

A time section of the forecasts for each of the schemes is shown in Figure 61 for the summer of 2002, relative to the observed precipitation (shaded). All schemes forecast the low-frequency envelope of the annual cycle. Both the MARS and the ANN model appear to show some resemblance of intraseasonal variability especially the first rainy cycle. Both show a decrease of precipitation during late June and early July but do not forecast a cessation of rainfall. The skill of these forecasts decrease substantially later in the season. Forecasts using the linear regression model show no evidence of intraseasonal variability.

Figure 62 compares the model forecasts using a number of statistical tools. The root mean square error (rmse) and forecast skill (skill) is defined as:

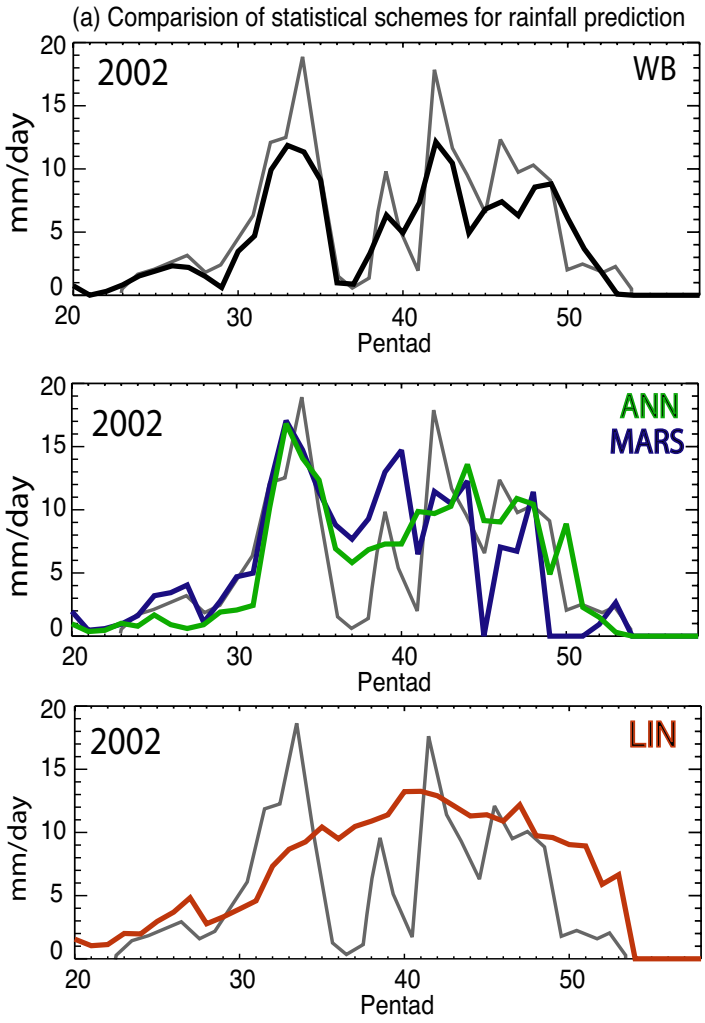

Figure 61: Comparison of three other schemes (neural net, ANN: multivariate adaptive splines, MARS: linear regression, LINEAR) with the WB scheme for a 20-day prediction for the Ganges valley GPI precipitation estimate. The observed precipitation rate is shown as the gray curve in each panel. The same physically based predictors were used in each scheme. The ANN and MARS schemes appear to anticipate the first active period quite well although both miss the mid-season break. The linear regression model (LIN) shows little correspondence to observations except for giving a fair reproduction of the annual cycle.

$$rmse = \sqrt{\frac{\sum_n (x(i) - \overline{x}(i))^2}{n}} \tag{1}$$

$$Skill = (1 - \frac{rmse(x)_{prediction}}{rmse(x)_{observation}}) * 100 \tag{2}$$

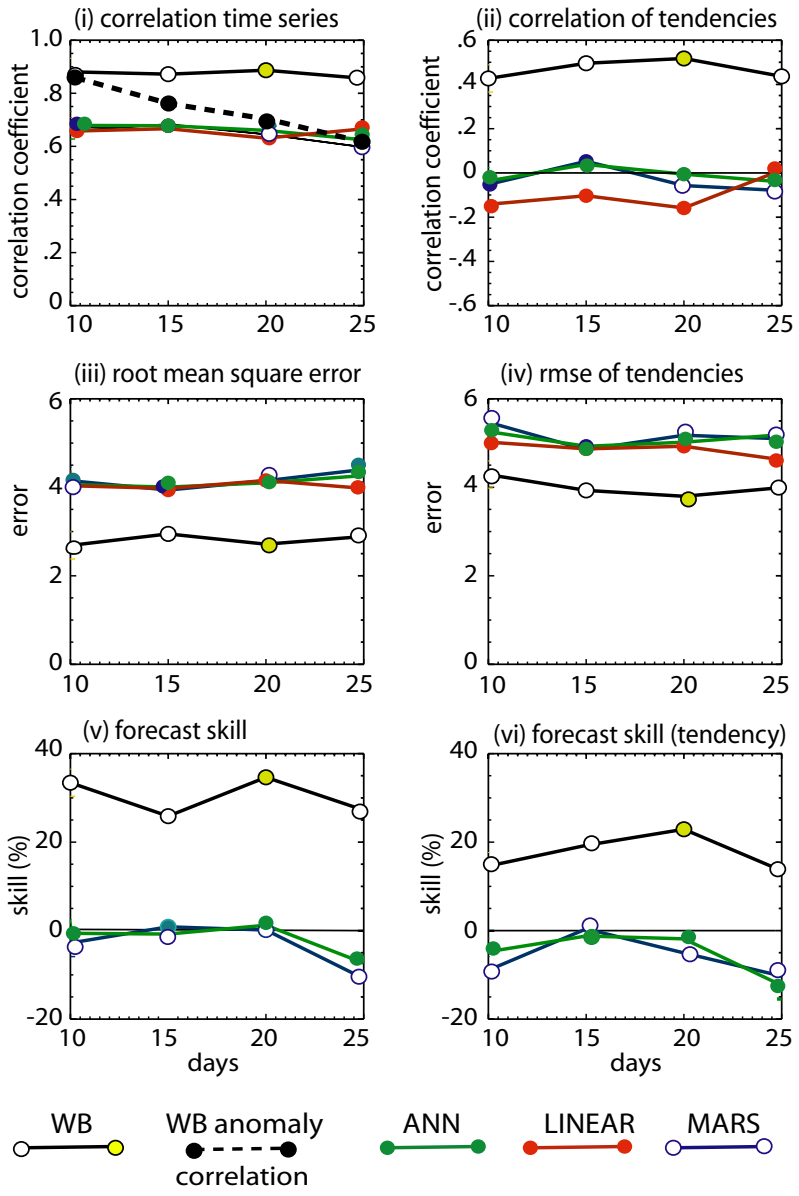

Figure 62: Comparison of the statistics of the four schemes for 10 years of hindcasts for GPI precipitation over the Ganges Valley. In all six measures of performance, the WB scheme scores best. In addition, the anomaly correlation coefficient is shown as the black dashed line in panel (i). The statistical measures are defined in the text.

where x may be the predictand $y(n)$ or the tendency of the predictand $(y(n)-y(n-1))$. On all lags the WB forecast outscores other methods. For example, correlations between forecasts and observations are >0.8 for WB but <0.6 for the other schemes. Most of the correlation skill in the MARS, ANN and linear schemes come from the

forecasting of the annual cycle envelope. Also the root-mean-square error is far smaller for WB than the other schemes. When tests are applied to tendencies of the predictands rather than absolute values, WB still outperforms the other schemes.

4.5 Why does the WB technique work?

In general, geophysical time series are made up of many temporal scales with coefficients that vary in time. These factors make the task of prediction more difficult. The wavelet banding technique attempts to improve forecasting skill by making proper use of all available spectral information. Figure 63 is a simple example of why combining traditional fitting tools with spectral techniques is useful. For explanatory purposes, the example we choose is very simple and we assume that the coefficients of the functions are constant in time.

Consider a predictand $F(t)$ that is represented by two periodic modes given by

$$F(t) = 2\sin(t) + \sin(6t) \tag{3}$$

as shown in Figure 63a. Assume that there are two predictors $G(t)$ and $H(t)$ that are also periodic and stationary

$$G(t) = \sin(t + 20) + \sin(3t) \tag{4}$$

and

$$H(t) = \sin(6t + 20) + \sin(4t) \tag{5}$$

The functional form of the predictors is shown in Figure 63b and 63c. Let us assume that we intend to do a 20-step forecast of $F(t)$ using the predictors $G(t)$ and $H(t)$. There are two methods we can employ. We can use the multivariate linear regression (e.g., LIN), or we can use the banded wavelet method (WB).

(i) Multivariate linear regression (LIN): We use the linear regression system (LIN), described in the text, to find a fitting expression and then compute the future values of the predictand $F(t)$. The predictand after 20 days lagging ($F'(t)$) is shown in

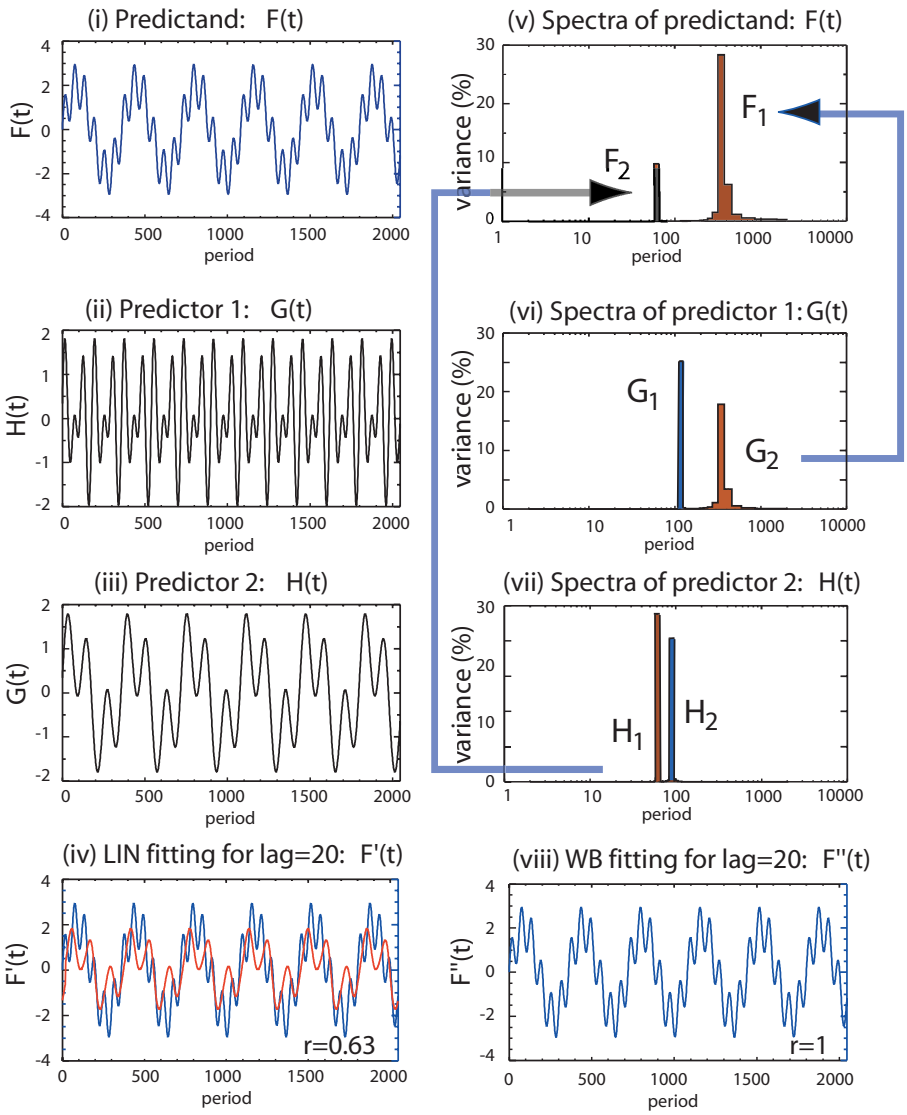

Figure 63: A simple periodic predictand $F(t)$ is chosen (panel a) with two periodic predictors $G(t)$ and $H(t)$ (panels b and c, respectively). Using a linear regression technique (e.g., LIN) to forecast 20 lags produces the function $F'(t)$ (panel d). The correlation between $F(t)$ and $F'(t)$ is 0.63. However, if the spectra of the predictand (panel e) is noted and a spectral (or wavelet) banding applied in which the predictors are also banded (panels f and g), only part of the predictor functions will be used to predict. Predictor components $G_1(t)$ and $H_1(t)$ are discarded and $G_2(t)$ is used to predict component $F_2(t)$ and $H_1(t)$ component $F_2(t)$ (large blue arrows). The result for this simple case is a perfect forecast $F''(t)$.

Figure 63d. The red curve shows 20-day forecasts of $F(t)$. The correlation coefficient between $F(t)$ and $F'(t)$ is 0.63.

(ii) Wavelet banding (WB): Instead of using the raw time series of the predictors, the prediction can be improved using the WB method. Note that in this simple case, the amplitude distribution of the wavelet at any time is the same as the average wavelet spectra. We divide $F(t)$ into two bands ($F(t) = F_1(t) + F_2(t)$)

$$F_1(t) = 2\sin(t) \tag{6}$$

and

$$F_2(t) = \sin(6t) \tag{7}$$

The predictors are also divided spectrally so that: $G_1(t) = \sin(t + 20)$, $G_2(t) = \sin(3t)$ and $H_1(t) = \sin(6t + 20)$, $H_2(t) = \sin(4t)$. Spectra for the three functions are shown in Figure 63e-g. However, the banding of the predictors is determined by the spectral bands of the predictand. Therefore $G_1(t)$ and $H_2(t)$ do not enter the procedure and only the matching spectral information is used to make the forecast. Thus, $G_2(t)$ is used to forecast $F_1(t)$ and $H_1(t)$ is used to forecast $F_2(t)$. The forecast $F''(t)$ is shown in Figure 63h. In this very simple case the forecast is perfect (correlation equal one).

4.6 Ongoing work on Empirical Forecasting

A strength of Bayesian statistics is that probabilities of occurrence can be calculated for a particular forecast. For applications the probability of an event occurring is an essential component of a forecast because it allows a cost/loss analysis to be made. For example, consider the first maximum in precipitation forecast in 2002 for Central India. At pentad 31 a maximum in precipitation was forecast at pentad 35. The forecast was for a precipitation rate averaged through the pentad of 9 mm/day. The observed value turned out to be 14 mm/day. A more useful forecast would have been to provide a range of probabilities of rainfall rate. Essentially, the forecast scheme used in this study weighs the evolution of the 10 predictors relative to the past

behavior of the predictors. That is, a forecast is made relative to the joint probabilities of a series of events occurring through the forecast period. Such occurrences are measured relative to their statistical "priors" that can be turned into probabilities. An immediate extension of the WB method is to take full advantage of the Bayesian structure of the model and develop probability density functions for each forecast.

Figure 54, which shows the composite behavior of the predictors and their variance, points towards how probabilities estimates are natural extensions of the WB scheme. The composites were constructed from 53 MISOs occurring since 1986. Thus, at any time during the monsoon season, there is a value occupied by each of the predictors. Based on their values and their tendencies, it will be possible to calculate probability distributions. A similar approach is to calculate joint probability density functions (PDFs) for each predictor at the respective lags. At each forecast time step and for each spectral band, the multilinear regression equation would be used several times in a Monte Carlo-like manner producing random values of each predictor. The random values will then be distributed as a conditional PDF derived from the corresponding joint PDF and the current state of the predictor. Finally, a PDF of the predictand could be computed from the evaluation of the regression equation using the generated random values of the predictors. A second method being explored uses the history of hindcasts to document residuals between the forecast and the validation field. This procedure establishes a history of uncertainty in the forecast. By examining the current residual patterns, residuals can be determined from the archive. As for any forecast there will be a family of nearest neighbors, a forecast probability distribution function of the predicted state can be determined.

There is also the possibility for a promising hybrid approach. In this technique, the WB technique is combined with ensemble integrations of operational general circulation models. In this case we use the European Centre for Medium Range Weather Forecast (ECMWF). The wavelet spectrum is calculated using the same procedure

as outlined before but extended using ECMWF 1-10 day operational forecasts tacked onto observational priors. This provides two extra lags (2 pentads) beyond the initiation period. In other words, the Bayesian priors are modified with new information. The time series are banded and regression is performed as before but including the new operational information. Given that there are 51 ensemble members in the operational scheme probabilities the forecasts are probabilistic. The forecast can updated each day using the new pentad information provided by new observations and the ECMWF ensemble forecasts. A series of overlapping probabilistic forecasts is then produced.

CHAPTER V

SKILL OF NUMERICAL MODELS FORECASTING ISO: EVALUATION OF A SERIAL-RUN EXPERIMENT USING THE ECMWF COUPLE MODEL.

One of the great challenges in meteorology and climate is the accurate numerical modelling and prediction of the MJO or, more generally, intraseasonal variability. Given its wide range of influences it is critical that the ISO is well simulated and that numerical models have the capability to forecast the variability. However, numerical weather prediction (NWP) and climate models generally have a poor representation of the oscillation. Slingo et al. (1996) found that no model was able to capture the spectral peak associated with the MJO in atmosphere only general circulation models (GCMs) used in the Atmospheric Model Intercomparison Project. Additionally, the skill of NWP models is in general less than that of statistical prediction techniques (e.g. Waliser 1999, Webster and Hoyos 2004) as pointed out in Chapter 4. A more recent analysis of 14 coupled GCMs participating in the IPCC Fourth Assessment (Lin et al. 2005) found very little improvement in the Atmosphere-only GCMs over what was found by Slingo et al. (1996).

Numerical models are often tested for their ability to simulate and predict intraseasonal variability based on spectral statistics of individual long-term runs. Here we use a more systematic approach of evaluation using an extensive series of integrations in forecasting mode allowing the ability of a model to be assessed at all

convective stages of an ISO. Using a forecast model rather than a traditional climate model approach provides a different measure of ISO simulation skill allowing a direct comparison of the forecast with an observed event, rather than climate ISO statistics, typically used to assess climate simulations.

This chapter focuses on the analysis of forecast experiments for the summer ISO. Results for the winter ISO are currently being evaluated and have been partially studied by Agudelo et al. (2006) and Woolnough et al. (2006).

5.1 Serial modeling experiment

A major recommendation emerging from the ECMWF/CLIVAR workshop on Simulation and Predictability of Intra-Seasonal Variability (ECMWF 2004) was the need to study the predictability of the MJO in all its stages (generation, propagation, decay) by performing a series of daily extended integrations using the ECMWF coupled Monthly Forecasting System. The basis of the recommendation comes from the observation that numerical models in general tend to have low variance in the 20-80 day period band and that little success has been achieved in prediction of intraseasonal events. Specifically, it was recommended that a series of integrations be performed for various well-documented intraseasonal events in an attempt to discern where in life cycle of an intraseasonal event the ECMWF model tends to fail in both simulation or prediction. The extensive series of integrations allow the ability of the climate model to be assessed at all stages of the lifetime of an ISO. The proposed experiment is similar in philosophy to the NMC/NOAA DERF (Dynamic Extended Range Forecast: Tracton et al. 1988, 1989) experiments conducted in the 1980's. The DERF experiment considered sets of 10 Day atmospheric model forecast initialized each day consecutively, for 30 days. These experiments allowed a detail study of error growth and propagation as a function of time (Reynolds et al. 1994)

The following experiments, shown schematically in Figure 64, are performed:

- A series of integrations, initialized each successive day for 30 days and integrated for each of 30-day duration, using the ECMWF coupled climate model are run at times of known ISO activity in the tropics.

- An ensemble of 5 members per each day.

- Integrations commence 20 days before the maximum of active phase of the ISO either in the western Pacific Ocean (winter) or Indian Ocean (summer). ERA-40 data is used in the initialization of the atmosphere and land and also as the "truth" against which the forecasts are tested. The oceanic data assimilation system used to produce the initial conditions of the ECMWF seasonal forecasting system was used to generate initial conditions for the oceanic component.

- Each experiment is run using a full ocean model and also with the mixed layer model.

To perform the integrations, we use the ECMWF ocean-atmosphere coupled model used in monthly forecasting framework (Vitart 2004). The atmospheric component is the ECMWF atmospheric model Integrated Forecast System (IFS) has a resolution of TL159 (about 1.125 x 1.125 degrees) with 40 levels in the vertical. The oceanic component is the full dynamics Hamburg Ocean Primitive Equation (HOPE) from the Max Plank institute and it has a zonal resolution of 0.3 degrees of latitude at the equator and 1.4 degrees in the extratropics by about 1.4 in longitude everywhere and 29 vertical levels (Wolff et al. 1997), with 10m resolution in the upper 100m. The coupling of the components is through the interface OASIS developed at CERFACS (Terray et al. 1995). The model is initialized in the same way as for the operational system with atmospheric initial conditions from ERA40 and perturbations to the initial conditions and stochastic physics active throughout the integration. The ocean initial conditions are taken from the ECMWF ocean analysis (Balmaseda et al. 2005) and are perturbed following the operational monthly forecasting approach (Vialard

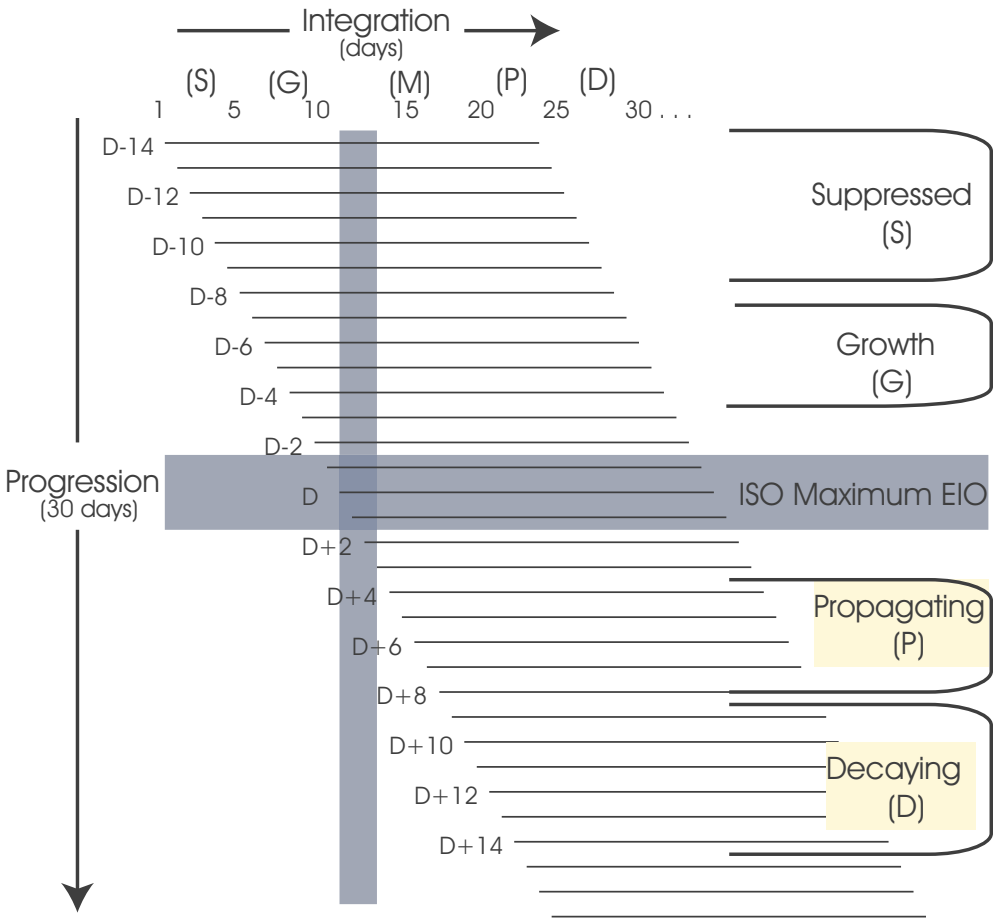

Figure 64: The serial integrations scheme for the investigation of the predictability of intraseasonal variability. The ECMWF coupled model is initialized 20 days prior to a known ISO at which time a 30-day prediction is made. The model is then initialized for the succeeding 30 days so that it is initialized before, during and after the maximum of the ISO convective activity. Gray regions show the timing of the maximum amplitude of the ISO (M) in a specified region. The aim is test the ability of the model to simulate and forecast the suppressed (S), growth (G), propagating (P) and decaying (D) phases of the event. Ensembles of 5 members are run each successive day.

et al. 2003). In the ECMWF monthly forecasting system, no artificial terms are introduced to try to reduce the drift of the model, and no steps are taken to remove or reduce any imbalances in the coupled model initial state. All the integrations were carried out using the ECMWF computer resources.

To examine the overall sensitivity of the extended simulations using the ECMWF monthly forecast system to the atmosphere ocean coupling, the same experiment was performed by replacing the full dynamical ocean model with a 1D mixed layer model. The mixed layer model is based on the K-Profile Parameterization vertical mixing scheme of Large et al. (1994). It has a vertical domain of 200m with 29 vertical levels. The top model level is 1.4m thick with 16 levels in the top 30m. The mixed layer model extends 44° of latitude, poleward of which the SST is provided by persistence of the initial conditions. To produce a smooth transition, the SST between 40°and 44° is a weighted average of the modeled and initial SSTs. In this case, the ocean initial conditions are not perturbed.

The experiments allow different diagnostics of the 4-dimensional characteristics of the intraseasonal variability in order to discern why, where and when the ECMWF model loses power in the intraseasonal band. In other words, the integrations allow the evaluation of the skill of the model through all of the stages of the ISO. It is hoped that the results of the outlined experiment will shed some light on the problems most models have in simulating and predicting ISOs in the tropics.

Three periods were selected for initial experimentation:

- Period starting December 15, 1992, to encompass the large intraseasonal oscillation during the TOGA COARE period in the Indo-Pacific basin.

- Period starting April 15, 2002 to capture the growth of the first active period of the monsoon (Southeast Asian monsoon onset) followed by a midseason break.

- Period starting May 18, 2004 to cover the growth of an active period associated

to the Southeast Asian monsoon onset (i.e., first MISO of the 2004 summer).

5.2 Measures of the Forecasting skill

An important aspect of the serial experiments is the identification of different metrics against which the integrations can be compared, as well as different methodologies that allow a precise assessment of the forecasting skill of the model. In the present work, the evaluation of the extended summer predictability is presented by studying relevant dynamical and convective features associated with the ISO as presented in previous chapters. Examples of metric might be atmospheric circulation at different levels (e.g. zonal winds) and convective anomalies (OLR). The vertical structure of the extended forecasts is also studied by analyzing the zonal and meridional mass stream function.

In the model evaluation, there are different aspects that need to be assessed in order to present a comprehensive view of the overall skill of the model. Different statistics need to be used to evaluate all relevant features. Correlation and root mean squared error (RMS) at different lead times are estimated in order to evaluate the phasing of the model results relative to the observations and the deviation of the integrations from the observations (absolute error), respectively. Both statistics are estimated for the raw unfiltered results and for intraseasonal filtered results in order to evaluate the extended forecasting skill.

In addition, the spread of the ensemble members is also evaluated as it is an important measure of predictability. In general, large ensemble spread is associated with low predictability and vice versa. As mentioned before, state-of-the-art models are not able to generate power in the intraseasonal band. For that reason, the amplitude of the intraseasonal spectral band is also evaluated by comparing observations with integrations at different lead times.

Non-parametric measures based on information theory, such as joint entropy and

mutual information are also used here in order to include all the information from the integrations (e.g. all ensemble members) in a single measure of the skill evaluation. The propagation structure of intraseasonal features is also evaluated by comparing Hovmoller diagrams of observations and integrations as well as maps and vertical cross-sections at different lead times.

In addition to the skill statistics, the propagation structure of the ISO related anomalies of observations and forecasts is also analyzed. The meridional and zonal mass stream functions are estimated in order to study the vertical structure of the ISO.

5.3 Regional Skill

As shown in previous chapters, the ISO introduces considerable anomalies of different variables in different regions of the Indian-West Pacific basin. In fact, those anomalies constitute the basis for the predictor selection of statistical forecasting schemes such as the example presented in Chapter 4. It is for that reason that correlation, RMS error, spread of the ensembles and ISO amplitude are estimated for different regions that possess strong intraseasonal variability. The ISO amplitude is quantified as the standard deviation of the intraseasonally filtered time series. The regions used for the evaluation are the Equatorial Indian Ocean (65-85°E, 5°S-5°N), Bay of Bengal (85-95°E, 10-20°N), South West of India (over ocean, 65-80°E, 5-15°N), and Central India (70-85°E, 15°S-25°N), and. The areas of the regions selected are not so small that spatial collocation errors are not responsible for the less than perfect forecasting skill and not so big that regional averaging artificially increases the skill of the model. For example, a basin-wide average over the entire Indian Ocean basin to estimate the skill of extended forecast of certain model gives little information about the skill of the model forecasting the ISO since the all the spatial features are masked and diluted by the averaging.

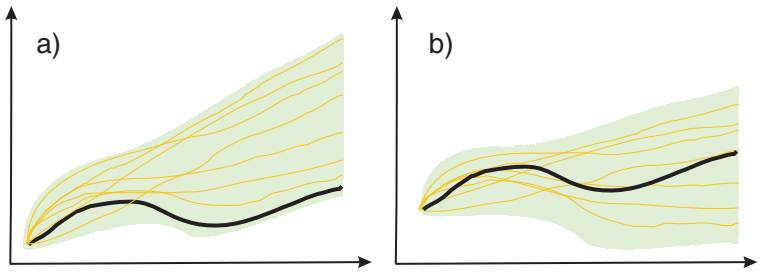

Figure 65: Schematic diagram of two different ensemble forecasts with similar "internal" spread but considerably different spread relative to the observations. The black thick line represent the observations, the orange lines the different ensembles and the light green area the spread of the ensembles.

All these statistics are estimated for different lead times. In other words, all forecasts for certain lead time (1, 2 30 days) are grouped and independently compared against the observations. For regional averages, forecasts for all lead times are arranged as time series of N elements, where N is the number of successive 30-day integrations.

The RMS error estimation used here is scaled by the standard deviation of the observations. In this way, when the scaled RMS error is equal to one, the magnitude of the forecast errors for that lead time is equal to the amplitude of the signal. It can be said that at that point there is no subsequent skill in the forecasts. The spread of the ensembles is estimated in two different ways, one relative to the ensemble itself providing information about the extended predictability (degree of reproducibility), and relative to the observations providing a measure of the skill of the forecasts. In a perfect model sense, a small spread among ensemble members implies high predictability. The ensemble spread was quantified as the ensemble standard deviation, relative to the ensemble mean and observations respectively, at different lead times. As shown in the schematic diagram in Figure 65, two different ensemble forecasts may have similar spread but very different forecasting skill.

In addition to the regional analysis, the spatial structure of the skill of the model is studied by constructing correlation and RMS maps for different lead times. The

structure of the errors could potentially provide explanation about the source of the errors.

5.4 Information Theory

Entropy and other concepts in information theory are very useful in the evaluation of the predictive skill of both empirical and numerical models. In particular, joint entropy and mutual information, which are non-parametric estimations, measure the relative dependence among different variables. In this case, the variables in question are an observed variable (e.g. 200mb zonal winds, Outgoing Longwave Radiation) and its prediction (results of the integrations).

Mutual information is based on the concept of entropy, which is associated with the randomness in a signal. C. E. Shannon (1948) originally defined entropy,$H(X)$ for a signal X as

$$H(X) = \sum_{x} f(x) \log_2 f(x) \tag{8}$$

where a random event x occurs with a probability $f(x)$. The joint entropy of two variables X and Y measures the entropy contained in the joint system and is defined as

$$H(X,Y) = \sum_{x,y} p(x,y) \log_2 p(x,y) \tag{9}$$

If X and Y are independent, the total entropy of the system would be equal to $H(X,Y)$. In all cases $H(X) \leq H(X,Y)$, and the equality is only achieved when X and Y are totally dependent. Based on these definitions, mutual information can be defined as

$$I(X,Y) = \sum_{x,y} p(x,y) \log_2 \frac{p(x,y)}{f(x)g(y)} \tag{10}$$

or as

$$I(X,Y) = H(X) + H(Y) - H(X,Y) \tag{11}$$

Joint entropy and mutual information are used here to estimate the predictive skill of the model in a non-parametric fashion and including all ensemble forecasts without

estimating regional or ensemble averages. Joint entropy and mutual information are estimated for different forecast lead times from 1 to 30 days.

5.5 Analysis of Summer Integrations

Both summer experiments correspond to intense intraseasonal convective anomalies propagating eastward towards the Pacific and northward into the Bay of Bengal and India generating active and break periods of rainfall (see Figure 66). Figure 67 shows the cumulative rainfall during the 2002 and 2004 numerical experiment periods as well as the rainfall time series for Indian Ocean, Bay of Bengal, and Western Ghats. The cumulative rainfall shows the typical pattern of early summer, with considerable rainfall over the Indian Ocean and Southeast Asia with a rainfall band extending from the South China Sea towards Japan, a narrow ITZC over the Pacific Ocean centered around 8°N, and well developed SPCZ. Rainfall is also observed over West Africa and eastern United States. Statistical and diagnostic analyses of the forecasting skill of the model are presented in the following paragraphs.

Figure 68 and 69 show the ensemble forecasts of 200mb zonal winds for Equatorial Indian Ocean, South West India, Central India and Bay of Bengal (EIO, SWI, CI and BB) as well as the standard deviation of the ensemble members for all successive forecasts (starting day) and during the whole integration period (target day). The standard deviation is computed relative to the observations and to the ensemble mean. The first quantity provides information about the skill of the model and the latter is an indication of predictability. It is clear from Figure 68 and 69 (top) that model integrations (colored lines) considerably deviate from observations (black line). The observed integration errors appear to be clustered in certain periods of time. The top and middle diagrams indicate that the forecasts particularly deviate from observations during periods of maxima ISO activity and corresponding to positive convective anomalies (negative OLR anomalies). For all the regions, the middle panel

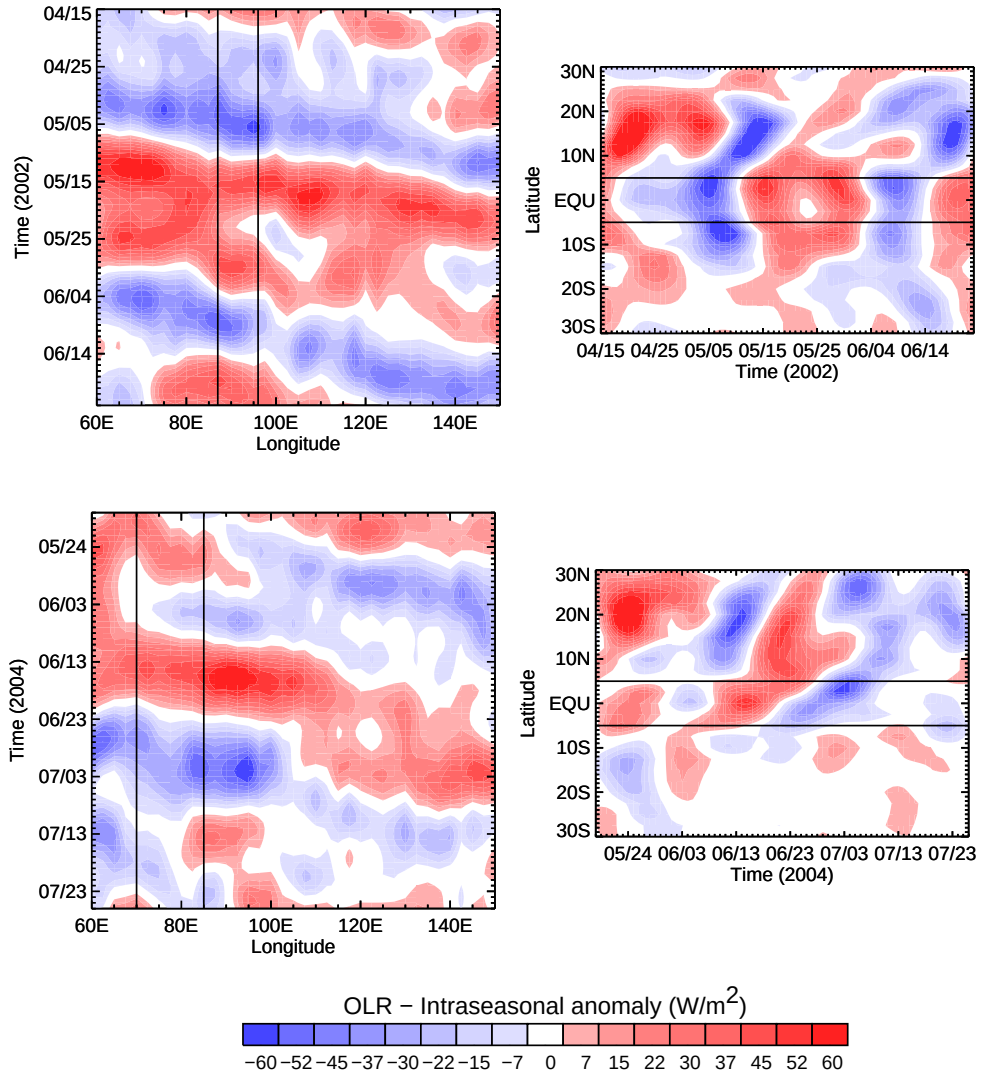

Figure 66: Longitude-Time and Time-Latitude diagrams of the observed Intraseasonal OLR anomalies during the 2002 (top) and 2004 (bottom) experiments periods.

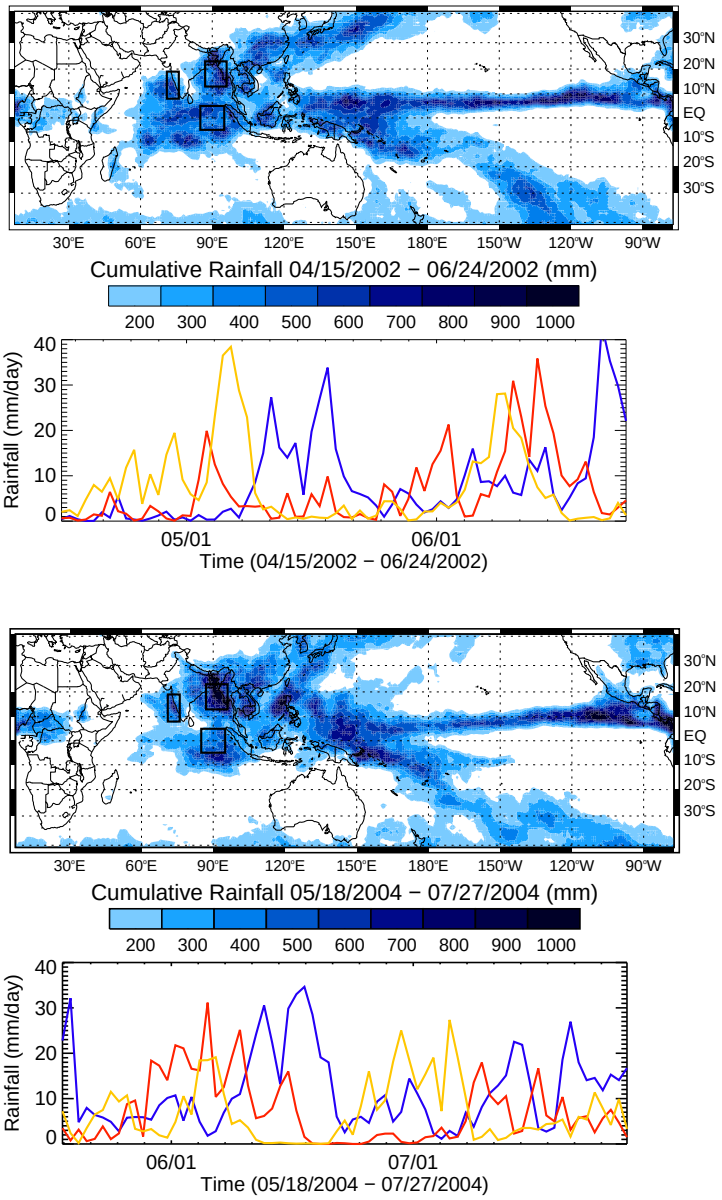

Figure 67: Cumulative rainfall (from daily GPCP product) during the numerical experiment period and rainfall time series for Indian Ocean (Orange, 85-95°E 5°S-5°N), Bay of Bengal (Blue, 85-95°E 10-20°N) and Western Ghats (Red, 70-75°E 10-20°N). The top panels correspond to the 2002 experiment and the bottom ones to 2004.

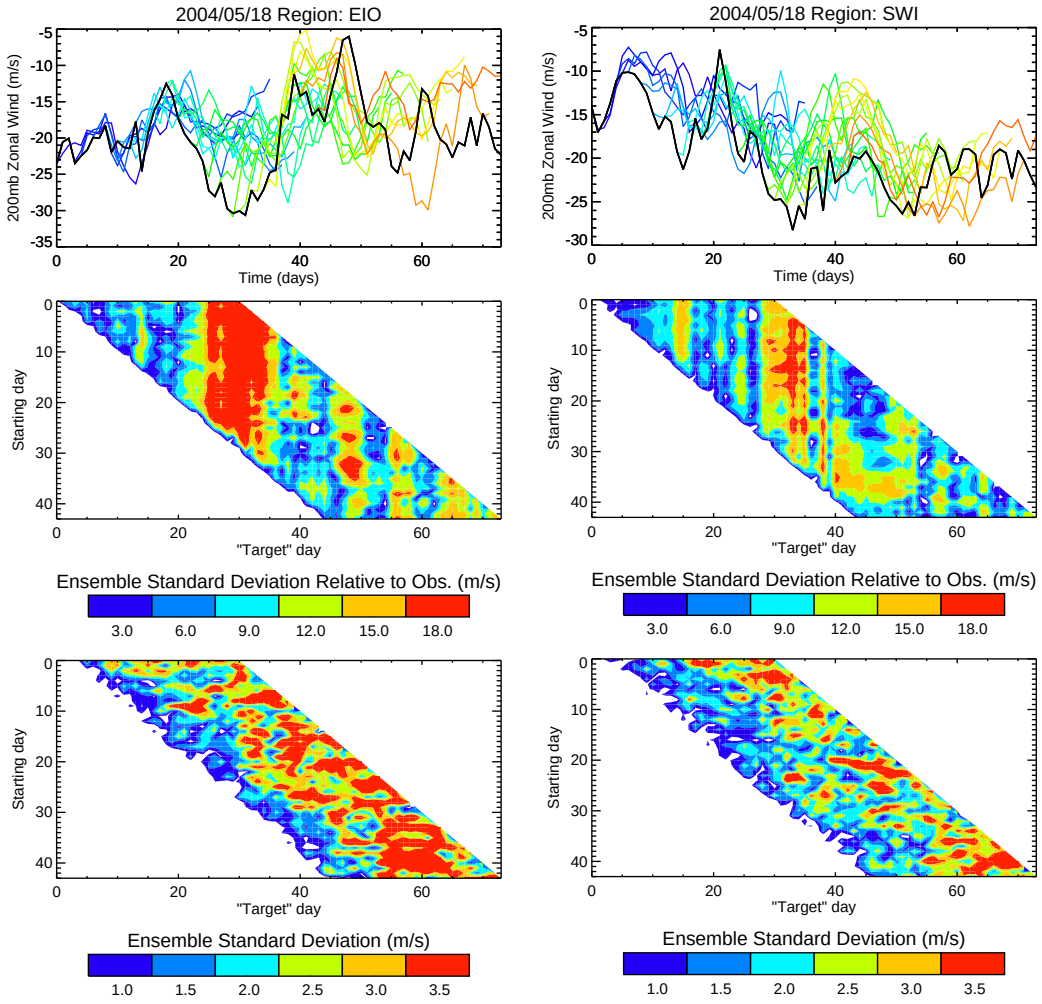

Figure 68: 200mb zonal winds ensemble forecasts for Equatorial Indian Ocean (EIO; left column) and and South West India (SWI; right column). The top dragrams show the 30-day evolution of the ensemble mean for the 2004 experiment (colored lines). The black line corresponds to the observations. The standard deviation of the ensemble members for all the succesive forecasts is shown in the middle and bottom diagrams. As an indication of the skill of the model as well as its scale of predictability, the standard deviation is computed relative to the obervations (middle) and relative to the ensemable mean (bottom), respectively.

shows periods with very marked deviation from the observations. In the diagram, these periods appear as vertical bands of high standard deviation relative to the observations (red areas) and are always associated with maximum ISO activity.

The vertical orientation of these high error regions in the diagram indicates that

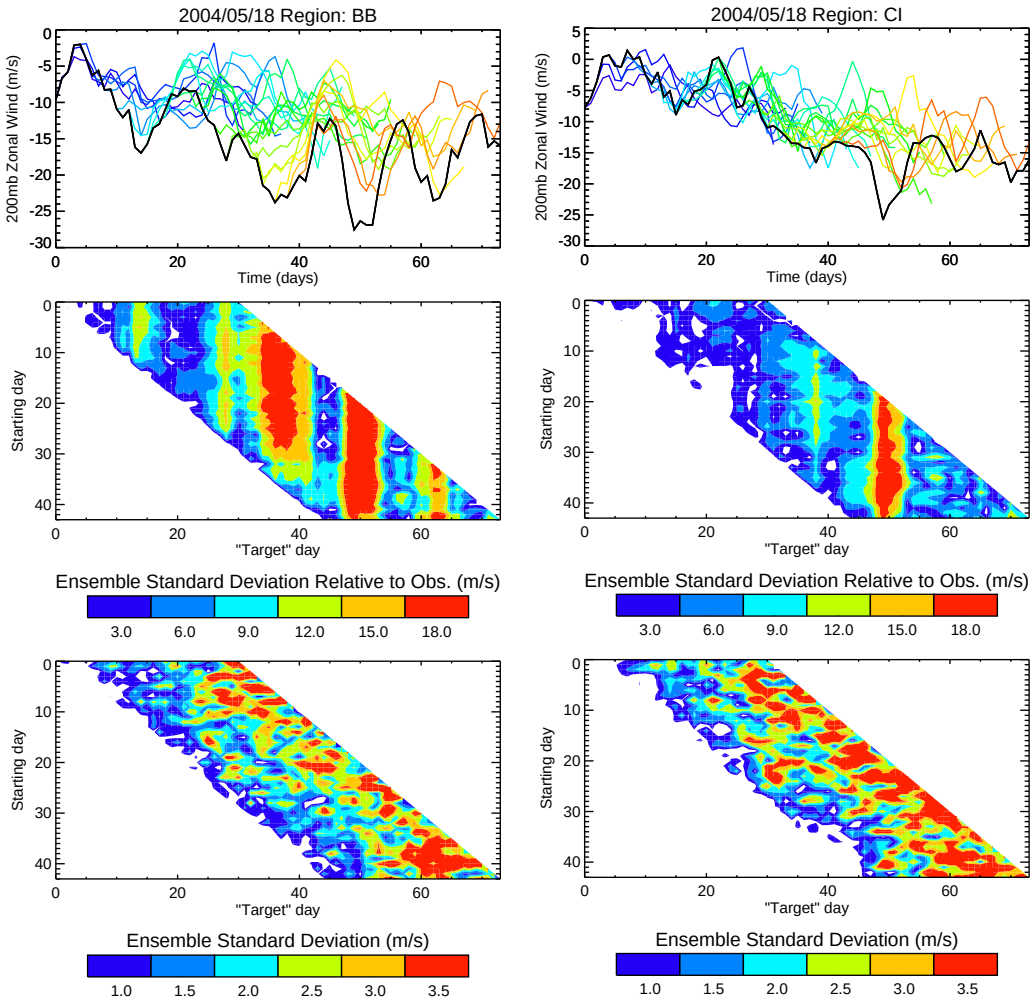

Figure 69: Same as Figure 68 for Bay of Begnal (BB; left column) and central India (CI; right column).

no matter how far ahead of the maximum ISO activity the model is initialized, the largest ensemble errors are always linked to maximum convection; e.g., for different forecast runs starting 15, 10 and 5 days prior to a maximum convective anomaly, the largest deviation from observations is going to appear around days 15, 10 and 5 respectively, indicating that the skill of the model is poor forecasting intraseasonal anomalies.

This fact does not contradict the expectation of growth of ensemble spread with the forecasting lead time due to nonlinear amplification of errors in the initial conditions in combination with uncertainties in the model itself (stochastic physics). The bottom panels of Figures 68 and 69 show how the ensemble spread grows as the forecasting lead time increases. Notice that the magnitude of the internal ensemble spread is considerably smaller than the deviation from observations during ISO maxima, indicating high reproducibility of the model. The extremely different shapes of both standard deviation diagrams suggests that integration errors linked to the ISO are not arising due to small uncertainties in the initial conditions or in the state of the art model physics in a stochastic sense. The results point to problems in the model physics but they appear not to be of a stochastic nature. For a model with improved physics, one would expect both diagrams having a very similar structure, with closer standard deviation magnitudes for models with better skill.

Figure 70 shows the correlation and standardized RMS for 200mb zonal winds and OLR at different forecasting lead times for EIO, SWI, CI and BB. The correlation and RMS were estimated using unfiltered data. The RMS is standardized by the observations standard deviation during the forecasting period. Results are shown for both summer experiments and using the full ocean dynamics and the mixed layer model. In general, the correlation decreases rapidly with forecasting lead time. RMS also changes considerably, increasing with lead time. While the general pattern is similar, correlation and RMS changes are observed between different variables and different

summer experiments. In general, results indicate that after day 7-10 the forecasting skill of the model is very poor, with RMS error comparable to the amplitude of the observed variability and not statistically significant or even negative correlations. It is important to note that the skill over CI is consistently better for all variables and both summer experiments. One possible explanation is that the amplitude of the ISO is not as high over CI as it is over EIO, SWI and BB, especially during early summer. No important differences in regional forecasting skill are seen between control forecasts and ensemble mean or between the full ocean model and mixed layer model results.

In order to estimate the forecasting skill for the entire Indo-West Pacific basin, the model results were first rebinned to a 5 degree grid to avoid collocation errors, and then correlations, RMS and ensemble spread were estimated for every grid within the basin (30°S-30°N 40°-180°E) and then spatially averaged to obtain a single value for the entire basin (Figure 71). The most important feature in the figure is the fact that the forecasting skill of the model is consistently better for 200mb zonal winds than for OLR, providing reasonably good forecasts during the first 10 days for zonal winds compared to about 6 days for OLR. This result is also true for winds at other levels, even near the surface (e.g. 925mb). As mentioned before, the ensemble spread is an indication of predictability. Clearly, the predictability time scale is longer (20-25 days) than the time scale of skillful forecasts (forecastability time scale) for both variables. The gap between the ensemble spread and the RMS can be regarded as unrealized predictability. In a perfect model, both lines should overlap.

Figure 72 shows the basin-wide analysis but restricted to intraseasonal variability. Due to the length of the forecasts (30 days) the intraseasonal variability is obtained by first removing the linear trend in the forecasts and concurrent observations followed by a 10-day moving average of the detrended time series. The linear trend corresponds to the annual cycle drift. The results possess a very similar structure to

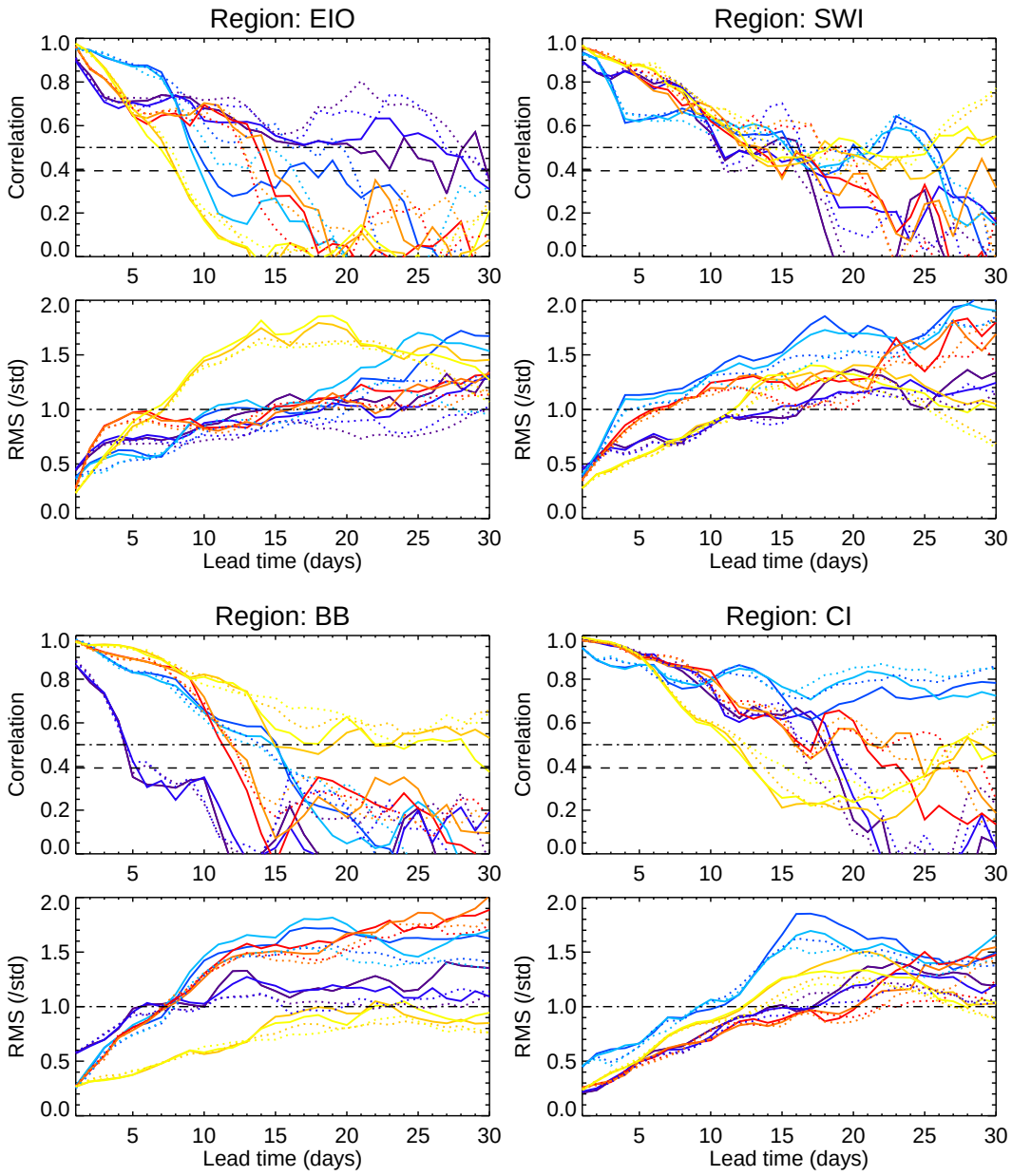

Figure 70: Correlation and standardized root mean square error estimated for 200mb zonal winds and OLR at different forecasting lead times and for both summer experiments. The RMS is standardized by the observations standard deviation during the forecasting period. The correlation and RMS is estimated relative to obervations for EIO, SWI, BB and CI. Results are shown for both summer experiments and using the full ocean dynamics and the mixed layer model The continuous line corresponds to the control forecasts and the dotted line to the ensemble mean. Blue lines correspond to OLR and yellow/red lines to 200mb zonal winds. The horizontal dashed line in the correlation diagram corresponds to the 99% significance level.

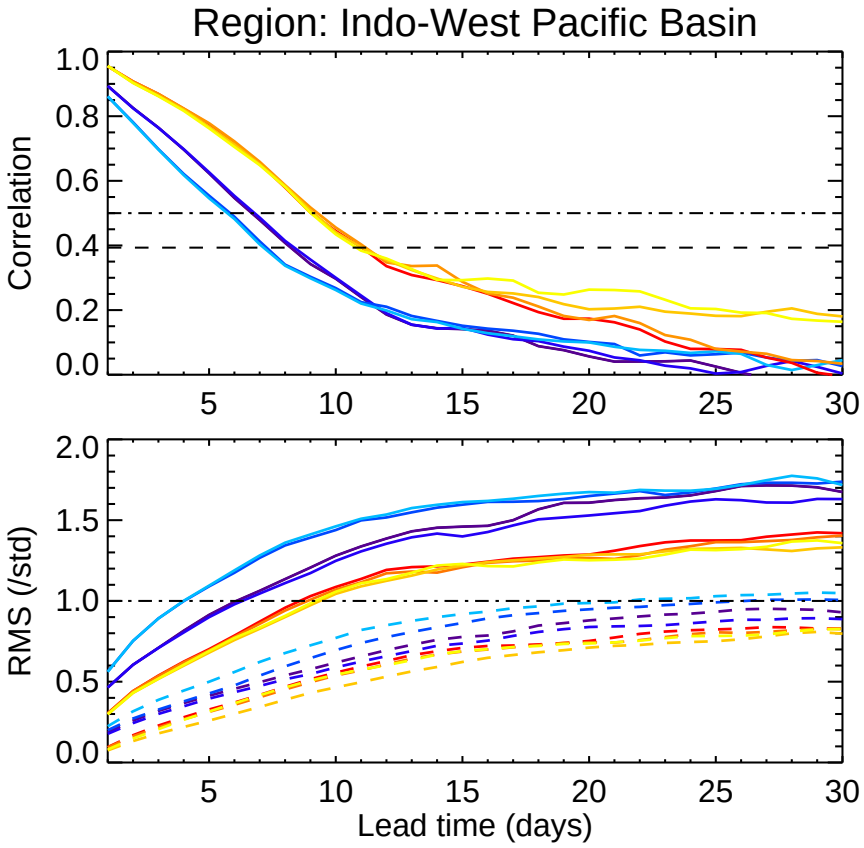

Figure 71: Average correlation and standardized RMS over the Indo-West Pacific basin (30°S-30°N 40°-180°E). Correlation and RMS are estimated for the ensemble mean over 5x5 degree cells and then spatially averaged in order to estimate the forecasting skill for the entire basin. The dotted lines correspond to the average standardized ensemble spread (ensemble standard deviation). The RMS and the ensemble spread are scaled (standardized) by the observations standard deviation during the forecasting period. Blue lines correspond to OLR and yellow/red lines to 200mb zonal winds.

that shown in Figure 71, perhaps with a forecastability scale reduced by a day or two and less separation between the zonal winds and OLR curves. The ensemble spread in this case is considerably less than the intraseasonal amplitude, further suggesting that forecasting errors associated with ISO in the ECMWF model are not the result of high sensitivity to initial conditions uncertainties. The poor ISO forecasting skill is not only evident in the phasing (correlation), and magnitude of the errors (RMS), but also in the amplitude of the simulated intraseasonal variability. The bottom diagram in Figure 72 shows, in percentage, the amplitude of the simulated intraseasonal variability relative to the observed amplitude. The simulated amplitude is in general considerably less than the observations, and it decreases with the forecasting lead time.

The analysis of the joint probability density function between (PDF) between observations and forecasts is important as it allows an examination of the structure of the forecasts at different percentiles. In addition, mutual information and joint entropy are based on the joint PDF and are useful to assess the forecastability time scale non-parametrically. Figure 73 and 74 show the joint PDF for different forecasting lead times (1, 8, 15 and 22) for 200mb zonal winds and OLR. There are two fundamental differences between both sets of PDFs: One difference is that the OLR joint PDF show considerably greater spreading (higher error). The other difference, and perhaps more important, is that while the errors in zonal winds are uniform in the entire range, and in particular for the first 8 days of the forecast, the errors in OLR are far from uniform, with considerably higher errors for low values of OLR which in the tropics are generally associated of convective clouds. A summary of all PDF 200mb and 850mb zonal winds and OLR is presented in Figure 75 in terms of information analysis and forecasting success rates.

Figure 75 shows the behavior of the mutual information and joint entropy for 200mb and 850mb zonal winds, and OLR. The figure also shows the forecast success

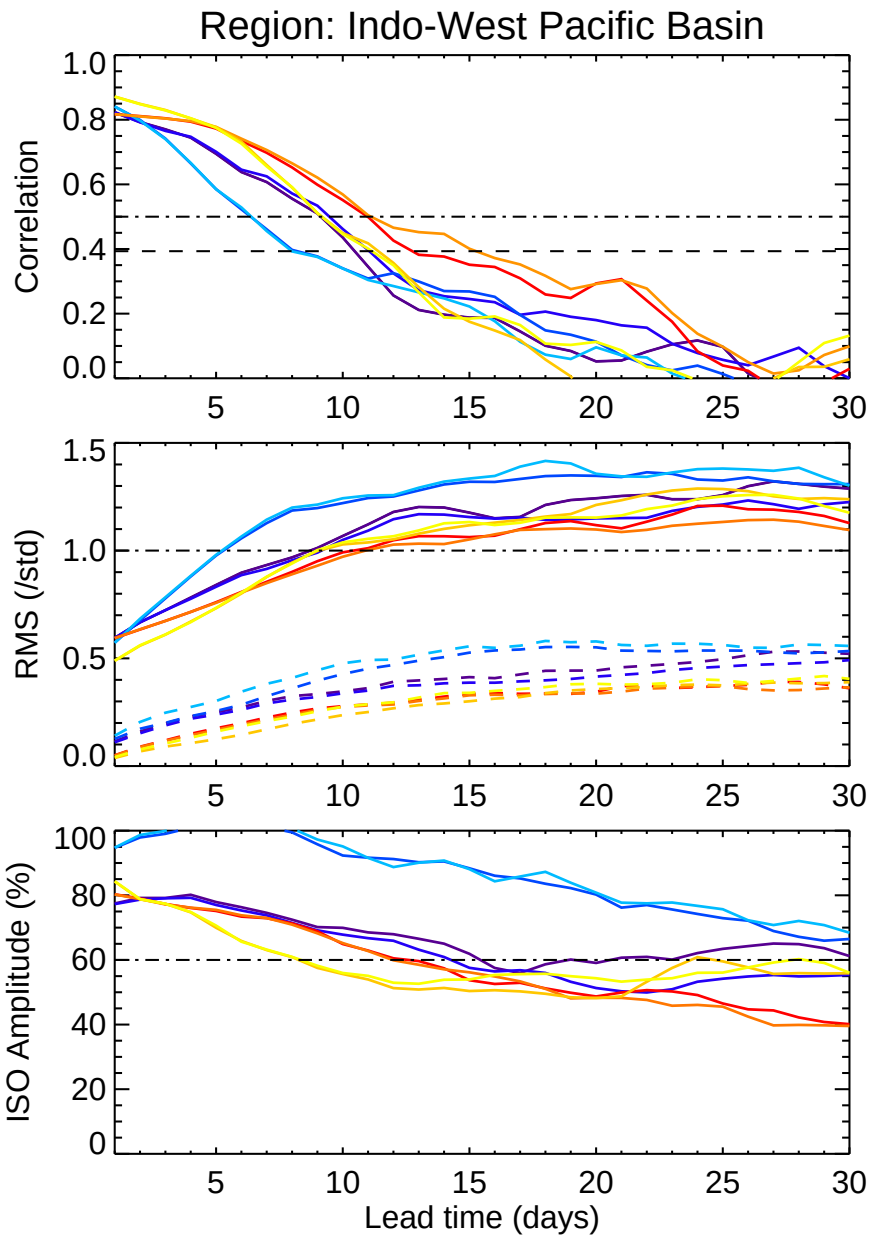

Figure 72: Similar to Figure 71 for intraseasonal variability. Due to the length of the forecasts (30 days) the intraseasonal variability is obtained by first removing the linear trend in the forecasts and concurrent observations (corresponding to the annual cycle drift) followed by a 10-day moving average of the detrended time series. The bottom panel shows the intraseasonal amplitude in the forecasted time series relative to that in the observations (recovered intraseasonal variability).

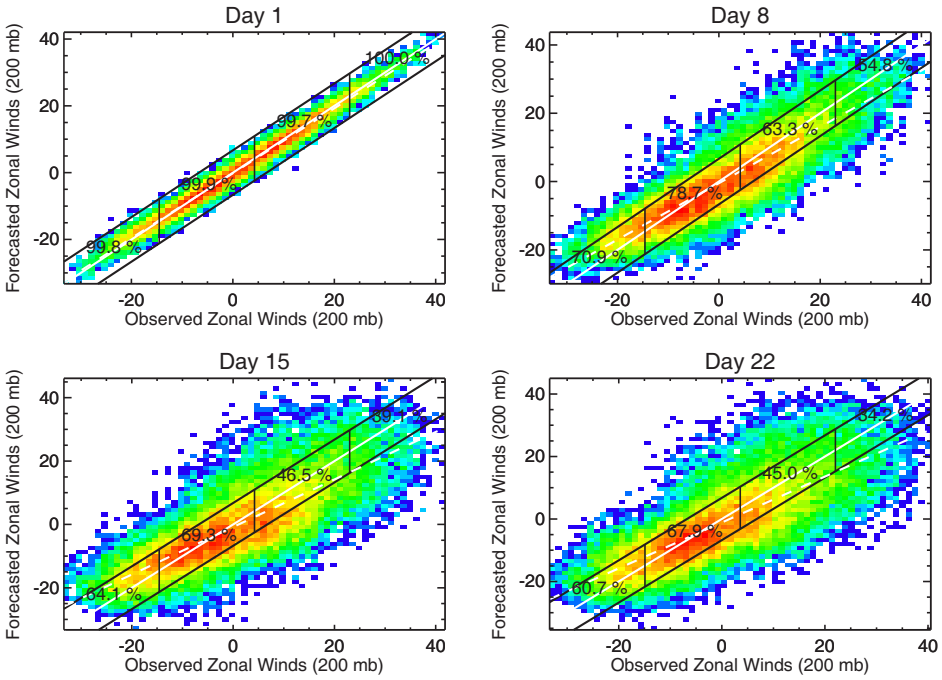

Figure 73: Joint probability density function between observed and forecasted 200mb zonal winds for different lead times (1, 8, 15 and 22) over the entire equatorial region (20°S-20°N 0°-360°E). The probability density increases from blue to red. The with continuous line corresponds to perfect forecasting and the dashed line to the actual linear fit between forecasts and observations. The black lines correspond to half standard deviation of the observations. The entire range is divided in four equal-area regions and the success rate in each area is studied.

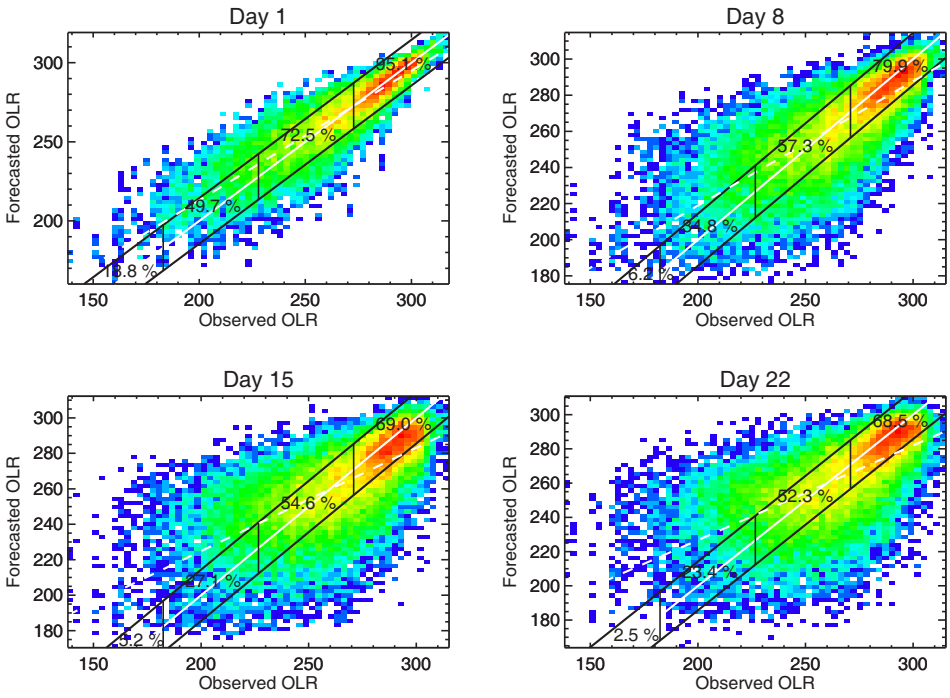

Figure 74: Joint probability density function between observed and forecasted OLR. See Figure 73 for details.

rate in four non-overlapping equal area regions. The areas are defined as one quarter of the variable range (from minimum to maximum) by one standard deviation of the observations (standard deviation). In this context, a forecast is regarded as successful if both the observation and the forecast fall in the same area. The success rate is then defined for each area as the ratio between the number of success forecasts and sum of successes and failures. From the mutual information and joint entropy diagrams, it is clear that while having a similar forecastability time scale (about 10 days, where the curve reaches a constant value), the information shared by observations and forecasts is less for OLR than that for zonal winds, even during the first 10 days. In other words, from the forecasts one has more information about circulation than convection. It is in this context that a hybrid empirical forecasting approach makes sense in order to achieve the same scale of forecastability for OLR and other fluxes. It is also clear that the success rate of OLR strongly depends on the actual magnitude. Low

values of OLR are poorly forecast while high values are better forecast. In other words, the model simulates the suppressed conditions better than transitional and convectively active conditions, supporting the findings of Agudelo et al. (2006). For zonal winds, there is a difference in the success rate relative to the area, but not as strong as for OLR. This difference is more notorious after the forecastability scale, with lower success rate for high magnitude westerlies, which statistically correspond to rare events.

A range of evidence has been presented suggesting that the model has skill problems associated with convection, and in particular, convection linked to an intraseasonal event. It is also clear that the skill of the model in forecasting ISO is poor. In addition to previous statistical estimations, the spatio-temporal distribution of the standardized RMS errors and correlation between forecasts and observations is also analized. Figure 76 and 77 show the spatial distribution of the standardized RMS errors of 200mb zonal winds for the summer 2002 and 2004 experiments for the first 8 days of the forecast and Figures 78 and 79 show the spatial distribution of the correlations fro the same variable. The spatial distribution of the errors and lower correlations of 200mb zonal winds for Days 1 and 2 are remarkably similar in both cases the cumulative precipitation distribution shown in Figure 67. This feature indicates that errors, even in the circulation, quickly appear in convective regions in the tropics. After Day 1 and 2, errors grow from the convective regions, covering the entire tropics, eroding the development of an intraseasonal oscillation.

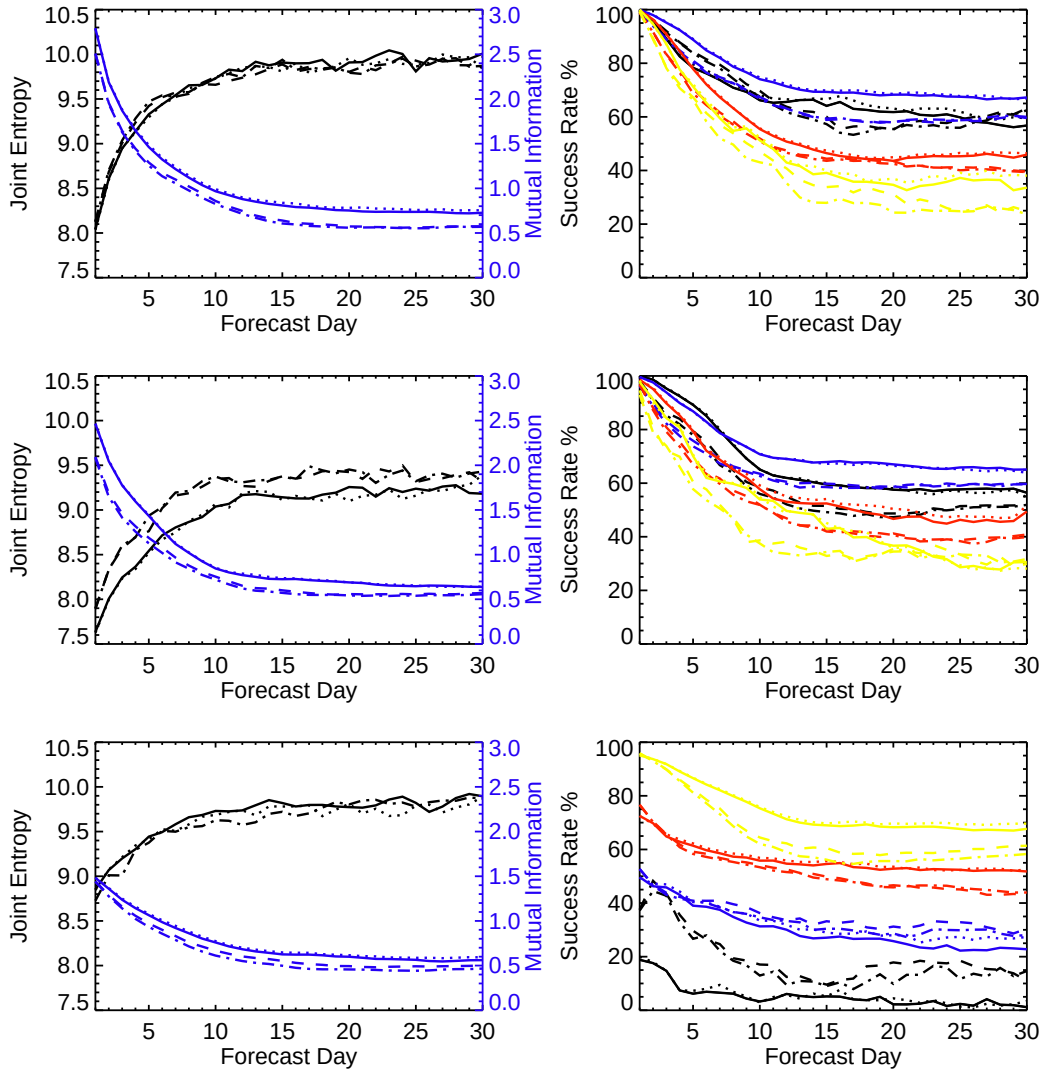

Figure 75: Behavior of the mutual information (blue) and joint entropy (black) for 200mb (top) and 850mb (middle) zonal winds, and OLR (bottom). In the left column, the success rate in four non-overlapping equal area regions is shown. See boundaries of the areas in Figures 73 and 74 and details in the text. In order, the black, blue, red and yellow lines correspond to first, second, third and fourth areas. From first to fourth, the areas cover the entire variable range from low to high values. The solid, dotted, dashed and dash-dotted lines correspond to the 2004-full ocean, 2004-mixed layer, 2002-full ocean, and 2002-mixed layer summer experiments respectively.

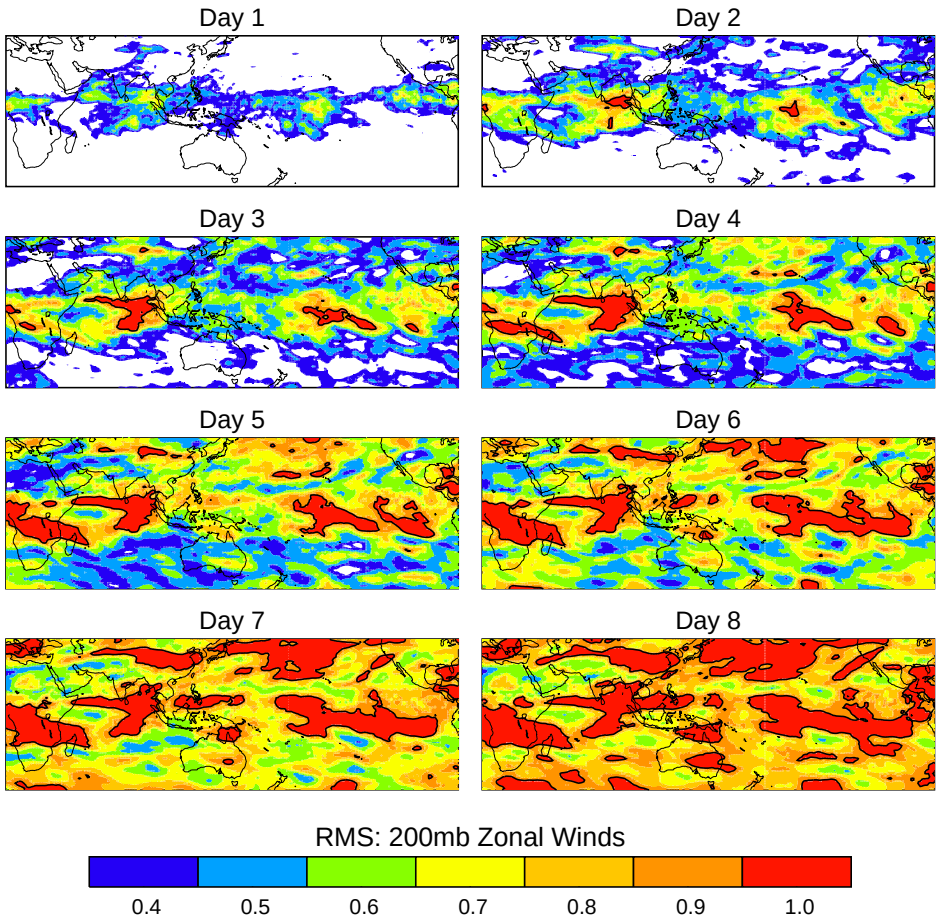

Figure 76: Spatial distribution of the standardized RMS for the summer 2004 experiment for different forecast lead times.

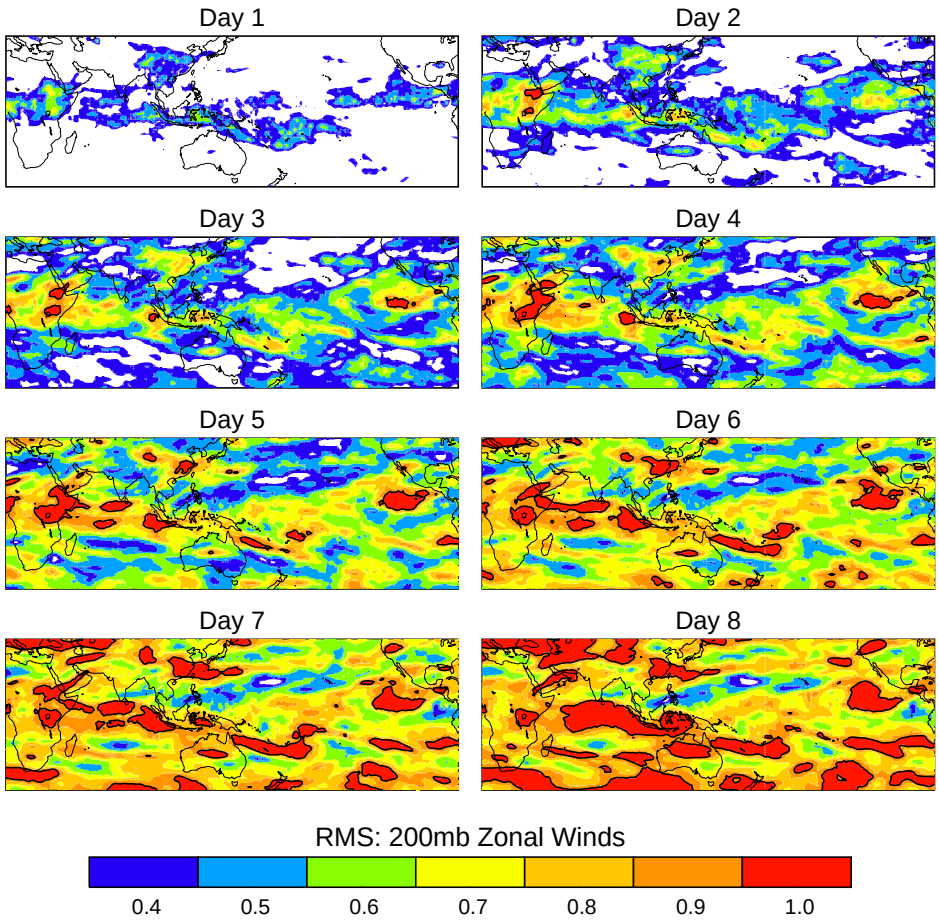

Figure 77: Similar to Figure 73 for the summer 2002 experiment.

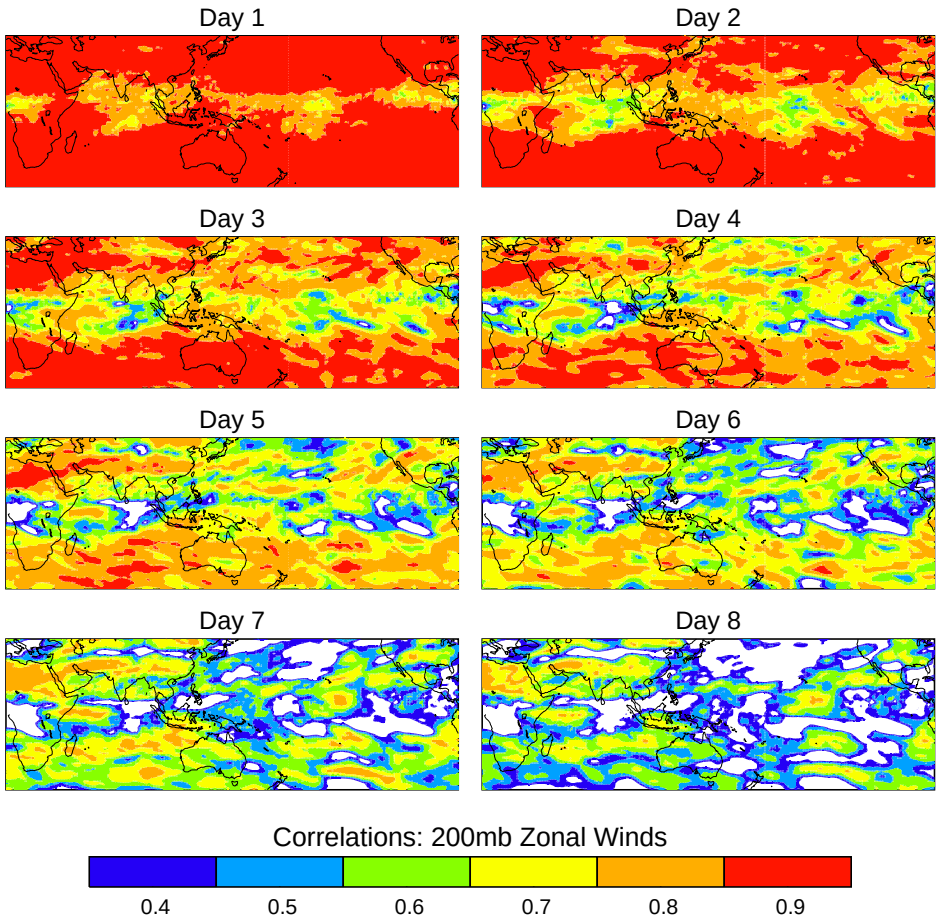

Figure 78: Similar to Figure 73 for correlations corresponding to the summer 2004 experiment.

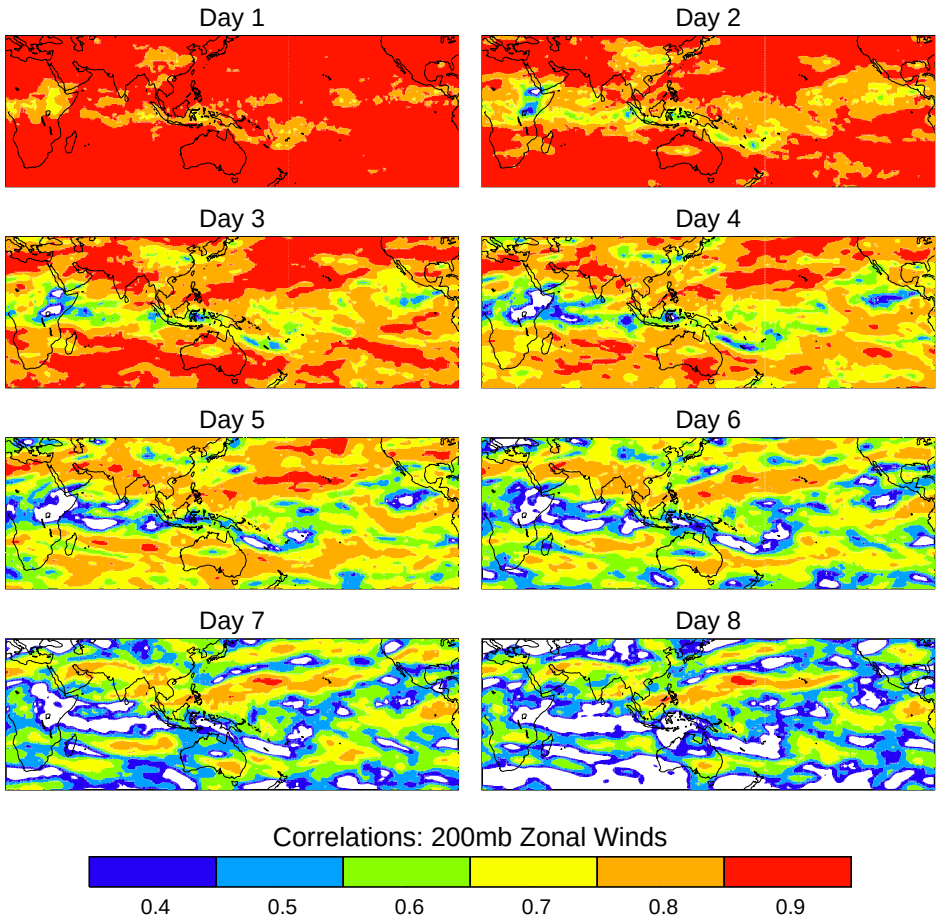

Figure 79: Similar to Figure 73 for correlations corresponding to the summer 2002 experiment.

CHAPTER VI

SLOW MANIFOLD MODELING: A NEW APPROACH TO SIMULATE ISO.

It has been shown that the coupled ECWMF model, a state of the art forecasting climate model that has been extensively used and tested, is not able to reproduce skillfully the convective and circulation anomalies related to the ISO, and that most likely the deficiencies of the model are due to its inability to correctly simulate the low-frequency anomalies of convection. Agudelo et al. (2006) showed that the ECMWF model does not reproduce the observed CAPE build-up and low-level moistening of the atmosphere during the transition from suppressed to active convection during an ISO event. In addition, as shown in the previous chapter, model errors originate in highly convective regions affecting not only variables directly linked to precipitation and convection but also introducing errors in the circulation. The culmination of these factors is that the intraseasonal variability in the model fails to develop. All evidence points to the model convective parameterization as the potential source of errors.

In the light of the model's inability to simulate correctly intraseasonal variability, and given that this is a common feature in all models and thus independent of a particular convective parameterizations, different strategies could be followed in order to overcome this issue. One strategy is to simply use empirical techniques to forecast relevant atmospheric variables since these techniques currently provide better forecasts (e.g. Webster and Hoyos 2004). However, to the date, all empirical techniques

are tailored to specific problems and hence are limited because they are either designed to forecast regional and not global intraseasonal or only provide the forecast of a single variable or a single orthogonal. While the empirical approach is important and a skillful technique constitutes an important step in the understanding of the problem, given the wide range of ISO related impacts and teleconnections, the goal is to provide dynamically consistent forecasts for the entire globe and that can only be achieved by using numerical models.

Another approach is to reduce convective parameterization errors by explicit cloud modeling in each grid box of the forecasting model such as the "super-parameterization" scheme suggested by Randall et al. (2003). During recent years the tendency in numerical prediction has been to increase spatial resolution as well as including cloud resolving processes in global models. Whereas this is an important step in atmospheric sciences and could potentially be successful in the future, the computer requirements to produce operational forecasts are prohibitive at the present time. Randall et al. (2003) estimates that there would be a thousand fold increase in computer time for the inclusion of a two-dimensional cloud resolving scheme and even higher order of computation power increases for three dimensional schemes.

It is then prudent to explore other methods that move towards simpler modeling rather than following the higher resolution explicit physics route. Given the success of empirical schemes such as the wavelet-banding scheme presented in Chapter 4 and the fact that high-frequency errors introduced by the convective parameterization erode the ISO in large scale numerical models, it is tempting to try to mimic in models the filtering ideas used in the Webster and Hoyos 2004 empirical approach. In this alternative strategy, the idea is to minimize the impact of the high frequency convective parameterization error while, at the same time, incorporating into the model the correct statistics of the convective heating, with the hope that this in turn would help to develop and maintain the vertical circulation anomalies closer to

observations. The hypothesis is that if the low-frequency modes can be "protected" from the noise of high-frequency errors (such as in the wavelet-banding method) by introducing a simple filter within the integration scheme, it may be possible to extend intraseasonal forecasts. This type of modeling is referred to as "slow manifold modeling" (SMM).

Krishnamurti et al. (1990, 1992, 1995) tested a similar procedure for the extended prediction of 30-50 day tropical modes. It was hypothesized that a major limitation of extended forecasting arose from the contamination of intraseasonal modes by energy exchanges higher frequency modes associated with the manner in which convection was parameterized in models. By only using low-frequency band passed initial data, the Krishnamurti studies found increased skill in forecasts out to 3-4 weeks (e.g., Krishnamurti et al. 1990). These studies are important because they show that reduction of convective noise increases the forecasting skill of the low-frequency modes. However, in the Krishnamurti et al. (1990) scheme, the same convective parameterization schemes were used in the forecast stage and these introduced high frequency errors after the initialization, allowing rapid "contamination" to occur.

As a first attempt to overcome the problem described above, is to develop an experimental scheme using the ECMWF model was developed with modifications not only to the initial data but also every day during the integrations. In this manner it is hoped that the secondary contamination found by Krishnamurti et al. (1990, 1992, 1995) would be avoided. The proposed integration scheme is shown schematically in Figure 80. To visualize the scheme, it is useful to consider a 30-day forecast starting at day D. Instead of using the standard initial conditions, i.e. a dataset describing the current state of the atmosphere and ocean obtained from many different sources in combination with an assimilation technique, the initial data for the forecast is constructed using data from $(D - N)$ to D, where N is a time interval (say 5 days) over which the data is averaged and centered on day $(D - N/2)$. All fields and

forcing functions are averaged in the same way. The goal is to select N so it matches a convective decorrelation time scale. The model is advanced to day $(D+1)$, and a new initial state is created using data from day $(D+1-N)$ to day $(D+1)$, the latter being the newly forecasted day. This initial state is centered on $(D+1-N/2)$. The model is run using these averaged fields to produce a new forecast for day $(D+2)$. This scheme is continued until reaching day (D+30). In summery, in order to forecast day $(D+T)$, the initial conditions used are the average fields from day $(D+T-1-N)$ to day $(D+T-1)$. If $T \leq N+1$, the initial conditions are a combination of data coming from the operational analysis and initial forecasts obtained using the SMM scheme. For $T > N+1$, all the fields being averaged correspond to forecasts.

To the date, three 30-day runs have been conducted starting June 1 2004 using N=3, 5 and 7. This particular date correspond to one day of the serial runs described in the previous chapter, allowing the comparison of the SMM scheme with the coupled model performance. Results of the three experiments are similar, with slightly better results for N=3 and 5. Figure 81 shows a regional evaluation of the SMM over South West of India compared to the ECMWF couple model simulations. Results show that all the ensemble members of the ECMWF couple model run reproduce accurately the observations during the first 10 days of the integration, after which it diverges from the observations during the convective anomaly (Days 25-35). In contrast, the SMM run with N=5 captures remarkably well the amplitude and phase of the intraseasonal variability.

In order to evaluate the SMM scheme relative the basin-wide features of the ISO event, including the eastward and northward propagation of convective anomalies, Longitude-Time and Time-latitude diagrams of intraseasonally filtered OLR (Figure 82) and 200mb zonal winds (Figure 83) were constructed during the period of integrations (30 days after June 1 20004) for observations, control run of the ECMWF coupled model and the SMM run using N=5. OLR from NCEP and 200m zonal

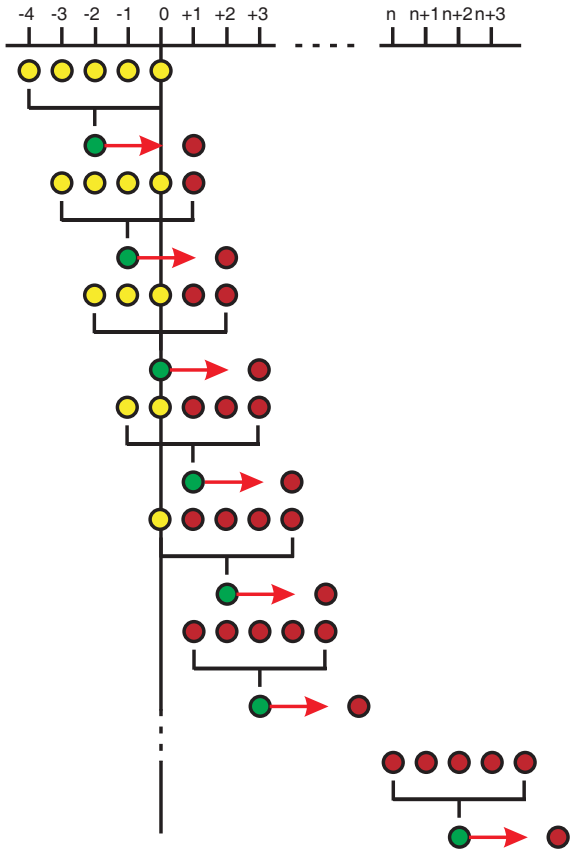

Figure 80: Schematic diagram of the slow manifold modeling (SMM). The integration scheme uses average initial data over certain period of time rather than the current assimilation at the time of the observations. The model is further integrated through the forecast period using new initial data calculated at each step using past data and data from the new prediction.

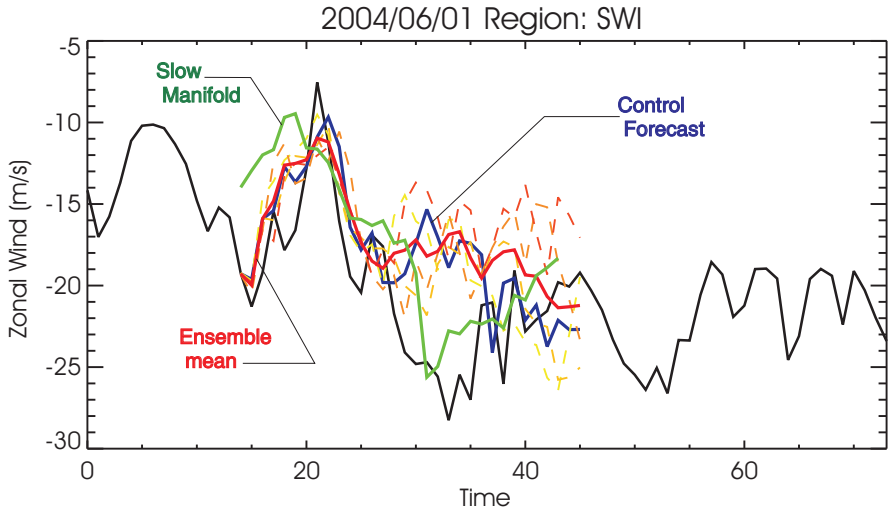

Figure 81: 200mb zonal winds results over South West of India. The figure shows the observations (black), the control forecast (blue), the ensemble mean (red) and each of the ensembles.

winds from the ECWMF operational analysis were used in comparison. It can be easily seen in the diagrams that the ECMWF coupled model run does not capture the observed eastward propagation of OLR and 200mb zonal winds anomalies. In fact, the ECMWF mode generates what appears to be a westward propagating convective event from the Maritime Continent into the Indian Ocean. The negative convective anomalies were properly simulated for about 10 days when the eastward propagation was interrupted by the above mentioned westward propagating event anomalies. The structure of the wind anomalies in the ECMWF model run appears almost out of phase with the observations. As mentioned in the previous chapter, the ECMWF run seems to capture the northward propagation over the Indian Ocean, although with a much smaller magnitude. On the other hand, the SMM run seems to capture reasonably well both eastward and northward propagation of OLR and zonal wind anomalies. The northward propagation occurs in the SMM run with very similar phase speed to the observations, while the resulting eastward propagation is somewhat slower than observed. While the results are in general similar for N=3, 5 and 7, the speed of the propagation appears to change be faster for N=3. Figure 84 shows

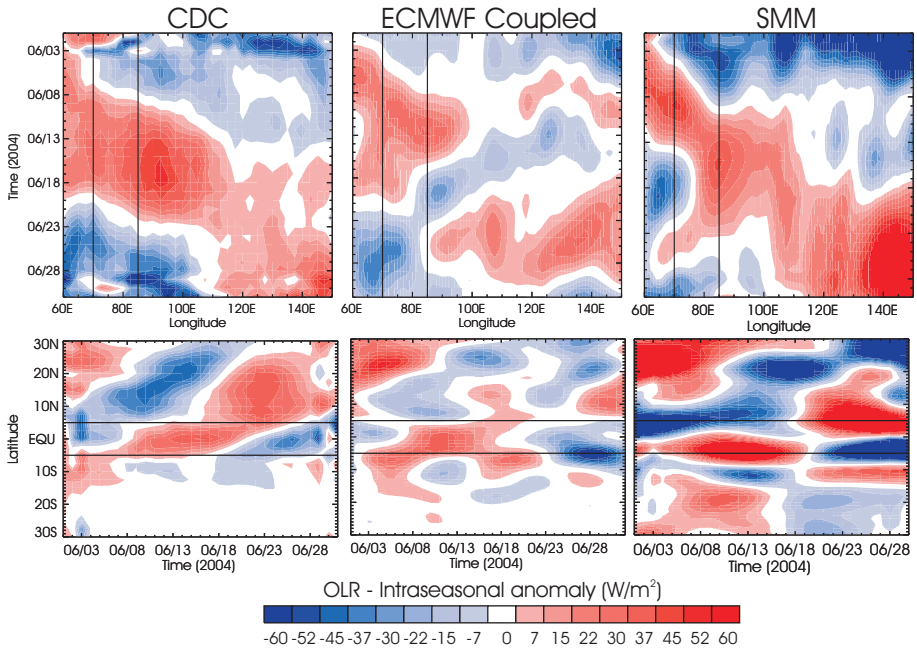

Figure 82: Time-Longitude and Time Latitude diagrams of intraseasonal OLR for the satellite observed OLR (left column), SMM integration for N=5 (middle) and the control forecast part of the serial integrations (right).

the Longitude-Time diagram of intraseasonal OLR for SMM runs with N=3, 5 and 7.

While the results are encouraging, the integrations described above represent the first attempt at slow manifold modeling and raise a number of important questions. Among the outstanding questions is the determination of the optimal value for N. Currently, SMM experiments are being extended in order to match the serial runs described in the previous chapter.

In addition to these experiments, a long term (multi-year) integration using the SMM scheme is required in order to generate statistics that could be compared with observations and the ECMWF coupled model without modifications. One important question is to see whether or not the SMM integration develops an intraseasonal spectral peak, since the ECMWF coupled model does not. In collaboration with Dr. In-Sik Kang and Hyemi Kim from Seoul National University, a 3-year slow

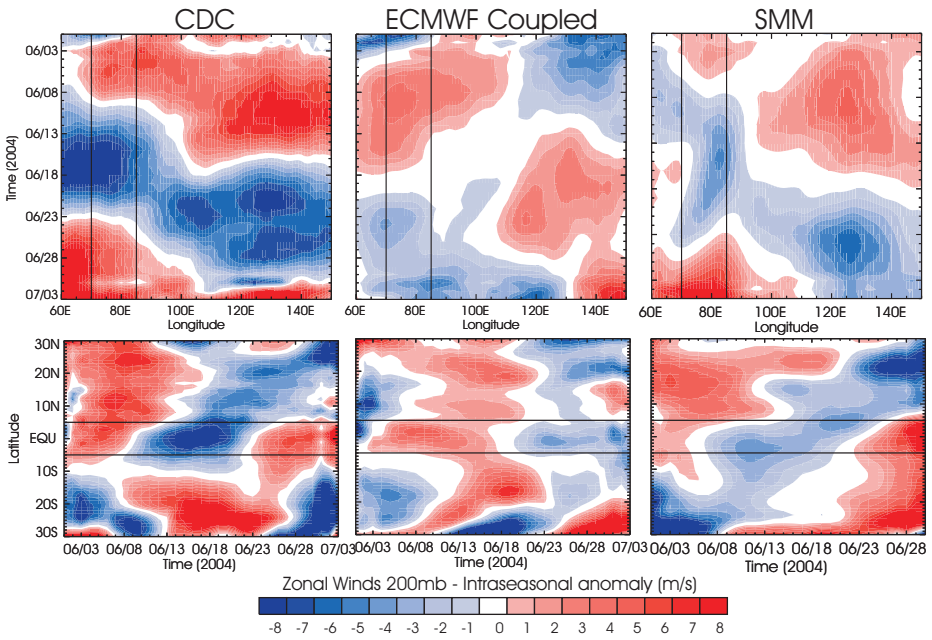

Figure 83: Same Time-Longitude and Time Latitude diagrams as in Figure 82 for 200mb zonal winds

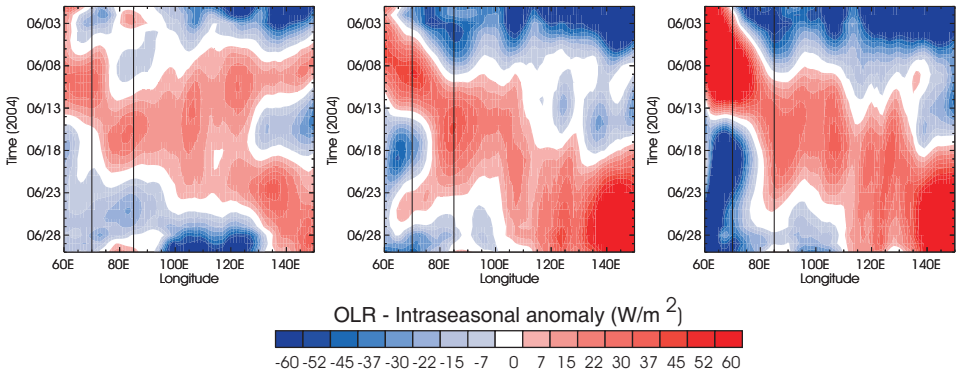

Figure 84: Time-Longitude of intraseasonal OLR for three SMM with N=3, 5 and 7 (left, middle and right respectively).

manifold run was performed using an atmospheric GCM with observed SSTs. Results show that the SMM integration method substantially improves the magnitude and spatial distribution of the variance in the intraseasonal band compared to a similar integration using the same model without the SMM scheme (Figure not shown).

There are a number of advantages to the SMM scheme. First, it does not require any modification of the forecasting climate model except the use of a module for the recalculation of new initial fields at the end of each forecast day. Second, the scheme appears to minimize the impact of incorrect convective parameterization that occurs on the time scales of hours. At the same time emphasizes the forcing produced by the integrals of the forcing. Inherent in this assumption is that the convective errors are high-frequency and the averaging of the initial fields effectively reduces the error. Substantial experimentation is required in order to show that this is the case. If the SMM does constitute an improvement to extended forecasting, its relatively simple design allows its implementation as part of an operational framework.

CHAPTER VII

CONCLUSIONS

Intraseasonal variability, with a local time scale between 25 to 80 days, constitutes a very important and coherent mode of oscillation in the climate system, in particular in the tropical environment. The amplitude of this mode of variability is particularly strong over the Indian Ocean and the Western Pacific, extending over South Asia during the boreal summer and over Australia during the boreal winter. The present work constitutes a comprehensive study of the intraseasonal variability observed in the ocean-atmosphere system, including contributions on ISO diagnostics distinguishing between boreal summer and winter, as well as contributions towards empirical and numerical ISO forecasts.

A variety of data sources, including several reanalysis and satellite data bases, were used to study details of the spatiotemporal structure of the observed ISO during winter and summer separately by estimating the composite life cycle of the oscillation. The selection of strong intraseasonal events is the basis for compiling useful diagnostics. During winter, the propagation of the ISO is predominantly eastward over the Indian Ocean, while during summer northward propagation of convective anomalies towards South Asia is an integral part of the oscillation. It was shown that during winter, the oscillation also contains a bifurcation of the sea level pressure anomalies, with a marked southward propagation into the South Pacific Convergence Zone. The structure of the eastward propagating oscillation strongly resembles that of a Rossby-Kelvin packet. It was also shown that due to the structure of the upper troposphere ISO anomalies, present during both active and suppressed phases, the cyclones/anticyclones located to the east of the convective anomaly reach the Americas

potentially acting as a tropical teleconnection.

Evidence of the strong coupling between the ocean (SST) and the atmosphere during the ISO was also discussed. It was shown that regions with high intraseasonal variability coincide very well with regions with long-term mean SST above 28C. When the SST is high, the source of the energy necessary to maintain the moist convection observed in association to the ISO is provided as well as the source of instability. Thus, from the climatology point of view, the only region in the globe where sustained enhanced convection for extended time periods can take place is the Indian-West Pacific Ocean basin.

When a positive anomaly of SST develops over the Indian Ocean, a subsequent convective anomaly follows. The time needed to destabilize the lower troposphere through the warming of the SST, due to enhanced downward solar radiation during the suppressed phase, and the cooling of the upper troposphere due to enhanced long-wave cooling over the Indian Ocean is the determinant of the local timescale of the ISO. This also implies that the depth of the oceanic mixed layer is very important for the ISO timescale. The zonal circulation established by the convection over the Indian Ocean is such that it generates a region of strong subsidence over the Western Pacific, favoring an increase of SST, and the following destabilization of the atmosphere. High SST over the West Pacific in combination with subsidence results in the low-level moistening of the atmosphere and the build-up of CAPE, preconditioning the atmosphere for deep convection. While these processes lead to convection over the western Pacific, the cloudiness associated with convection over the Indian Ocean reduces the solar radiation reaching the surface, cooling the surface of the ocean, switching off the convective anomalies. This results in the apparent eastward propagation of the large-scale convective center of the MJO due to consecutive development of new convective systems, each on average slightly to the east of the previous one. Some of these ideas arising from the composite analysis need to be

tested using regional or global numerical coupled models.

The impacts of ISO are acknowledged as important in different regions around the globe. Perhaps one of the most important impacts is the modulation of the summer South Asian monsoon generating active and break periods. In addition, the ISO plays a determining role in the long-term average spatial structure of the precipitation as well as introducing internal interannual variability.

Many studies have tried to establish a relationship between the seasonal monsoon rainfall and external factors such as ENSO to explain the interannual variability of the monsoon. Over a 150 year period, about 30% of the variance can be explained by different ENSO indices, with El Niño normally associated with below-average summer Indian precipitation and La Niña with above-average summer rains (e.g. Shukla and Paolino 1983). However the correlations between these two phenomena have changed considerably over the last few decades. Furthermore, it was shown that there is a lack of regional coherence on interannual time scales in the Asian monsoon, due to the large internal monsoon variability introduced by the MISO. In fact both the amplitude and the distribution of the cumulative MISO-related rainfall strongly varies from year to year, constituting the most important internal monsoon interannual variability. To a large degree, this internal intraseasonal variability explains many important features of the seasonal rainfall distribution.

It was noted that large scale ocean-land temperature gradients cannot explain the mean seasonal precipitation patterns and is especially unrelated to the BoB precipitation maximum. However, the strongest MISO signal occurs over the BoB following the bifurcation of the near-equatorial convective anomalies to the west of Sumatra. After the northward propagation of the low pressure system, the center of the low is positioned over India, generating cyclonic circulation that tends to drive moist air towards the Burma mountain range, which possesses an average elevation of about 1800 m. The upslope flow considerably enhances rainfall in the northeast corner of the Bay

explaining much of the observed seasonal maximum parallel to the mountains. The mountains of Burma do not seem to play a defining role in the MISO evolution itself, nor in the northward propagations but it would seem that they directly influence the cumulative MISO associated rainfall and, hence, the magnitude of the observed seasonal rainfall. Other studies (Grossman and Durrand 1984, Grossman and Garcia 1990, Xie et al. 2005) have noted the importance of orographic features in the spatial organization of the monsoon rainfall. However, where this study differs in particular is that it considers the interaction of orography with a variety of circulation patterns of different time scales. Xie et al. (2005), for example, used monthly precipitation thus excluding by this choice important intraseasonal time scales. The determination of the interaction between the MISO and orography is an important result since it suggests that in order for the climate models to reproduce the observed seasonal monsoon rainfall structure, they would need to simulate better the intraseasonal activity observed and also be able to include the important effects of tall narrow mountains.

It is quite possible that due to the sensitivity of the models to initial conditions and the nonlinear nature of a MISO event, even perfect models will not be able to forecast more than one MISO event ahead of time. As a consequence, the full MISO activity during the summer season cannot be completely anticipated. However, because of the regular and coherent nature of the MISO, in order to estimate better the spatial structure of the seasonal rainfall, a summary of the statistical nature of intraseasonal activity prior to the summer season may help. Such a statistical quantification of the MISO would have to come from a model that is able to sustain intraseasonal variance with a magnitude similar to that observed.

This study of the intraseasonal variability has provided some key aspects that help in understanding the processes that determine the seasonal distribution of summer and winter rainfall. While the large scale dynamical features of the ISO appear to be very robust, much work is still required to understand the role of the background

state on individual intraseasonal event propagation.

It has been argued that the optimal time scale for practical applications, in particular in agriculture is about 15-25 days. Forecasts at longer time scales (e.g., the mean summer rainfall over the entirety of India) have a smaller practical value than forecasts of the intraseasonal variability because of downscaling problems. A relatively simple statistical scheme based on the physical components of the intraseasonal oscillations is able to produce forecasts with considerable skill on time scales that are useful for applications. Whereas a careful choice of the predictors is a necessary condition, it is not sufficient to produce skillful forecasts. The determining feature of the method is the use of wavelet banding. Simply, the scheme works because of the careful choice of predictors and the separation of frequency bands that does not permit noise in one band to influence signals in another band.

For applications, the probability of an event occurring is an essential component of a forecast because it allows a cost/loss analysis to be made. A necessary extension of the wavelet banding scheme is to take full advantage of the Bayesian structure of the model and develop probability density functions for each forecast. Among all possible ways of obtaining skillful probability forecasts, the so-called hybrid approach, in which the banding technique is used in combination with ensemble integrations of operational general circulation models (10-day lead time), deserves careful attention not only because it allows the generation of a PDF but also because the way it is designed can be used to improve the 10-day forecast of OLR and rainfall in the model forecast since the banding technique strongly relies on circulation fields which are forecasted with better skill.

One of the great challenges in meteorology and climate is the accurate numerical modeling and prediction of the MJO or, more generally, intraseasonal variability. In general, state-of-the-art climate models are not able to reproduce the observed ISO statistics. A serial integrations experiment was designed to evaluate the extended

forecasting skill of the ECMWF operational model. The experiment allows the evaluation of the model skill throughout the entire life cycle of selected ISO events. Different statistics (correlation, RMS, mutual entropy and success rate) indicated that the model is not able to forecast the ISO anomalies most likely due to errors introduced by convective parameterizations. Furthermore, the forecasting skill appears considerably higher for circulation variables like zonal winds at different levels than for OLR. A very low skill or success rate is associated with low values of OLR. In addition, the ensemble members deviate the most from observation during convective ISO stages.

In the light of the model's inability to simulate correctly intraseasonal variability, and given that this is a common feature in all models using diverse convective parameterizations, different strategies could be followed to overcome this issue. During recent years the tendency in numerical prediction has been to increase spatial resolution as well as including cloud resolving processes in global models in order to improve extended forecasts. However, the computer requirements to produce operational forecasts are prohibitive at the present time. Given the success of empirical schemes such as the wavelet-banding scheme presented in Chapter 4 and the fact that high-frequency errors introduced by the convective parameterization erode the ISO in models, it is tempting to try to mimic in models the filtering ideas used in the empirical approach. A simple integration scheme was introduced in order to minimize the impact of the high frequency convective parameterization. The hypothesis is that if the low-frequency modes can be "protected" from the noise of high-frequency errors (such as in the wavelet-banding method) by introducing a simple filter within the integration scheme, it may be possible to improve intraseasonal forecasts. This type of modeling is referred to as slow manifold modeling. The propagation features associated to ISO activity are greatly improved. Wavelet banding and SMM both forecast intraseasonal variability with considerable skill. However, only the SMM provides 30-day daily self-consistent global forecasts.

While the results are encouraging, the integrations described above represent the first attempt at slow manifold modeling and more experiments are needed in order to confirm what appears to be a considerable improvement in forecasting skill.

APPENDIX A

DATA SOURCES

A.1 Outgoing Longwave Radiation (OLR)

OLR data from the Climate Diagnostics Center (CDC) interpolated dataset (Liebmann and Smith 1996) is used as a proxy of convection in the Tropics. The OLR data is collected by the National Oceanic and Atmospheric Administration (NOAA) polar-orbiting satellites. The daily data set has a global coverage with a spatial resolution of 2.5 degree. The temporal coverage spans from June 1974 to the present.

The data set can be obtained at: `www.cdc.noaa.gov/cdc/data.interp_OLR.html`

A.2 GOES Precipitation Index (GPI) Rainfall Products

The GOES (Geostationary Operational Environmental Satellites) Precipitation Index was developed by Arkin and Meisner (1987). The GPI technique estimates tropical rainfall using cloud-top temperature as the sole predictor. The data, available for the Tropics (40S-40N) is obtainable in monthly (since 1986), pentad (since 1986) and daily (since 1996) temporal resolution.

The data set can be obtained at:

`www.cpc.ncep.noaa.gov/products/global_precip/html/wpage.gpi.html`

A.3 Global Precipitation Climatology Project (GPCP) products

Monthly and daily rainfall products of the global merged precipitation analysis (GPCP; Huffman et al. 1997, Huffman et al. 2001, Adler et al. 2003) were used in this work. The monthly precipitation data set covers a 27-year period from January 1979 to the

present. This product, with 2.5 spatial resolution, is based on many different precipitation measures, including microwave and infrared retrievals, covering different periods within the entire data record (Huffman et al. 1997, Huffman et al. 2001, Adler et al. 2003). The daily GPCP data set, with one-degree spatial resolution, covers the period from 1997 to the present.

This dataset is obtainable from: `precip.gsfc.nasa.gov`

A.4 NCEP/NCAR Reanalysis

Data representing different atmospheric variables was obtained from the National Centers for Environmental Prediction/National Center for Atmospheric Research (NCEP-NCAR) reanalysis product (Kalnay et al. 1996, Kistler et al. 2001), archived on a 2.5 grid. The NCEP/NCAR reanalysis uses a frozen modern global data assimilation system, and a data base as complete as possible. The most recent reanalysis project uses a 3-dimensional variational (3D-Var) assimilation scheme and a T62 global spectral model with 28 "sigma" vertical levels.

Reanalysis data can be obtained at: `www.cdc.noaa.gov/cdc/reanalysis/`

A.5 TRMM precipitation product

The 3-hourly Tropical Rainfall Measuring Mission (TRMM product 3B42; Adler et al. 2000) data are used to describe the rainfall patterns within the wet and dry spells associated with monsoon intraseasonal variability. The spatial resolution of this data set is 0.25 with data from January 1998 to the present. This product is obtained by combining the TRMM high quality estimates with the infrared precipitation estimates (Adler et al. 2000), providing enhanced rain-rate estimates compared to calibrated infrared estimates, with the same superior time sampling of the latter. The algorithm uses data derived from the Precipitation Radar, the TRMM Microwave Imager, Visible Infrared Scanner, as well from a combination of the PR and TMI (TRMM Combined Instrument). TRMM Precipitation Radar data (product 2A25)

are also used to provide details of the vertical structure of rainfall.

TRMM data sets are distributed by Goddard Distributed Active Archive Center at: `lake.nascom.nasa.gov/data/dataset/TRMM/`

A.6 TRMM Microwave Imager (TMI) Sea surface Temperature (SST)

3-day average 0.25 gridded TMI (TRMM Microwave Imager) SST data (Wentz 1997) was used in the study. TMI has the advantage over Infrared based SST data by being able to measure SST in the presence of non-precipitating clouds (Wentz and Schabel 2000). The important feature of microwave retrievals is that SST can be measured through clouds, which are nearly transparent at 10.7 GHz. This is a distinct advantage over the traditional infrared SST observations that require a cloud-free field of view. Ocean areas with persistent cloud coverage can now be viewed on a daily basis missing a lot of the intraseasonal variability. Furthermore, microwave retrievals are not affected by aerosols and are insensitive to atmospheric water vapor. However, the microwave retrievals are sensitive to sea-surface roughness, while the infrared retrievals are not.

This data set can be obtained at: `www.ssmi.com/tmi/tmi_browse.html`

A.7 Links of other Data Sets

Optimally interpolated SST: This data set is described in Reynolds et al. (2002). This analysis has been produced at the National Oceanic and Atmospheric Administration (NOAA) using both in situ and satellite data from November 1981 to the present. The data set can be obtained at:

`www.cdc.noaa.gov/cdc/data.noaa.oisst.v2.html`

GTOPO30: A global digital elevation model (DEM) with a horizontal grid spacing of 30 arc seconds (approximately 1 kilometer). The data set can be obtained at: `edc.usgs.gov/products/elevation/gtopo30/gtopo30.html`

QuikSCAT: Wind speed and direction 10 meters above the water surface, derived from surface roughness (wind stress) using the microwave scatterometer SeaWinds flying on the QuikBird satellite since June 1999. The data set can be downloaded from: `www.ssmi.com/qscat/qscat_browse.html`

REFERENCES

[1] ADPC, 2004: *Initial Report on the Indian Monsoon Drought of 2002*. (Ed. A. Subbiah), available from Asian Disaster Preparedness Center, Bangkok, Thailand.

[2] Agudelo, P. A., J. A. Curry, C. D. Hoyos, P. J. Webster, 2006: Transition Between Suppressed and Active Phases of Intraseasonal Oscillations in the Indo-Pacific Warm Pool. *J. Climate*, Submitted.

[3] Adler, R.F., and Coauthors, 2003: The Version-2 Global Precipitation Climatology Project (GPCP) Monthly Precipitation Analysis (1979-present). *J. Hydrometeor.*, **4**, 1147-1167.

[4] Adler, R. F., G. J. Huffman, D. T. Bolvin, S. Curtis, and E. J. Nelkin, 2000: Tropical rainfall distributions determined using TRMM combined with other satellite and rain gauge information. *J. Appl. Meteor.*, **39**, 2007-2023.

[5] Annamalai, H., and J. M. Slingo, 2001: Active/Break Cycles: Diagnosis of the Intraseasonal Variability of the Asian Summer Monsoon. *Clim. Dyn.*, **18**, 85-102.

[6] Arkin, P. A, and B. N. Meisner, 1987: The relationship between large-scale convective rainfall and cloud cover over the western hemisphere during 1982-1084. *Mon. Wea. Rev.*, **115**, 51-74.

[7] Balmaseda, M. A., D. L. T. Anderson, and A. Vidard, 2005: Ocean analysis at ECMWF: from real time ocean initial conditions to historical reanalysis. Pp. 24-32 in ECMWF Newsletter No. 105, Autumn 2005, available at `http://www.ecmwf.int/publications/newsletters`

[8] Bamzai, A. S. and J. Shukla, 1999: Relation between Eurasian snow cover, snow depth, and the Indian summer monsoon: An observational study. *J. Climate*, **12**, 3117-3132.

[9] Blade, I., D. L. Hartmann 1993: Tropical Intraseasonal Oscillations in a Simple Nonlinear Model. *J. Atmos. Sci.*, **50**,2922-2939.

[10] Burpee, R.W., 1972: The origin and structure of easterly waves in the lower troposphere of North Africa. *J. Atmos. Sci.*, **29**, 77-90

[11] Emanuel, K A. 1987: An Air-Sea Interaction Model of Intraseasonal Oscillations in the Tropics. *J. Atmos. Sci.*, **44**, 2324-2340.

[12] CFAB, 2002: *Climate Forecasting Applications in Bangladesh Project Report 3: Application of Climate Forecasts in the Agriculture Sector*, 29 pp. Available from Asian Disaster Preparedness Center, Bangkok, Thailand.

[13] Carlson, T.N., 1969: Some remarks on African disturbances and their progress over the Tropical Atlantic. *Mon. Wea. Rev.*, **97**, 716-726.

[14] Chang, C.-P., and H. Lim, 1988: Kelvin wave-CISK: A possible mechanism for the 30-50 day oscillations. *J. Atmos. Sci.*, **45**, 1709-1720.

[15] Chang, C.-P., 1977: Viscous internal gravity waves and low-frequency oscillations in the tropics. *J. Atmos. Sci.*, **34**, 901-910.

[16] Clark, C. O., J. E. Cole and P. J. Webster, 2000: SST and Indian summer rainfall: predictive relationships and their decadal variability. *J. Climate*, **13**, 2503-2519.

[17] Collins, D., C.D. Hoyos, and P.J. Webster, 2006: Intraseasonall rainfall variability over West African during the summer monsoon season. *Submitted to* .

[18] Dickson, R. R., 1984; Eurasian snow cover versus Indian monsoon rainfall- An extension of the Hahn-Shukla results. *J. Clim. Appl. Meteorol.*, **23**, 171-173.

[19] ECMWF, 2004: Simulation and prediction of intra-seasonal with emphasis on the MJO. ECMWF/CLIVAR Workshop proceedings. A copy of the document could be obtained by contacting ECMWF library (library@ecmwf.int)

[20] Ferranti, L., J. M. Slingo, T. N. Palmer and B. J. Hoskins, 1997: Relations between interannual and intraseasonal monsoon variability as diagnosed from AMIP integrations. *Q. J. R. Meteorol. Soc.*, **123**, 1323-1357.

[21] Flatau, M. K., P. J. Flatau, D. Rudnick, 2001: The dynamics of double monsoon onsets. *J. Climate*, **21**, 4139-4146.

[22] Friedman, J.H., 1991: Multivariate Adaptive Regression Splines. *Annals of Stats*, **19**, 1-67.

[23] Gadgil, S., P. R. Seshagiri and K. Narahari Rao, 2002: Use of climate information for farm-level decision making: rainfed groundnut in southern India. *Agricultural Systems*, **74**, 431-457.

[24] Gadgil, S., P. R. Seshagiri and S. Sridhar, 1999: Modelling impact of climate variability on rainfed groundnut. *Current Science*, **76**, 557-569.

[25] Gadgil, S., 1996: Climate change and agriculture-An Indian perspective, *In Climate Variability and Agriculture*. Eds., Y. R. Abool, S. Gadgil and G. B. Pant, pp. 1-18, Narosa, New Delhi, India.

[26] Gadgil, S., and S. Sanjani, 1998: Monsoon precipitation in the AMIP runs. *Climate Dyn.*, **14**, 659-689.

[27] Gill, A. E., 1980: Some simple solutions for heat induced tropical circulation. *Q. J. R. Meteorol. Soc.*, **106**, 447-462.

[28] Goswami, B. N., and P. K. Xavier, 2003: Potential Predictability and Extended Range Prediction of Indian Summer Monsoon Breaks, *Geophys. Res. Lett.*, **30**, 1966, doi:10.1029/2003GL017810.

[29] Goswami, B. N., R. S. Ajayamohan, P. K. Xavier, and D. Sengupta, 2003: Clustering of synoptic activity by Indian summer monsoon intraseasonal oscillations, *Geophys. Res. Lett.*, **30**, 1431, doi:10.1029/2002GL016734,.

[30] Goswami B. N., R. S. A. Mohan, 2001: Intraseasonal oscillations and interannual variability of the Indian summer monsoon, *J. Climate*, **14**, 1180-1198.

[31] Goswami, B.N. and J. Shukla, 1984: Quasi-periodic oscillations in a symmetric general circulation model, *J. Atmos. Sci.*, **41**, 20-37.

[32] Grossman, R.L., and D.R. Durran, 1984: Interaction of low level flow with the Western Ghat mountains and off-shore convection in the summer monsoon. *Mon. Wea. Rev.*, **112**, 652-672.

[33] Grossman R.L., O. Garcia, 1990: The distribution of deep convection over ocean and land during the Asian summer monsoon, *J. Climate*, **3**, 1032-1044.

[34] Gruber, A., and A. F. Krueger, 1984: The status of the NOAA outgoing longwave radiation data set. *Bull. Amer. Meteor. Soc.*, **65**, 958-962.

[35] Hahn D. and J. Shukla, 1976: An apparent relationship between Eurasian snow cover and Indian monsoon rainfall. *J. Atmos. Sci.*, **33**, 2461-2462.

[36] Hartmann, D.L., 1994: *Global Physical Climatology.* Academic Press, 411 pp.

[37] Hartmann, D. L., H. H. Hendon, and R. A. Houze Jr., 1984: Some implications of the mesoscale circulations in tropical cloud clusters for large-scale dynamics and climate. *J. Atmos. Sci.*, **41**, 113121.

[38] Harzallah, A. and R. Sadourny, 1997: Observed lead-lag relationships between Indian summer monsoon and some meteorological variables. *Clim. Dyn.*, 13, 635-648 .

[39] Hastenrath, S., 1986: Tropical climate prediction: A progress report 1985-90, *Bull. Am. Meteorol. Soc.*, **67**, 819-825.

[40] Hastenrath, S., 1987: On the prediction of India summer rainfall anomalies, *J. Clim. Appl. Meteorol.*, **26**, 847-857.

[41] Hendon H. H., C. D. Zhang and J. D. Glick, 1999: Interannual variation of the Madden-Julian oscillation during austral summer. *J. Climate*, **12** , 2538-2550.

[42] Hendon, H. H., B. Liebmann, J.D. Glick, 1998: Oceanic Kelvin Waves and the Madden-Julian Oscillation. *J. Atmos. Sci.*, **55**, 88-101.

[43] Hendon, H. H., and M. L. Salby, 1996: Planetary-scale circulations forced by intraseasonal variations of observed convection. *J. Atmos. Sci.*, **53**, 1751-1758.

[44] Hendon, H.H., and M.L. Salby, 1994: Life cycle of the Madden Julian oscillation. *J. Atmos. Sci.*, **51**, 2225-2237.

[45] Higgins, R. W., Shi, W. 2001: Intercomparison of the Principal Modes of Interannual and Intraseasonal Variability of the North American Monsoon System. *J. Climate*, **14**, 403-417.

[46] Higgins, R. Wayne, Mo, Kingtse C. 1997: Persistent North Paci?c Circulation Anomalies and the Tropical Intraseasonal Oscillation. *J. Climate*, **10**, 223-244.

[47] Houze, R. A., Jr., S. S. Chen, D. E. Kingsmill, Y. Serra, and S. E. Yuter, 2000: Convection over the Pacific warm pool in relation to the atmospheric Kelvin-Rossby wave. *J. Atmos. Sci.*, **57**, 3058-3089.

[48] Houze R.A. Jr. 1993. *Cloud dynamics*. Academic Press, 573pp.

[49] Houze, R.A. 1997. Stratiform precipitation in regions of convection. *Bull. Amer. Meteor. Soc.*, **78**, 2179-2195.

[50] Hu, Q., Randall, D. A. 1994: Low-Frequency Oscillations in Radiative-Convective Systems. *J. Atmos. Sci.*, **51**, 1089-1099.

[51] Huffman, G. J., R. F. Adler, M. M. Morrissey, D. T. Bolvin, S. Curtis, R. Joyce, B. McGavock, and J. Susskind, 2001: Global precipitation at one-degree daily resolution from multisatellite observations. *J. Hydrometeor.*, **2**, 36-50.

[52] Huffman, G. J., and Coauthors, 1997: The Global Precipitation Project (GPCP) combined precipitation dataset. *Bull. Amer. Meteor. Soc.*, **78**, 5-20.

[53] Jiang, X., T. Li, and B. Wang, 2004: Structures and Mechanisms of the Northward Propagating Boreal Summer Intraseasonal Oscillation. *J. Climate*, **17**, 1022-1039.

[54] Joyce, R., and P. A. Arkin, 1997: Improved estimates of tropical and subtropical precipitation using the GOES Precipitation Index. *J. Atmos. Ocean. Tech.*, **10**, 997-1011.

[55] Kalnay, E., and 21 Coauthors, 1996: The NCEP/NCAR 40-Year Reanalysis Project. *Bull. Amer. Meteor. Soc.*, **77**, 437-471.

[56] Kiladis, G. N., and K. M. Weickmann, 1992: Circulation anomalies associated with tropical convection during northern winter. *Mon.Wea. Rev.*, **120**, 1900-1923.

[57] Kirtman, B. P., and J. Shukla, 2000: On the influence of the Indian summer Monsoon on ENSO. *Quart. J. Roy. Meteor. Soc.*, **126**, 213-239.

[58] Kemball-Cook, S., and B. Wang, 2001: Equatorial waves and air-sea interaction in the boreal summer intraseasonal oscillation. *J. Climate*, **14**,2923-2942.

[59] Knutson, T. and K. Weickmann, 1987: 30-60 day atmospheric oscillations: Composite life cycles of convection and circulation anomalies. *Mon. Wea. Rev.*, **115**, 1407-1436.

[60] Kripalani R.H., S.V. Singh and P.A. Arkin, 1991: Large scale features of rainfall and outgoing longwave radiation over Indian and adjoining regions. *Contributions to Atmospheric Physics*, **64**, 159-168.

[61] Krishnakumar, V. and K.-M Lau 1998: Possible role of symmetric instability in the onset and abrupt transitions of the Asian monsoon. *J. Meteor. Soc. Japan*, **76**, 363-383.

[62] Krishnamurti, T. N., M. Subramaniam, D. K. Oosterhof and G. Daughenbaugh, 1990: predictability of low-frequency modes. *Meteor. Atmos. Phys.*, **44**, 63-83.

[63] Krishnamurti, T. N., M. Subramaniam, G. Daughenbaugh, D. K. Oosterhof and J. H. Xue, 1992: One-month forecasts of wet and dry spells of the monsoon. *Mon. Wea. Rev.*, **120**, 1191-1223.

[64] Krishnamurti, T. N., S. O. Han, and V. Misra, 1995: Prediction of the wet and dry spells of the Australian monsoon. *Int. J. Clim.*, **15**, 753-771.

[65] Kumar K.K., B. Rajagopalan B. and M. A. Cane, 1999: On the weakening relationship between the Indian monsoon and ENSO. *Science*, **284**, 2156-2159.

[66] Large, W. G., J. C. McWilliams, and S. C. Doney, 1994: Oceanic vertical mixing: A review and a model with a nonlocal boundary layer parametrization. *Rev. Geophys.*, **32**, 363-403.

[67] Lal, M., K. K. Singh, G. Srinivasan, L. S. Rathore, D. Naidu, and C. N. Tripathi, 1999: Growth and yield responses of soybean in Madhya Pradesh, India to climate variability and change. *Agric. For. Meteor.*, **93**, 53-70.

[68] Lau, K.-M., and D. E. Waliser, Eds., 2005: *Intraseasonal Variability of the Atmosphere-Ocean Climate System*, Springer, Heidelberg, Germany, 474.

[69] Lau, K.-M., L. Peng, C. H. Sui, and T. Nakazawa, 1989: Dynamics of super cloud clusters, westerly wind bursts, 3060 day oscillations and ENSO: A unified view. *J. Meteor. Soc. Japan*, **67**, 205219.

[70] Lau, K.-M., and H. Weng, 1995: Climate Signal Detection Using Wavelet Transform: How to Make a Time Series Sing. *Bull. Amer. Meteor. Soc.*, **76**, 2391-2402.

[71] Lau, K.-M., Chan, P. H. 1988: Intraseasonal and Interannual Variations of Tropical Convection: A Possible Link between the 4050 Day Oscillation and ENSO?. *J. Atmos. Sci.*, **45**, 506-521.

[72] Lau, K.-M., Peng, L. 1987: Origin of Low-Frequency (Intraseasonal) Oscillations in the Tropical Atmosphere. Part I: Basic Theory. *J. Atmos. Sci.*, **44**, 950-972.

[73] Lawrence, D., and P. J. Webster, 2002: The boreal summer intraseasonal oscillation and the South Asian monsoon. *J. Atmos. Sci.*, **59**, 1593-1606.

[74] Lawrence, D., and P. J. Webster, 2001: Interannual variability of intraseasonal convection and the Asian monsoon. *J. Climate*, **14**, 2910-2922.

[75] Leonard T. and J. S. J. Hsu, 1999: *Bayesian Methods: an analysis for Statisticians and Interdisciplinary Researchers*. Cambridge Series in Statistical and Probabilistic Mathematics. Cambridge University Press, 333pp.

[76] Liebmann, B., and C. A. Smith, 1996: Description of a complete (interpolated) outgoing longwave radiation dataset. *Bull. Amer. Meteor. Soc.*, **77**, 1275-1277.

[77] Liebmann, B., Hartmann, D. L. 1984: An Observational Study of TropicalMid-latitude Interaction on Intraseasonal Time Scales during Winter. *J. Atmos. Sci.*, **41**, 3333-3350.

[78] Lin, J.L., G.N. Kiladis, B.E. Mapes, K.M. Weickmann, K.R. Sperber, W.Y. Lin, M. Wheeler, S.D. Schubert, A. Del Genio, L.J. Donner, S. Emori, J.-F. Gueremy, F. Hourdin, P.J. Rasch, E. Roeckner, and J.F. Scinocca, 2005: Tropical intraseasonal variability in 14 IPCC AR4 climate models. Part I: Convective signals. *J. Climate*, in press.

[79] Lindzen, R. S., and S. Nigam, 1987: On the role of sea surface temperature gradients in forcing low level winds and convergence in the tropics. *J. Atmos. Sci.*, **44**, 2418-2436.

[80] Lo, F. and H. H. Hendon, 2000: Empirical Prediction of the Madden-Julian Oscillation. *Mon. Wea. Rev.*, **128**, 2528-2543.

[81] Madden, R.A., and P.R. Julian, 1971: Description of the 40-50 day oscillation in the zonal wind in the tropical Pacific, *J. Atmos. Sci.*, **29**, 1109-1123.

[82] Madden, R.A., and P. R. Julian, 1972: Description of global-scale circulation cells in the Tropics with a 40-50-day period. *J. Atmos. Sci.*, **29**, 1109-1123.

[83] Madden, R.A. and P. R. Julian, 1994: Observations of the 40-50 day tropical oscillation: A review. *Mon. Wea. Rev.*, **122**, 814-837.

[84] Maloney, E. D., and J. T. Kiehl, 2002: MJO-related SST Variations over the Tropical Eastern Pacific During Northern Hemisphere Summer. *J. Climate*, **15**, 675-689.

[85] Maloney, E. D. and Hartmann, D. L., 2000: Modulation of hurricane activity in the Gulf of Mexico by the Madden-Julian oscillation. *Science*, **287**,2002-2004.

[86] Matsuno, T., 1966: Quasi-geostrophic motions in the equatorial area. *J. Meteor. Soc. Japan*, **44**, 25-43.

[87] Mo, K. C., 2001: Adaptive filtering and prediction of intraseasonal oscillations. *Mon. Wea. Rev.*, **129**, 802-817.

[88] Mo, K. C. 2000: Intraseasonal Modulation of Summer Precipitation over North America. *Mon. Wea. Rev.*, **128**, 1490-1505.

[89] Mo, K. C., Higgins, R. W. 1998: Tropical Influences on California Precipitation. *J. Climate*, **11**, 412-430.

[90] Murakami, T. 1976: Cloudiness fluctuations during the summer monsoon. *J. Meteor. Soc. Jpn.*, **54**, 175-181.

[91] Nakazawa, T., 1988: Tropical super clusters within intraseasonal variation over the western Pacific. J. *Meteor. Soc. Japan*, **66**, 823-839.

[92] Neelin, J. D., Held, I. M., Cook, Kerry H., 1987: Evaporation-Wind Feedback and Low-Frequency Variability in the Tropical Atmosphere. *J. Atmos. Sci.*, **44**, 2341-2348.

[93] Nogues-Paegle, J., and K. C. Mo 1997: Alternating Wet and Dry Conditions over South America during Summer. *Mon. Wea. Rev.*, **125**, 279-291.

[94] Palmer, T. N., 1994: Chaos and the predictability in forecasting the monsoons, *Proc. Indian. Natn. Sci. Acad., Part A.*, **60**, 57–66.

[95] Parthasarathy B., Munot A.A., Kothawale D.R., 1995. *Monthly and seasonal rainfall series for all-India homogeneous regions and meteorological subdivisions : 1871-1994*. Research Report No. RR-065,Indian Institute of Tropical Meteorology, Pune, 113pp.

[96] Parthasarathy, B., A. A. Munot, and D. R. Kothawale, 1988: Regression model for estimation of Indian food grain production from Indian summer rainfall, *Agric. For. Meteorol.*, **42**, 167-182.

[97] Parthasarathy, B., N. A. Sontakke, A. A. Munot, and D. R. Kothawale, 1987: Droughts/floods in the summer monsoon rainfall season over different meteorological subdivisions of India for the period 1871-1984. *J. Climatol.*, **7**, 57-70.

[98] Paegle, J. N., Byerle, L. A., Mo, K. C. 2000: Intraseasonal Modulation of South American Summer Precipitation. *Mon. Wea. Rev.*, **128**, 837-850.

[99] Peixoto, J.P., and A.H. Oort, 1992: *Physics of Climate*. American Institute of Physics, 520 pp.

[100] Poveda G., C. Hoyos, J. F. Meja, L. F. Cavajal, O. J. Mesa, A. Cuartas and J. Barco, 2001: Prediccin no lineal de los caudales medias mensuales del rio nare. *Avances en Recursos Hidraulicos*, **8**, 65-76.

[101] Randall, D., Khairoutdinov, M., Arakawa, A., Grabowski, W., 2003: Breaking the cloud parameterization deadlock. *Bull. Amer. Meteorol. Soc.*, **84**, 1547.

[102] Reynolds, C., P. J. Webster, and E. Kalnay, 1994: Random error growth in the numerical prediction models. *Mon. Wea. Rev.*, **122**, 1281-1305.

[103] Reynolds, R. W., D. C. Marsico, 1993: An Improved Real-Time Global Sea Surface Temperature Analysis. *J. Climate*, **6**, 114-119.

[104] Rui, H. and Wang B., 1990: Development characteristics and dynamic structure of tropical intraseasonal convection anomalies, *J. Atmos. Sci.*, **47**, 357-379.

[105] Salby, M. L., and H. H. Hendon, 1994: Intraseasonal behavior of clouds, temperature, and motion in the Tropics. *J. Atmos. Sci.*, **51**, 2207-2224.

[106] Selvaraju, R. 2003: Impact of the El Nino Southern Oscillation on Indian foodgrain production. *Int. J. Clim.*, **23**, 187-206.

[107] Sengupta, D., B. N. Goswami, B. N. and R. Senan, 2001: Coherent intraseasonal oscillations of ocean and atmosphere during the Asian summer monsoon, *Geophys. Res. Lett.*, **21**, 4127-4130.

[108] Schumacher, C., and R. A. Houze Jr., 2003: Stratiform rain in the tropics as seen by the TRMM Precipitation Radar. *J. Climate*, **16**, 1739-1756.

[109] Shukla, J., 1987: Long-range forecasting of monsoon. In *Monsoons*, (eds. J. Fein and P. L. Stephens), 523-548, John Wiley and Sons.

[110] Shukla, J. and D. A. Mooley, 1987: Empirical prediction of the summer monsoon rainfall over India. *Mon Wea. Rev.*, **115**, 695-703.

[111] Shukla, J. and D. A. Paolino, 1983: The Southern Oscillation and long range forecasting of the summer monsoon over India. *Mon. Wea. Rev.*, **111**,1830-1837.

[112] Sikka, D. and S. Gadgil, 1980: On the maximum cloud zone and the ITCZ over5 Indian longitudes during the southwest monsoon. *Mon. Wea. Rev.*, **108**, 1840-1853.

[113] Singh S.V., R.H. Kripalani and D.R. Sikka, 1992: Interannual variability of the Madden-Julian Oscillation in Indian summer monsoon rainfall. *J. Climate*, **5**, 973-978.

[114] Slingo J.M., K. R. Sperber and J. S. Boyle, 1996: Intraseasonal oscillations in 15 atmospheric general circulation models: Results from an AMIP diagnostic subproject. Clim. Dyn, 12, 325-357.

[115] Sperber, K.R., 2003: Propagation and vertical structure of the Madden-Julian oscillation. *Mon. Weather. Rev.* **131**, 3018-3037.

[116] Sultan, B., S. Janicot, and A. Diedhiou, 2003:West African monsoon dynamics. Part I: Documentation of intraseasonal variability. *J. Climate*, **16**, 33893406.

[117] Sperber K.R., C. Brankovic C., M. Deque, C. S. Frederiksen, R. Graham, A. Kitoh, C. Kobayashi, T. Palmer, K. Puri , W. Tennant and E. Volodin, 2001: Dynamical seasonal predictability of the Asian summer monsoon. *Mon Wea. Rev.*, **129**, 2226-2248.

[118] Sperber K.R., J. M. Slingo and H. Annamalai, 2000: Predictability and the relationship between subseasonal and interannual variability during the Asian summer monsoon. *Q. J. Roy. Met. Soc.*, **126**, 2545-2574.

[119] Sperber, K.R., and T. Palmer, 1996: Interannual tropical rainfall variability in general circulation model simulations associated with the Atmospheric Model Intercomparison Project. *J. Climate*, **9**, 2727-2750.

[120] Stephens, G. L., P. J. Webster, R. H. Johnson, R. Engelen, and T. L'Ecuyer, 2004: Observational Evidence for the Mutual Regulation of the Tropical Hydrological Cycle and Tropical Sea Surface Temperatures. *J. Climate*, **17**, 2213-2224.

[121] von Storch, H. and J. Xu, 1990: Principal oscillation pattern analysis of the 30- to 60-day oscillation in the tropical troposphere. *Clim. Dyn.*, **4**, 175-190.

[122] von Storch, H. and F. W. Zwiers, 1999: *Statistical analysis in Climate Research.* Cambridge University Press, 484 pp.

[123] Terray, L., E. Sevault, E. Guilyardi and O. Thual, 1995: OASIS 2.0, user's guide and reference manual. Technical report. [Available from CERFACS, France].

[124] Tomas, R. and P. J. Webster, 1997: On the location of the intertropical convergence zone and near-equatorial convection: The role of inertial instability. *Quar. J. Roy. Met. Soc.*, **123**, 1445-1482.

[125] Tomas, R., J. R. Holton and P. J. Webster, 1999: On the theory of the location of convection in strong cross-equatorial pressure gradient flows. *Q. J. Roy. Meteor. Soc.*, **125**, 1107-1127.

[126] Torrence, T. and P. J. Webster, 2000: Interdecadal changes in the ENSO-Monsoon System. *J. Climate*, **12**, 2679-2690.

[127] Torrence, C. and P. J. Webster, 1999: Interdecadal changes in the ENSO-Monsoon System. *J. Climate*, **12**, 2679-2690.

[128] Torrence, C., and G. P. Compo, 1998: A practical guide to wavelet analysis. *Bull. Amer. Meteor. Soc.*, **79**, 61-78.

[129] Tracton M.S., K. Mo, W. Chen, E. Kalnay, R. Kistler, G. White, 1989: Dynamical extended-range forecasting (DERF) at the National Meteorological Service. *Mon. Wea. Rev.*, **117**, 1604-1635.

[130] Tracton, M. S., and R. E. Kistler, 1988: Dynamic extended range forecasting (DERF) at NMC, Eighth Conference on Numerical Weather Prediction, February 22-26, Baltimore, Maryland.

[131] Vialard, J., F. Vitart, M. A. Balmaseda, T. Stockdale, and D. L. T. Anderson, 2003: An ensemble generation method for seasonal forecasting with and ocean-atmosphere coupled model. *Mon. Wea. Rev.*, **133**, 441-453.

[132] Vitart, F. 2004: Monthly Forecasting at ECMWF. *Mon. Wea. Rev.* **132**, 2761-2779.

[133] Waliser, D. E., R. Murtugudde, P. Strutton, and J.-L. Li, 2005: Subseasonal organization of ocean chlorophyll: Prospects for prediction based on the Madden-Julian Oscillation, *Geophys. Res. Lett.*, **32**, L23602, doi:10.1029/2005GL024300.

[134] Waliser, D., W. Stern, S. Schubert, and K. M. Lau, 2003a: Dynamical predictability of intraseasonal variability associated with the Asian summer monsoon. *Quart. J. Roy. Meteor. Soc.*, **129**, 2897-2925.

[135] Waliser, D. E., K. Jin, I.-S. Kang, W. F. Stern, S. D. Schubert, M.L.C Wu,K.-M. Lau, M.-I. Lee, V. Krishnamurthy, A. Kitoh, G. A. Meehl, V. Y. Galin, V. Satyan, S. K. Mandke, G. Wu, Y. Liu, and C.-K. Park, 2003b: AGCM Simulations of Intraseasonal Variability Associated with the Asian Summer Monsoon, *Clim. Dyn.*, **21**, 423-446.

[136] Waliser D.E., Lau K-. M., Stern W. and C. Jones, 2003c: Potential predictability of the Madden-Julian oscillation, *B. Amer. Meteor. Soc.*, **84**, 33-50.

[137] Waliser, D., S. Schubert, A. Kumar, K. Weickmann, and R. Dole, 2003d: *Proceedings from a workshop on "Modeling, Simulation and Forecasting of Subseasonal Variability"*, 4-5 June 2003, University of Maryland, College Park, Maryland, NASA/CP 2003-104606, vol. 25, pp. 62.

[138] Waliser, D. E., C. Jones, J. K. Schemm and N. E. Graham, 1999: A Statistical Extended-Range Tropical Forecast Model Based on the Slow Evolution of the Madden-Julian Oscillation. *J. Climate*, **12**, 1918-1939.

[139] Waliser, D. E. and N. E. Graham, 1993: Convective Cloud Systems and Warm-Pool SSTs: Coupled Interactions and Self-Regulation. *J. Geoph. Res.*, **98**, 12881-12893.

[140] Walker, G. T., 1923: Correlations in seasonal variations of weather. VIII, A preliminary study of world weather. *Mem. Indian Meteorl. Dept.*, **24**, 75-131.

[141] Wang, B., P. J. Webster, and H. Teng: 2005, Antecedents and self-induction of active-break south Asian monsoon unraveled by satellites, *Geophys. Res. Lett.*, **32**, L04704, doi:10.1029/2004GL020996.

[142] Wang, B. and LinHo, 2002: Rainy seasons of the Asian-Pacific monsoon. *J. Climate*, **15**, 386-398.

[143] Wang, B., and X. Xie, 1998: Coupled modes of the warm pool climate system. Part I: The role of air-sea interaction in maintaining Madden-Julian oscillations. *J. Climate*, **8**, 2116-2135.

[144] Wang B. and H. Rui, 1997: Synoptic climatology of transient tropical intraseasonal convective anomalies. *Meteor. Atmos. Phys.*, **74**, 1975-1985

[145] Qang, B. and X. Xie, 1997: A model for boreal summer Intraseasonal Oscillation. *J. Atmos. Sci.*, **54**, 72-86.

[146] Wang, B. 1988: Dynamics of Tropical Low-Frequency Waves: An Analysis of the Moist Kelvin Wave. *J. Atmos. Sci.*, **45**, 2051-2065.

[147] Webster, P. J, and C. Hoyos, 2004: Prediction of Monsoon Rainfall and River Discharge on 15-30 day Time Scales. *Bull. Amer. Met. Soc.*, **85**, 1745-1765.

[148] Webster, P., and Coauthors, 2002: The JASMINE pilot study. Bull. Amer. Meteor. Soc., 83, 1603-1630.

[149] Webster, P.J., T. Palmer, M. Yanai, R. Tomas, V. Magaa, J. Shukla, and A. Yasunari, 1998: Monsoons: Processes, predictability and the prospects for prediction. *J. Geophys. Res.*, **103**, 14 451-14 510.

[150] Webster, P. J. and S. Yang, 1992: Monsoon and ENSO: Selectively Interactive Systems. *Quart. J. Roy. Meteor. Soc.*, **118**, 877-926.

[151] Webster, P. J., 1983: Mechanisms of Monsoon Transition: Surface Hydrology Effects. *J. Atmos. Sci.*, **40**, 2110-2124.

[152] Webster, P. J. 1972: Response of the Tropical Atmosphere to Local Steady Forcing. *Mon. Wea. Rev.*, **100**, 518-541.

[153] Wentz, F. J., 1997: A well-calibrated ocean algorithm for special sensor microwave/imager. *J. Geophys. Res.*, **102**, 8703-8718.

[154] Wentz, F. J., and M. Schabel, 2000: Precise climate monitoring using complementary satellite data sets. *Nature*, **403**, 414-416.

[155] Wheeler, M.C. and H.H. Hendon, 2004: An all-season real-time multivariate MJO index: Development of an index for monitoring and prediction. *Mon. Wea. Rev.*, **132**, 1917-1932.

[156] Wheeler, M. and K. M. Weickmann, 2001: Real-time monitoring and prediction of modes of coherent synoptic to intraseasonal tropical variability. *Mon. Wea. Rev.*, **129**, 2677-2694.

[157] Wheeler, M. and G. N. Kiladis, 1999: Convectively coupled equatorial waves: Analysis of clouds and temperature in the wavenumber-frequency domain. *J. Atmos. Sci.*, **56**, 374-399.

[158] Woolnough, S. J., F. Vitart, and M.A. Balsameda, 2005: The role of the ocean in the Madden-Julian Oscillation: Implications for MJO prediction. *Q. J. R. Meteorol. Soc.* Submitted.

[159] Yasunari, T., 1979: Cloudiness fluctuations associated with the Northern Hemisphere summer monsoon. *J. Meteor. Soc. Japan*, **57**, 227-242.

[160] Yasunari, T., 1980: A quasi-stationary appearance of the 30-40 day period in the cloudiness fluctuations during the summer monsoon over India. *J. Meteorol. Soc. Jpn*, **58**, 225-229.

[161] Yasunari, T., 1981: Structure of an Indian summer monsoon system with around 40-day period. *J. Meteor. Soc. Japan*, **59**, 336-354.

[162] Xie, S.-P., H. Xu, N.H. Saji, Y. Wang, and W.T. Liu, 2005: Role of narrow mountains in large-scale organization of Asian monsoon convection. *J. Climate*, in press.

[163] Zhang, C., 2005: Madden-Julian Oscillation. *Rev. Geophys*, **43**, RG2003, doi:10.1029/2004RG000158.

[164] Zuidema, P., 2003: Convective Clouds over the Bay of Bengal. *Mon. Wea. Rev.*, **131**, 780-798.